

# APPLIED COMPUTATIONAL ELECTROMAGNETICS SOCIETY JOURNAL

May 2022  
Vol. 37 No. 5  
ISSN 1054-4887

**The ACES Journal is abstracted in INSPEC, in Engineering Index, DTIC, Science Citation Index Expanded, the Research Alert, and to Current Contents/Engineering, Computing & Technology.**

The illustrations on the front cover have been obtained from the ARC research group at the Department of Electrical Engineering, Colorado School of Mines

Published, sold and distributed by: River Publishers, Alsbjergvej 10, 9260 Gistrup, Denmark

# THE APPLIED COMPUTATIONAL ELECTROMAGNETICS SOCIETY

<http://aces-society.org>

## EDITORS-IN-CHIEF

**Atef Elsherbeni**

Colorado School of Mines, EE Dept.  
Golden, CO 80401, USA

**Sami Barmada**

University of Pisa, ESE Dept.  
56122 Pisa, Italy

## ASSOCIATE EDITORS

**Maokun Li**

Tsinghua University  
Beijing 100084, China

**Wei-Chung Weng**

National Chi Nan University, EE Dept.  
Puli, Nantou 54561, Taiwan

**Paolo Mezzanotte**

University of Perugia  
I-06125 Perugia, Italy

**Mauro Parise**

University Campus Bio-Medico of Rome  
00128 Rome, Italy

**Alessandro Formisano**

Seconda Università di Napoli  
81031 CE, Italy

**Luca Di Rienzo**

Politecnico di Milano  
20133 Milano, Italy

**Yingsong Li**

Harbin Engineering University  
Harbin 150001, China

**Piotr Gas**

AGH University of Science and Technology  
30-059 Krakow, Poland

**Lei Zhao**

Jiangsu Normal University  
Jiangsu 221116, China

**Riyadh Mansoor**

Al-Muthanna University  
Samawa, Al-Muthanna, Iraq

**Long Li**

Xidian University  
Shaanxa, 710071, China

**Sima Noghianian**

Commscope  
Sunnyvale, CA 94089, USA

**Lijun Jiang**

University of Hong Kong, EEE Dept.  
Hong, Kong

**Steve J. Weiss**

US Army Research Laboratory  
Adelphi Laboratory Center (RDRL-SER-M)  
Adelphi, MD 20783, USA

**Qiang Ren**

Beihang University  
Beijing 100191, China

**Shinishiro Ohnuki**

Nihon University  
Tokyo, Japan

**Jiming Song**

Iowa State University, ECE Dept.  
Ames, IA 50011, USA

**Nunzia Fontana**

University of Pisa  
56122 Pisa, Italy

**Kubily Sertel**

The Ohio State University  
Columbus, OH 43210, USA

**Toni Bjorninen**

Tampere University  
Tampere, 33100, Finland

**Stefano Selleri**

DINFO - University of Florence  
50139 Florence, Italy

**Giulio Antonini**

University of L Aquila  
67040 L Aquila, Italy

**Santanu Kumar Behera**

National Institute of Technology  
Rourkela-769008, India

**Yu Mao Wu**

Fudan University  
Shanghai 200433, China

**Antonio Musolino**

University of Pisa  
56126 Pisa, Italy

**Daniele Romano**

University of L Aquila  
67100 L Aquila, Italy

**Fatih Kaburcuk**

Sivas Cumhuriyet University  
Sivas 58140, Turkey

**Abdul A. Arkadan**

Colorado School of Mines, EE Dept.  
Golden, CO 80401, USA

**Alireza Baghai-Wadji**

University of Cape Town  
Cape Town, 7701, South Africa

**Huseyin Savci**

Istanbul Medipol University  
34810 Beykoz, Istanbul

**Salvatore Campione**

Sandia National Laboratories  
Albuquerque, NM 87185, USA

**Marco Arjona López**

La Laguna Institute of Technology  
Torreon, Coahuila 27266, Mexico

**Zhixiang Huang**

Anhui University  
China

**Ibrahim Mahariq**

American University of the Middle East  
Kuwait and University of Turkish Aeronautical Association  
Turkey

**Kaikai Xu**

University of Electronic Science and  
Technology of China  
China

## EDITORIAL ASSISTANTS

**Matthew J. Inman**  
University of Mississippi, EE Dept.  
University, MS 38677, USA

**Shanell Lopez**  
Colorado School of Mines, EE Dept.  
Golden, CO 80401, USA

## EMERITUS EDITORS-IN-CHIEF

**Duncan C. Baker**  
EE Dept. U. of Pretoria  
0002 Pretoria, South Africa

**Allen Glisson**  
University of Mississippi, EE Dept.  
University, MS 38677, USA

**Ahmed Kishk**  
Concordia University, ECS Dept.  
Montreal, QC H3G 1M8, Canada

**Robert M. Bevensee**  
Box 812  
Alamo, CA 94507-0516

**Ozlem Kilic**  
Catholic University of America  
Washington, DC 20064, USA

**David E. Stein**  
USAF Scientific Advisory Board  
Washington, DC 20330, USA

## EMERITUS ASSOCIATE EDITORS

**Yasushi Kanai**  
Niigata Inst. of Technology  
Kashiwazaki, Japan

**Mohamed Abouzahra**  
MIT Lincoln Laboratory  
Lexington, MA, USA

**Alexander Yakovlev**  
University of Mississippi, EE Dept.  
University, MS 38677, USA

**Levent Gurel**  
Bilkent University  
Ankara, Turkey

**Sami Barmada**  
University of Pisa, ESE Dept.  
56122 Pisa, Italy

**Ozlem Kilic**  
Catholic University of America  
Washington, DC 20064, USA

**Erdem Topsakal**  
Mississippi State University, EE Dept.  
Mississippi State, MS 39762, USA

**Alistair Duffy**  
De Montfort University  
Leicester, UK

**Fan Yang**  
Tsinghua University, EE Dept.  
Beijing 100084, China

**Rocco Rizzo**  
University of Pisa  
56123 Pisa, Italy

**Atif Shamim**  
King Abdullah University of Science and  
Technology (KAUST)  
Thuwal 23955, Saudi Arabia

William O'Keefe Coburn  
US Army Research Laboratory  
Adelphi, MD 20783, USA

**Mohammed Hadi**  
Kuwait University, EE Dept.  
Safat, Kuwait

**Amedeo Capozzoli**  
Univerita di Naoli Federico II, DIETI  
I-80125 Napoli, Italy

**Wenxing Li**  
Harbin Engineering University  
Harbin 150001, China

## EMERITUS EDITORIAL ASSISTANTS

**Khaleb ElMaghoub**  
Trimble Navigation/MIT  
Boston, MA 02125, USA

**Kyle Patel**  
Colorado School of Mines, EE Dept.  
Golden, CO 80401, USA

**Christina Bonnington**  
University of Mississippi, EE Dept.  
University, MS 38677, USA

**Anne Graham**  
University of Mississippi, EE Dept.  
University, MS 38677, USA

**Madison Lee**  
Colorado School of Mines, EE Dept.  
Golen, CO 80401, USA

**Allison Tanner**  
Colorado School of Mines, EE Dept.  
Golden, CO 80401, USA

**Mohamed Al Sharkawy**  
Arab Academy for Science and Technology, ECE Dept.  
Alexandria, Egypt

## MAY 2022 REVIEWERS

<b>Agarwal</b>	<b>Antonio Orlandi</b>
<b>Ravi Kumar Arya</b>	<b>Pavel Roy Paladhi</b>
<b>Ahmed Attiya</b>	<b>Andrew Peterson</b>
<b>Luigi Boccia</b>	<b>Sergio Pignari</b>
<b>Fangyuan Chen</b>	<b>CJ Reddy</b>
<b>Thippesha D.</b>	<b>Kannadhasan S.</b>
<b>Arkaprovo Das</b>	<b>Mohammed Salim</b>
<b>Shian Hwu</b>	<b>Suganthi Santhanam</b>
<b>Aydin Ilhan</b>	<b>Huseyin Savci</b>
<b>Pankaj Jha</b>	<b>Qusai Hadi Sultan</b>
<b>Anubhav Kumar</b>	<b>Ye Tian</b>
<b>Matteo Bruno Lodi</b>	<b>Grzegorz Tytko</b>
<b>Fabrizio Loreto</b>	<b>Salvatore Ventre</b>
<b>Valentin Mateev</b>	<b>Salah I. Yahya</b>
<b>Lin Meiyun</b>	<b>Abubakar Yakubu</b>
<b>Michel M. Ney</b>	<b>Wentao Yuan</b>
<b>Mahdi Oliaei</b>	<b>Qiwei Zhan</b>

TABLE OF CONTENTS

A Brief History of Finite Element Method and Its Applications to Computational Electromagnetics  
Stefano Selleri ..... 517

Complex Inhomogeneous Dielectric Target Modeling and Scattering Estimation using a Self-Designed Software  
Muyu Hou, Shuhong Gong, Yanchun Zuo, and Yu Liu ..... 526

Isolation Enhancement using CSRR Slot in the Ground for Compact Two-Element Textile MIMO Antenna  
Navneet Sharma, Anubhav Kumar, Asok De, and R. K. Jain ..... 535

Wearable Panda-Shaped Textile Antenna with Annular Ring-Defected Ground Structure for Wireless Body Area Networks  
T. Annalakshmi and S. Ramesh ..... 546

An Empirical Loss Model for an Additively Manufactured Luneburg Lens Antenna  
Brian F. LaRocca and Mark S. Mirotznik ..... 554

A Parasitic Hat for Microstrip Antenna Design Based on Defected Structures for Multiband Applications  
Faten F. Ismail, Mostafa A. El-Aasser, and Nasr H. Gad ..... 568

Solar Cell Integrated Wearable Patch Antenna on Artificial Magnetic Conductor for On-Body and In-Body Communications  
Suresh Babu T. Naganathan and Sivakumar Dhandapani ..... 576

Dual-Band Highly Isolated Eight-Element MIMO Antenna for 5G Mobile Phone  
Yonghao Wang, Xin Wang, Junlin Wang, and Rui Shao ..... 588

Triple Bands UWB Antenna with Minimum Printed Area for Power Harvesting Applications  
Nourhan D. Sehsah, Tamer G. Abouelnaga, and Hamdi A. Elmikati ..... 597

Design of a Novel Circularly Polarized MIMO Antenna with Enhanced Isolation for Ultra-wideband Communication Lei Zhang, Quanyuan Feng, and Muhammad K. Khan .....	607
Multi-Mode Excitation by Interleaved EBG Structure for Suppression of Power/Ground Noise in Multi-Layer PCBs Ding-Bing Lin, Yen-Hao Chen, and Min-Hung Hsieh .....	619
Calculation and Characteristics Analysis for Radiated Electromagnetic Field of High Voltage Converter Valve Hongsen Zou, Lin Zheng, Yuan Zhang, Jianan Zhang, Yajie Wang, and Huafeng Wang .....	624
Model of Ferrite-cored Driver-pickup Coil Probe Application of TREE Method for Eddy Current Nondestructive Evaluation Siquan Zhang and Chengkai Ye .....	632
Research on the Characteristics of the Pantograph Arc and Analyzing its Influence on the ILS Yingchun Xiao, Feng Zhu, Nan Lu, Zixuan Wang, and Shengxan Zhuang .....	639
Rule for Mode Coupling Efficiency in Optical Waveguide Crossing Billel Bentouhami and Zaia D. Kaddour .....	648

# A Brief History of Finite Element Method and Its Applications to Computational Electromagnetics

Stefano Selleri

Department of Information Engineering  
University of Florence, Florence I-50139, Italy  
stefano.selleri@unifi.it

**Abstract** – The development of the finite element method is traced, from its deepest roots, reaching back to the birth of calculus of variations in the 17th century, to its earliest steps, in parallel with the advent of computers, up to its applications in electromagnetics and its flourishing as one of the most versatile numerical methods in the field. A survey on papers published on finite elements, and on *ACES Journal* in particular, is also included.

**Index Terms** – Finite elements, history of computation, numerical methods.

## I. THE PRODROMES

If, by finite elements (FEs), we intend the piecewise polynomial approximation of the solution of a partial differential equation (PDE) with adequate boundary conditions, then an exact date of its birth is known: January 1943. In an appendix to [1], Richard Courant (Figure 1), who had already investigated finite differences (FDs) in 1928 [2], sketched in two pages the essence of FE as intended above [3].

The paper was the written record of a dissertation on the equilibrium and vibrations of 2D domains: plates, membranes, and the like. The dissertation was held on May 3, 1941, and submitted as a paper on June 16, 1942. The matter treated in the appendix, the numerical solution of the problem, was indeed not included in the dissertation.

While Courant founded the computational part of FE, its essence was in the variational problem he was addressing, and variational problems are much older than FE.

Johan Bernoulli in 1696 proposed the problem of the shortest time path connecting two points at different altitudes A and B [4]. This was something Galileo Galilei had already investigated, showing, experimentally, that a straight path is slower than an arc of circumference, but there was no proof that, in this latter, time was minimum [5].

Indeed, Isaac Newton, Jakob Bernoulli, Gottfried Wilhelm von Leibnitz, Ehrenfried Walter von

Tschirnhaus, and Guillaume de l'Hôpital provided their own solution. In particular, Leibnitz exploited a piecewise linear approximation, which was a first step in his development of differential calculus, which he finally published [6], independently and shortly before Newton [7]. The question on the priority of this development lasted for decades. Leonhard Euler later worked on these kinds of problems and developed a brand-new branch of mathematics: the Calculus of Variations, a name suggested to Euler by Joseph-Louis Lagrange.

Indeed, also the idea of approximating a 2D variational problem on a mesh of triangles is older than Courant. Karl H. Schellbach in 1851 proposed a FE-like solution for determining the surface  $S$  of minimum area enclosed by a given curve by using a piecewise approximation of  $S$  on triangles [8].

A subsequent, important, step was done by John W. Strutt, Lord Rayleigh, who proposed a variational approach to the solution of PDEs with appropriate boundary conditions, which is of boundary value problems (BVPs) [9]. This approach was later developed by Walther Ritz, who conceived an approximation of the BVP solution as a finite linear combination of continuous functions [10]. One classical approach to FEs is indeed called Rayleigh–Ritz method.

An alternative approach to FE is that based on the idea of the minimization of an error defined in terms of an orthogonality condition versus some appropriate finite-dimensional sub-space. This technique was first suggested by Boris G. Galerkin [11] and developed by Alessandro Faedo [12], to what is now called a Faedo–Galerkin approach to FEs.

Before Courant, an FEs harbinger is the tear method introduced by Gabriel Kron, where a large and complex system is reduced to a network of interconnected small and simpler systems (1939). This was not indeed a solution of a PDE since the simple systems, the elements, were exactly specified, and, hence, the issue was just the algebraic interconnection [13]. Later, in 1941, Alexander Hrennikoff solved plane elasticity problems by splitting up the domain into little finite pieces whose stiffness



Fig. 1. Left to right: Richard Courant (1888-1972), John H. Argyris (1913-2004), and Ray W. Clough (1920-2016).

was approximated by ideal bars, beams, and springs [14]. Shortly later, Douglas McHenry exploited a similar lattice analysis [15], leading to solutions which were primitive in mathematical and physical terms, but which were clearly leading to something implying a piecewise linear approximation over square or cubic cells.

John H. Argyris (Figure 1) then began in the 1950s to put all these ideas together by developing further Kron's technique and adding an approximation which was truly based on a variational method [16]. In the same years, Samuel Levy introduced an evolution of Hrennikoff and McHenry lattice models by analyzing the behavior of aircraft wings via an assembly of box-elements comprising beams, torsion bars, rods, and shear panels [17]. Levy's direct stiffness method had a great impact on aircraft structure analysis.

Actually, it is interesting to note that, after the early mathematical developments, the main actors on FEs in the 1950s and 1960s were not mathematicians but engineers, concerned more with design issues of airplanes than on the theoretical aspects of the method.

## II. EARLY FINITE ELEMENTS

The first work truly embodying the essence of FEs and which can be pointed to as giving birth to the method is that of M. Jon Turner and co-workers [18]. In this paper, an attempt to exploit both a local approximation of the PDE of elasticity and an assembly strategy among local approximations was carried out, even if no variational principle was used. This paper was followed by the one by Ray W. Clough (Figure 1) where the name FE method finally appeared [19].

In the 1960s, the engineering community started to recognize the usefulness of FEs in its variational for-

mulation, which is that of Rayleigh and Ritz, which, indeed, was applicable only to symmetric operators. In these years, aeronautics was the main application, and the Dayton Conferences on FEs held in 1965, 1968, and 1970 were occasions of remarkable and innovative accomplishments. In these same years, the fact that FEs could also be applied to unsymmetric operators became clear, with the solution of Navier-Stokes equations by J. Tinsén Oden (Figure 2) [20–22].

The first comprehensive textbook on FEs appeared in those same years, authored by Olgierd C. Zienkiewicz (Figure 2) and Yau K. Cheung in 1967 [23], shortly followed by one by Zienkiewicz alone [24].

Of course, these developments were made possible by the parallel development of digital computers, born around World War II, and of adequate programming languages, like FORTRAN introduced in 1954.

In the late 1960s, FEs were ported to wave electromagnetics by Peter P. Silvester (Figure 2) [25, 26] and, about a decade later, the first FEs book devoted to electrical engineers was published [27]. This is still, in its third edition, the bible of FEs for electrical engineers.

While practice was going fast, theory lagged. The first proof of convergence of FEs might be traced to Feng Kang [28], but the paper, being in Chinese, was overlooked. A second paper focused on a rigorous proof of convergence was published by M.W. Johnson and Richard W. McLay in 1968 [29]. Even if these are the first example of a rigorous theoretical approach to FEs, the tools we are now familiar with are a little older; simply, they were not explicitly applied.

Distribution theory, which indeed is at the basis of FE theory, was developed by Sergej L. Sobolev in 1936, when he introduced generalized functions to work with

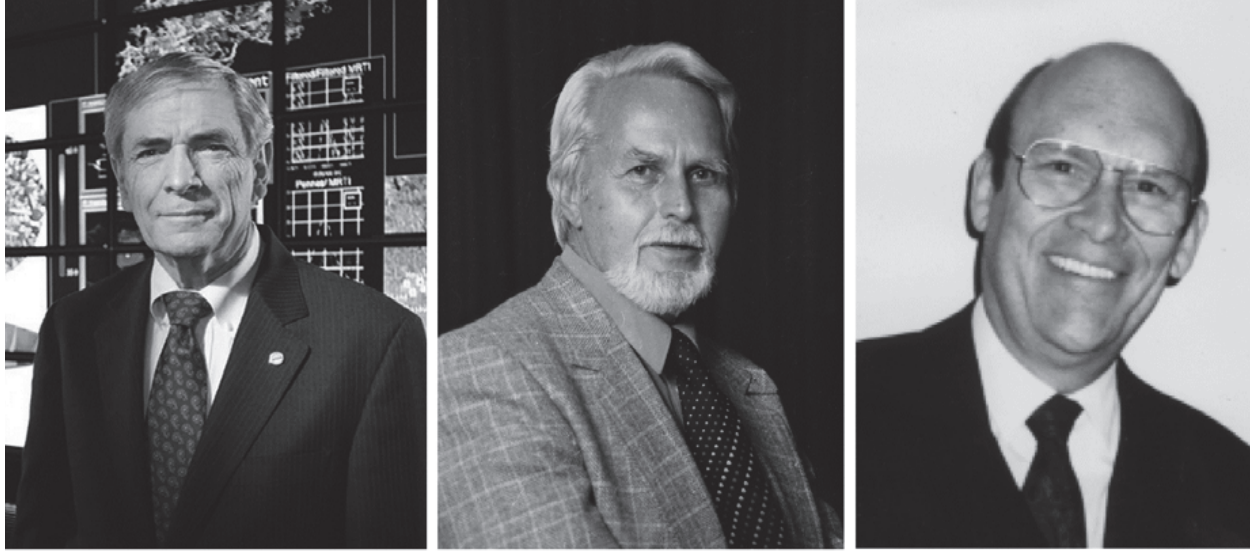


Fig. 2. Left to right: J. Tinsley Oden (1936-), Olgierd C. Zienkiewicz (1921-2009), and Peter P. Silvester (1935-1996).

weak solutions of PDEs [30]. Later, Laurent Schwartz, in the 1940s, put together a sound theory of distributions [31, 32].

PDE theory and approximation theory in the mathematical world remained separate from variational methods and, hence, from FE application up to the late 1960s, when FE methodology and the theory of PDE approximation via functional analysis finally unite.

Then, in the 1970s, a great leap forward was done in the mathematical background of FEs: *a-priori* error estimator came out, elliptic linear problems were fully known, while parabolic and hyperbolic problems, also non-linear, were at their beginning in the FEs' world.

Element interpolation characteristics were studied by Miloš Zlámal [33] followed by a fundamental comprehensive work by Ivo M. Babuška and A. Kadir Aziz [34], where Sobolev spaces and elliptic problems are comprehensively treated in an FE framework.

### III. ELECTROMAGNETICS

Early applications to wave electromagnetics, developed after [25], tried to handle the vector nature of the fields by treating them component-by-component. Unfortunately, all these early vectorial methods were plagued by the occurrence of spurious modes, which are solutions of the numerical FEM problem which were non-physical [35].

An early analysis of spurious modes, which indeed were present also in FDs [36], can be found in Adalbert Konrad's Ph.D. thesis [37] and in his paper where he first solves the vector curl-curl equation [38]. His analysis suggested that spurious modes were solutions, where the energy norm on the domain vanishes, but boundary con-

ditions are not satisfied, and this was due to a lack of solenoidality of the FEM procedure.

Subsequent efforts on enforcing the vanishing of  $\nabla \cdot \mathbf{B}$  removed part of the spurious modes. Much research was done in this area by applying a penalty parameter effectively pushing spurious modes eigenvalues out of the range of interest yet having negligible effect on physical modes [39]. The issue on selecting the right value for the penalty parameter was addressed in [40]; yet, it was finally proven [41] that the curl-curl scheme inevitably led to spurious modes difficult to handle even with penalty scheme, while Helmholtz equation has spurious modes too, but these were ruled out by enforcing physical boundary conditions.

Jon P. Webb and Konrad applied a different approach based on an *a-posteriori* imposition of a set of constraints on the equation to guarantee solenoidality [42, 43]; however, this approach did not prove general.

In the same years, the concept of edge elements was developed by Jean-Claude Nedelec and others [44–48]. Edge elements do not over-constrain continuity of the field at element nodes but just enforce the physical continuity of the tangential field component at the edges, easily handling dielectric interfaces. Yet, these edge elements' origin can be traced back to an FE unrelated work by Hassler Whitney few decades older [49].

These elements finally lead to a more accurate representation of the field in terms of element bases, getting rid of the spurious modes which had plagued the method in the beginning [50].

Current state-of-the-art elements not only exclude spurious modes [51] but also allow to consider the

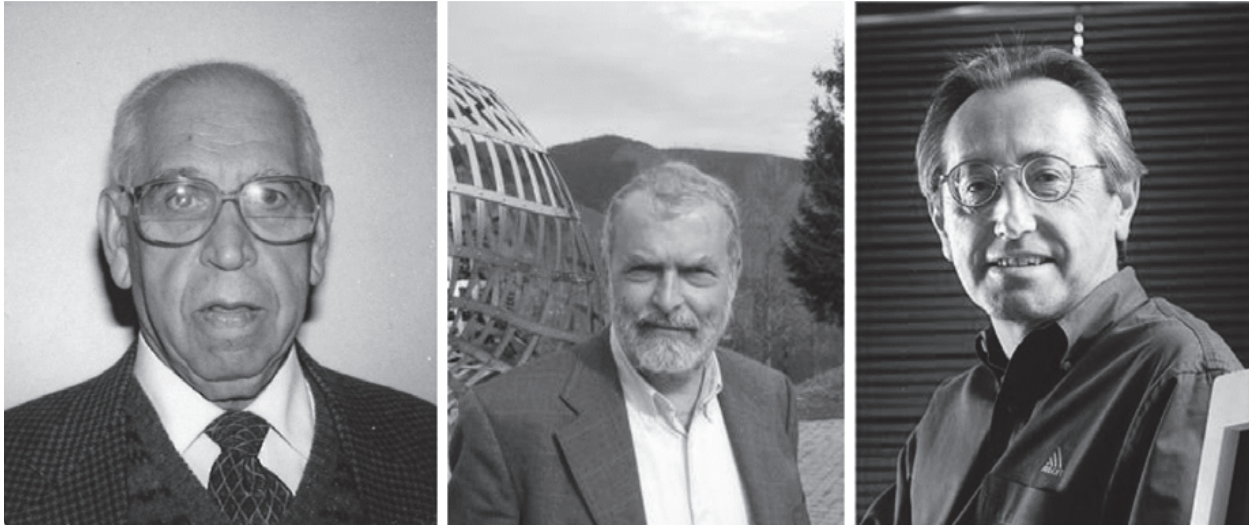


Fig. 3. Left to right: A. Kadir Aziz (1923-2016), Jean-Claude Nedelec (1943- ), and Zoltan Cendes (1946- ).

divergent behavior of the electromagnetic field at edges and tips [52, 53].

Another key point in FE development in the 1970s and 1980s was handling unbounded radiation problems, FE being of course applicable only on domains of finite extension. Two lines of development emerged. In the first, the description of the field outside the finite domain was done in terms of a modal expansion (unimoment method [54], transfinite element method [55], and by moment method [56]) or in terms of an integral representation (FEs/boundary integral [57], FEs/method of moments [58], and field-feedback formulation [59]), but these were plagued by non-physical solutions too, that is, interior resonances [60]. Furthermore, these conditions, called *exact* were of global nature and spoiled the sparsity of the solving matrix. In the second line, local conditions – hence not spoiling sparsity – were enforced on the boundary assuming a far-field behavior. These so-called absorbing boundary conditions (ABC) are approximate, due to the far field assumption, and must be placed at a distance from the scatterer to have good accuracy; yet, they rapidly gained popularity either in 2D [61] or in 3D [62]. Another approach, in this contest, is that of adding a layer of absorbing material, either realistic [63] or fictitious and, hence, only numerical [64]. This latter, the so-called perfectly matched layer (PML) gained the greatest popularity in the end. Some wider insight on these developments can also be found in [65].

#### IV. MATURITY

By 1980, even if FEs have reached a good maturity in mechanical and civil engineering and in electromagnetics was still struggling with spurious modes, several “general purpose” codes began to be available to the

engineers to treat broad classes of linear and nonlinear problems.

DYNA3D, originally developed by John O. Hallquist at Lawrence Liver more National Laboratory (LLNL), started in 1976 and became commercial in the 1980s.

ANSYS (ANalysis SYStems) ported its punched-card codes to Apple II in 1980, allowing for a first true graphical interface.

FEMAP was born in 1985 as a pre- and post-processor for one of the oldest codes, NASTRAN (NASa STRucture ANalysis). NASTRAN itself was developed by CSC and released to NASA in 1968. In 2001, NASA made the code publicly available.

StressCheck, released in 1989, was one of the first commercially available products to utilize the p-version of the FEs for structural analysis. P-version implies the possibly local increase of the order of the polynomial FE bases within an element to achieve higher accuracy, and is opposed to h-method, where the order of the bases is fixed and higher accuracy is achieved by refining the mesh into smaller elements.

In electromagnetism, Zoltan and Nicholas Cendes (Figure 3) founded Ansoft in 1984, marketing HFSS (high frequency structure simulator). Ansoft, after a long partnership with Hewlett-Packard, was finally acquired by ANSYS in 2008. HFSS is currently the standard, *de facto*, in FE analysis for electromagnetic waves.

Modern software package, on the other hand, comprises many different solvers to provide the users with maximum flexibility and multiphysics capabilities; so, nowadays, most of the EM simulation suites do include also FEs, as it is the case for CST, FEKO, COMSOL, etc.

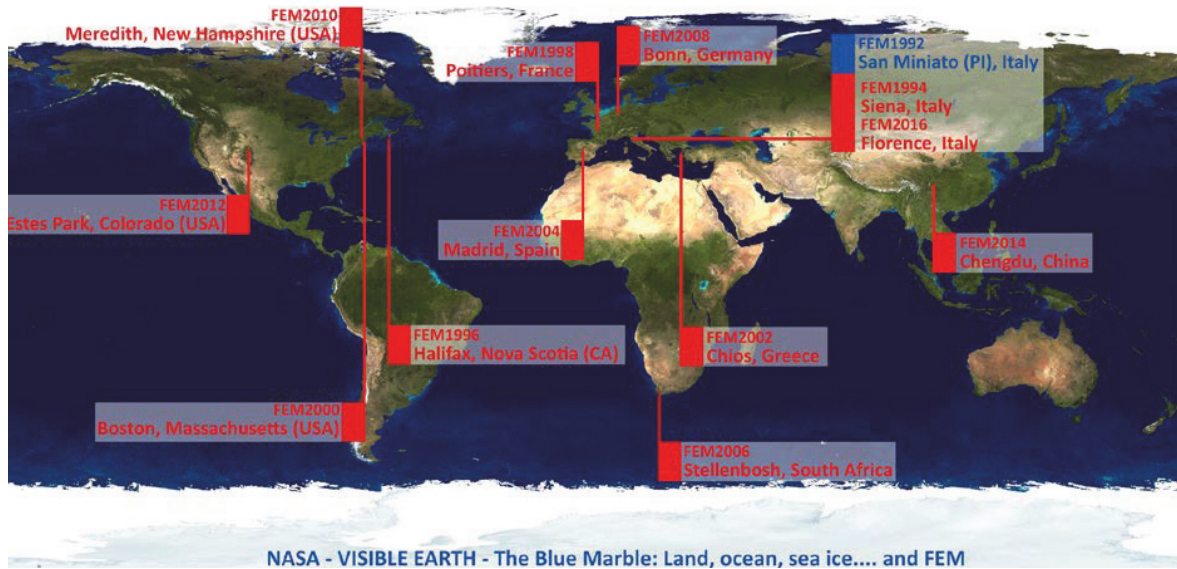


Fig. 4. Location of the 13 FEM workshops for microwave engineering editions.

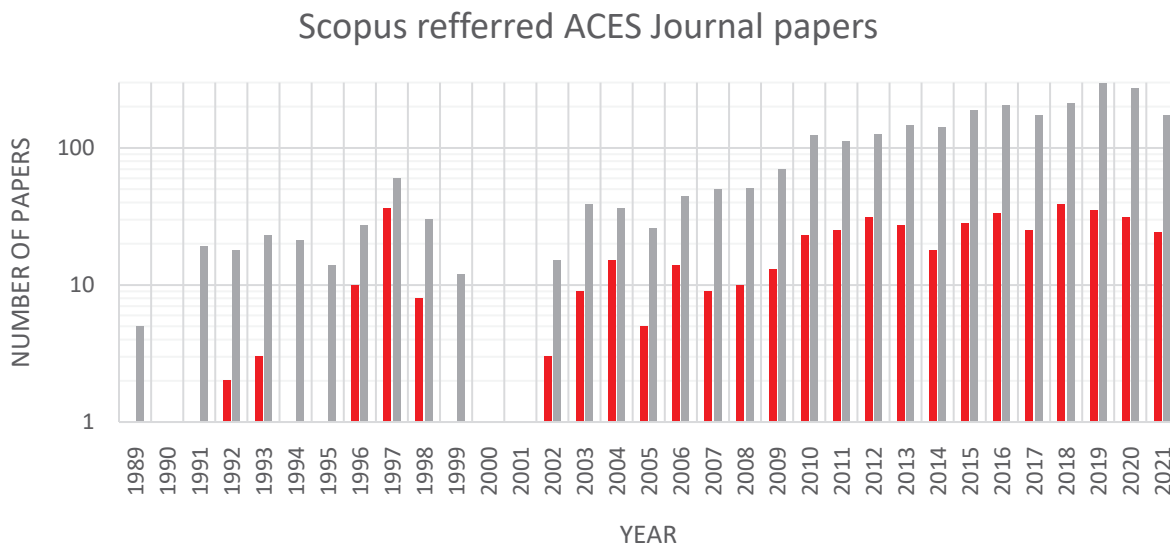


Fig. 5. Finite elements (red bars) and total papers (gray bars) per year published on ACES Journal and referred in Scopus.

Finally, for electromagnetics, and for wave electro-magnetics, I wish to remember the biannual workshop, fully dedicated to FEs for Microwave Engineering which originated by a collaboration between the University of Florence, Italy and McGill University of Montreal, Canada, where P.P. Silvester was a professor. The workshop totaled 13 editions, the last independent one being in Florence in 2016 (Figure 4). A full history of these workshops can be found in [66, 67], while a deeper insight in the history of FEs in general can be found in [68].

## V. ACES JOURNAL

It is interesting to analyze the presence of FE in scientific literature and on *ACES Journal* in particular. The Scopus database offers the possibility of advanced searches [69]. By limiting the search to *ACES Journal* (ISSN1054-4887), the total number of papers referred in Scopus per year can be obtained and, by further limiting the search to the paper containing the keyword "Finite Element\*" in any field, the number of papers specifically dealing with FE is produced.

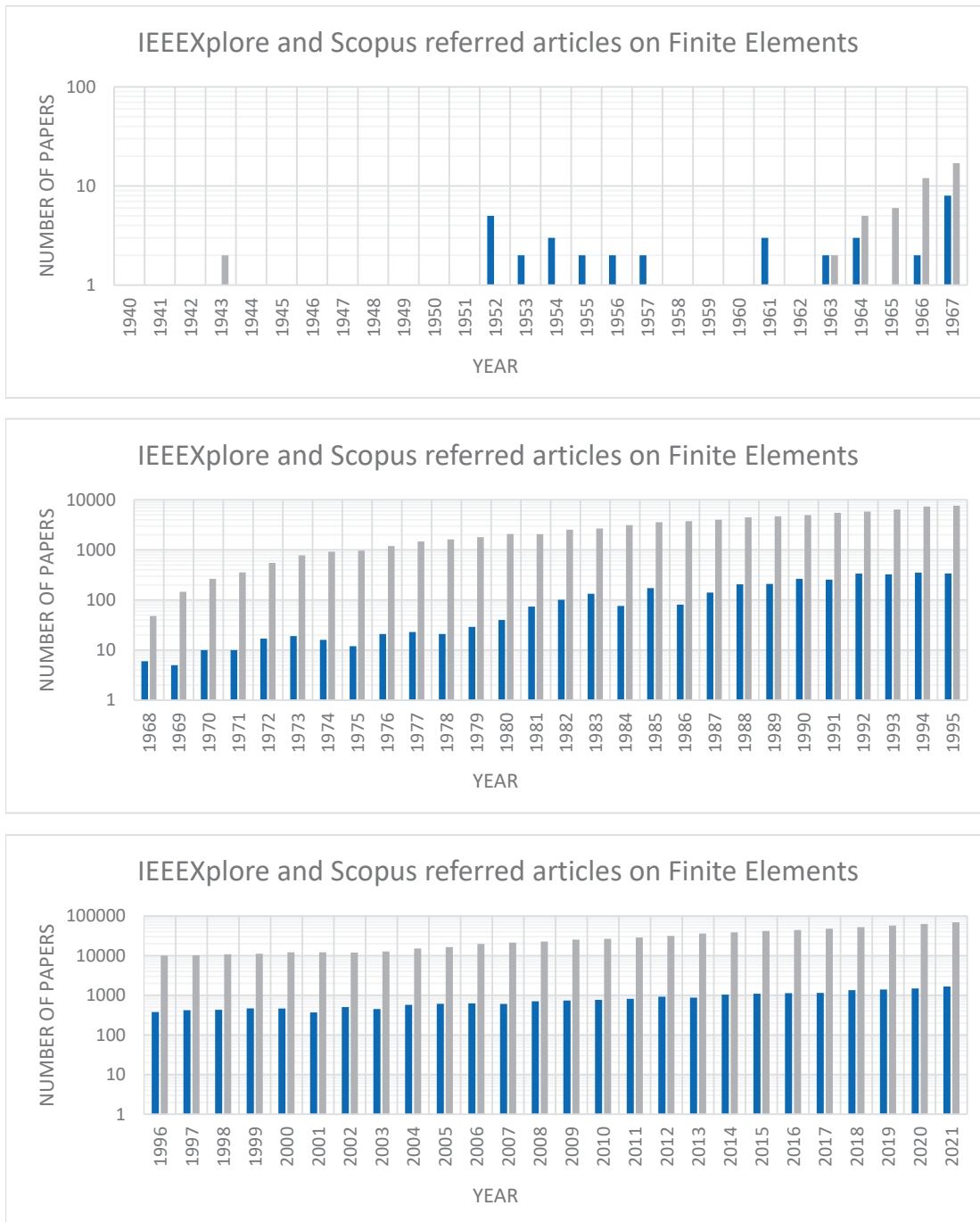


Fig. 6. Finite elements papers per year referred on IEEExplore (blue bars) and on Scopus (gray bars) per year.

The result of these queries is sketched in Figure 5, showing in gray the total number of ACES papers indexed per year, starting from the first year where a paper on FE appeared (1989, just a single paper) up to 2021. While Scopus archives are apparently incomplete, since they index no paper at all in some years (1990 and 2000), they nevertheless provide an interesting insight:

in the last 20 years, the number of FE papers was never below 10% of the total published ACES papers, with an average of 19% and a peak of 42% in 2004. Graphs are on logarithmic vertical scale to better appreciate the number of papers when they are few.

As a comparison, Figure 6 reports a similar query with the keyword “Finite Element\*” in any field on the

whole Scopus database and on IEEEExplore; results are limited to journal papers, again in logarithmic scale. Up to 1965, the presence of FE papers was sporadic; from 1966 to 2000, there was a steady increase, and from 2001 onwards, the increase was still present but less dramatic. This is well in accordance with what was stated earlier about the reach of maturity at the beginning of our century. Figure 6 is currently used on a Ph.D. course on FEs held both at the University of Florence and the Politecnico di Milano [70] and is derived from original bibliographical research in [71]. Small discrepancies with [71] are due to the different database used and their ever-going updates.

## VI. CONCLUSION

A brief history of FE has been sketched, with a focus on its earliest, pioneering developments, followed by a bibliographical analysis on the number of FE papers in open literature in general on IEEE journals and on *ACES Journal* in particular. The latter, being committed to computational electromagnetics, hosted in this last 20 years a remarkable number of papers dealing with FEs and its applications.

## ACKNOWLEDGMENTS

The author wishes to thank Prof. G. Pelosi, University of Florence, for the useful discussions provided in preparing this paper.

## REFERENCES

- [1] R. Courant, "Variational methods for the solution of problems of equilibrium and vibrations," *Bull. Amer. Math. Soc.*, vol. 49, no. 1, pp. 1-23, 1943.
- [2] R. Courant, K. O. Friedrichs, and H. Lewy, "Über die partiellen differenzgleichungen der mathematischenphysic [About the partial difference equations of the mathematical physic]," *Math. Ann. (in German)*, vol. 100, pp. 32-74, 1928.
- [3] J. Bernoulli, "Problema novum ad cuius solutionem mathematici invitantur [A new problem to whose solution mathematicians are invited]," *ActaEruditorum (in Latin)*, vol. 18, p. 269, 1696.
- [4] G. Pelosi, "The finite-element method, Part I: R.L. Courant," *IEEE Antennas Propagat. Mag.*, vol. 49, pp. 180-182, 2007.
- [5] G. Pelosi and S. Selleri, "A prelude to finite elements: The fruitful problem of the brachistochrone," *URSI Radio Science Bulletin*, no. 367, pp. 10-14, 2018.
- [6] G. Leibnitz, "Nova Methodus pro Maximi set Minimis [A new method for maxima and minima]," *ActaEruditorum (in Latin)*, vol. III, pp. 439-473, 1684.
- [7] I. Newton, *Philosophiæ Naturalis Principia Mathematica [Mathematical principles of natural philosophy]*, J. Steater (in Latin), London UK, 1687.
- [8] K. Schellbach, "Probleme der variationsrechnung [Problems of the calculation of variations]," *Journal für die reine und angewandte Mathematik (in German)*, no. 41, pp. 293-363, 1851.
- [9] J. W. Strutt and L. Rayleigh, *The Theory of Sound*, MacMillan & Co., London, UK, 1894 (vol. I) - 1896 (vol. II).
- [10] W. Ritz, "Über eine neue methode zur lösung gewisser variationsprobleme der mathematischenphysic [About a new method for solving certain variation problems in mathematical physics]," *Journal für die reine und angewandte Mathematik (in German)*, vol. CXXXV, pp. 1-6, 1908.
- [11] B. G. Galerkin, "Series occurring in various questions concerning the elastic equilibrium of rods and plates," *Engineers Bulletin (Vestnik Inzhenerov - In Russian)*, vol. 19, pp. 897-908, 1915.
- [12] S. Faedo, "Un nuovo metodo per l'analisi esistenziale e quantitativa dei problemi di propagazione [A new method for the existential and quantitative analysis of propagation problems]," *Ann. Scuola Norm. Sup Pisa Cl. Sci. (in Italian)*, vol. 1, no. 3, pp. 1-40, 1949.
- [13] G. Kron, *Tensor Analysis of Networks*, John Wiley & Sons, New York, NY, 1939.
- [14] A. Hrennikoff, "Solution of problems in elasticity by the framework method," *J. Appl. Mech.*, vol. 8, pp. 619-715, 1941.
- [15] D. McHenry, "A lattice analogy for the solution of plane stress problems," *J. Inst. Civ. Eng.*, vol. 21, pp. 59-82, 1949.
- [16] J. H. Argyris, "Energy theorem and structural analysis," *Aircraft Engineering*, vol. 26, pp. 347-358 and 383-387, 394, 1954.
- [17] S. Levy, "Structural analysis and influence coefficients for delta wings," *J. Aeronautical Sc.*, vol. 20, pp. 449-454, 1953.
- [18] M. J. Turner, R. W. Clough, H. C. Martin, and L. J. Topp, "Stiffness and deflection analysis of complex structures," *J. Aeronautical Sc.*, vol. 23, pp. 805-823, 854, 1956.
- [19] R. W. Clough, "The finite element method in plane stress analysis," *Proc. 2<sup>nd</sup> ASCE Conf. on Electronic Comput.*, Pittsburg, PA, 1960.
- [20] J. T. Oden, "A general theory of finite elements; I topological considerations," *Int. J. Num. Meth. Eng.*, vol. 1, pp. 205-221, 1969.
- [21] J. T. Oden, "A general theory of finite elements; II applications," *Int. J. Num. Meth. Eng.*, vol. 1, pp. 247-259, 1969.

- [22] J. T. Oden, "A finite elements analogue of the Navier-Stokes equations," *J. Eng. Mech. Div. ASCE*, vol. 96, pp. 529-534, 1970.
- [23] O. C. Zienkiewicz and Y. K. Cheung, *The Finite Element in Structural and Continuum Mechanics*, London, UK: McGraw-Hill, 1967.
- [24] O. C. Zienkiewicz, *The Finite Element Method in Engineering Science*, McGraw-Hill, London, UK, 1971.
- [25] P. P. Silvester, "Finite elements solution of homogeneous waveguide problems," *Alta Frequenza*, vol. 38, pp. 313-317, 1969.
- [26] R. Ferrari, "The Finite-Element Method, Part 2: P.P. Silvester, an Innovator in Electromagnetic Numerical Modeling," *IEEE Antennas Propagat. Mag.*, vol. 49, pp. 216-234, 2007.
- [27] P. P. Silvester and R. L. Ferrari, *Finite Elements for Electrical Engineers*, Cambridge University Press, Cambridge, UK, 1983.
- [28] F. Kang, "A difference formulation based on the variational principle," *Appl. Math. Comp. Math. (in Chinese)*, vol. 28, pp. 963-971, 1965.
- [29] M. W. Johnson and R. W. McLay, "Convergence of the finite element method in the theory of elasticity," *J. Appl. Mech.*, vol. 35, pp. 274-278, 1968.
- [30] S. L. Sobolev, "Méthode nouvelle à résoudre le problème de Cauchy pour les équations linéaires hyperboliques normales [New method to solve the Cauchy problem for normal hyperbolic linear equations]," *Matematicheskii Sbornik - Rec. Math. Moscou (in French)*, vol. 1, pp. 39-71, 1936.
- [31] L. Schwartz, "Généralisation de la notion de fonction, de dérivation, de transformation de Fourier et applications mathématiques et physiques [Generalization of the notion of function, derivation, Fourier transformation and their mathematical and physical applications]," *Annales Univ. Grenoble (in French)*, vol. 21, pp. 57-74, 1945.
- [32] L. Schwartz, *Théorie des Distributions [Distribution Theory]*, Hermann (in French), Paris, F, vol. I, 1950, vol. II, 1951.
- [33] M. Zlámal, "On the finite element method," *Numerische Mathematik*, vol. 12, pp. 394-409, 1968.
- [34] I. Babuška and A. K. Aziz, "Survey lectures on the mathematical foundation of the finite element method," in *The Mathematical Foundations of the Finite Element Method with Applications to Partial Differential Equations*, A. K. Aziz, Academic Press, New York, NY, pp. 5-359, 1972.
- [35] Z. J. Cendes and P. P. Silvester, "Numerical solution of dielectric loaded waveguides: I-Finite element analysis," *IEEE Trans. Microw. Theory Tech.*, vol. 18, pp. 1124-1131, 1970.
- [36] D. G. Corr and J. B. Davies, "Computer analysis of the fundamental and higher order modes in single and coupled microstrip," *IEEE Trans. Microw. Theory Tech.*, vol. 20, pp. 669-678, 1972.
- [37] A. Konrad, "Triangular finite elements for vector fields in electromagnetics," Ph.D. Thesis, McGill Univ. 1974.
- [38] A. Konrad, "Vector variational formulation of electromagnetic fields in anisotropic media," *IEEE Trans. Microw. Theory Tech.*, vol. 24, pp. 553-559, 1976.
- [39] B. M. A. Rahman and J. B. Davies, "Penalty function improvement of waveguide solution by finite elements," *IEEE Trans. Microw. Theory Tech.*, vol. 32, pp. 922-928, 1984.
- [40] K. D. Paulsen and D. R. Lynch, "Elimination of vector parasites in finite element Maxwell solutions," *IEEE Trans. Microw. Theory Tech.*, vol. 39, pp. 395-404, 1991.
- [41] D. R. Lynch and K. D. Paulsen, "Origin of vector parasites in numerical Maxwell solutions," *IEEE Trans. Microw. Theory Tech.*, vol. 39, no. 3, pp. 383-394, Mar. 1991.
- [42] J. P. Webb, "Efficient generation of divergence-free fields for the finite element analysis of 3D cavity resonances," *IEEE Trans. Magn.*, vol. 24, pp. 162-165, 1981.
- [43] A. Konrad, "A method for rendering 3D finite element vector field solutions non-divergent," *IEEE Trans. Magn.*, vol. 25, pp. 2822-2834, 1989.
- [44] J. C. Nedelec, "Mixed finite elements in  $\mathbb{R}^3$ ," *Numerische Mathematik*, vol. 35, pp. 315-341, 1980.
- [45] M. Hano, "Finite-element analysis of dielectric-loaded waveguides," *IEEE Trans. Microw. Theory Tech.*, vol. 32, pp. 1275-1279, 1984.
- [46] M. L. Barton and Z. J. Cendes, "New vector finite elements for three-dimensional magnetic field computation," *J. Appl. Physics*, vol. 61, pp. 3919-3921, 1987.
- [47] C. W. Crowley, P. P. Silvester, and H. Hurwitz, "Covariant projection elements for 3D vector field problems," *IEEE Trans. Magn.*, vol. 24, pp. 397-400, 1988.
- [48] J. F. Lee, "Analysis of passive microwave devices by using three-dimensional tangential vector finite elements," *Int. J. Numer. Model.*, vol. 3, pp. 235-246, 1990.
- [49] H. Whitney, *Geometric Integration Theory*. Princeton University Press, Princeton, NJ, 1957.
- [50] D. Sun, J. Manges, X. Yuan, and Z. Cendes, "Spurious modes in finite-element methods," *IEEE Antennas Propagat. Mag.*, vol. 37, pp. 12-24, 1995.

- [51] R. D. Graglia, A. F. Peterson, and F. P. Andriulli, "Curl-conforming hierarchical vector bases for triangles and tetrahedra," *IEEE Trans. Antennas Propagat.*, vol. 59, pp. 950-959, 2011.
- [52] R. D. Graglia and G. Lombardi, "Singular higher order complete vector bases for finite methods," *IEEE Trans. Antennas Propagat.*, vol. 52, pp. 1672-1685, 2004.
- [53] A. F. Peterson and R. D. Graglia, "Basis functions for vertex, edge, and corner singularities: a review," *IEEE J. Multiscale Multiphys. Comput. Tech.*, vol. 1, pp. 161-175, 2016.
- [54] K. K. Mei, "Unimoment method of solving antenna and scattering problems," *IEEE Trans. Antennas Propagat.*, vol. 22, pp. 760-766, 1974.
- [55] S. K. Jeng and C. H. Chen, "On variational electromagnetics; theory and application," *IEEE Trans. Antennas Propagat.*, vol. 32, pp. 902-907, 1984.
- [56] A. C. Cangellaris and R. Lee, "The bymoment method for two-dimensional electromagnetic scattering," *IEEE Trans. Antennas Propagat.*, vol. 38, pp. 1429-1437, 1990.
- [57] P. P. Silvester and M. S. Hsieh, "Finite-element solution of 2-dimensional exterior-field problems," *IEE Proc. H*, vol. 118, pp. 1743-1747, 1971.
- [58] J.-M. Jin and J. L. Volakis, "A hybrid finite element method for scattering and radiation by microstrip patch antennas and arrays radiating in a cavity," *IEEE Trans. Antennas Propagat.*, vol. 39, pp. 1598-1604, 1991.
- [59] M. A. Morgan and B. E. Welch, "Field feedback formulation for electromagnetic scattering computations," *IEEE Trans. Antennas Propagat.*, vol. 34, pp. 1377-1382, 1986.
- [60] A. F. Peterson, "The 'interior resonance' problem associated with surface integral equations of electromagnetics: Numerical consequences and a survey of remedies," *Electromagnetics*, vol. 10, pp. 293-312, 1990.
- [61] B. Engquist and A. Majda, "Absorbing boundary conditions for the numerical simulation of waves," *Math. Comp.*, vol. 31, pp. 629-651, 1977.
- [62] A. F. Peterson, "Absorbing boundary conditions for the vector wave equation," *Microw. Opt. Techn. Lett.*, vol. 1, pp. 62-64, 1988.
- [63] J.-M. Jin, L. Volakis, and V. V. Liepa, "Fictitious absorber for truncating finite element meshes in scattering," *IEEE Proc. H*, vol. 139, pp. 472-476, 1992.
- [64] J. P. Berenger, "A perfectly matched layer for the absorption of electromagnetic waves," *J. Comp. Physics*, vol. 114, pp. 185-200, 1994.
- [65] R. Coccioli, T. Itoh, G. Pelosi, and P. P. Silvester, "Finite-element methods in microwaves: a selected bibliography," *IEEE Antennas Propagat. Mag.*, vol. 38, pp. 34-48, 1996.
- [66] R. D. Graglia, G. Pelosi, and S. Selleri [Eds.], "International Workshop on Finite Elements for Microwave Engineering - From 1992 to present & Proceedings of the 13th Workshop," Firenze University Press, Florence, I, 2016.
- [67] S. Selleri, "13th International workshop on finite elements for microwave engineering [Meeting Reports]," *IEEE Antennas Propagat. Mag.*, vol. 58, pp. 13-14, 2016.
- [68] J. T. Oden, "Historical Comments on Finite Elements," in Stephen G. Nash (ed.), *A History of Scientific Computing*, ACM Press, New York, NY, 1990.
- [69] <https://www.scopus.com>
- [70] S. Selleri, "Finite Elements for Engineers," Ph.D. course notes; course held at the *Politecnico di Milano*, Milan, Italy, 2021.
- [71] P. P. Silvester and G. Pelosi [Eds.], *Finite Elements for Wave Electromagnetics: Methods and Techniques*, IEEE Press, New York, NY, 1994.



**Stefano Selleri** received the Laurea degree (*cum laude*) in electronic engineering and the Ph.D. degree in computer science and telecommunications from the University of Florence, Italy, in 1992 and 1997, respectively.

He was a Visiting Scholar with the University of Michigan, Ann Arbor, MI, USA, in 1992; the McGill University, Montreal, QC, Canada, in 1994; and the Laboratoire d'Electronique, University of Nice Sophia Antipolis, Nice, France, in 1997. From February 1998 to July 1998, he was a Research Engineer with the Centre National d'Etudes et Telecommunications (CNET) France Telecom, La Turbie, France. He is currently an Associate Professor of electromagnetic fields with the University of Florence, where he conducts research on numerical modeling of microwave devices and circuits with particular attention to numerical optimization. He is the author of about 150 articles on peer-reviewed journals on the aforementioned topics, as well as books and book chapters. He is also active in the field of telecommunications and electromagnetism history, having published about 30 articles or book chapters.

# Complex Inhomogeneous Dielectric Target Modeling and Scattering Estimation using a Self-Designed Software

Muyu Hou<sup>1</sup>, Shuhong Gong<sup>1,2</sup>, Yanchun Zuo<sup>1</sup>, and Yu Liu<sup>1</sup>

<sup>1</sup>School of Physics and Optoelectronic Engineering

Xidian University, Xi'an 710071, China

myhou2022@163.com, yczuoemail@163.com, 13649292113@163.com

<sup>2</sup>Collaborative Innovation Center of Information Sensing and Understanding

Xidian University, Xi'an 710071, China

shgong@xidian.edu.cn

**Abstract** – This paper presents a method to finely model the arbitrarily irregular-shaped and inhomogeneous dielectric target. The target is first geometrically divided into a set of homogeneous and isotropic tetrahedral regions. Each region is precisely matched with a set of electromagnetic parameters. As a result, this can accurately model the target which has an extremely complex dielectric constant distribution and an irregular shape. Regarding the electromagnetic scattering evaluation of the established model, the method of moments (MoM) is adopted in consideration of the coupling between these tetrahedral regions, and the total scattering is obtained by solving the matrix equation. The above two computational sections are integrated into a self-designed software. One can just input the spatial distribution of the dielectric constant and then the designed software automatically processes the target's geometric information and meshes the target. Finally, the scattered electric field and radar cross section (RCS) of the target are output from the software. The designed software provides an effective and accurate way to study the electromagnetic scattering characteristics of the complex inhomogeneous objects.

**Index Terms** – Dielectric inhomogeneous target, fine geometric modeling, MoM, scattering evaluation.

## I. INTRODUCTION

Inhomogeneous dielectric objects with irregular shapes are ubiquitous, and their electromagnetic scattering characteristics have enormous applications, such as the aerosol particle multi-scattering in weather radar [1], the turbulence scattering in tropospheric communication [2], and the aircraft wake scattering in anti-stealth [3]. However, the electromagnetic scattering evaluation methods in the open literature pursue calculation

efficiency by reducing the complexities of the algorithm or the model. This obviously causes errors in the estimation of the scattering properties of the target. A self-designed software is released in this paper to accurately reconstruct the complex inhomogeneous targets with numbers of homogeneous tetrahedrons. Meanwhile, the corresponding scattering is calculated using the in-house code of MoM, which has been integrated into the designed software.

Regarding the modeling of inhomogeneous targets with irregular shapes, target models are often simplified. For example, in calculating the aircraft wake scattering characteristics, the radial density gradient (RDG) model is adopted to approximate the wake vortex as a dielectric cylinder [4, 5], and the adiabatic transport (AT) model regards the vortex wake as a circle whose cross-sectional radius is the function of the vortex distance [4]. All these methods reduce the complexities of calculation, but these approximations also reduce the abilities to accurately describe real scenarios. It is also reported that programming platforms can be utilized together with commercial computational software to obtain the scattering of inhomogeneous dielectric targets. In 2015, Farahbakhsh *et al.* proposed a MATLAB toolbox to model inhomogeneous media combined with the commercial software FEKO. Users can utilize a deterministic function of the target's dielectric constant with relation to the spatial position,  $\epsilon_r(x, y, z)$ , to model the dielectric targets [6]. However, if the dielectric constant distribution cannot be explicitly expressed, the above-mentioned toolbox is no longer applicable. Moreover, it is difficult to accurately reconstruct the geometric irregular targets using small cubes (adopted in [6]), which is easy to produce large modeling errors in scattering calculation.

Regarding scattering estimation, empirical formulas are often used to calculate the scattering of complex inhomogeneous targets. For instance, in the

empirical formula of turbulent scattering, the structure constant and frequency determine the radar cross section (RCS) [7, 8]. In the Ulaby empirical model, incident angle and six undetermined coefficients determine the backscattering of the terrain [9]. Empirical formulas reduce the complexities and the time cost of electromagnetic scattering calculation, but the accuracy of undetermined coefficients depends on large numbers of experimental data.

The main contributions of this work are three-fold:

- 1) For the electromagnetic scattering simulation of random media (such as the atmospheric turbulence), a spatial spectrum function and Monte Carlo simulation-based method is first proposed (to our best knowledge) in this paper to obtain the spatial distribution of dielectric constant. On this basis, one can apply existing numerical methods to analyze the electromagnetic scattering characteristics of the inhomogeneous target whose dielectric constant fluctuates in 3-D space, which is no longer solely dependent on empirical models.
- 2) To precisely reconstruct the irregular-shaped and inhomogeneous dielectric target for the electromagnetic scattering simulation, a novel method based on computer graphics and tetrahedron meshing strategy is proposed.
- 3) Integrated with the above methods and the method of moments (MoM), a user-friendly software for the electromagnetic scattering simulation of complex inhomogeneous targets is developed. This software is not only applicable for the target with a continuously varying dielectric constant, but also can handle the target whose dielectric constant is arbitrarily distributed.

The rest of this paper is organized as follows. The methodology and the designed software are introduced in detail in Section II. Methods include obtaining the dielectric constant spatial distribution according to a deterministic formula or a spatial spectrum function, modeling the irregular-shaped and inhomogeneous dielectric target with tetrahedron elements, and estimating electromagnetic scattering by MoM. In Section III, simulations are performed to test the designed software. Section VI concludes this paper.

## II. METHODOLOGY AND SOFTWARE DESIGN

This section discusses the corresponding methods, which are involved in modeling and electromagnetic scattering calculation of complex inhomogeneous dielectric targets, and the software developed based on these methods. Specifically, the designed software provides

two separated data processing channels, say Channel-A and Channel-B. For Channel-A, the input is the point cloud data of the dielectric constant. Then, this information is used to reconstruct the profile of the target. Following this, meshing and simulation modeling are carried out. The electromagnetic scattering from the inhomogeneous dielectric target is finally calculated by MoM. As to Channel-B, the geometric profile and the spatial spectrum (or deterministic formula) of the target's dielectric constant are sent to the designed software as inputs. Then, the simulation model of the target is established based on the computer graphics and Monte Carlo method. At last, the electromagnetic scattering of the obtained model is evaluated by MoM. The whole simulation process is illustrated in Figure 1.

### A. Obtaining the spatial distribution of the dielectric constant

An inhomogeneous dielectric target is characterized by a four-dimensional vector  $[x, y, z, \epsilon_r]$ , where  $[x, y, z]$  is the coordinate of the sampling point and  $\epsilon_r$  is the dielectric constant at this point. In practical applications, the dielectric constant distribution of inhomogeneous dielectric targets may be given by point cloud data obtained by measurement or simulation or by a deterministic formula or a spatial spectrum function. To obtain the dielectric constant distribution that can match the target model used for electromagnetic simulation, we propose the following two solutions corresponding to the above two cases.

*Case 1:* When the spatial distribution of dielectric constant is explicitly given by point cloud data, the outer boundary of the target can be automatically extracted from the point cloud data using the Delaunay algorithm [10]. Notably, the point cloud data may be evenly distributed or unevenly distributed. The evenly distributed

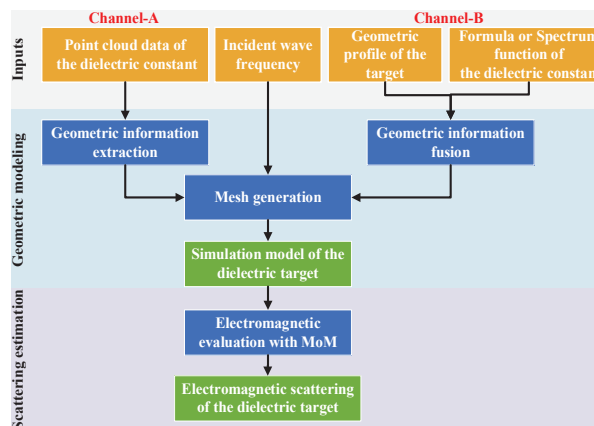


Fig. 1. Flowchart of modeling and scattering estimation for the inhomogeneous target.

sampling strategy can well describe the distribution characteristics when the spatial variation of dielectric constant is relatively smooth, as shown in Figure 2 (a). To ensure the effectiveness of sampling, the distance between two adjacent sampling points is recommended to satisfy  $\max(\Delta x, \Delta y, \Delta z) < \lambda_e/36$ , where  $\lambda_e$  is the wavelength of the incident wave. In addition, considering that the dielectric constant distribution of the targets may have significant regional fluctuation, finer sampling is needed, as shown in Figure 2 (b). To tackle the potential situation that there are no samples in some subdivision elements (tetrahedrons) due to the sparse sample distribution, the linear interpolation method [11] is integrated into this channel to supplement the necessary data.

*Case 2:* In some special application scenarios, the spatial distribution of the target's dielectric constant may be given by a deterministic formula or a spatial spectrum function. The former case has been mentioned in [6] and will not be described in detail in this paper. Here, we propose a Monte Carlo method to access the dielectric constant spatial distribution by the spatial spectrum function. Monte Carlo method is a broad class of computational algorithms that rely on repeated ran-

dom sampling to obtain numerical results [12]. It has been used to form complex terrain (such as rough sea surfaces [13] and mountainous regions [14]) and to modify phase factors [15, 16]. The atmosphere is a typical random medium, and its dielectric constant cannot be directly expressed by a deterministic formula related to spatial position. It can only be described with spectrum functions. Taking the atmosphere fluid as an example, the steps of using Monte Carlo method to obtain the dielectric constant spatial distribution are as follows:

- 1) Generate a 3-D Hermitian Gaussian random matrix  $\mathbf{G}_{p \times q \times s}$ .
- 2) Filter  $\mathbf{G}_{p \times q \times s}$  by the spatial spectrum of dielectric constant fluctuation  $\Phi(\mathbf{K}_{r'})$ , that is,

$$F(\mathbf{K}_{r'}) = \mathbf{G}_{p \times q \times s} \sqrt{\Phi(\mathbf{K}_{r'})}. \quad (1)$$

The spatial spectrum of the atmospheric turbulence [8] is expressed as

$$\Phi(\mathbf{K}_{r'}) = 0.033C^2 |\mathbf{K}_{r'}|^{-11/3}, \quad (2)$$

where  $\mathbf{r}'$  is the position vector of a certain point  $(x, y, z)$  in space,  $\mathbf{K}_{r'} = (K_x, K_y, K_z)$  is the wave vector,  $|\mathbf{K}_{r'}| = 2\pi/l$  and  $2\pi/L_0 < |\mathbf{K}_{r'}| < 2\pi/l_0$ ,  $l$  represents the size of turbulence,  $L_0$  and  $l_0$  are the outer scale and the inner scale of fluids, respectively, and  $C$  is a constant.

- 3) Obtain the spatial distribution of the dielectric constant fluctuation  $\Delta\epsilon_r(\mathbf{r}')$  by the inverse Fourier transform [12]. That is,

$$\Delta\epsilon_r(\mathbf{r}') = \iiint_{-\infty}^{\infty} F(\mathbf{K}_{r'}) e^{i\mathbf{r}' \cdot \mathbf{K}_{r'}} d\mathbf{K}_{r'}. \quad (3)$$

- 4) Eventually, the dielectric constant spatial distribution of turbulence  $\epsilon(\mathbf{r}')$  can be obtained by

$$\epsilon_r(\mathbf{r}') = \epsilon_{r0} + \Delta\epsilon_r(\mathbf{r}') = 1 + \Delta\epsilon_r(\mathbf{r}'), \quad (4)$$

where  $\epsilon_{r0}$  is the average dielectric constant of the random media and is set to 1 for the turbulence case here. Combined with the given geometric profile, this kind of target can be reconstructed accurately.

## B. Modeling of the inhomogeneous dielectric target

Fine modeling is one of the key steps to explore the electromagnetic scattering characteristics of complex dielectric targets. Here, for the sake of fidelity, a large number of homogeneous tetrahedrons is used to reconstruct the inhomogeneous dielectric target rather than cubes used in [6]. Then, combined with the spatial distribution of dielectric constant, each tetrahedron is assigned an independent dielectric constant value. Specifically, four main steps are as follows:

- 1) Extract the vertex coordinates of each mesh element (tetrahedron) from the mesh file.
- 2) Sample dielectric constants in the target domain. As previously mentioned, the dielectric constant data

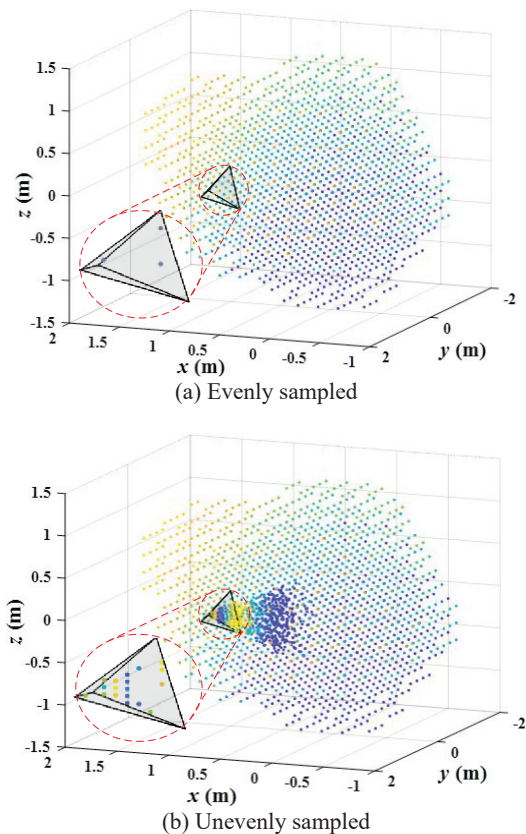


Fig. 2. Diagram of the target's dielectric constant data sampling.

can be obtained by a deterministic function related to the spatial position  $(x, y, z)$ , the spatial spectrum function of random medium, or other simulation software.

- 3) Obtain the average dielectric constant of each tetrahedron. Let the four vertex coordinates of the  $i$ th tetrahedron be  $V_{i1} = (x_{i1}, y_{i1}, z_{i1})$ ,  $V_{i2} = (x_{i2}, y_{i2}, z_{i2})$ ,  $V_{i3} = (x_{i3}, y_{i3}, z_{i3})$ , and  $V_{i4} = (x_{i4}, y_{i4}, z_{i4})$ , respectively. Then, the  $i$ th sampling position  $P_i = (x'_i, y'_i, z'_i)$  in the  $i$ th tetrahedron must satisfy

$$D_v \cdot D_0 > 0 \quad v = 1, 2, 3, 4, \quad (5)$$

with

$$D_0 = \begin{vmatrix} x_{i1} & y_{i1} & z_{i1} & 1 \\ x_{i2} & y_{i2} & z_{i2} & 1 \\ x_{i3} & y_{i3} & z_{i3} & 1 \\ x_{i4} & y_{i4} & z_{i4} & 1 \end{vmatrix}, D_1 = \begin{vmatrix} x'_i & y'_i & z'_i & 1 \\ x_{i2} & y_{i2} & z_{i2} & 1 \\ x_{i3} & y_{i3} & z_{i3} & 1 \\ x_{i4} & y_{i4} & z_{i4} & 1 \end{vmatrix}, \quad (6)$$

$$D_2 = \begin{vmatrix} x_{i1} & y_{i1} & z_{i1} & 1 \\ x'_i & y'_i & z'_i & 1 \\ x_{i3} & y_{i3} & z_{i3} & 1 \\ x_{i4} & y_{i4} & z_{i4} & 1 \end{vmatrix}, D_3 = \begin{vmatrix} x_{i1} & y_{i1} & z_{i1} & 1 \\ x_{i2} & y_{i2} & z_{i2} & 1 \\ x'_i & y'_i & z'_i & 1 \\ x_{i4} & y_{i4} & z_{i4} & 1 \end{vmatrix}, \quad (7)$$

$$D_4 = \begin{vmatrix} x_{i1} & y_{i1} & z_{i1} & 1 \\ x_{i2} & y_{i2} & z_{i2} & 1 \\ x_{i3} & y_{i3} & z_{i3} & 1 \\ x'_i & y'_i & z'_i & 1 \end{vmatrix}. \quad (8)$$

Especially, if any other  $D_v = 0$ , then  $P_i$  lies on the boundary (formed by the other three points other than  $V_{iv}$ ). Average the dielectric constant values of all sampling points in each tetrahedron, that is,

$$\bar{\epsilon}_{ri} = \sum_{j=1}^{N_i} \epsilon_{rj} / N_i, \quad (9)$$

where  $\bar{\epsilon}_{ri}$  is the average dielectric constant of the  $i$ th tetrahedron,  $N_i$  is the number of sampling points in the  $i$ th tetrahedron, and  $\epsilon_{rj}$  is the dielectric constant of the  $j$ th sampling point in the  $i$ th tetrahedron (including the sampling point on the surface).

- 4) Assign all average dielectric constant values to the corresponding tetrahedrons and then create a simulation model for electromagnetic scattering calculation.

### C. Electromagnetic scattering estimation

Here, the volume integral equation method of moments (VIE-MoM) is employed to simulate the scattering characteristics of inhomogeneous dielectric targets. According to the principle of volume equivalence, the scattered electric field  $\mathbf{E}^{\text{sca}}$  can be written as [17]

$$\mathbf{E}^{\text{sca}}(\mathbf{r}) = -j\omega\mu_0 \left(1 + \frac{1}{k_0^2} \nabla \nabla \cdot\right) \int_V G(\mathbf{r}, \mathbf{r}') \mathbf{J}_V(\mathbf{r}') dV', \quad (10)$$

where  $\omega$  is the angular frequency,  $\mu_0$  is the magnetic permittivity,  $k_0$  is the wave number in free space,  $\mathbf{J}_V$  represents the equivalent volume current,  $G(\mathbf{r}, \mathbf{r}')$  represents

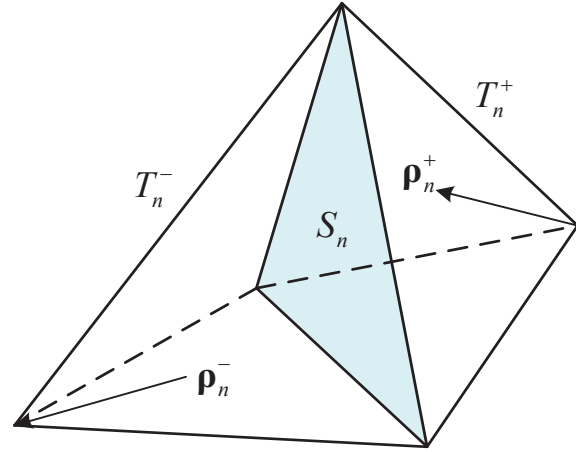


Fig. 3. The geometry of the SWG function.

the Green's function, and

$$G(\mathbf{r}, \mathbf{r}') = e^{-jk|\mathbf{r}-\mathbf{r}'|} / (4\pi|\mathbf{r}-\mathbf{r}'|), \quad (11)$$

$\mathbf{r}$  and  $\mathbf{r}'$  represent position vectors of the observation point and the source point, respectively.

To solve (10), we adopt the Galerkin method with the SWG basis function

$$\mathbf{f}_n(\mathbf{r}) = \begin{cases} \boldsymbol{\rho}_n^+ S_n / (3V_n^+) & r \in T_n^+ \\ \boldsymbol{\rho}_n^- S_n / (3V_n^-) & r \in T_n^- \\ 0 & \text{otherwise} \end{cases}. \quad (12)$$

In eqn (12),  $S_n$  is the area of common triangles, and  $V_n^+$  and  $V_n^-$  are volumes of tetrahedrons  $T_n^+$  and  $T_n^-$ , respectively.  $\boldsymbol{\rho}_n^+$  is the position vector of the free vertex pointing to the point inside tetrahedron  $T_n^+$ , and  $\boldsymbol{\rho}_n^-$  is the position vector of the internal point pointing to the free vertex of tetrahedron  $T_n^-$ . It should be noted that the half-SWG functions are also needed at the outer boundary. The geometry of the SWG function is shown in Figure 3. The details about the SWG functions are referred to [18].

Therefore, the corresponding impedance matrix equation can be built below

$$\mathbf{A}\mathbf{x} = \mathbf{b}, \quad (13)$$

where  $\mathbf{A} = (a_{ij})_{N \times N}$  is an impedance matrix with

$$a_{ij} = \int_{V_i} \mathbf{f}_i(\mathbf{r}) \cdot [-j\omega\mu_0 (1 + \frac{1}{k_0^2} \nabla \nabla \cdot) \times \int_{V_j} G(\mathbf{r}, \mathbf{r}') \mathbf{f}_j(\mathbf{r}') dV'_j] dV', \quad (14)$$

where  $x = [x_1, x_2, \dots, x_N]^T$  is the vector of unknowns,  $b = [b_1, b_2, \dots, b_N]^T$  is the excitation vector with

$$b_n = \int_{V_n} \mathbf{f}_n(\mathbf{r}) \cdot \mathbf{E}^{\text{inc}}(\mathbf{r}) dV'_n, \quad n = 1, 2, \dots, N. \quad (15)$$

In eqn (15),  $E^{\text{inc}}(\mathbf{r})$  denotes the electric field of the incident wave. Eqn (13) is then solved by the generalized minimum residual method (GMRES) method [19].

**D. Software implementation and user guide**

For the convenience of systematically analyzing the electromagnetic scattering characteristics of various inhomogeneous dielectric targets, we have developed a user-friendly software, which integrates the above-mentioned methods. To apply to most kinds of inhomogeneous dielectric targets, the dielectric constant information and geometric structure information of the target are grouped into a data input module of the software. The input module accepts the point cloud data file, deterministic formula, and spatial spectrum of the target’s dielectric constant and supports the geometric file in mainstream formats, such as .stp and .igs.

In the settings of simulation frequency, incident angle, and scattering angle, we follow the setting habits of existing simulation software, including the initial value, terminal value, and number of samples. To link with different radar systems, two polarization modes, HH and VV, are given for users to choose. The software sets up two graph windows to visualize the spatial distribution of the target dielectric constant and the corresponding scattering results, as shown in the right part of Figure 4. At the same time, the software is equipped with a data output port, which is convenient for users to further analyze the scattering data. The interface for modeling the inhomogeneous dielectric targets is shown in Figure 4. The main operation procedures are as follows:

- 1) Select one of the following three methods to obtain the dielectric constant distribution in the target domain: loading the spatial point cloud data file of the target’s dielectric constant according to the entered data file path; entering the formula of the dielectric constant varying with position; entering the spatial spectrum function of the target’s dielectric constant. The corresponding geometry file is also required when adopting the latter two methods.

- 2) Input simulation conditions, including incident zenith angle, incident azimuth angle, scattering zenith angle, scattering azimuth angle, polarization type, and frequency.
- 3) Press the “Run” button to start the electromagnetic scattering simulation for the target.
- 4) Press the “Save” button to save the scattering calculation results of the target.

Benefiting from the designed software, we have successfully carried out electromagnetic scattering simulations for various inhomogeneous dielectric targets, two of which are given in the next section.

**III. SIMULATIONS WITH DESIGNED SOFTWARE**

In this section, we first verify our algorithm by comparing the simulation results (given by the software) of an inhomogeneous sphere, of which the dielectric constant continuously varies with the spatial position,  $\epsilon_r(x, y, z)$ , with numerical solutions in [20]. Then, we apply our software to analyze electromagnetic scattering characteristics of a cloud-like inhomogeneous dielectric target, of which the dielectric constant is determined by a spatial spectrum function.

**A. Algorithm validation based on an inhomogeneous dielectric sphere**

In this section, an inhomogeneous sphere is modeled by our software for verification. Specifically, the sphere is centered at (0,0,0) with radius  $R = 1$  m. The constitutive parameters are  $\epsilon_r = \exp[(x + y + z + 2)/2]$  and  $\mu_r = 1$ . The reconstructed inhomogeneous sphere is shown in Figure 5. The magnitude of the far zone scattered field ( $r|\mathbf{E}_s|$ ) as a function of angle is calculated at  $f_e = 100\text{MHz}$  using the proposed method in Section II.

The simulation results are compared with the numerical ones, as shown in Figure 6. The lines in Figure 6 are the results obtained by the proposed method, and the symbols indicate the results in [20]. It can be seen that they are in excellent agreement. This verifies the correctness of our algorithm (integrated into the designed software) in calculating the electromagnetic scattering from inhomogeneous targets and demonstrates that our method also has high solution accuracy same as [20].

**B. Electromagnetic scattering estimation of a cloud-like inhomogeneous target with the designed software**

In practice, many objects have irregular structures, and the spatial distribution of dielectric constant usually cannot be expressed by a deterministic formula, such as the reservoir formation minerals, atmospheric turbulence, and so on. But many times, we can obtain their spatial spectrum functions of dielectric constants.

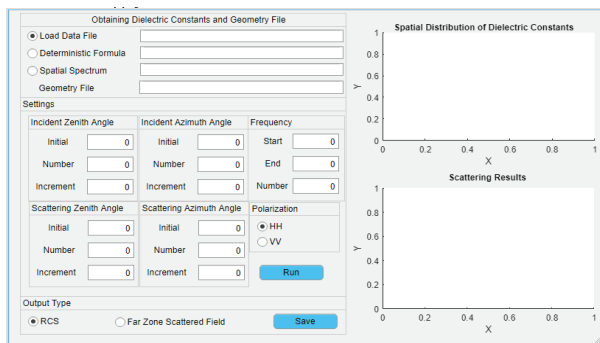


Fig. 4. Designed software to model arbitrarily inhomogeneous dielectric targets.

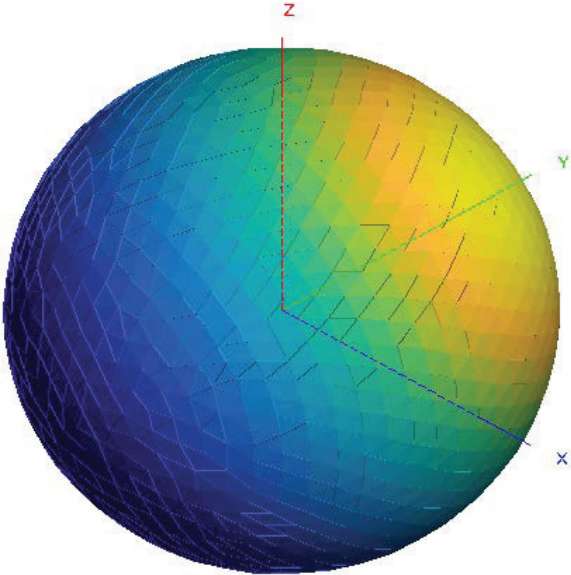


Fig. 5. Reconstruction of the inhomogeneous sphere ( $R = 1\text{m}$ ,  $\epsilon_r = \exp((x + y + z + 2)/2)$ , and  $\mu_r = 1$ ) with our software.

Table 1: Basic parameters of this kind of random media

$L_0$			$l_0$	$C$	$\epsilon_{r0}$
$L_{0x}$	$L_{0y}$	$L_{0z}$			
0.43 m	0.16 m	0.22 m	0.003 m	$10^{-7}\text{m}^{-1/3}$	1

In this section, we introduce our software to solve this kind of random media and establish an inhomogeneous target with a cloud-like shape for instruction. The detailed modeling processes and scattering calculation of the cloud-like target based on our software (introduced in Section II) are as follows:

- 1) Get the geometry file information and input the spatial spectrum function. For the import of the geometry file, the supported file formats are “\*.stp,” “\*.igs,” etc. The geometry of the cloud-like inhomogeneous target is shown in Figure 7 (a). The maximum length of the media is 0.43 m in the  $x$ -direction, 0.16 m in the  $y$ -direction, and 0.22 m in the  $z$ -direction. The spatial distribution of the dielectric constant is consistent with the atmosphere fluid, that is,  $\Phi(\mathbf{K}_{\nu'}) = 0.033C^2 |\mathbf{K}_{\nu'}|^{-11/3}$  (see Section II-A), and basic parameters of the fluid are shown in Table 1. The outer scale is the geometry size of the target in  $x$ -,  $y$ -, and  $z$ -directions, and the inner scale of the fluid is set to 0.003 m. The constant  $C$  and the average dielectric constant  $\epsilon_{r0}$  are set to  $10^{-7}\text{m}^{-1/3}$  and 1, respectively.
- 2) Generate the subdivision (tetrahedral elements) of the target according to the incident wave frequency

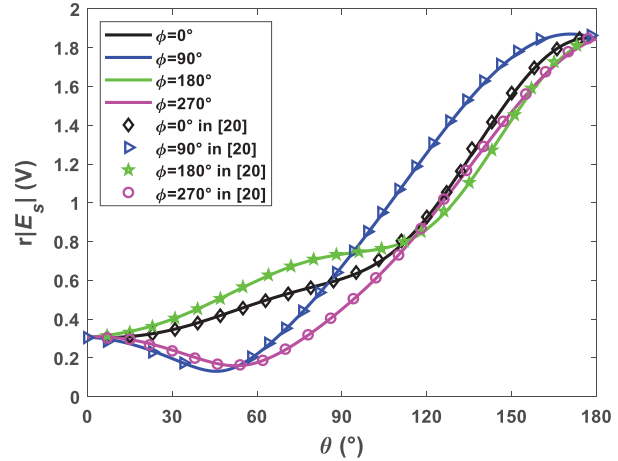


Fig. 6. Magnitude of the far zone scattered field ( $r|\mathbf{E}_s|$ ) as a function of angle for the inhomogeneous sphere at  $f_e = 100\text{MHz}$ .

$f_e$ . In this case, the incident wave frequency is set to 3 GHz; thus, 31,115 tetrahedral cells are obtained. The geometry after subdivision is shown in Figure 7 (b).

- 3) Determine the dielectric constant sampling points. According to the spatial spectrum function to obtain the dielectric constant spatial distribution of random media (see Section II-A), let  $p = q = s = 71$ ; then 357,911 sampling points are generated, as shown in Figure 7 (c). Notably, the more the sampling points, the more accurate it will be. The number of sampling points can be determined according to the specific application requirements.
- 4) Count the sampling points in each tetrahedral element according to eqn (5)–(8), calculate the average dielectric constant by (9), and assign the average dielectric constant to the corresponding tetrahedral element. The vertex coordinates and average dielectric constant of each tetrahedral element are shown in Table 2. The reconstruction of the cloud-like target is shown in Figure 7 (d).
- 5) Set simulation parameters. We set the start frequency to 300 MHz, the end frequency to 3 GHz, and the frequency increment to 37.5 MHz. The incident angle is set to  $\theta_i = 180^\circ$  (zenith angle) and  $\phi_i = 0^\circ$  (azimuth angle). The scattering angle is set to  $\theta_r = 180^\circ$  and  $\phi_r = 0^\circ$  (backscattered field). The detailed settings of the software in this case are shown in Figure 8.
- 6) Run the software to call the MoM algorithm for the electromagnetic scattering calculation of the target and save the results for further analysis.

It should be noted that, for the sake of statistical significance, we randomly generate 30 samples. Figure 9

Table 2: Vertex coordinates and average dielectric constant of each tetrahedral element

Tetra	$V_1$ (m)	$V_2$ (m)	$V_3$ (m)	$V_4$ (m)	$\bar{\epsilon}_r$
1	(-0.023,0.008,0.025)	(-0.036,0.013,0.025)	(-0.028,0.021,0.021)	(-0.023,0.009,0.015)	1.000200048
2	(-0.023,0.008,0.025)	(-0.023,0.018,0.031)	(-0.028,0.021,0.021)	(-0.028,0.012,0.031)	1.000200255
3	(-0.035,0.003,0.023)	(-0.036,0.013,0.025)	(-0.023,0.008,0.025)	(-0.023,0.009,0.015)	1.000199723
4	(-0.062,-0.014,-0.017)	(-0.059,-0.004,-0.014)	(-0.060,-0.016,-0.008)	(-0.052,-0.007,-0.011)	1.000199942
5	(-0.062,-0.014,-0.017)	(-0.052,-0.007,-0.011)	(-0.052,-0.020,-0.010)	(-0.051,-0.016,-0.018)	1.000199881
⋮	⋮	⋮	⋮	⋮	⋮

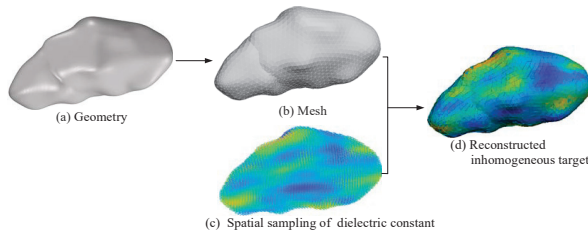


Fig. 7. Processes of reconstructing the inhomogeneous cloud-like target by our software.

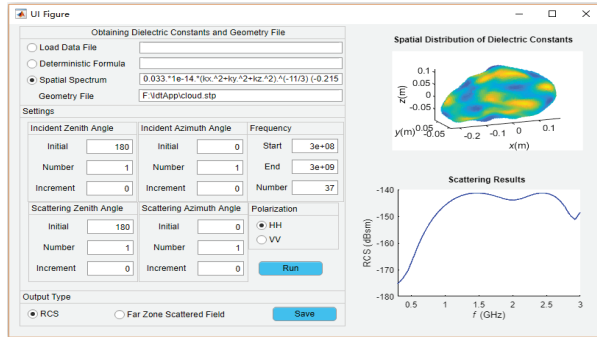


Fig. 8. Detailed settings of the software for modeling the inhomogeneous cloud-like target.

plots three samples of the spatial fluctuation of the cloud-like target's dielectric constant.

Figure 10 plots the simulation results (monostatic RCS) of the cloud-like target at different incident frequencies ( $f_e \in [0.3, 3]$  GHz). The thin gray-blue lines are

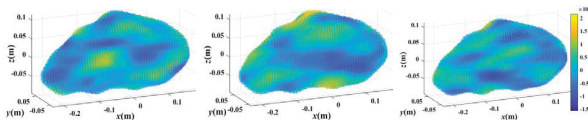


Fig. 9. Three cases of the dielectric constant spatial fluctuation of the cloud-like target.

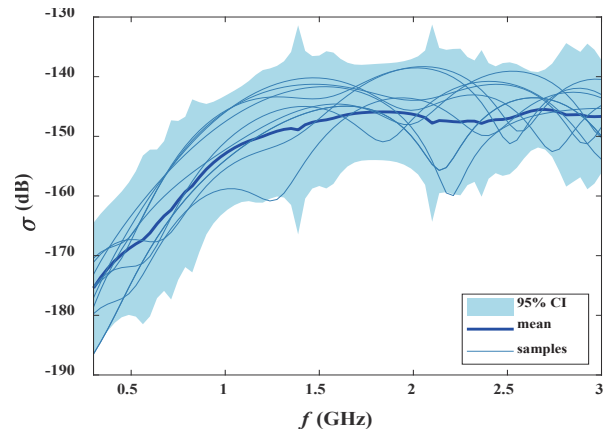


Fig. 10. Monostatic RCS versus the incident wave frequency.

the results of several samples, and the thick blue line is the average value of the 30 samples.

The light blue area in Figure 10 denotes the 95% confidence interval (CI) of the cloud-like target's RCS, which intuitively gives the amplitude range of echo signals from the target at each incident wave frequency.

It should be emphasized that, from the thick blue line, we observe that as the frequency increases, RCS gradually increases and tends to be stable at about 1 GHz. According to the Bragg scattering conditions, the scattering is stronger when the effective scatterer size is half of the incident wavelength [21]. In this case, this means that the size of the cloud-like target should reach the decimeter level, which is indeed the case (see Table 1). This proves that our results are reasonable, that is, our software can be used for electromagnetic scattering simulation of random inhomogeneous dielectric targets. The turbulent scattering is also generally estimated by the empirical formula given in [8], which suggests that the scattering result of turbulence is proportional to the cubic root of electromagnetic frequency. However, this result does not strictly conform with Bragg's law. Therefore,

our method can be better used to analyze the spectral characteristics of turbulence than empirical formulas.

#### IV. CONCLUSION

A practical method to model the arbitrarily irregular-shaped and inhomogeneous dielectric targets is presented in this paper. The simulation example of an inhomogeneous sphere with a continuously varying dielectric constant fully verifies the correctness of our method, where the scattered far-field results obtained by the proposed method are consistent with numerical results. More importantly, a user-friendly software is developed based on our method and the designed software can be applied to calculate the electromagnetic scattering from complex, irregular, and random inhomogeneous targets. In this paper, a cloud-like target, of which the dielectric constant distribution is obtained by Monte Carlo simulation with the spatial spectrum of atmospheric turbulence dielectric constant fluctuation, is taken as an example, and the results are in accordance with the Bragg's law. This fully verifies the wide applicability of the designed software.

Added up, our software can not only be applied to modeling the inhomogeneous target with a deterministic dielectric constant function and a regular shape but also the complex target with a spatial spectrum function and an irregular shape. It provides a convenient way to solve the electromagnetic scattering simulation problems of complex inhomogeneous targets in engineering applications.

#### ACKNOWLEDGMENT

This work was supported by the National Natural Science Foundation of China under Grant 61771375 and Grant 92052106.

#### REFERENCES

- [1] G. Zhang, *Wave Scattering by a Single Particle from: Weather Radar Polarimetry*, CRC Press, London, 2016.
- [2] C. Li, X. Chen, and X. Liu, "Cognitive tropospheric scatter communication," *IEEE Trans. Vehicul. Technol.*, vol. 67, no. 2, pp. 1482-1491, Feb. 2018.
- [3] R. Grant, *The Radar Game: Understanding Stealth and Aircraft Survivability*, Mitchell Institute Press, Mitchell, 2010.
- [4] K. Shariff and A. Wray, "Analysis of the radar reflectivity of aircraft vortex wakes," *J. Fluid Mech.*, vol. 463, pp. 121-161, Jan. 2002.
- [5] X. Wang, J. Li, L. Qu, C. Pang, and F. Niu, "Temporal evolution of the RCS of aircraft wake vortices," *Aerosp. Sci. Technol.*, vol. 24, no. 2, pp. 204-208, Feb. 2013.
- [6] A. Farahbakhsh, D. Zarifi, and A. Abdolali, "Using MATLAB to model inhomogeneous media in commercial computational electromagnetics software," *Applied Computational Electromagnetics Society (ACES) Journal*, vol. 30, no. 9, pp. 1003-1007, Sep. 2015.
- [7] P. Zhang, B. Du, and T. Dai, *Radar Meteorology*, Meteorology Press, Beijing, 2000.
- [8] I. V. Tatarski, *Wave Propagation in a Turbulent Medium*, Courier Dover Publications, USA, 2016.
- [9] F. T. Ulaby and U. Ravaioli, *Fundamentals of Applied Electromagnetics*, Prentice-Hall, USA, 2015.
- [10] N. P. Weatherill and O. Hassan, "Efficient three-dimensional Delaunay triangulation with automatic point creation and imposed boundary constraints," *Int. J. Numer. Meth. Eng.*, vol. 37, no. 12, pp. 2005-2039, 1994.
- [11] N. M. Noor, M. M. Al Bakri Abdullah, A. S. Yahaya, and N. A. Ramli, "Comparison of linear interpolation method and mean method to replace the missing values in environmental data set," *Mater. Sci. Forum*, vol. 803, pp. 278-281, 2014.
- [12] V. M. Jansoone, "Dielectric properties of a model fluid with the Monte Carlo method," *Chem. Phys.*, vol. 3, pp. 78-86, 1974.
- [13] X. Meng, L. Guo, S. Chai, and Y. Jiao, "The investigation of backscattering characteristics of 3-D local sea surface with time-varying overturning wave crest," *Applied Computational Electromagnetics Society (ACES) Journal*, vol. 33, no. 6, pp. 675-682, 2021.
- [14] C. Miesch, X. Briottet, Y. Kerr, and F. Cabot, "Monte Carlo approach for solving the radiative transfer equation over mountainous and heterogeneous areas," *Appl. Optics*, vol. 38, no. 36, pp. 7419-7430, 1999.
- [15] M. Man, Z. Lei, Y. Xie, B. Chen, and Q. Wang, "Monte Carlo simulation of the echo signals from low-flying targets for airborne radar," *Int. J. Antenn. Propag.*, vol. 2014, Nov. 2014.
- [16] T. Kamalakis, T. Sphicopoulos, S. S. Muhammad, and E. Leitgeb, "Estimation of the power scintillation probability density function in free-space optical links by use of multicanonical Monte Carlo sampling," *Opt. Lett.*, vol. 31, no. 21, pp. 3077-3079, 2006.
- [17] W. C. Gibson, *The Method of Moments in Electromagnetics*, CRC Press, New York, 2015.
- [18] D. H. Schaubert, D. R. Wilton, and A. W. Glisson, "A tetrahedral modeling method for electromagnetic scattering arbitrarily shaped inhomogeneous dielectric bodies," *IEEE T. Antenn. Propag.*, vol. 32, no. 1, pp. 77-85, 1984.
- [19] J. Drkošová, A. Greenbaum, M. Rozložník, and Z. Strakoš, "Numerical stability of GMRES," *BIT.*, vol. 35, no. 3, pp. 309-330, 1995.
- [20] E. Khodapanah, "Calculation of electromagnetic scattering from an inhomogeneous sphere," *IEEE*

*T. Antenn. Propag.*, vol. 67, no. 3, pp. 1771-1778, 2019.

- [21] A. S. Gurvich and A. I. Kon. "The backscattering from anisotropic turbulent irregularities," *J. Electromagnet Wave*, vol. 6, no. 6, pp. 107-118, Mar. 2015.



**Muyu Hou** received the B.S. degree in applied physics from Xi'an Shiyu University, Xi'an, China, in 2015. She is currently working toward the Ph.D. degree in radio physics with Xidian University, Xi'an, China. Her current research interests include tropospheric scatter propagation and tropospheric artificial metamorphosis.



**Shuhong Gong** was born in Shanxi, China, in 1978. He received the B.S. degree in physics education from Shanxi Normal University, Xi'an, China, in 2001, and the M.S. and Ph.D. degrees in radio physics from Xidian University, Xi'an, China, respectively, in 2004 and 2008.

He is currently a Professor with Xidian University. His research work has been focused on novel antenna design, radio wave propagation, and their applications.



**Yanchun Zuo** received the B.E. degree from Xinyang Normal University, Xinyang, China, in 2013 and the M.E. degree from Xidian University, Xi'an, China, in 2014. He is currently working toward the D.E. degree in electromagnetic field and microwave technology. His main research interests include electromagnetic scattering modeling and scattering measurements.



**Yu Liu** received the B.S. degree in applied physics from the Xi'an University of Posts & Telecommunications, Xi'an, China, in 2016. He is currently working toward the Ph.D. degree in radio physics with Xidian University, Xi'an, China, under the guidance of Prof. S. Gong. His current research interests include underwater wireless communication and mechanical antenna.

# Isolation Enhancement using CSRR Slot in the Ground for Compact Two-Element Textile MIMO Antenna

Navneet Sharma<sup>1</sup>, Anubhav Kumar<sup>1</sup>, Asok De<sup>2</sup>, and R. K. Jain<sup>1</sup>

<sup>1</sup>Department of Electronics and Communication Engineering  
Shobhit Institute of Engineering & Technology (Deemed to be University), Meerut (U.P.) 250110, India  
navneet1979@gmail.com, rajput.anubhav@gmail.com, rakesh.jain@shobhituniversity.ac.in

<sup>2</sup>Delhi Technological University, Delhi 110042, India  
asok.de@gmail.com

**Abstract** – A textile integrated, two-element, multiple-input multiple-output (MIMO) antenna is designed for Wi-Fi, wireless local area network (WLAN), and wearable biomedical applications. A CSRR slot and horn-shaped decoupling structure increases impedance matching and reduces the current movement from one element of antenna to another element which increases the isolation to 7.4 dB. The CSRR slot in the ground is accomplished between the elements to mitigate the surface current and enhance the isolation up to 27.4 dB. The 10-dB radiation exists from 4.65 to 5.97 GHz with more than 20-dB isolation in the full operating band where the maximum isolation is found to be 49.45 dB at 4.7 GHz. MIMO parameters are investigated in a two-element antenna, in which acceptable results are obtained. Bending analysis and phantom analysis are performed for wearable applications which demonstrate the acceptable results.

**Index Terms** – Defected ground structure (DGS), flexible antenna, isolation enhancement, MIMO antenna, textile antenna.

## I. INTRODUCTION

There has been an extreme influence of body worn antennas for communication system recently. To satisfy the demands of communication in today's scenario, the antenna has to be robust, flexible, cost effective, compact, and reliable for wearable applications [1]. Flexible and textile antenna could be easily incorporated in the wearable and portable devices, but accomplishing the antenna in the compact space is a challenging task for a researcher. Among several technologies of antenna design, the use of multiple-input multiple-output (MIMO) antenna is a popular choice because in MIMO, same data is sent as multiple signals simultaneously through multiple

antennas. This results in high data rate, diversity performance, high channel bandwidth, link reliability, high channel capacity, multiple transmission and reception capability, as well as spatial multiplexing [2, 3]. When multiple antennas are incorporated in small space, the distance between antennas is minimized due to which the mutual coupling increases and affects the MIMO parameters. High isolation between antenna elements could primarily be achieved in MIMO antennas by positioning the radiators at high distance ( $> \lambda/2$ ) from each other so that mutual coupling is neutralized. This results in a large sized antenna that is not suitable for wearable applications. Other methods to escape mutual coupling is to place the radiator either perpendicularly [3] or at orthogonal positions [4, 5]. Extended ground structure [6] or a conductive line between the radiators [7] also considerably reduces the size of antenna by bringing the radiators closer. To further reduce the size, which is compatible to the requirements of wearable devices, several decoupling structures such as meander lines, slots, stubs, as well as metamaterial structures such as EBG and SRR are utilized. Meander line structures are easy to implement on rigid FR-4 substrate [8] and provide good isolation, but antennas have to compromise with flexibility. Meander lines are also implemented on flexible jeans substrate to enhance isolation [2], but this approach increases design and fabrication complexities. Alternatively, T-shaped [9–12] and E-shaped [13] stubs, vertical and horizontal slotted ground [14], funnel-shaped defected ground structure [15], neutralized line between the radiators along with defected partial ground [16], decoupling stubs [17], and combination of vertical and horizontal ground for enhanced isolation [14] are very common, easy to implement, and simpler approach on jeans substrate. Researchers had also utilized dielectric resonators along with annular rings [18] to curb mutual coupling. In [19], four-element CPW-fed MIMO antenna is proposed for UWB applications with CSRR notch,

where distance between antenna and parasitic stub is used to improve the isolation. Researchers have also used metamaterial structures such as H-shaped EBG [20] for isolation enhancement. Orthogonal feed with stubs [4], defected ground structures, and square patch with chamfered feed [21] are some of the hybrid structures deliberately utilized for improved isolation and reducing size of antenna.

An antenna with flexible textile substrate has the following advantages over their fixed counterparts.

- The antenna can be designed conformal, enabling it to fit to the design of the device. Flexible textile antennas are also shock resistant, especially applicable on fast moving devices or wearables such as shoes or wrist watch.
- Fabric antennas are environment friendly when disposed and are immune to high temperature deformations that may exist in antennas with fixed substrates.

There are several types of textile materials that are used as a substrate to design flexible antennas [22] where jeans material, popularly known as denim material, is an obvious choice for research on wearable antennas because of its rugged and long lasting quality [23], low cost, and time saving fabrication techniques [1]. The fabric is highly researched and the textile characteristics are rigorously studied [24] and dielectric constant is determined [25].

The proposed textile antenna could be used in wearable applications with the following novelty and technical contributions.

1. The proposed antenna design is modest as compared to other structures [2, 9, 16] and is integrated on most popular, rugged, flexible, easily available, and inexpensive jeans textile material.
2. The suggested decoupling structure in this work enhances the port to port isolation significantly up to 49.45 dB which is expressively higher than the other related works [2, 4, 13, 15, 17].
3. The antenna is analyzed on different curvatures and maintains its band for wireless local area network (WLAN), Wi-Fi, and 5.8 GHz (ISM) with minimal effect on impedance matching as well as isolation.
4. To analyze the on-body radiation effect of antenna, specific absorption rate (SAR) is obtained using four layered phantom model. The obtained SAR is 0.2680 W/Kg which is lower than other reported work [2, 13, 16].

The antenna is designed with required Wi-Fi, WLAN, and ISM band applications and fulfilled the compact and flexible requirement for wearable applications. The demonstration of human body effect on the

antenna is discussed in the manuscript where antenna is designed with traditional equations, explained in eqn (1)–(3), and CSRR mitigates the current which is explained in Figure 1 (f). The low envelope correlation coefficient (ECC) and high isolation ensures that the antenna can be used for wireless communication applications.

## II. MIMO ANTENNA DESIGN AND EVOLUTION STEPS

The optimized, compact two-element MIMO antenna is fabricated on lossy [24, 26] jeans material of 1 mm thickness (dielectric constant,  $\epsilon_r = 1.7$ ) [2, 6, 24] which is illustrated in Figure 1 (a) with a prototype in hardware as shown in Figure 1 (b). The edge-to-edge dimensions of the antenna are 28 mm ( $W_b$ )  $\times$  24 mm ( $W_h$ ). Primarily, we have to design a single element antenna and calculate the length ( $\lambda_g$ ) and the width of the feed with help of eqn (1)–(3) [27]. In MIMO antenna design, two elements are incorporated with the conventional edge-to-edge distance.

$$\text{For } \frac{W}{h} > 1,$$

where  $W$  = width of the patch, and  $h$  = height of the substrate where dielectric constant ( $\epsilon_r$ ) for jeans (denim) material is 1.7.

The effective dielectric constant is given by

$$\epsilon_{\text{reff}} = \frac{\epsilon_r + 1}{2} + \frac{\epsilon_r - 1}{2} \left( 1 + 12 \frac{h}{W} \right)^{-\frac{1}{2}}, \quad (1)$$

$$\lambda_g = \frac{300}{f} \sqrt{\epsilon_{\text{eff}}}, \quad (2)$$

where  $f$  = resonant frequency.

The characteristic impedance  $Z_0$  can be given by

$$Z_0 = \frac{120\pi}{\sqrt{\epsilon_{\text{reff}}} \left[ \frac{w}{h} + 1.393 + 0.667 \ln \left( \frac{w}{h} + 1.444 \right) \right]}. \quad (3)$$

For MIMO antenna, the two elements are placed minimum at the distance of  $\lambda/4$  for considerable isolation. However, this distance could be reduced by using isolation structures such as SRR and EBG. The calculated feed is  $W_1 = W_2 = 2.7$  mm (width) and  $W_3 = W_4 = 13.6$  mm (height) with  $Z_0 = 52.36 \Omega$ .

Other dimensions of two-element MIMO antenna in mm are:  $W_5 = 3.9$ ,  $W_6 = 23$ ,  $W_7 = 8.5$ ,  $W_8 = 8$ ,  $W_9 = 8.9$ ,  $r_1 = 6.7$ ,  $r_2 = 6.6$ ,  $W_{10} = 1.5$ , and  $W_{11} = 1.5$ . The simulation of flexible and textile MIMO antenna is performed on Ansys HFSS-19 simulation software.

The two-element MIMO is evolved in four major iterations/steps, as is demonstrated in Figure 1 (c). In step-1, the ground height is 3.9 mm with 13.6-mm microstrip feed height where feed width of 2.7 mm is used to achieve approximately 50- $\Omega$  impedance matching. The  $|S_{11}|$  in dB exists from 4.75 to 5.69 GHz, whereas the averaged isolation is at 10 dB with highest isolation of 13.66 dB as revealed in Figures 1 (d) and

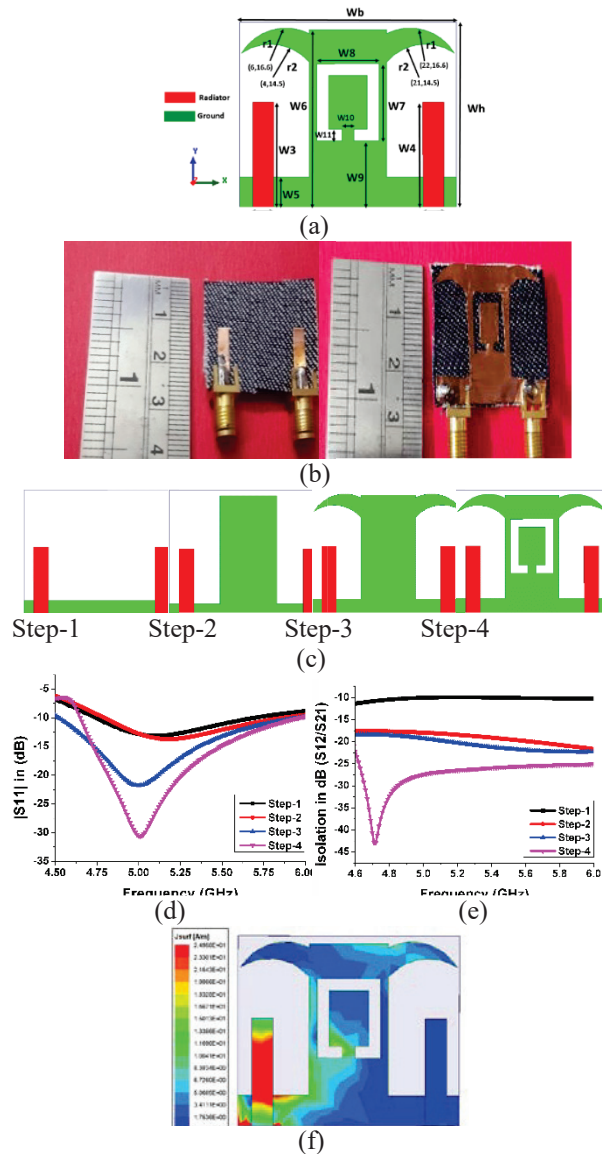


Fig. 1. (a) Proposed MIMO antenna (dimensions). (b) Prototype (fabricated). (c) Steps (evolution). (d)  $|S_{11}|$  parameters (steps) in dB. (e)  $|S_{12}|$  parameters (steps) in dB. (f) Surface current distribution at 5.8 GHz.

(e), respectively. In step-2, while increasing the ground vertically between two elements, isolation increases  $|S_{21}|$  because this modification perturbs the current movement toward the modified ground structure from port one [6]. The  $|S_{11}|$  in dB ranges from 4.80 to 5.87 GHz, whereas isolation is improved at this stage and ranges close to 17 dB, as is evident from Figures 1 (d) and (e). In step-3, a horn-shaped structure is implemented in the ground, which curates the impedance matching of antenna and increases the  $|S_{11}|$  that varies from 4.53 to 5.96 GHz. The horn-shaped decoupling structure reduces the surface

current between antenna elements and improves the isolation by 7 dB. In the last step, CSRR slot is accomplished in the decoupling structure, thereby mitigating the surface current and improving the isolation up to 27 dB. The  $|S_{11}|$  characteristics are further improved, which varies from 4.65 to 5.97 GHz with enhancement in isolation. The isolation at this stage has reached a peak of 49.45 dB, which is an improvement of 123.09% as compared to step-3 (without CSRR). Surface current analysis of two-port antenna is analyzed at 5.8 GHz which clearly demonstrates that the CSRR effectively diminishes the surface current and improves the isolation as shown in Figure 1 (f).

### III. BENDING ANALYSIS OF ANTENNA

To study the performance of two-port antenna with structural deformations, the antenna is deliberately bent on a polystyrene base cylinder with diameter of 25, 20, 15, and 10 cm using the wrapping tool in HFSS 19 [28]. The cylinder is then removed and simulation is performed. The screenshots are shown in Figure 2 (a), whereas Figure 2 (b) depicts the placement of designed antenna on polystyrene base. The  $|S_{11}|$  and  $|S_{12}|$  characteristics in dB (simulated) are shown in Figures 2 (c) and (d). Figure 2 (f) shows the variation in radiation efficiency, where small variations are observed. The size of antenna is reducing and impedance matching varies when bending process is applied on two-port antenna; therefore,  $|S_{11}|$  and  $|S_{12}|$  are shifted toward higher frequency, where small variation is found [36]. The minimum variation is found in gain of antenna in bending process is due to small variations in efficiency as depicted in Figure 2 (e). The bending analysis proves that the proposed antenna is working effectively, without compromising with the radiating bandwidth and isolation.

### IV. PHANTOM ANALYSIS

The wearable antennas are used near the human tissues; therefore, certain parameters of radiation have to be studied for wearable applications. The effect of radiation on different layers of human skin is measured in terms of SAR.

Absorption of electromagnetic (EM) energy when exposed to radiation of antenna is calculated in SAR. In other words, it is the radiated power absorbed by human tissue of 1 Kg, averaged at 1 or 10 g, as illustrated in eqn (4)

$$\text{SAR}_{\text{average}}(r, \omega) = \frac{1}{V} \int \frac{\sigma(r, \omega) |E(r, \omega)|^2}{2\rho(r)} dr, \quad (4)$$

where  $|E(r, \omega)|$  is electrical field in volt/meter,  $V$  = volume in meter cube,  $r$  = position of vector,  $\sigma$  is sample density, and  $(r, \omega)$  is the conductivity in Siemens/meter.

As per internationally approved standards, the value of SAR has to be under 1.6 W/Kg for safe use of antenna

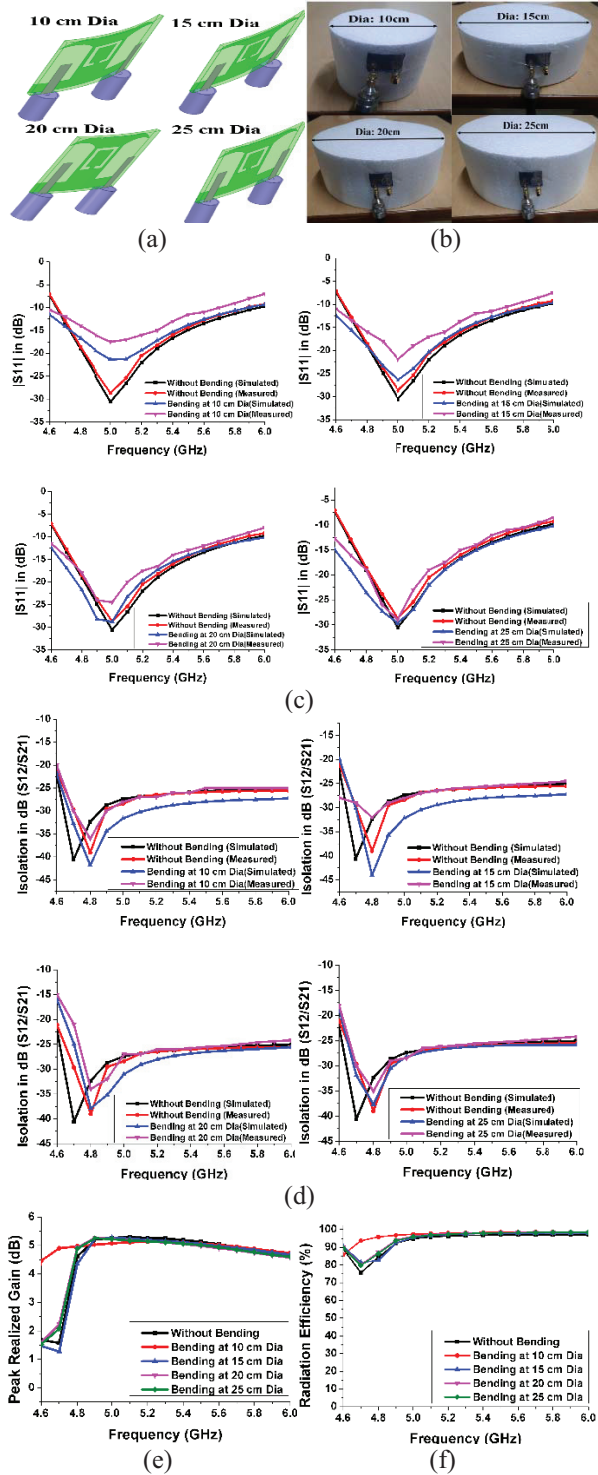


Fig. 2. Bending of antenna at 10, 15, 20, and 25 cm diameter (simulated). (b) Bending of antenna at 10, 15, 20, and 25 mm diameter (measured). (c)  $|S_{11}|$  in dB for bending analysis (simulated and measured). (d)  $|S_{12}/21|$  in dB for bending analysis (simulated and measured). (e) Peak realized gain variations on bending. (f) Radiation efficiency variations on bending.

Table 1: Characteristic values of human body tissues (5.8 GHz) [31]

Tissue	Conductivity (S/m)	Relative permittivity ( $\epsilon_r$ )	Loss tangent ( $\sigma$ )
Skin	3.717	35.114	0.32807
Muscles	4.9616	48.485	0.31715
Fat	0.29313	4.9549	0.18335
Breast fat	0.41974	4.4976	0.28924
Bone	1.1544	9.6744	0.36981

near human body [29]. An analysis of the antenna positioned at 20-mm distance from a phantom model is performed. The phantom model (four layered) is composed of skin layer (2-mm thick), fat layer (3.5-mm thick), muscular layer (10-mm thick), and bone (10-mm thick) as depicted in Figure 3 (a). The tissue characteristics such as conductivity, loss tangent, and relative permittivity at 5.8-GHz frequency are given in Table 1. The  $|S_{11}|$  and  $|S_{12}|$  parameters of antenna in dB without phantom and with phantom are shown in Figures 3 (c) and (d). The minimum variations are observed in s-parameters when the four-layered phantom model is positioned at 20 mm from antenna, and this could be a feasible distance for wearable applications. The maximum SAR value was evaluated as 0.2680 W/Kg when averaged on 10 g of phantom model, when excited with a source power of 10 mW as is relevant from Figure 3 (b). The radiation efficiency and realized gain, in the absence and presence of phantom model, are depicted in Figures 3 (e) and (f), and a small variation in gain is found as a result of grating lobe reflection from the phantom model.

## V. RESULTS AND DISCUSSIONS

The measurements were executed using VNA (Anritsu MS 2025B). The simulated and measured results of  $|S_{11}|$  and  $|S_{12}|$  in dB are depicted in Figures 4 (a) and (b), where  $|S_{11}|$  in dB extends from 4.7 to 5.9 GHz with more than 20-dB isolation and minimum variation is found in the measured results. The anechoic chamber measurement for gain, where the amplitude of the transmitted signal ( $P_t$ ) from MIMO is measured on the received signal ( $P_r$ ) by horn antenna at a distance of 3 m. The gain is determined using formulae as given in eqn (5).

$$\frac{P_r}{P_t} = G_t G_r \left( \frac{\lambda}{4\pi d} \right)^2, \quad (5)$$

where  $G_t$  and  $G_r$  are antenna gains of the MIMO antenna and horn antenna, respectively, and  $d$  is the distance between the two antennas and  $\lambda$  is the measured wavelength. The realized gain varies

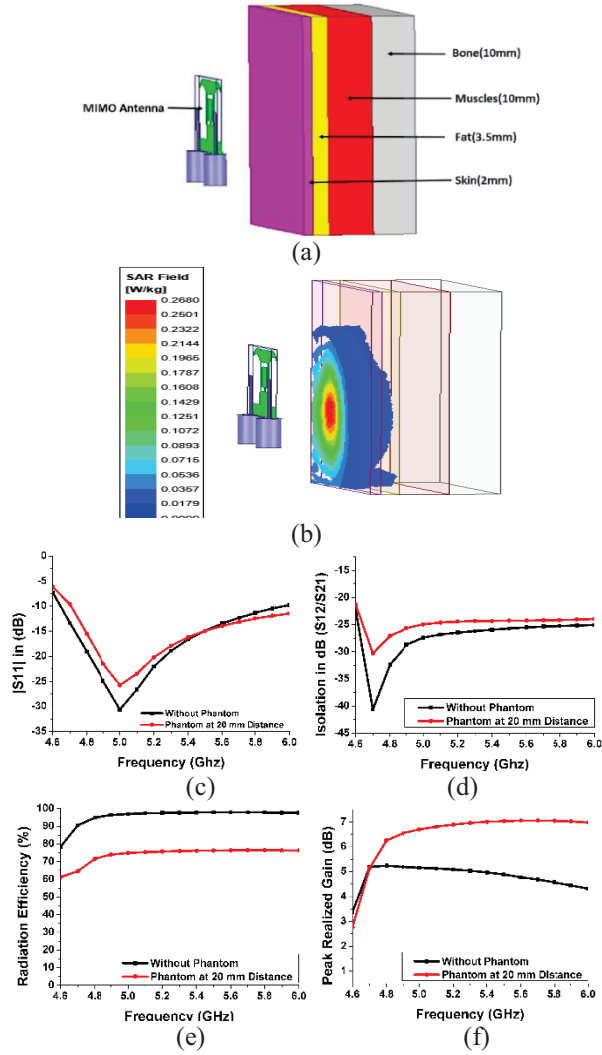


Fig. 3. Antenna positioned on phantom [30]. (b) Analysis of SAR (phantom). (c)  $|S_{11}|$  in dB on phantom. (d)  $|S_{12}|$  on phantom. (e) Radiation efficiency on phantom. (f) Peak realized gain on phantom.

from 3.37 to 5.23dB and less than 0.5 dB variation is observed with measured results due to environment losses associated with high frequency as depicted in Figure 4 (b). Radiation efficiency (simulated) is higher than 90% as is given in Figure 4 (c). The two-port antenna is measured on different body positions such as wrist, thigh, chest, and biceps for “on-body” wearable analysis as depicted in Figure 4 (f). The measured  $|S_{11}|$  and  $|S_{12}|$  in dB are depicted in Figures 4 (h) and (i). The results show that the antenna is performing satisfactorily when placed on any body part and also the antenna is able to maintain its isolation at less than 20 dB. Further, the antenna is placed on cap, shoes, bag, and riding helmet for portable wearable analysis as depicted in

Figure 4 (g), where the antenna has minimum variations in  $s$ -parameters due to coupling effect, but the experimental results show acceptable performance in terms of  $|S_{11}|$  and  $|S_{12}|$  in dB as shown in Figures 4 (j) and (k). The measurement of radiation pattern is performed in anechoic chamber and the normalized patterns in  $x$ - $z$  and  $y$ - $z$  planes at 5.8 GHz frequency are shown in Figure 4 (e) and during measurement port 2 is terminated with 50- $\Omega$  terminator and port 1 is excited. The difference between co- and cross-plane is observed at more than 20 dB in end-fire direction and stable radiations are observed. Figure 4 (d) represents the simulated and measured VSWR.

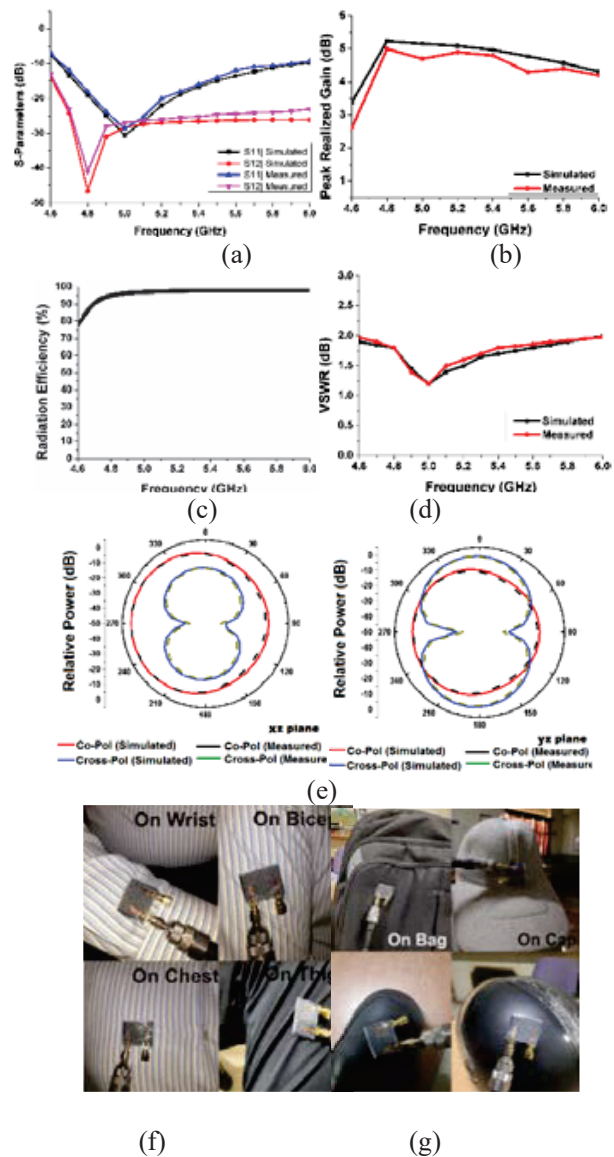


Fig. 4. Continued.

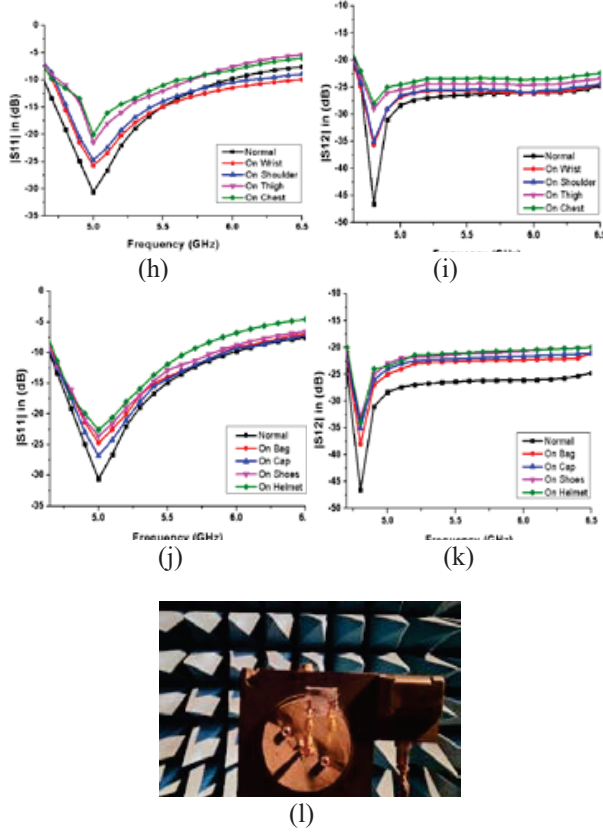


Fig. 4. Results (measured and simulated). (a)  $S$ -parameters (measured and simulated). (b) Realized gain (dB) (measured and simulated). (c) Radiation efficiency. (d) Simulated and measured VSWR. (e) Normalized radiation patterns in  $yz$  and  $xz$  planes at 5.8 GHz (measured and simulated). (f) Antenna placed on various body parts. (g) Antenna placed on different objects. (h)  $|S_{11}|$  characteristics in dB on different body parts. (i)  $|S_{12}|$  characteristics on different body parts. (j)  $|S_{11}|$  in dB on different objects. (k)  $|S_{12}|$  in dB on different objects. (l) Measurement of antenna in anechoic chamber.

## VI. ANALYSIS OF ECC, CCL, TARC, AND DG

### A. Formulation

For evaluating MIMO performance in diversity environment, certain parameters such as channel capacity loss (CCL), diversity gain (DG), total active reflection coefficient (TARC), and ECC are taken into consideration. All the parameters are measured using the eqn (6)–(9) [4]

$$\text{ECC} = \frac{|S_{11}^* S_{12} + S_{21}^* S_{22}|^2}{(1 - |S_{11}|^2 - |S_{21}|^2)(1 - |S_{22}|^2 - |S_{12}|^2)} \quad (6)$$

$$\text{DG} = 10\sqrt{1 - |\text{ECC}|^2}. \quad (7)$$

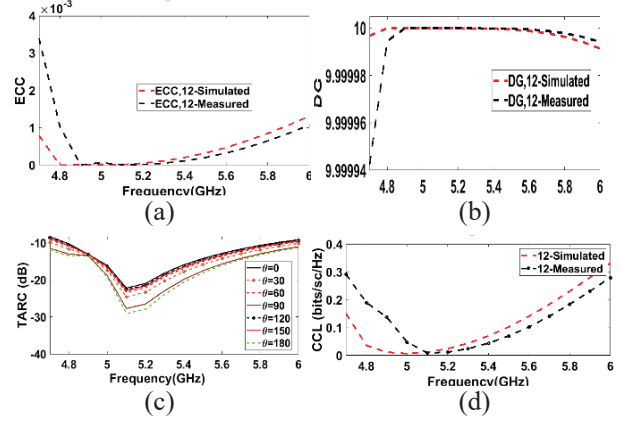


Fig. 5. MIMO parameters. (a) ECC. (b) Diversity gain. (c) TARC. (d) CCL.

$$\text{TARC} = \sqrt{|S_{11} + S_{12}e^{j\theta}|^2 + |S_{22} + S_{21}e^{j\theta}|^2} / \sqrt{2}, \quad (8)$$

where  $\theta$  = phase angle between adjacent/diagonal ports.

$$\text{CCL} = -\log_2 \det(\psi^R), \quad (9)$$

and  $\psi$  = correlation matrix at the receiving end.

### B. Explanation

ECC is an important parameter that represents the correlation between the antenna elements. ECC ranges from 0 to 1 where 0 represents no correlation and antennas are completely decoupled, whereas 1 indicates identical pattern and high coupling between antennas. A truly uncorrelated channel is highly unlikely; therefore, ECC, which is close to 0, is desirable, thereby exhibiting high diversity performance and DG [19]. ECC and DG are calculated from  $s$ -parameters and are extracted from eqn (6) and (7). The measured and simulated DG and ECC are illustrated in Figures 5 (b) and (a), in which ECC is less than 0.005 and DG is near 10 dB.

Radiating efficiency and bandwidth of MIMO are not accurately characterized by scattering matrix; therefore, TARC is used [20]. Two element antenna scattering parameters are used to extract the TARC from eqn (8). TARC with  $\theta = 0^\circ, 30^\circ, 60^\circ, 90^\circ, 120^\circ, 150^\circ, \text{ and } 180^\circ$  is given in Figure 5 (c), where minimum variations are observed.

CCL is a measure of throughput of antenna, where the CCL value should practically be less than 0.4 bit/s/Hz [11]. For the whole operating band, which represents high throughput. The CCL is measured through eqn (9). The measured and simulated CCL is depicted in Figure 5 (d) and is lower than 0.4 bits/s/Hz.

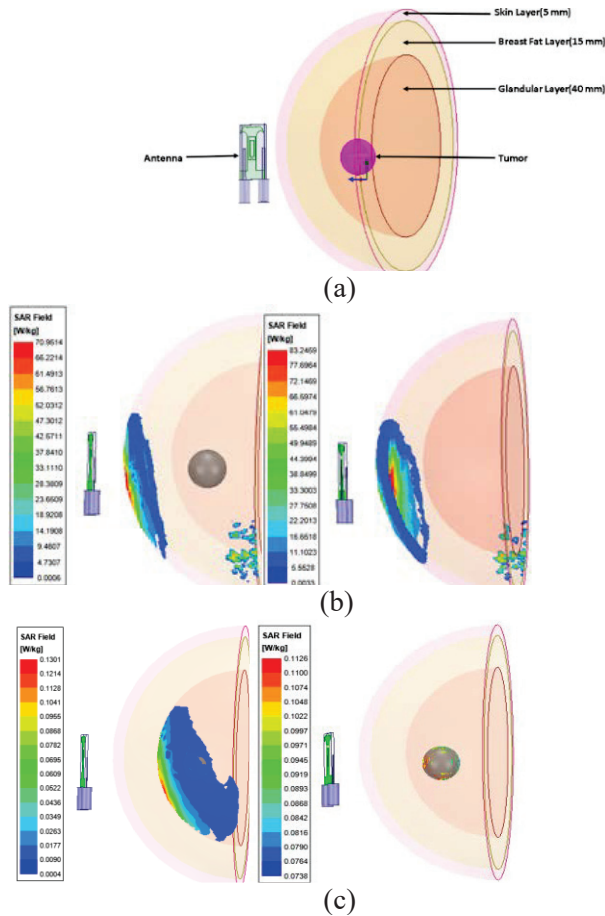


Fig. 6. (a) Breast model. (b) SAR of skin (without and with tumor). (c) SAR of glandular cell (with tumor) and SAR of tumor.

## VII. TUMOR ANALYSIS ON FEMALE BREAST PHANTOM MODEL

Tumor in the female breast is very common in the soft glandular tissue, which is more vulnerable to developing malignant cells. In this paper, tumor analysis is investigated on female breast phantom model, with respect to SAR analysis.

The characteristics of tissue such as permittivity and permeability vary on occurrence of malignant (tumor) cell, thereby changing the SAR characteristics of the cell [32, 33]. Therefore, SAR analysis is the direct method for prediction of tumorous cells. A three-dimensional breast model (female) is illustrated in Figure 6 (a) for SAR analysis. The distance between breast model and antenna is 15 mm. The breast model with tumor size of 8 mm radius is composed of glandular tissue ( $r = 40$  mm), breast fat ( $r = 55$  mm), and outermost skin layer ( $r = 60$  mm). The respective thickness of the layers is 40, 15, and 5 mm of glandular, breast fat, and skin layers [30, 32].

Table 2: SAR analysis (with and without tumor)

SAR (W/Kg) analysis at 5.8 GHz				
Tissue		With tumor	Without tumor	SAR diff.
Skin	Max	70.951	83.2459	12.2945
	Min	0.0006	0.0033	0.0027
Breast fat	Max	2.6118	2.6283	0.0165
	Min	0.0004	0.0003	0.0001
Glandular cell	Max	0.1301	0.1240	0.0061
	Min	0.0004	0.0003	0.0001
Tumor cell	Max	0.1126	–	–
	Min	0.0738	–	–

### A. Detection of tumor

As the microwave field penetrates the tissue, the power is subsequently rejected through reflections and dissipation. Several tumor detection techniques are conventionally accounted [34, 35]. In the proposed method, tumor detection could be accomplished by using two different hypotheses. In the first hypothesis, the SAR value of the tumor and glandular tissue in the vicinity is analyzed for the detection of tumor cell; here, it is observed that the higher  $SAR_{(avg)}$  value of the glandular tissue with tumor varies from 0.1301 to 0.0004 W/Kg, whereas SAR value of tumor tissue in glandular cell varies from 0.1126 to 0.0738 W/Kg, as shown in Figure 6 (c). The SAR difference denotes the presence of tumor, where the huge difference of minimum SAR value is detected in tumor cell and its neighboring glandular cell. In the second hypothesis, the difference in average SAR proves the presence of malignant (tumor) cell. It is observed that SAR values are decreased with the presence of tumor as given in Figure 6 (b). SAR difference (with and without tumor) is depicted in Table 2. In this investigation, the tumor analysis is observed effectively, which can be valuable for cancer detection and biomedical applications. In Table 3, the proposed two-port textile MIMO antenna is compared to the existing MIMO antenna, where proposed antenna is flexible and compact, based on textile material, with high isolation and have acceptable MIMO parameters, which can be applicable for WLAN and Wi-Fi communication in wearable applications.

## VIII. CONCLUSION

A two-element MIMO antenna is designed and fabricated on denim textile as a substrate for 5G, WLAN frequency bands: Wi-Fi/WLAN (HIPERLAN, U-NII) (IEEE 802.11 a/h/j) working group as well as biomedical (ISM) band at 5.8 GHz. The isolation is achieved from defected ground decoupling structure such as horn-shape and CSRR. The horn-shaped ground disturbs the surface current and improves the isolation up to 5 dB, whereas

Table 3: Proposed MIMO antenna compared with existing MIMO antenna

Ref	Size (mm <sup>2</sup> )	10 dB (GHz)	Isolation (dB)	Gain (dB)	Substrate	Flexibility	Isolation technology used	ECC
[2]	60 × 97	1.5–3.8, 4.1–6.1	15, 20	4	Jeans	Yes	Meander line structures	0.1
[4]	31 × 31	3.3–4.3	24	3.45	Jeans	Yes	Stubs and DGS, and orthogonal feed	0.2
[7]	140 × 70	2.33–2.5	26	4.7	Shieldit Textile	Yes	Conductive line	0.01
[9]	76 × 37	2.00–6.23	29.26	2.88	Felt	Yes	T-shaped stubs, ring-shaped slots, and meander line	0.01
[11]	80 × 170	3.4–3.6 and 3.9–4.5	20	6.8	FR4	No	T-shaped decoupling structure	0.3
[12]	18 × 44	3.3–3.65 and 4.8–5.5	18	5.93	FR4	No	Inverted T-shaped slot	0.002
[13]	55 × 35	2.4–9.0	18	9	Jeans	Yes	E-shaped stubs	0.06
[14]	71.7 × 50	3.24–3.05	19	4.7	FR4	No	Vertical and horizontal slotted ground	0.0035
[15]	35 × 30	3.11–5.15, 4.81–7.39	19, 21	NA	Jeans	Yes	Funnel-shaped DGS	0.18
[16]	30 × 50	3.14–9.73	32	2.7	Jeans	Yes	Neutralized ground	0.12
[17]	70 × 40	1.83–8	22	4	Jeans	Yes	I-shaped stubs	0.01
[21]	93 × 93	2.16–2.75	15	4.02	FR4	No	Square patch with circular chamfered corners	0.03
<b>Proposed</b>	<b>24 × 28</b>	<b>4.65–5.97</b>	<b>20</b>	<b>4.57</b>	<b>Jeans</b>	<b>Yes</b>	<b>Horn-shaped defected coupling structure with CSRR</b>	<b>0.005</b>

CSRR-shaped slot effectively diminishes the surface current and improves the isolation up to 27 dB. Overall, 20-dB isolation is achieved on the 10-dB impedance bandwidth of the proposed antenna that exists from 4.65 to 5.97 GHz; the antenna has simple decoupling structure and flexible substrate. The two-port MIMO antenna parameters are under the acceptable limit and antennas have minimum effect in  $s$ -parameter when analysis on bending was performed; this shows that the antenna is a suitable choice for wearable applications. Wi-Fi antennas are updated with MIMO technologies that allow group of devices to connect simultaneously to create efficient network and enhance speed and coverage. The MIMO antennas that are compact and integrated on fabrics could invariably be used for such applications in near future. The future technology holds easy-to-use and easy-to-fabricate antennas on other wearable textile substrates for 5G and 6G technologies that would be used in future. In future, more than two antenna elements would be designed for Internet of Things (IoT), sports, entertainment, and wearable technologies.

## REFERENCES

- [1] C. L. G. Monti and L. Tarricone, "Wearable antennas: Nontextile versus fully textile solutions," *IEEE Antennas and Propagation Magazine*, vol. 61, no. 2, pp. 71–83, 2019.
- [2] R. Sourav, G. Soumendu, S. P. Soumya, and C. Ujjal, "Dual-polarized textile-based two/four element MIMO antenna with improved isolation for dual wideband application," *International Journal of RF and Microwave Computer-Aided Engineering*, vol. 30, no. 9, pp. e22292, 2020.
- [3] A. A. Ibrahim, J. Machac, and R. M. Shubair, "UWB MIMO antenna for high speed wireless applications," *Applied Computational Electromagnetics Society (ACES) Journal*, pp. 1294–1299, 2019.
- [4] K. A. Asok De and R. K. Jain, "Circular polarized two-element textile antenna with high isolation and polarization diversity for wearable applications," *International Journal of Microwave and Wireless Technologies*, pp. 1–9, 2022.

- [5] D. Chengzhu, Y. Zhipeng, J. Gaoya, and Z. Shunshi, "Design of a co-planar waveguide-fed flexible ultra-wideband-multiple-input multiple-output antenna with dual band-notched characteristics for wireless body area network," *International Journal of RF and Microwave Computer-Aided Engineering*, vol. 32, no. 3, pp. e22997, 2022.
- [6] J. Pankaj, K. Anubhav, D. Asok, and K. J. Rakesh, "Flexible and textile two-port compact antenna for WLAN and wearable applications," *2021 8th International Conference on Signal Processing and Integrated Networks (SPIN)*. IEEE, pp. 308-311, 2021.
- [7] A. Ismahayati, R. K. Muhammad, H. R. Ali, H. Norshakila, A. R. Hasliza, A. W. M. Wan Zuki, I. M. Arif, J. Muzammil, and M. Y. Mohd Najib, "Investigation on wearable antenna under different bending conditions for wireless body area network (WBAN) applications," *International Journal of Antennas and Propagation*, 2021.
- [8] J. Deng, J. Li, L. Zhao, and L. Guo "A dual-band inverted-F MIMO antenna with enhanced isolation for WLAN applications," *IEEE Antennas and Wireless Propagation Letters*, vol. 16, pp. 2270-2273, 2017.
- [9] K. K. Binod, K. Ashwani, S. Kunal, and K. Sachin, "Wideband textile multiple-input-multiple-output antenna for industrial, scientific and medical (ISM)/wearable applications," *International Journal of RF and Microwave Computer-Aided Engineering*, vol. 30, no. 12, e22451, 2020.
- [10] K. A. Asok De and R. K. Jain, "Size miniaturization and isolation enhancement of two-element antenna for sub-6 GHz applications," *IETE Journal of Research*, pp. 1-8, 2021.
- [11] J. Pankaj, K. Anubhav, D. Asok, and K. J. Rakesh, "Modified CSRR based dual-band four-element MIMO antenna for 5G smartphone communication," *Progress In Electromagnetics Research Letters*, vol. 101, 2021.
- [12] A. Chatterjee, M. Midya, L. Mishra, and M. Mitra, "Dual-element Multiple-input-multiple-output system for sub-6 GHz (5G) and WLAN applications with enhanced isolation," *Progress In Electromagnetics Research M*, vol. 103, pp. 197-208, 2021.
- [13] S. Rekha and G. Shine Let, "Design and SAR analysis of wearable UWB MIMO antenna with enhanced isolation using a parasitic structure," *Iranian Journal of Science and Technology, Transactions of Electrical Engineering*, pp. 1-11, 2022.
- [14] A. Kumar, N. K. Narayaswamy, H. Venkatesh Kumar, B. Mishra, S. A. Siddique, and A. K. Dwivedi, "High-isolated WiFi-2.4 GHz/LTE MIMO antenna for RF-energy harvesting applications," *AEU-International Journal of Electronics and Communications*, vol. 141, pp. 153964, 2021.
- [15] B. Ashim Kumar and U. Chakraborty, "Reconfigurable wide band wearable multiple input multiple output antenna with hanging resonator," *Microwave and Optical Technology Letters*, vol. 62, no. 3, pp. 1352-1359, 2020.
- [16] B. Ashim Kumar and U. Chakraborty, "Investigation on decoupling of wide band wearable multiple-input multiple-output antenna elements using microstrip neutralization line," *International Journal of RF and Microwave Computer-Aided Engineering*, vol. 29, no. 7, pp. e21723, 2019.
- [17] B. Ashim Kumar and U. Chakraborty, "A compact wide band textile MIMO antenna with very low mutual coupling for wearable applications," *International Journal of RF and Microwave Computer-Aided Engineering*, vol. 29, no. 8, pp. e21769, 2019.
- [18] D. Gourab, A. Sharma, and R. K. Gangwar, "Dielectric resonator-based two-element MIMO antenna system with dual band characteristics," *IET Microwaves, Antennas & Propagation*, vol. 12, no. 5, pp. 734-741, 2018.
- [19] K. Anubhav, "Compact 4x4 CPW-Fed MIMO antenna with Wi-Fi and WLAN notch for UWB applications," *Radioelectronics and Communications Systems*, vol. 64, no. 2, pp. 92-98, 2021.
- [20] K. A. Asok De and R. K. Jain, "Novel H-shaped EBG in E-plane for isolation enhancement of compact CPW-fed Two-port UWB MIMO antenna," *IETE Journal of Research*, pp. 1-7, 2020.
- [21] A. D. Chaudhari and K. P. Ray, "A compact five-element printed MIMO antenna with pattern and polarization diversity for 2.45 GHz WLAN applications," *Journal of Electromagnetic Waves and Applications*, pp. 1-13, 2022.
- [22] M. Sarmad Nozad, J. I. Asnor, S. Tale, A. Hussein, A. Sameer, I. Alyani, and C. S. Azura, "Recent advances in wearable antenna technologies: a review," *Progress in Electromagnetics Research B*, vol. 89, pp. 1-27, 2020.
- [23] K. N. Paracha, S. K. Abdul Rahim, P. J. Soh, and M. Khalily "Wearable antennas: A review of materials, structures, and innovative features for autonomous communication and sensing," *IEEE Access*, vol. 7, pp. 56694-56712, 2019.
- [24] A. Mohamed Ismail, M. F. Ahmed, and A. H. A. Shaalan, "Novel electro-textile patch antenna on jeans substrate for wearable applications," *Progress In Electromagnetics Research C*, vol. 83, pp. 255-265, 2018.

- [25] S. Sankaralingam and B. Gupta, "Determination of dielectric constant of fabric materials and their use as substrates for design and development of antennas for wearable applications," *IEEE Transactions on Instrumentation and Measurement*, vol. 59, no. 12, pp. 3122-3130, 2010.
- [26] L. Seung Yoon, C. Moogoong, J. Sohyeon, and H. Wonbi "Optically transparent nano-patterned antennas: A review and future directions," *Applied Sciences* vol. 8, no. 6, pp. 901, 2018.
- [27] C. A. Balanis, *Antenna Theory Analysis and Design*. John Wiley & Sons, 2015.
- [28] B. Prudhvi Nadh, B. T. P. Madhav, M. Siva Kumar, T. Anil Kumar, M. Venkateswara Rao, and S. S. Mohan Reddy, "MEMS-based reconfigurable and flexible antenna for body-centric wearable applications," *Journal of Electromagnetic Waves and Applications*, pp. 1-15, 2022.
- [29] A. Fatemeh, M. M. Paulides, and G. C. Van Rhoon, "SAR thresholds for electromagnetic exposure using functional thermal dose limits," *International Journal of Hyperthermia*, vol. 34, no. 8, pp. 1248-1254, 2018.
- [30] S. Navneet, K. Anubhav, A. De, and R. K. Jain, "Design of compact hexagonal shaped multiband antenna for wearable and tumor detection applications," *Progress In Electromagnetics Research M*, vol. 105, pp. 205-217, 2021.
- [31] Inst. of Appl. Phys., Italian Nat. Res. Council, "Calculation of the dielectric properties of body tissues in the frequency range 10 Hz-100 GHz," Florence, Italy. [Online]. Available: <http://niremf.ifac.cnr.it/tissprop>.
- [32] S. Navneet, K. Anubhav, A. De, and R. K. Jain, "Compact circular polarized CPW antenna for WLAN and biomedical applications," *Frequenz*, vol. 76, 2021.
- [33] S. Subramanian, B. Sundarambal, and D. Nirmal, "Investigation on simulation-based specific absorption rate in ultra-wideband antenna for breast cancer detection," *IEEE Sensors Journal*, vol. 18, no. 24, pp. 10002-10009, 2018.
- [34] N. K. Nikolova, "Microwave imaging for breast cancer," *IEEE Microwave Magazine*, vol. 12, no. 7, pp. 78-94, 2011.
- [35] B. Ria, A. A. Thathamkulam, and P. Mythili, "An overview of microwave imaging for breast tumor detection," *Progress In Electromagnetics Research B*, vol. 87, pp. 61-91, 2020.
- [36] M. U. A. Khan, R. Raad, F. Tubbal, and P. I. Theoharis, "The impact of bending on radiation characteristics of polymer-based flexible antennas for general IoT applications," *Applied Sciences*, vol. 11, no. 19, pp. 9044, 2021.



**Navneet Sharma** is having an excellent academic record. He received the bachelor's degree in engineering from the Prestigious Delhi College of Engineering (presently, Delhi Technological University), New Delhi, India, in the field of electronics and communication engineering.

He received the master's degree in technology from Dr. Abdul Kalam Technical University, Lucknow, India. Currently, he is working toward the Ph.D. degree from the Shobhit Institute of Engineering and Technology (deemed to be university) Meerut, Uttar Pradesh, India, in the field of microwave engineering, where his specialization is wearable and biomedical antennas. He has published his research in SCI/ESCI as well as Scopus indexed journals and also presented papers in scores of national and international conferences. He has 14 years of teaching experience.



**Anubhav Kumar** received B.Tech. and M.Tech. degrees from Uttar Pradesh Technical University (now Dr. APJ AKTU), Lucknow, India, in electronics and communication engineering (ECE). He has more than 10 years of teaching experience.

He is currently working toward the Ph.D. from the Shobhit Institute of Engineering and Technology (deemed to be university), Meerut, Uttar Pradesh, India. He has published many SCIE/ESCI and Scopus indexed research papers in International Journals. His research interests include microstrip antenna, metamaterial, FSS, MIMO, wearable, EBG antenna and Image processing.



**Asok De** received the B.Tech. and M.Tech. degrees from Jadavpur University, Kolkata, India, and the Ph.D. degree from the Indian Institute of Technology, Kharagpur, India. He served as Faculty with the University of Delhi, University of Kolkata, India, from 1984 to 1997. He joined

as a Professor of Electronics and Communication Engineering with the Delhi College of Engineering (at present, Delhi Technological University) in 1997. He was the Founder Principal of Ambedkar Institute of Advanced Communication Technology and Research (2005–2012). He served National Institute of Technology Patna as Director from 2012 to 2017. He also served the National Institute of Technology Durgapur as Director (Additional Charge) from 2015 to 2017.

Prof. De has published more than 200 research papers in international journals and international conferences. He supervised 16 Ph.D. scholars. At present, he is an Emeritus Professor with Delhi Technological University.



**R. K. Jain** received the Ph.D. degree from Banaras Hindu University, Varanasi, India, in 1990. He is a Professor and Associate Dean with the School of Engineering & Technology, Shobhit Institute of Engineering and Technology (deemed to be university), Meerut, India,

where he has been teaching and doing research with the

collaboration of BHU, Varanasi and BARC, Mumbai. He has also received Postdoctoral fellowship with the Department of Physics, North Carolina State University, Raleigh, NC, USA from May 2002 to June 2003 and worked on low-intensity and low-energy proton beams for the development of low-energy proton detectors (needed to detect protons emitted in neutron beta decay). He has nearly 23 years of teaching experience and 30 years of research after Ph.D.

# Wearable Panda-Shaped Textile Antenna with Annular Ring-Defected Ground Structure for Wireless Body Area Networks

T. Annalakshmi<sup>1</sup> and S. Ramesh<sup>2</sup>

<sup>1</sup>Department of Electronics and Communication Engineering  
New Prince Shri Bhavani College of Engineering and Technology, Chennai 600074, Tamil Nadu, India  
lakshmishanmu15@gmail.com

<sup>2</sup>Department of Electronics and Communication Engineering  
SRM Valliammai Engineering College, Kattankulathur, Chennai 603203, Tamil Nadu, India  
rameshs.ece@valliammai.co.in

**Abstract** – This research presents a compact panda-shaped wearable antenna with a defected ground structure (DGS). It is fabricated using a flexible material to work at 2.4-GHz industrial scientific medical (ISM) band, confirming the wireless body area network (WBAN) application requirements. The annular ring DGS and circular and elliptical slots in the patch aid in achieving the operating frequency. Good impedance bandwidth is maintained during on-body and bending analysis. Furthermore, this antenna exhibits a peak gain of 7.3 dB and a minimum specific absorption rate (SAR) of 0.0233 W/kg for 1 g tissue and 1.02 W/kg for 10 g tissue. The investigation shows that an antenna with good robustness, compact, high flexibility, and very low SAR makes it a strong candidate for WBAN applications.

**Index Terms** – Annular ring DGS, bending analysis, flexible, SAR, slot.

## I. INTRODUCTION

In the new millennia, there has been constant technological advancement, specifically in wireless body area network (WBAN) communication. The technology has been used across multiple fields, including military and health care [1]. This significant improvement requires the scientific world to invest time and energy to develop WBAN systems, especially wearable antennas that seamlessly integrate into people's daily wear. This requirement poses a significant challenge for the scientific community to ensure that the wearable antenna designed is flexible, conductive, compact, light-weight, yet non-abrasive, and, importantly, meets the emission standards put forth by international standard organizations [2]. As the antenna is expected to be used on the human body, the parameters that need to be evaluated are frequency shifting, efficiency degradation, and radiation

distortion when used near human tissues, as stringent rules cover are applicable for the SAR [3]. Previous research studies prove that the performance of the wearable antenna is impacted when working near a human subject [4].

Several pieces of research have been proposed so far for wearable application in narrowband. Some of the notable contributions are as follows: in [5], a combination of EBG defected ground structure (DGS) technique was employed. In this work, EBG increases the isolation between the human bodies with an antenna, whereas DGS enhances the bandwidth. The L-shaped inverted element with DGS is proposed for the improvement of the bandwidth and gain [6]. In [7], an asymmetric arch-shaped DGS was utilized to reduce the cross-polarization and enhance the gain. The ground plane is modified with four L-shaped slots to radiate the antenna in dual band [8]. Using floating ground planes, the authors produced low specific absorption rate (SAR) value, reduced backward radiation, and improved gain [9]. Adding the meandering slits on the ground plane and fractal structure achieved size miniaturization and bandwidth improvement [10]. In [11], high gain, wideband, and low SAR were obtained using an array antenna with an EBG structure on the ground plane. In [12], dielectric resonator antenna with slotted ground suppresses the substrate effect, reducing the backward radiation. Based on the analysis, DGS is the best choice for the excellent characteristics of the antenna as it supports miniaturization, improving gain, bandwidth, and suppressing backward radiation. This article introduces a compact panda-shaped flexible textile antenna with annular ring DGS for WBAN applications. The suggested antenna is designed as the right choice for wearable applications due to its compactness, flexibility, excellent characteristics in on-body and bending scenarios with low SAR value, and charming shape. There are four sections in this article.

The antenna design topology and DGS technique are demonstrated in Section II. The outcome and analysis of the antenna are enlightened in Section III. The conclusion part is discussed in Section IV.

## II. ANTENNA DESIGN

### A. Antenna topology

An elliptical-shaped patch forms the basic structure of the antenna as the face and it is shown in Figure 1.

$$M_{\text{eff}} = m \left[ 1 + \frac{2t}{\pi \epsilon_r m} \left\{ \ln \left( \frac{m}{2t} \right) + (1.41 \epsilon_r + 1.77) + \frac{t}{m} (0.268 \epsilon_r + 1.65) \right\} \right]^{\frac{1}{2}}, \quad (1)$$

$$f_r = \frac{15}{\pi e M_{\text{eff}}} \sqrt{\frac{q_{11}}{\epsilon_r}}, \quad (2)$$

$$q_{11} = -0.0063e + 3.8316e^2 - 1.1351e^3 + 5.2229e^4, \quad (3)$$

$$e = \frac{\sqrt{m^2 - n^2}}{m}. \quad (4)$$

The mathematical analysis of elliptical patch geometry is derived using the approximated Mathieu's function as depicted in eqn (1)–(4) [13–16], where  $M_{\text{eff}}$  is the effective semi-major axis,  $m$  is the semi-major axis,  $n$  is the semi-minor axis,  $\epsilon_r$  is the dielectric constant of substrate,  $t$  is the substrate height,  $e$  is the eccentricity of ellipse,  $f_r$  is the resonance frequency, and  $q_{11}$  is the approximated Mathieu function. Originally, the radiating patch is designed for 2.8 GHz using eqn (2). To improve the  $S_{11}$  level, gain, and bandwidth, two annular rings are attached as left and right ears on both sides. By increasing the perimeter of the patch bandwidth broadening is achieved [17]. Further, two circle-shaped slots are etched from the face as right and left side eyes. Finally, at the center, an elliptical slot is also etched as a nose. By adding more slots in the patch, more current is interrupted and more energy is radiated from the slot. This

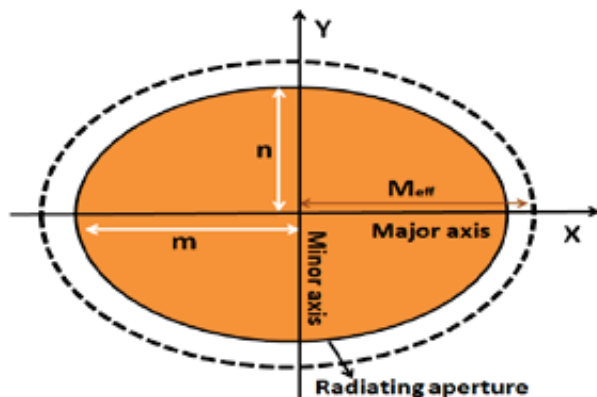


Fig. 1. Elliptical structure.

boosts the gain and efficiency by increasing the radiated power [18]. This slotted structure forms a panda's head that attracts people to wear. A feed line is extended from the edge of the face to the bottom of the substrate.

### Impact of DGS – on the Antenna Behavior

In the DGS technique, the ground is etched with a defect or slot to improve the antenna's performance regarding resonance frequency,  $S_{11}$ , gain, bandwidth, and efficiency [19], [20]. It interrupts the current path of the ground surface and enhances the performance [21]. The shape, size, and position of DGS are calibrated to meet the optimal characteristics. This article introduces a novel idea of annular ring DGS etched on the ground surface. Due to the impact of DGS, resonance frequency shifted from 2.8 to 2.44 GHz with an improved level of  $S_{11}$  from  $-22$  to  $-53$  dB. Further, it also raises the bandwidth from 40 to 130 MHz. Thus, the overall performance of the antenna is satisfied only with the presence of DGS. The construction of antenna topology is presented in a step-by-step process and is shown in Figure 2. Table 1 shows the detailed measurement of the antenna and the simulation is carried out with CST microwave studio software. The front and back views of the designed antenna are depicted in Figure 3.

### B. Fabricated antenna

The ground structure and patch are fabricated with flexible conductive fabric having  $0.05 \Omega/\text{square}$  surface resistivity. The commonly available jeans cloth is used as a substrate. Its dielectric constant is 1.7, and its thickness is 1 mm [22]. The material is chosen due to its lower dielectric constant value, reducing the surface wave losses and enhancing impedance bandwidth [23]. The substrate thickness is selected as the minimum value of 1 mm to increase the antenna efficiency. The loss tangent value of denim jeans is 0.025. The precise shape of the patch and ground is cut by a laser machine

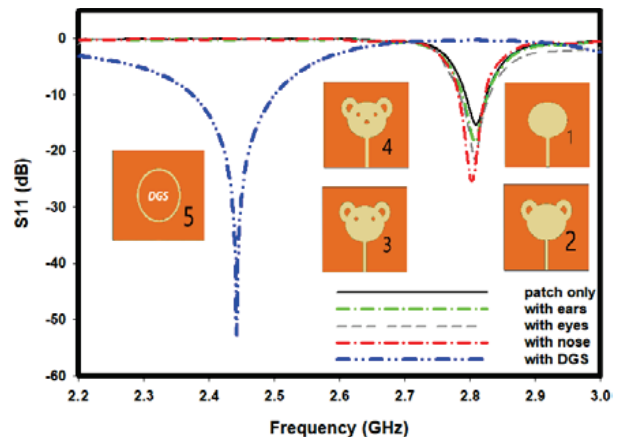


Fig. 2. Simulated  $S_{11}$  for stepwise design.

Table 1: Measurements of the antenna structure

Parameters	Size in mm
Face-X radius	11.5
Face-Y radius	8.5
Ear-outer radius (left, right)	5
Ear-inner radius (left, right)	2
Nose-X radius	1.5
Nose-Y radius	0.5
Eye (left, right) radius	1
Ground slot – outer radius	12
Ground slot – inner radius	11

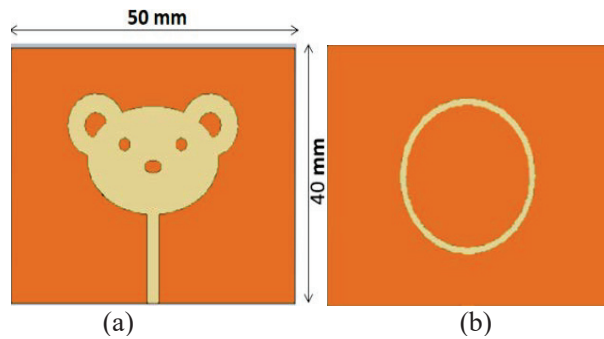


Fig. 3. Antenna topology. (a) Front view. (b) Back view.

SENFNNG – SF1610. This process provides extreme accuracy and clean cuts and minimizes fraying. The substrate is attached to the patch and ground fabric using fabric glue. A 50Ω SMA connector is affixed to the feed line for the antenna's excitation. Figure 4 depicts the antenna prototype in different views.

### III. ANTENNA PERFORMANCE

Analysis of the antenna in on-body and free space scenarios was performed to study the standard parameters and SAR and bending analysis. A body phantom with dimension  $100 \times 100 \times 13$  mm consisting of skin, fat, and muscle is created using a CST microwave studio for on-body simulation. Table 2 lists the physical



Fig. 4. Antenna topology. (a) Front view. (b) Back view.

Table 2: Properties of different tissue

Properties	Skin	Fat	Muscle
Thickness (mm)	2	3	8
Permittivity	41.3	5.3	54.8
Density ( $\text{Kg}/\text{m}^3$ )	1100	910	1041
Conductivity (S/m)	0.895	0.049	0.955

attributes of each layer [24]. An 8-mm thick jean substrate is implemented between the antenna and body phantom. This creates the real-life scenario of the human wearing clothes. Figure 5 shows the human body phantom and real human models when the antenna is placed.

The real human body of the female model is used for an on-body measurement. The female model is 41 years old with 154-cm height and 64-Kg weight. The test is performed by placing the antenna on the back of the human model. A gap of 8 mm was maintained between the antenna and the human model. The clothes worn by the human model and the adhesive tape used to fix the antenna on the clothes create a separation of 8 mm.

#### A. Reflection coefficient ( $S_{11}$ )

The measurement was performed using a vector network analyzer (VNA) with a 0–26 GHz range. The result exhibits good impedance bandwidth covering the industrial scientific medical (ISM) band across 2.40–2.4835 GHz as shown in Figure 6. The  $S_{11}$  magnitude of the antenna can also be measured by placing the antenna on the body. The dielectric loading effect and conductive nature of the lossy human tissue in close proximity to the worn patch antenna model result in a slight deviation in resonance frequency from 2.45 to 2.47 GHz

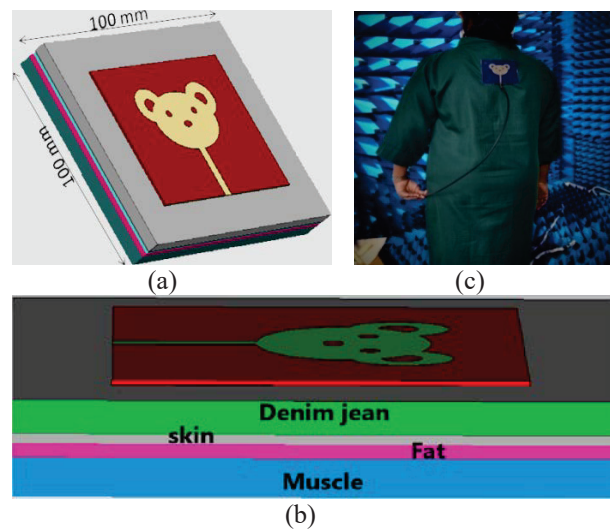


Fig. 5. The human body phantom model. (b) Side view. (c) The real model in a chamber.

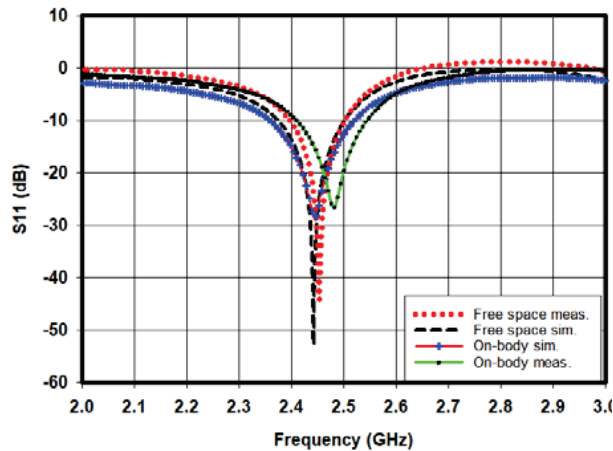


Fig. 6. Reflection coefficient ( $S_{11}$ ) response.

(20 MHz) and a reduction in  $S_{11}$  magnitude [25, 26]. Though there is a deviation in resonance frequency, it covers the required impedance bandwidth.

### B. Far-field radiation pattern

A shielded anechoic chamber measuring  $5.7 \times 3.5 \times 3$  m with an operating range of 700 MHz to 18 GHz frequency was used. The photographs of the antenna placement in  $E$ -plane and  $H$ -plane directions are shown in Figure 7. The observed radiation pattern (co-polar and cross-polar) in both  $E$ -plane and  $H$ -plane directions for on-body, free space flat, and bending antennas are presented in Figures 8 and 9. In  $H$ -plane and  $E$ -plane, the antenna produces nearly a bi-directional and omnidirectional pattern, respectively, at 2.4 GHz. From the radiation characteristics, it is evident that there is a good isolation between co-polarization and cross-polarization in all scenarios due to the presence of DGS [27]. The radiation patterns are slightly changed when the antenna is bent with higher radius, due to the deformity of the antenna structure. The suggested antenna achieved stable measured radiation performance, which is a good match

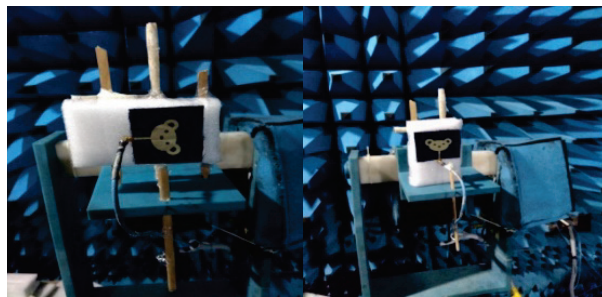


Fig. 7. Antenna measurement inside the chamber  $H$ -plane  $E$ -plane  $E$ -plane orientation (left)  $H$ -plane orientation (right).

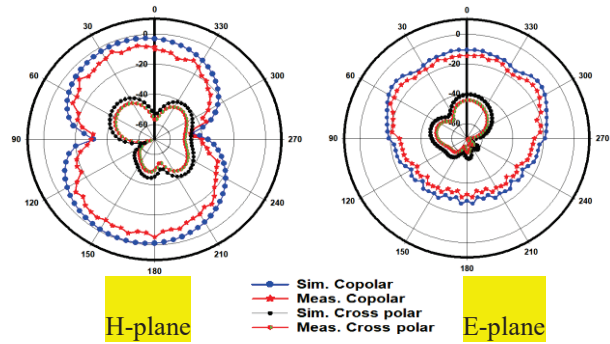


Fig. 8. Radiation pattern in on-body scenario.

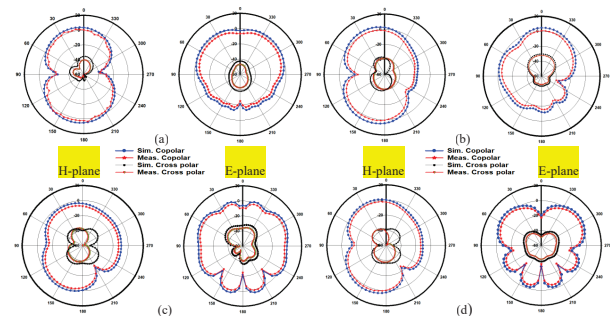


Fig. 9. Simulated and measured radiation pattern in free space. (a) Flat antenna. (b) Bending antenna at 80-mm radius. (c) Bending antenna at 60-mm radius. (d) Bending antenna at 40-mm radius.

with the simulation results in on-body, free space flat and bending antennas.

### C. Bending analysis

The bending analysis was performed to ascertain that the antenna is congruous and robust. The simulation and measurements for different radius curves are predicted in Figures 10 and 11. The bending is done with an 80-, 60-, and 40-mm radius in free space simulation and measurement. The result shows the resonance frequency is being shifted to the left side in the  $E$ -plane direction. Contrarily to this, the resonance frequency is shifted to the right side in the  $H$ -plane direction. But in both conditions, it nearly covers the required bandwidth. The simulated and measured values are almost the same except for the magnitude of  $S_{11}$ , as seen in the graph. It may be due to the antenna's deformity and losses in the fabricated antenna [28].

### D. Efficiency and gain response

The efficiency response and gain measurement are illustrated in Figure 12. In a free space environment, the designed antenna achieves a gain of 7.3 dBi in simulation and 5.3 dBi in measurement. The gain variation is due to the losses in the fabricated antenna.

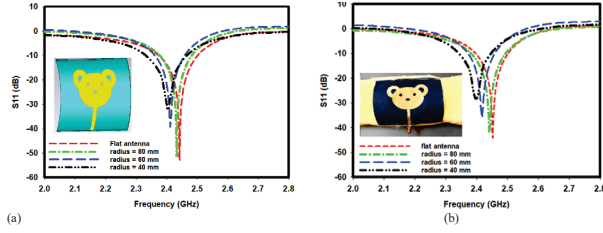


Fig. 10. Bending performance at *H*-plane orientation. (a) Simulated  $S_{11}$ . (b) Measured  $S_{11}$ .

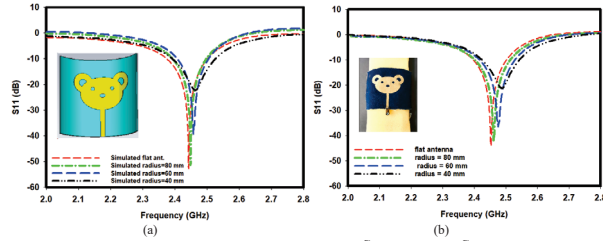


Fig. 11. Bending performance at *E*-plane orientation. (a) Simulated  $S_{11}$ . (b) Measured  $S_{11}$ .

There is a further reduction in gain up to 4.8 dBi due to the losses present in the human body. The graph shows that radiation efficiencies in free space are 86% and 82% on a phantom model at 2.4 GHz.

**E. SAR analysis**

SAR is the measure of energy the human body perceives when an antenna is placed on it. Theoretically, SAR can be analyzed through eqn (5), where  $E$  is the electric field intensity in V/m,  $\sigma$  is the conductivity in S/m, and  $\rho$  is the mass density in Kg/m<sup>3</sup> [29].

$$SAR = \frac{\sigma |E|^2}{\rho} \tag{5}$$

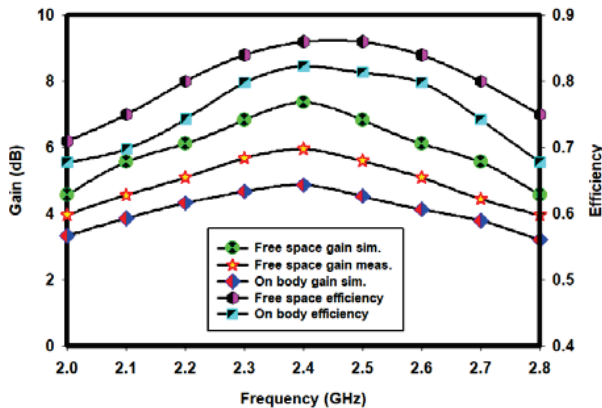


Fig. 12. Gain and efficiency response.

Table 3: Comparison of DGS antenna with plain ground antenna

Parameters	Antenna without DGS	Antenna with DGS
Resonance freq. at	2.8 GHz	2.44 GHz
Bandwidth	40 MHz	130 MHz
Gain	3.8 dB	7.3 dB
Efficiency	73%	86%

In practical scenario, SAR is calculated by taking an average volume of 1 and 10 g tissue. For 1-g average tissue, the permissible SAR value is < 1.6 W/kg as per Federal Communication Commission (FCC) standard. For 10 g tissue, the allowable SAR value is < 2 W/kg as per European Standard of the International Electro-Technical Commission (IEC) [30]. The simulated SAR Distribution at frequency 2.4 GHz is shown in Figure 13. Prolonged exposure will result in a high SAR value, which is hazardous to the human body, while the lower value of SAR is desirable as it enhances efficiency. This antenna exhibits a minimum of SAR 0.233 and 1.02 W/Kg for 1 and 10 g tissue, respectively. The value of SAR falls below the standard limits in both cases, making the antenna suitable for wearable applications.

**F. Overall comparison in the presence and absence of DGS**

Finally, the impact of DGS has been compared with many antenna parameters in the presence and absence of DGS. Table 3 indicates that the antenna with DGS structure has exactly resonated at 2.44 GHz with broader bandwidth and higher gain. It also fulfilled the SAR safety limit with better efficiency. This proves that the presence of DGS is required to achieve the optimal result.

The proposed work has been compared with the results from various literatures in Table 4. The originality of this work is the elegant shape with extreme flexibility in terms of both conductive and substrate materials. The suggested antenna exhibited higher gain (7.3 dBi) in the smaller dimensions structure within SAR safety limits.

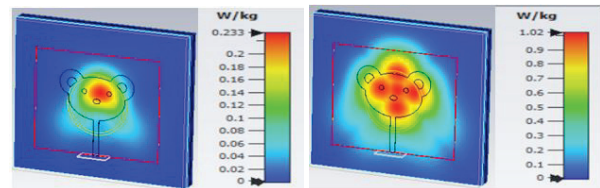


Fig. 13. Simulated SAR at 1 g tissue (left-side) and 10 g tissue (right-side).

Table 4: Comparison of proposed antenna with existing antenna

References	Size (mm <sup>2</sup> )	Substrate material	Patch material	Operating frequency (GHz)	Gain (dBi)	SAR (W/Kg)
Ref. [4]	100 × 100	Felt	Nickel–copper–polyester tape	4.55–13	6	10 g: 0.107
Ref. [10]	39 × 39	Roger RT/duroid 5880	Copper cladding	2.4	2.06	1 g: 0.34 10 g: 0.26
Ref. [24]	115 × 123	Cotton	Zari–silver metallic yarn	2.4	7.11	1 g: 0.032 10 g: 0.0115
Ref. [30]	40 × 30	FR-4	Copper etching	2.4/5.8	5.08	1 g: 0.19 10 g: 1.18
Ref. [31]	81 × 81	Felt	Nora-Dell-CR fabric	2.4	7.3	1 g: 0.554 10 g: 0.23
Ref. [32]	50 × 16	Jean	Copper tape	2.4	1.98	1 g: 0.52 10 g: 0.27
Proposed work	50 × 40	Jean	Copper fabric	2.4	7.3	1 g: 0.233 10 g: 1.02

#### IV. CONCLUSION

This research paper proposed a panda-shaped flexible textile antenna that can operate in 2.4 GHz and support WBAN applications. This antenna covers the entire ISM band (2.40–2.4835 GHz). The annular ring DGS was developed to boost antenna bandwidth, gain, and efficiency. In the free space scenario, 7.3 dBi gain is observed at 86% efficiency. On-body condition exhibits 4.8 dBi gain at 82% efficiency. The antenna had good radiation properties with minimal cross-polarization in simulations and measurements. The bending analysis proves that the antenna performs well in *E*- and *H*-plane orientations. The value of SAR stays within permissible limits in both 1 and 10 g average tissue. Because of its flexibility and attractive shape, this delightful panda-shaped antenna will blend well with the design of garments. The exhibited features of the proposed antenna make it most appropriate for use in WBAN applications.

#### ACKNOWLEDGMENT

The authors wish to acknowledge DST-FIST supporting facilities in the Electronics and Communication Engineering Department, SRM Valliammai Engineering College, Chennai, Tamil Nadu, India.

#### REFERENCES

- [1] A. G. Al-Sehemi, A. A. Al-Ghamdi, N. T. Dishovsky, N. T. Atanasov, and G. L. Atanasova, "Flexible and small wearable antenna for wireless body area network applications," *Journal of Electromagnetic Waves and Applications*, vol. 31, no. 11-12, pp. 1063-1082, 2017.
- [2] A. Kashkool, S. Yahya, H. Al-Rizzo, A. Al-Wahhamy, and A. A. Issac, "On the design and simulation of antennas on ultra-thin flexible substrates," *Applied Computational Electromagnetics Society (ACES) Journal*, vol. 33, no. 7, Jul. 2018.
- [3] A. Gupta and V. Kumar, "DGS-based wide-band MIMO antenna for on-off-body communication with port isolation enhancement operating at 2.45GHz industrial scientific and medical band," *Journal of Electromagnetic Waves and Applications*, vol. 35, no. 7, pp. 888-901, 2020.
- [4] H. Yalduz, T. E. Tabaru, V. T. Kilic, and M. Turkmen, "Design and analysis of low profile and low SAR full-textile UWB wearable antenna with metamaterial for WBAN applications," *AEÜ International Journal of Electronics and Communications*, vol. 126, pp. 1-12, Sep. 2020.
- [5] A. Y. I. Ashyap, S. H. Bin Dahlan, Z. Z. Abidin, and M. H. Dahri, "Robust and efficient integrated antenna with EBG-DGS enabled wide bandwidth for wearable medical device applications," *IEEE Access*, vol. 8, pp. 56346-56358, 2020.
- [6] H. F. Abutarboush, W. Li, and A. Shamim, "Flexible-screen-printed antenna with enhanced bandwidth by employing defected ground structure," *IEEE Antennas and Wireless Propagation Letters*, vol. 19, no. 10, pp. 1803-1807, Oct. 2020.
- [7] C. Kumar and D. Guha, "Asymmetric and compact DGS configuration for circular patch with improved radiations," *IEEE Antennas and Wireless Propagation Letters*, vol. 19, no. 2, pp. 355-357, Feb. 2020.

- [8] S. Bhattacharjee, S. Maity, S. R. B. Chaudhuri, and M. Mitra, "A compact dual-band dual-polarized omnidirectional antenna for on-body applications," *IEEE Transactions on Antennas and Propagation*, vol. 67, no. 8, pp. 5044-5053, Aug. 2019.
- [9] C. Wang, L. Zhang, and X. Wu, "A wearable flexible microstrip antenna based on the floating-ground backplane," *International Journal of RF and Microwave Computer-Aided Engineering*, vol. 31, no. 1, pp. 1-15, Nov. 2020.
- [10] A. Arif, M. Zubair, M. Ali, M. U. Khan, and M. Q. Mehmood, "A compact, low-profile fractal antenna for wearable on-body WBAN applications," *IEEE Antennas and Wireless Propagation Letters*, vol. 18, no. 5, pp. 981-985, May 2019.
- [11] H. Zu, B. Wu, P. Yang, W. Li, and J. Liu, "Wide-band and high-gain wearable antenna array with specific absorption rate suppression," *Electronics*, vol. 10, no. 17, pp. 2056, Aug. 2021.
- [12] M. Boyuan, J. Pan, E. Wang, and D. Yang, "Wristwatch-style wearable dielectric resonator antennas for applications on limbs," *IEEE Access*, vol. 8, pp. 59837-59844, 2020.
- [13] P. Mythili and A. Das, "Simple approach to determine resonant frequencies of microstrip antennas," *Antennas Propag. IEE Proc. -Microw.* vol. 145, no. 2, pp. 159-162, Apr. 1998.
- [14] J. V. Jose, A. S. Rekh, and M. J. Jose, "Design techniques for elliptical micro-strip patch antenna and their effects on antenna performance," *International Journal of Innovative Technology and Exploring Engineering*, vol. 8, no. 12, pp. 2317-2326, Oct. 2019.
- [15] S. Murugan, B. Rohini, P. Muthumari, and M. Padma Priya, "Multi-frequency T-slot loaded elliptical patch antenna for wireless applications," *Applied Computational Electromagnetics Society (ACES) Journal*, vol. 1, no. 7, pp. 212-215, Jul. 2016.
- [16] A. Agrawal, D. Vakula, and N. V. S. N. Sarma, "Design of elliptical microstrip patch antenna using ANN," *PIERS Proceedings, Suzhou, China*, pp. 264-268, 2011.
- [17] S. R. Patre and P. Surya Singh, "CPW-fed flower-shaped patch antenna for broadband applications," *Microwave and Optical Technology Letters*, vol. 57, no. 12, pp. 2908-2913, 2015.
- [18] P. Seyed, "Bandwidth enhancement techniques," *Trends in Research on Microstrip Antennas*, edited by Sudipta Chattopadhyay. London: IntechOpen, 2017. DOI: 10.5772/intechopen.70173.
- [19] A. Yadav, V. K. Singh, and H. Mohan, "Design of a U-shaped circularly polarized wearable antenna with DGS on a fabric substrate for WLAN and C-band applications," *Journal of Computational Electronics*, vol. 18, pp. 1103-1109, May 2019.
- [20] M. Haran, G. Dilip Kumar, A. Ferris Garvin, and S. Ramesh, "Hexagonal microstrip patch antenna for early stage skin cancer identification," *International Journal of Telecommunications and Radio Engineering*, vol. 79, no. 7, pp. 555-566, Jun. 2020.
- [21] B. B. Q. Elias, P. J. Soh, A. A. Al-Hadi, P. Akkaraekthalin, and G. A. E. Vandenbosch, "Bandwidth optimization of a textile PIFA with DGS using characteristic mode analysis," *Sensors*, vol. 21, no. 7, pp. 2516, Apr. 2021.
- [22] T. Annalakshmi and S. Ramesh, "Performance and analysis of UWB aesthetic pattern textile antenna for WBAN applications," *Applied Computational Electromagnetics Society (ACES) Journal*, vol. 35, no. 12, pp. 1525-1531, Dec. 2020.
- [23] D. Ram Sandeep, N. Prabakaran, T. P. Madhav Boddapati, and K. L. Narayana, "Circularly polarized jute textile antenna for Wi-MAX, WLAN and ISM band sensing applications," *Applied Computational Electromagnetics Society (ACES) Journal*, vol. 35, no. 12, pp. 1493-1499, Dec. 2020.
- [24] A. Anbalagan, E. F. Sundarsingh, and V. S. Ramalingam, "Design and experimental evaluation of a novel on-body textile antenna for unicast applications," *Microwave and Optical Technology Letters*, vol. 62, pp. 789-799, 2020.
- [25] F. S. Esther, M. Kanagasabai, and G. N. M. Alsath, "An investigation of a wearable antenna using human body modeling," *Applied Computational Electromagnetics Society (ACES) Journal*, vol. 29, no. 10, pp. 777-783, 2014.
- [26] V. Karthik and T. R. Rao, "Performance investigations of a quad-band microstrip antenna for body wearable wireless devices," *Applied Computational Electromagnetics Society (ACES) Journal*, vol. 36, no. 08, pp. 980-988, Oct. 2021.
- [27] N. RajeshKumar, P. D. Sathya, S. K. A. Rahim, and A. A. Eteng, "Reduced cross-polarization patch antenna with optimized impedance matching using a complimentary split ring resonator and slots as defected ground structure," *Applied Computational Electromagnetics Society (ACES) Journal*, vol. 36, no. 6, pp. 718-725, Nov. 2021.
- [28] S. Varma, S. Sharma, M. John, R. Bharadwaj, A. Dhawan, and S. K. Koul, "Design and performance analysis of compact wearable textile antennas for IoT and body-centric communication applications," *International Journal of Antennas and Propagation*, vol. 2021, Article ID 7698765, p. 12, 2021.
- [29] S. Singh and S. Verma, "SAR reduction and gain

enhancement of compact wideband stub loaded monopole antenna backed with electromagnetic band gap array,” *International Journal of RF and Microwave Computer-Aided Engineering*, vol. 31, no. 10, pp. 1-11, Jul. 2021.

- [30] S. Ahmad, A. Ghaffar, N. Hussain, and N. Kim, “Compact dual-band antenna with paired L-shape slots for on- and off-body wireless communication,” *Sensors*, vol. 21, no. 23, pp. 7953, Nov. 2021.
- [31] G. Gao, B. Hu, S. Wang, and C. Yang, “Wearable circular ring slot antenna with EBG structure for wireless body area network,” *IEEE Antennas and Wireless Propagation Letters*, vol. 17, no. 3, pp. 434-437, Mar. 2018.
- [32] I. Gil and R. Fernandez Garcia, “Wearable PIFA antenna implemented on jean substrate for wireless body area network,” *Journal of Electromagnetic Waves and Applications*, vol. 31, no. 11-12, pp. 1194-1204, Jul. 2017.



**T. Annalakshmi** received the B.Tech. degree in electronics and communication engineering from Pondicherry University in 2002 and the M.E. degree in communication systems from Anna University in 2011, and is currently working toward the Ph.D. degree with the

Department of Electronics and Communication Engineering, SRM Valliammai Engineering College, Chennai, India.

Her research interest includes antennas and propagation and wireless communications. She is currently working as an Associate Professor with the Department of Electronics and Communication Engineering, New Prince Shri Bhavani College of Engineering and Technology, Chennai, India, with 15 years of experience. She is a lifetime member of ISTE and ISRD.



**S. Ramesh** received the B.E. degree in electronics and communication engineering from the University of Madras, Chennai, India, the M.Tech. degree in communication engineering from VIT University, Vellore, India, and the Ph.D. degree from SRM University, Chennai, India, in

2001, 2004, and 2015, respectively. He is currently working as an Associate Professor with the Department of Electronics and Communication Engineering, SRM Valliammai Engineering College, Chennai, India, with experience of 19.3 years. He is a senior member (S'10-M'17-SM'18) of IEEE Antennas & Propagation Society and Life member in IETE, ISTE, SEMCE, and BES. He authored papers in reputed journals and international/national conferences. His area of research interest includes antennas & propagation and wireless communications. He is guiding research scholars in the field of antennas and RF filter under Anna University, Chennai, India. He is associated with IEEE AP-S Madras chapter as a member in executive committee during 2018–2019 and IEEE MTT-S Madras Chapter for the year 2017.

# An Empirical Loss Model for an Additively Manufactured Luneburg Lens Antenna

Brian F. LaRocca<sup>1</sup> and Mark S. Mirotznik<sup>2</sup>

<sup>1</sup>Department of the Army  
Aberdeen Proving Ground, Aberdeen, MD 21005, USA  
brian.f.larocca.civ@army.mil

<sup>2</sup>Electrical Engineering Department  
University of Delaware, Newark, DE 19716, USA  
mirotzni@udel.edu

**Abstract** – This research applies Effective Medium Theory and 3D Finite Element Analysis to model the transmissive loss through a waveguide fed additively manufactured Luneburg lens. New results are presented that provide rational function approximations for accurately modeling the aperture, beam, and radiation loss factors of the antenna. It introduces a normalized loss tangent and shows that the loss factors are dependent on the product of this parameter and the lens radius. Applying the constraint that the main beam of the radiation pattern contains 50% of accepted power, a maximum useful radius is tabulated for common polymers used in additive manufacturing.

**Index Terms** – Additive manufacturing, dielectric loss, effective medium theory, lens antenna, luneburg lens.

## I. INTRODUCTION

While spatially graded dielectrics, also known as graded-index (GRIN) structures, are popular devices in optics and photonics they have historically been used less frequently at radio frequencies (RF). However, there has been a surge of interest in using RF GRIN antennas as low-cost passive beam-formers. One of the most popular RF GRIN structures is the well-known Luneburg lens (LL) [1-6]. The LL is a spherical device in which every point on the surface is the focal point of a plane wave incident from the opposing surface. This unique property can be leveraged to realize passive beam steering antennas capable of directing a single or multiple beams over wide scan angles.

While the LL concept has been known for nearly 80 years [1], our ability to reliably manufacture them has been aided by recent advancements in additive manufacturing (AM) technologies and materials. Prior to AM,

fabricating a structure with spatially graded dielectric properties was an expensive and challenging manufacturing problem.

Over the last eight years, a host of papers have been published on the use of AM to fabricate the LL and other GRIN devices [7-14]. While these previous studies have demonstrated AM's ability to fabricate functional RF GRIN lenses, what has not been well characterized is how the choice of AM material and unit cell architecture influences performance in terms of aperture, beam, and radiation efficiency. All which factor into the maximum useful gain that can be achieved for a particular design.

In this paper, a full wave computational study is presented that quantifies the effect of material choice and unit cell architecture on the performance of AM fabricated LL antennas. Specifically, the aperture, beam and radiation loss factors are evaluated as a function of the LL's material properties, unit cell geometry and overall electrical size. An empirical model is provided that accurately describes these relationships. This model is then used to predict the maximum useful gain of an antenna for a given material and unit cell structure. These results will serve as a useful guide for antenna design engineers when determining the specific AM fabrication materials and approach best suited for their application.

The product of lens radius in terms of free space wavelengths and the normalized loss tangent is introduced as being a key metric in characterizing the radiation pattern of a LL with loss. Although somewhat dependent upon the unit cell geometry, this product identifies three important thresholds. Listed in order of increasing severity they are as follows: (a) at a value of  $\approx 0.06$ , the main lobe contains only 50% of the accepted power; (b) at a value of  $\approx 0.3$ , the gain has reached the peak value that is possible for the given material and unit cell geometry. Increasing the lens size further results in a decrease in antenna gain; (c) at a value of  $\approx 0.8$ , radiated

power is reduced to  $\approx 13\%$  of the accepted power, and the main beam is nearly extinguished containing only  $\approx 3\%$  of the radiated power.

The outline for the subsequent portion of the paper is as follows. Following an introduction to the computer model and workflow, Section II-A presents the effective medium models that represent unit cell structures. Section II-B provides the range of model parameters simulated. Section II-C defines the far-field loss factors for which rational functional approximations are given in Section II-D. The accuracy of these approximations is shown in Section III-A. The normalized loss tangent is introduced in Section III-B and applied to tabulate the maximum useful radius of common polymers used in the manufacture of GRIN components. Section III-C tabulates thresholds of performance in terms of the lens radius and normalized loss tangent product. Section IV further discusses the primary results and suggests future research.

## II. MODELING AND ANALYSIS

The data for this research is derived using a computer model comprised of a spherical LL, an open-ended cylindrical waveguide, and a spherical Perfectly Matched Layer (PML). The lens model is inhomogeneous, continuous, and isotropic. Material loss is accounted for by incorporating Effective Medium Theory (EMT) to predict an effective loss tangent for the inhomogeneous air/material mixture that makes up the lens. The open-ended waveguide serves as the antenna feed, which supplies monochromatic and fundamental mode excitation. The PML allows for efficient simulation by providing a high-performance absorbing boundary that fully encloses the lens and waveguide. It effectively truncates the computational domain, such that the near field only be computed out to a short distance beyond the lens and waveguide.

Finite Element Analysis (FEA) of the above-described model is carried out using COMSOL Multiphysics software equipped with the RF Module [23]. Due to the complete symmetry of the model about the  $z$  axis, an otherwise 3D simulation is reduced to a 2D axisymmetric simulation. This results in enormous savings in computer resources, allowing for simulations that would not otherwise be possible on less than exotic computing platforms. A sketch of the axisymmetric model is provided in Fig. 1. The half-plane model is rotated  $360^\circ$  around the  $z$  axis to create a 3D model including a spherical lens, a cylindrical open ended waveguide port, and the spherical PML shell.

Upon completion of FEA for each parameter combination modeled, the COMSOL RF Module is used to convert the resulting electromagnetic field along the inner surface of the PML shell to the far-field gain. A

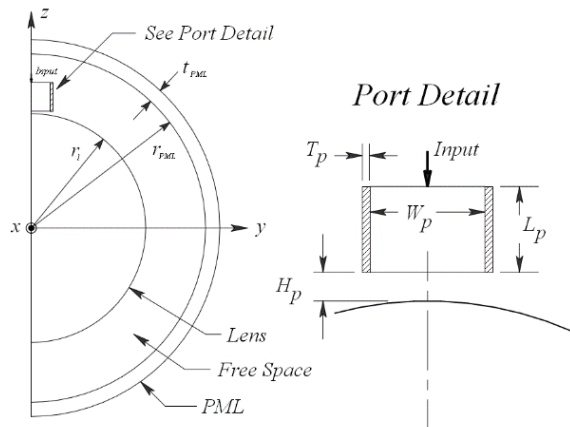


Fig. 1. 2D sketch of axisymmetric model used in the simulation.

2D cut of the gain is saved to a text file with a unique name that identifies the parameter combination. Post-processing and visualization are carried out in MATLAB. Beyond extraction of boresight gain, this stage includes calculation of aperture efficiency  $\eta_a$ , radiation efficiency  $\eta_r$ , and beam efficiency  $\eta_b$ . The loss factor for each efficiency is computed, being a positive number defined in decibels as:

$$L_x = -10 \cdot \log_{10}(\eta_x). \quad (1)$$

Finally, the MATLAB Global Optimization Toolbox [24] is then used to provide a rational function approximation for each of the three loss factors, including a fourth, being  $L_b + L_r$ .

### A. Effective medium modeling

EMT provides a quantitative means to describe the properties of a composite material, knowing the ratio and properties of its individual constituents. In the case of an additively manufactured component such as the LL, the constituents are air and the printed material. Moreover, we are only interested in the effective permittivity of the resulting composite. Throughout the following, all permittivities are relative, and caret accents are used to denote a complex quantity.

The point of view adapted here is that the lens is a composite formed from a spherical host volume of free space, into which precise amounts of printed material are deposited. The material deposited thus forms discrete solid inclusions, having a natural complex relative permittivity  $\hat{\epsilon}$ . In any region of the sphere, the effective permittivity of the composite in that region depends on the volumetric ratio of printed material to free space. This ratio is referred to as the volume fraction  $f$  and varies throughout the lens. Furthermore, it is necessary that the dimension of the largest inclusion be much smaller than the shortest operational wavelength required.

Starting with the definition for  $\hat{\epsilon}$ :

$$\begin{aligned}\hat{\epsilon} &= \epsilon' - j \cdot \epsilon'', \\ &= \epsilon' \cdot \left(1 - j \cdot \frac{\epsilon''}{\epsilon'}\right), \\ &= \epsilon' \cdot (1 - j \cdot \tan(\delta)).\end{aligned}\quad (2)$$

In (2),  $\epsilon'$ ,  $\epsilon''$  and  $\tan(\delta)$  represent the dielectric constant, the imaginary component of  $\hat{\epsilon}$ , and the loss tangent respectively of the printed material at the operational frequency.

EMT provides several quantitative relationships relating  $f$ ,  $\hat{\epsilon}$  and the effective permittivity of the composite. These are termed mixing formulas, and this work employs the Maxwell Garnett (MG) and the Linear mixing formulas. It is shown below that the Linear mixing rule predicts a higher loss tangent for the composite than does the MG mixing rule. By providing results for both mixing rules, the intent is to provide a realistic range of values that may occur.

Allowing  $\hat{\epsilon}_{MG}$  to represent the MG prediction for the effective permittivity of the composite, and  $f_{MG}$  the respective volume fraction, we have [21]:

$$\begin{aligned}\hat{\epsilon}_{MG} &= 1 + \frac{3f_{MG} \cdot (\hat{\epsilon} - 1)}{\hat{\epsilon} + 2 - f_{MG} \cdot (\hat{\epsilon} - 1)}, \\ &= \epsilon'_{MG} \cdot (1 - j \cdot \tan(\delta_{MG})).\end{aligned}\quad (3)$$

For materials where  $\epsilon'' \ll \epsilon'$ , the following observation is useful [21]:

$$\epsilon'_{MG} \approx 1 + \frac{3f_{MG} \cdot (\epsilon' - 1)}{\epsilon' + 2 - f_{MG} \cdot (\epsilon' - 1)}.\quad (4)$$

Now, in terms of the cylindrical coordinate system  $(r_c, z, \phi)$  used for the 2D axisymmetric model [23], the Luneburg permittivity distribution  $\epsilon_{LB}$  is given by:

$$\epsilon_{LB} = 2 - \left(\frac{r_c^2 + z^2}{r_l^2}\right),\quad (5)$$

where  $r_l$  denotes the radius of the LL measured in free-space wavelengths  $\lambda$ . This is a real quantity, and it is necessary that the volume fraction throughout the lens, be set such that the real component of the effective permittivity results in  $\epsilon_{LB}$ . Thus, setting  $\epsilon'_{MG} = \epsilon_{LB}$ , and solving for  $f_{MG}$  in (4), we have:

$$f_{MG} \approx \frac{2\epsilon_{LB} - \epsilon' + \epsilon' \epsilon_{LB} - 2}{2\epsilon' - \epsilon_{LB} + \epsilon' \epsilon_{LB} - 2}.\quad (6)$$

A similar procedure is carried out in determining the volume fraction for modeling Linear mixing; however, the relationship is now exact. Allowing  $\hat{\epsilon}_{Lin}$  to represent the Linear mixture prediction for the effective permittivity of the composite, and  $f_{Lin}$  the respective volume fraction, we have [21]:

$$\begin{aligned}\hat{\epsilon}_{Lin} &= (1 - f_{Lin}) + f_{Lin} \cdot \hat{\epsilon}, \\ &= \epsilon'_{Lin} \cdot (1 - j \cdot \tan(\delta_{Lin})).\end{aligned}\quad (7)$$

The real component of (7) is:

$$\epsilon'_{Lin} = 1 + f_{Lin} \cdot (\epsilon' - 1),\quad (8)$$

and, upon setting  $\epsilon'_{Lin} = \epsilon_{LB}$ , and solving for  $f_{Lin}$  in (8), we have:

$$f_{Lin} = \frac{\epsilon_{LB} - 1}{\epsilon' - 1}.\quad (9)$$

As an illustrative example,  $\epsilon'_{Lin}$  and  $\tan(\delta_{Lin})$  are shown in Fig. 2 across a planar slice through the center of a LL. The material used has a dielectric constant of 4.0 and a loss tangent of 0.1, i.e.,  $\hat{\epsilon} = 4 \cdot (1 - j \cdot 0.1)$ .

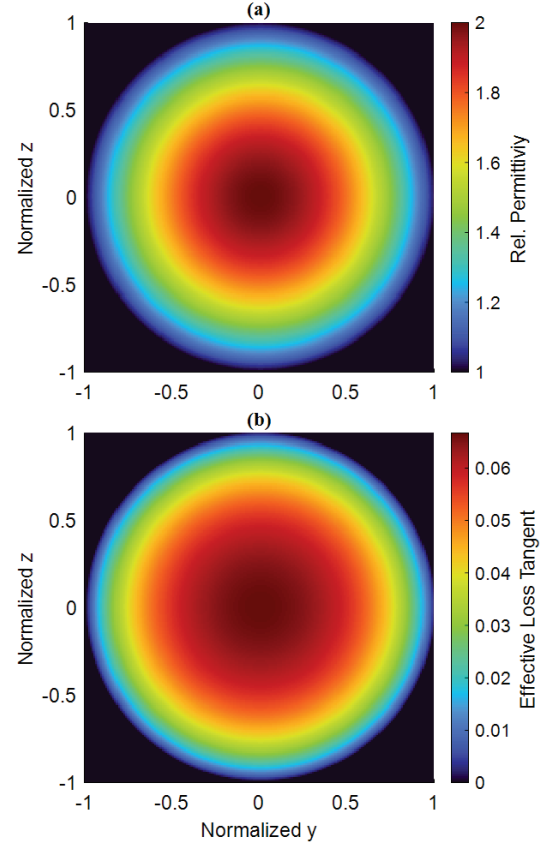


Fig. 2. Relative permittivity in (a) and effective loss tangent in (b) of a LL using Linear mixing rule.

Due to the spherical symmetry of the LL, the choice of the cut plane used in Fig. 2 is arbitrary, and the  $y$ - $z$  plane is chosen. Therefore, (5) may be rewritten as:

$$\begin{aligned}\epsilon_{LB} &= 2 - \left(\frac{y^2 + z^2}{r_l^2}\right), \\ &= 2 - \left(\left(\frac{y}{r_l}\right)^2 + \left(\frac{z}{r_l}\right)^2\right), \\ &= 2 - \left(\bar{y}^2 + \bar{z}^2\right).\end{aligned}\quad (10)$$

For generality, in (10) we have defined the normalized coordinates  $\bar{y} = y/r_l$  and  $\bar{z} = z/r_l$ . By doing so, all points within the lens satisfy  $(\bar{y})^2 + (\bar{z})^2 \leq 1$ .

Knowing that  $\epsilon'_{Lin} = \epsilon_{LB}$ , (10) is used directly to create Fig. 2 (a). For Fig. 2 (b), the necessary volume

fraction for the lens is computed using (9), then the lens complex effective permittivity  $\hat{\epsilon}_{Lin}$  is computed using (7). Since:

$$\hat{\epsilon}_{Lin} = \epsilon'_{Lin} - j \cdot \epsilon''_{Lin}, \quad (11)$$

then by definition, the effective loss tangent is given by:

$$\tan(\delta_{Lin}) = \frac{\epsilon''_{Lin}}{\epsilon'_{Lin}}. \quad (12)$$

The Linear rule predicts a greater effective loss tangent for the lens than does the MG rule. This is demonstrated in Fig. 3 for a material with a dielectric constant of 4.0 and a loss tangent of 0.1. For generality, results are plotted with respect to the normalized radius  $\bar{r}$ , defined as:

$$\bar{r} = \frac{\sqrt{r_c^2 + z^2}}{r_l}. \quad (13)$$

Substitution of  $(\bar{r})^2$  into (5) yields:

$$\epsilon_{LB} = 2 - (\bar{r})^2, \quad (14)$$

noting that for all points within the lens,  $0 \leq \bar{r} \leq 1$ . Now, since the real part of effective permittivity is required to equal  $\epsilon_{LB}$ , then the difference between the two rules must reside in the imaginary component. To show this, the MG prediction is computed by first determining the required

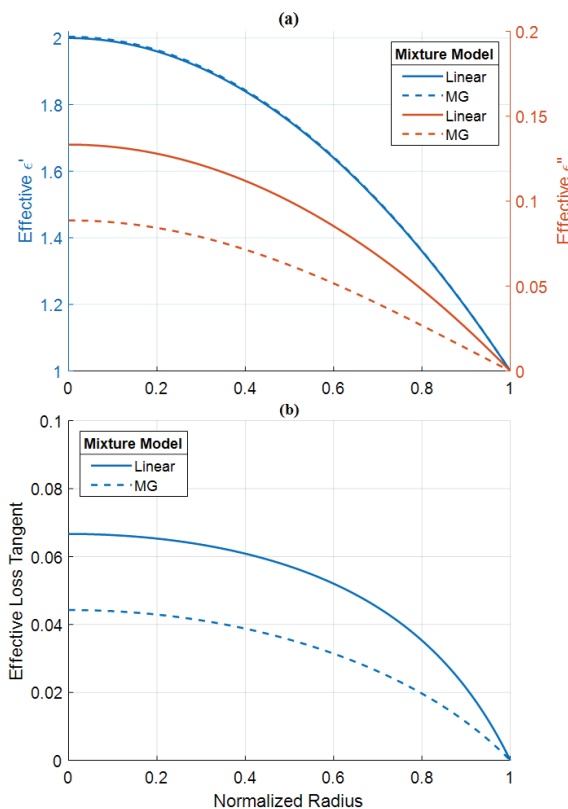


Fig. 3. Comparison of mixture models. In (a), effective  $\epsilon'$  and  $\epsilon''$  versus normalized radius. In (b), the effective loss tangent versus normalized radius.

volume fraction using (6), and then (3) is applied to compute  $\hat{\epsilon}_{MG}$ . The Linear prediction is computed by using (9) to obtain  $f_{Lin}$  and then using (7) to compute  $\hat{\epsilon}_{Lin}$ . As seen in Fig. 3 (a),  $\epsilon''_{MG} \leq \epsilon''_{Lin}$ , thus  $\tan(\delta_{MG}) \leq \tan(\delta_{Lin})$ , which is observed in Fig. 3 (b). The disparity widens for materials with larger dielectric constants.

## B. Parameter combinations modeled

The AM of a LL requires the use of materials having a dielectric constant of 2 or more. In the simulations conducted for this research, the dielectric constant of the material used to print the lens, takes on one of nine values:

$$\epsilon' = [2.3, 2.5, 2.8, 3.5, 4, 5, 6, 8, 10]. \quad (15)$$

The non-uniform distribution in (15) has been found necessary to adequately track the gradient of loss for low values of  $\epsilon'$ . Figure 4 demonstrates why this is necessary for the specific case of the beam loss factor. The magnitude of the gradient changes quickly for low values of  $\epsilon'$ . Therefore, developing an accurate empirical model necessitates denser sampling of  $\epsilon'$  in this region. The effect is similar for all loss factors studied in this research. The LL model used to create this figure has a radius of  $40\lambda$  and a material loss tangent of 0.1.

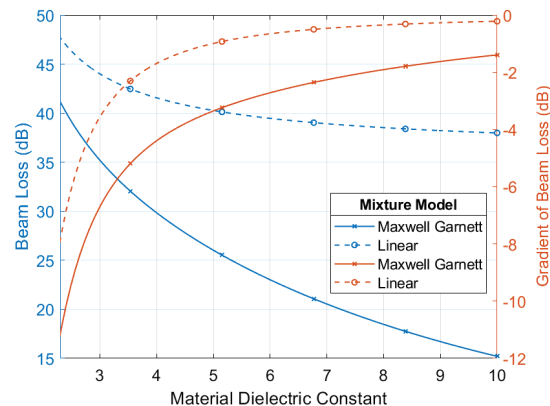


Fig. 4. Maximum beam loss factor and gradient versus material dielectric constant  $\epsilon'$ .

For each dielectric constant in (15), a  $20 \times 20$  semi-uniform grid is used to sweep over material loss tangent and lens radius. Thus, loss tangent is swept from 0 to 0.01 in 0.001 increments, and from 0.01 to 0.1 in 0.01 increments. Lens radius is swept from 2 to 40 wavelengths  $\lambda$ , in  $2\lambda$  increments. A depiction of the sample grid is shown in Fig. 5, using a material with a dielectric constant of 4.0 and MG mixing. Each sample point is the result of a distinct 3D FEA simulation. Moreover, a total of 3,600 FEA simulations are conducted for each of the two mixture models studied. Loss tangents greater than 0.1 are considered too high for practical LL based applications and are therefore not investigated.

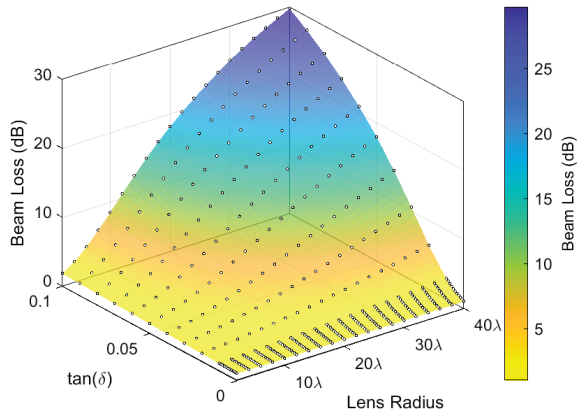


Fig. 5. Sample grid overlaid on surface plot of Beam Loss.

**C. Far field loss factors**

In this section we describe the specific far field loss factors that are used to quantify and compare antenna performance.

With reference to the spherical coordinate system depicted in Fig. 6, the total radiated power by the antenna, in Watts, is given by [22]:

$$P_r = \frac{P_0}{4\pi} \int_{\phi=0}^{2\pi} \int_{\theta=0}^{\pi} g(\theta, \phi) \sin(\theta) d\theta d\phi, \quad (16)$$

where  $g(\theta, \phi)$  represents the far-field gain and  $P_0$  is the power accepted by the antenna, again in Watts. However, due to the complete symmetry of the model about the  $z$  axis, the gain is independent of  $\phi$ . This is observed in Fig. 7 (a), in which  $10 \cdot \log_{10}(g(\theta, \phi))$  is shown for a LL of radius  $2\lambda$ . Thus, no loss of information occurs

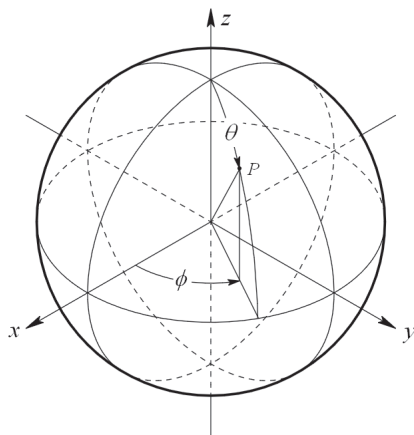


Fig. 6. Spherical coordinate system used to define far-field values, such as antenna gain  $g(\theta, \phi)$ . The lens is centered at the origin.

representing the gain as  $g(\theta)$ . Therefore, (16) reduces to:

$$P_r = \frac{P_0}{2} \int_{\theta=0}^{\pi} g(\theta) \sin(\theta) d\theta. \quad (17)$$

We continue by defining  $P_b$  as the radiated power contained only in the main beam of the radiation pattern. Defined in Watts, this is given by:

$$\begin{aligned} P_b &= \frac{P_0}{4\pi} \int_{\phi=0}^{2\pi} \int_{\theta=\theta_{FN}}^{\pi} g(\theta, \phi) \sin(\theta) d\theta d\phi, \quad (18) \\ &= \frac{P_0}{2} \int_{\theta=\theta_{FN}}^{\pi} g(\theta) \sin(\theta) d\theta. \end{aligned}$$

In the above definition,  $\theta_{FN}$  is the zenith angle corresponding to the first null in the radiation pattern relative to boresight. Upon inspection of the pattern shown in Fig. 7 (b), it is seen that for this example,  $\theta_{FN} = 161^\circ \approx 0.894\pi$  radian.

Trapezoidal integration is substituted for the continuous integrals defined in (17) and (18). By estimating  $\theta_{FN}$  before hand, the angular spacing between pattern samples  $\Delta\theta$ , is set to ensure accuracy using the numerical

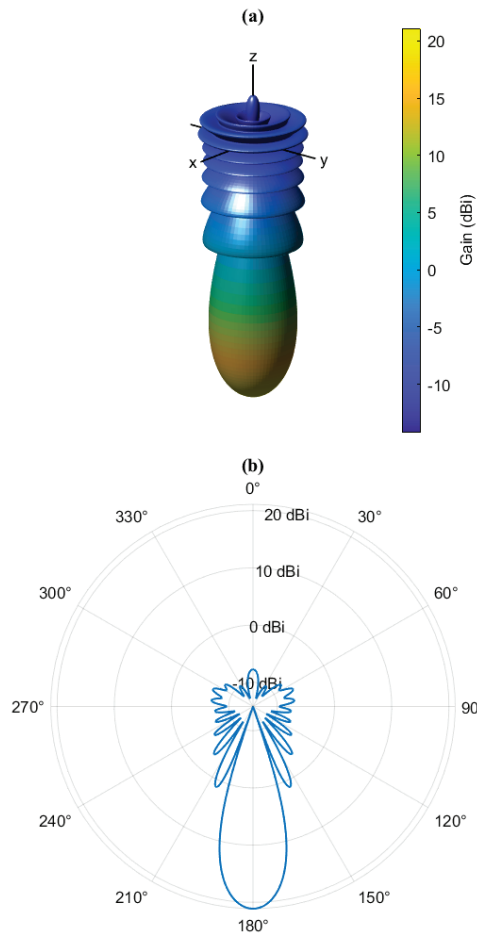


Fig. 7. Example far-field gain pattern. In (a), the full 3D pattern. In (b) a representative 2D cut.

surrogate. After experimentation, a sufficient resolution for this purpose is  $\Delta\theta \leq \frac{\theta_{FN}}{20}$ . Accurate prediction of  $\theta_{FN}$  is accomplished using the equation for an ideal Luneburg lens fed by a cosine point source [26]:

$$g_{LB}(\theta) = 4\pi^2 r_l^2 \left[ \frac{2 J_1(2\pi r_l \sin(\theta))}{2\pi r_l \sin(\theta)} \right]^2, \quad (19)$$

where  $J_1(\cdot)$  represents the Bessel function of the first kind of order one, and  $r_l$  is the lens radius measured in free-space wavelengths  $\lambda$ . Upon application of numerical peak detection on the reciprocal of (19), it is found that to a high degree of accuracy:

$$2 \cdot \theta_{FN} = \frac{70.08^\circ}{r_l}. \quad (20)$$

Now, upon solving for  $\Delta\theta$  yields:

$$\begin{aligned} \Delta\theta &\leq \frac{70.08^\circ}{2 \times 20 \times r_l}, \\ &\leq \frac{1.75^\circ}{r_l}. \end{aligned} \quad (21)$$

The angle  $2 \cdot \theta_{FN}$  is referred to as the First Null Beam Width *FNBW* [27]:

$$FNBW = 2 \cdot \theta_{FN}. \quad (22)$$

In Fig. 8, a comparison is provided between the *FNBW* measured using  $g(\theta)$  obtained from FEA simulations and with  $\tan(\delta) = 0$ , to that predicted by (20). For  $r_l \geq 10\lambda$ , the two match within 0.7°. The minimum *FNBW* shown is 1.90°, occurring for a lens radius of  $40\lambda$ . Thus, for large lenses, the FEA matches closely with (20) derived for lens driven by cosine point source.

The radiation efficiency  $\eta_r$ , is defined as [27]:

$$\eta_r = \frac{P_r}{P_0}, \quad (23)$$

and the radiation loss factor is defined as:

$$L_r = -10 \cdot \log_{10}(\eta_r). \quad (24)$$

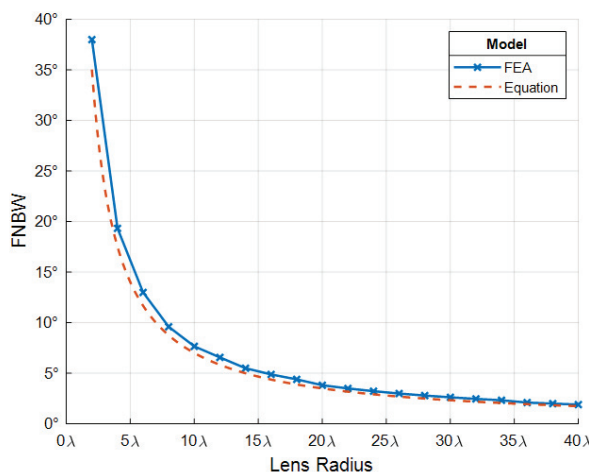


Fig. 8. First Null Beam Width versus lens radius.

The beam efficiency  $\eta_b$  and corresponding loss factor are defined as [27]:

$$\eta_b = \frac{P_b}{P_r}. \quad (25)$$

$$L_b = -10 \cdot \log_{10}(\eta_b). \quad (26)$$

Using (23) and (25), it is obvious that:

$$\frac{P_b}{P_0} = \eta_r \cdot \eta_b, \quad (27)$$

and therefore:

$$L_b + L_r = -10 \cdot \log_{10} \left( \frac{P_b}{P_0} \right). \quad (28)$$

It should be noted that the radiation efficiency only accounts for material losses generated within the LL while the beam efficiency describes the LL's ability to form a beam.

And finally, the aperture efficiency  $\eta_a$  and the corresponding loss factor are defined as [22]:

$$\begin{aligned} \eta_a &= \frac{g(\theta)_{max}}{4\pi^2 r_l^2}, \\ &= \frac{g(\pi)}{4\pi^2 r_l^2}. \end{aligned} \quad (29)$$

$$L_a = 10 \cdot \log_{10}(4\pi^2 r_l^2) - 10 \cdot \log_{10}(g(\pi)). \quad (30)$$

In the above,  $r_l$  is measured in free-space wavelengths  $\lambda$ . Given the orientation of the waveguide feed, maximum gain occurs at  $\theta = 180^\circ = \pi$  rad, which is aligned with the antenna boresight.

#### D. Curve fitting of loss factors

The loss factors defined in the previous section have an implicit dependence on the mixing rule, the printed material's dielectric constant  $\epsilon'$  and loss tangent  $\tan(\delta)$ , and the lens radius  $r_l$ . In this section, new results are presented that show for each loss factor  $L_x$ , and each mixing rule  $y$ , a rational function curve fit of an auxiliary variable  $u_y$ , provides an accurate and wide range empirical model. Thus:

$$L_x^y(\epsilon', \tan(\delta), r_l) \approx R_x^y(u_y), \quad (31)$$

for  $x \in \{a, b, r\}$  and  $y \in \{MG, Lin\}$ , and where:

$$u_y = \frac{r_l \cdot \tan(\delta)}{F_y(\epsilon')}. \quad (32)$$

$$R_x^y(u) = \frac{p_1 u^3 + p_2 u^2 + p_3 u + p_4}{u^2 + q_1 u + q_2}. \quad (33)$$

$$F_y(\epsilon') = \frac{c_1 \cdot (\epsilon')^{c_2} + c_3}{c_1 \cdot (2.3)^{c_2} + c_3}. \quad (34)$$

The coefficients for (33) are broken into two tables, depending on whether MG or Linear mixing is being modeled. Table 1 contains coefficients for MG mixing and Table 2 for Linear mixing. The coefficients for the pair of normalization functions defined by (34) are provided in Table 3.

Although the procedure used for determining (33) and (34) is heuristic in nature, two distinct steps are

Table 1:  $R_x^{MG}$  coefficients.  $R_{b+r}$  generates  $R_b + R_r$ 

$R_x^{MG}$	$p_1$	$p_2$	$p_3$	$p_4$	$q_1$	$q_1$
$R_a$	4.02	37.9	77.2	2.31	1.62	2.68
$R_b$	4.43	25.8	4.19	1.07	0.0793	1.03
$R_r$	0.309	8.19	5.41	0.003	0.321	0.209
$R_{b+r}$	4.56	36.3	88.4	2.79	1.38	2.72

Table 2:  $R_x^{Lin}$  coefficients.  $R_{b+r}$  generates  $R_b + R_r$ 

$R_x^{Lin}$	$p_1$	$p_2$	$p_3$	$p_4$	$q_1$	$q_1$
$R_a$	4.62	42.0	67.3	1.73	1.32	1.98
$R_b$	4.93	30.9	3.16	0.857	0.115	0.804
$R_r$	0.283	8.45	3.98	0.0031	0.229	0.133
$R_{b+r}$	5.25	39.8	80.3	2.19	1.13	2.11

identified. The first step involves experimentation with the MATLAB Curve Fitting Toolbox (CFT) to determine the best functional form of the respective equations. In this regard, the term “best”, should be taken as a positive combination of succinctness, flexibility, and accuracy. The choice of the rational function in (33) and the power series in (34), possess these attributes.

With the functional forms of (33) and (34) in hand, the second step involves finding an optimized set of coefficients. For this, the MATLAB Global Optimization Toolbox (GOT) is employed. Whereas the CFT is designed to try out diverse functional fits quickly, it does not search and compare multiple bins of attraction as do the GOT methods [24]. In particular, the GOT provides an efficient implementation of the Multi-Start algorithm and a straightforward optimization framework [28].

Data for the CFT and GOT is comprised of nine three dimensional surfaces as visualized in Fig. 5, for each loss factor and for each mixing rule. The nine surfaces represent the nine dielectric constants of (15) that FEA is conducted. Since each surface contains 400 points, the curve fitters have 3,600 points to work with for each set of coefficients listed in Tables 1-3. Upon completion of the Multi-Start algorithm, the coefficients are saved to appropriately named files for fast access. All results that are reported in this research round the coefficients to three significant digits, as reported in Tables 1-3.

A key observation is that the substitution of  $u_y$  in (31), effectively reduces the dimensionality of the problem from three to one. Moreover, since we are now dealing with functions of a single variable, straightforward curve fitting is possible, as in (33). To demonstrate why this is possible, results are presented that first reduce

Table 3:  $F_{MG}$  and  $F_{Lin}$  coefficients

$F_y$	$c_1$	$c_2$	$c_3$
$F_{MG}$	7.57	0.799	-5.13
$F_{Lin}$	-3.88	-1	3.85

the dimensionality from three to two, and then from two to one.

Consider the surface plot of the beam loss factor provided in Fig. 5. This figure is generated using the MG mixture model, with a printed material dielectric constant  $\epsilon' = 4.0$ . The loss factor is shown explicitly as a function of the variables  $r_l$  and  $\tan(\delta)$ . However, adapting the notation  $L_b^{MG}(\epsilon', \tan(\delta), r_l)$ , we refer to it as a function of three variables, namely:  $\epsilon'$ ,  $\tan(\delta)$  and  $r_l$ . Alternatively,  $L_b^{MG}$  as well as  $L_b^{Lin}$ , can be closely approximated as a function of only two variables:  $\epsilon'$  and the product  $r_l \cdot \tan(\delta)$ . This is observed for the FEA results given in Fig. 9 for the MG mixture model and Fig. 10 for Linear mixing. In both figures, results are plotted for the several dielectric constants, i.e.,  $\epsilon' = [2.3, 2.8, 4, 10]$ , each trace corresponding to a unique  $\epsilon'$ .

The resulting traces are not strictly continuous, but nearly so, and especially so for MG mixing and  $\epsilon' \geq 4$ . This characteristic is observed for all the loss factors considered in this research. Thus, for a given mixture model, the individual loss factors can be accurately represented as a function of  $\epsilon'$  and the product of lens radius  $r_l$  times the loss tangent  $\tan(\delta)$ .

The normalization factors  $F_{MG}(\epsilon')$  and  $F_{Lin}(\epsilon')$  are graphed in Fig. 11. Their purpose is explained below, using an illustrative example. Consider the loss trace in Fig. 9 for  $\epsilon' = 4$ , which we will express here as  $L_b^{MG}(4, r_l \cdot \tan(\delta))$ . Using the coefficients in Table 3 and (34),  $F_{MG}(4)$  is found to be  $\approx 1.853$ . Careful

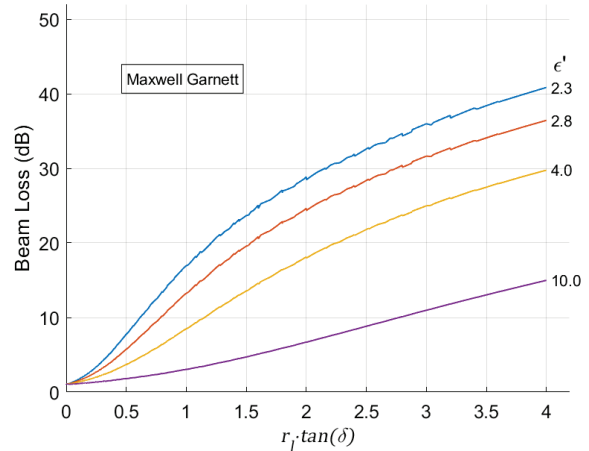


Fig. 9. FEA results showing the beam loss factors versus  $r_l \cdot \tan(\delta)$  for the MG mixture model.

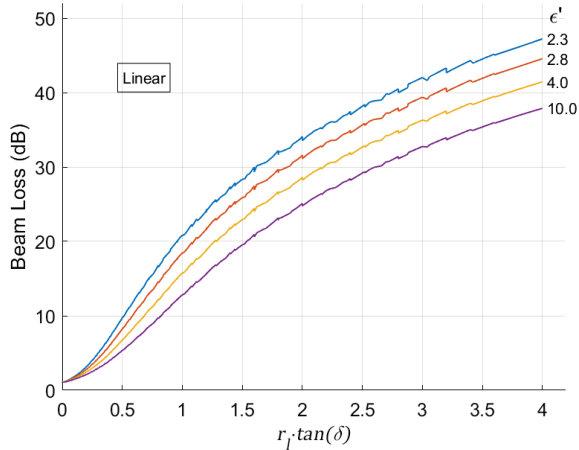


Fig. 10. FEA results showing the beam loss factors versus  $r_l \cdot \tan(\delta)$  for the Linear mixture model.

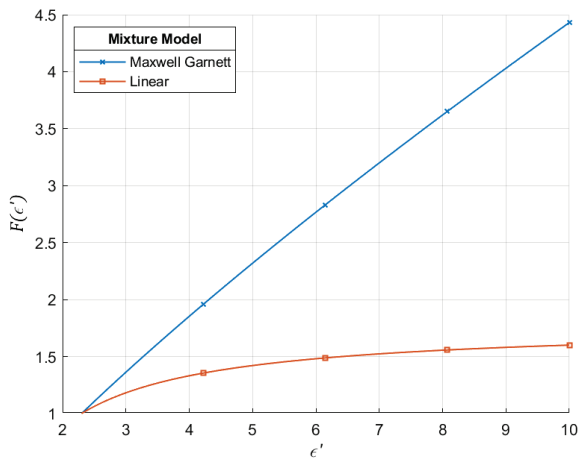


Fig. 11. Normalization factors  $F_{MG}(\epsilon')$  and  $F_{Lin}(\epsilon')$ .

examination of Fig. 9 verifies that the following approximation holds:

$$L_b^{MG}(4, r_l \cdot \tan(\delta)) \approx L_b^{MG}\left(2.3, \frac{r_l \cdot \tan(\delta)}{1.853}\right), \quad (35)$$

and in general:

$$L_x^y(\epsilon', r_l \cdot \tan(\delta)) \approx L_x^y\left(2.3, \frac{r_l \cdot \tan(\delta)}{F_y(\epsilon')}\right). \quad (36)$$

Thus, given an arbitrary  $\epsilon'$ , the normalization factors map the corresponding loss factors onto respective portions of a reference trace having  $\epsilon' = 2.3$ . Since  $\epsilon'$  is fixed for the reference trace, we are effectively left with an equation of a single variable  $u_y$ , defined by (32). This is demonstrated in Fig. 12, where the FEA results for beam loss are shown for the same set of dielectric constants used in Fig. 9 and Fig. 10. The FEA results for any particular  $\epsilon'$ , extends from  $(0, L_b^y(0))$  to the respectively labeled  $\circ$  marker. For a given mixture model  $y$ , the loss

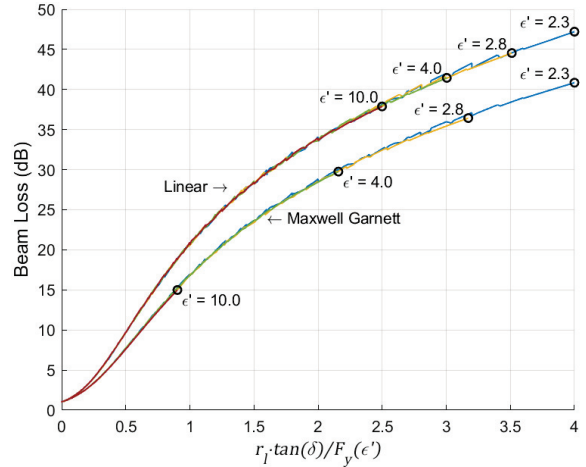


Fig. 12. FEA results showing beam loss factors  $L_b^{MG}$  and  $L_b^{Lin}$  versus  $u_y = r_l \cdot \tan(\delta) / F_y(\epsilon')$ .

Table 4: Study wide rmse of curve fit for loss factors

$R_x$	$\text{rmse}_x^{MG}$ (dB)	$\text{rmse}_x^{Lin}$ (dB)
$R_a$	0.074	0.098
$R_b$	0.073	0.104
$R_r$	0.027	0.032
$R_{b+r}$	0.067	0.093

factor can be accurately represented as a function of the single auxiliary variable  $u_y$ .

### III. RESULTS AND DISCUSSION

In this section the rational function curve fits  $R_x^y$  are compared with the respective loss factors  $L_x^y$  obtained through FEA simulation. Additionally,  $R_x^y$  is used to determine the maximum useful lens radius for several common low loss polymers.

#### A. Curve fit performance and discussion

Table 4 provides the root mean square error (rmse) of the individual curve fits. On average, the rmse for the Linear mixture fit is 33% higher than that of the MG fit, however, in all cases the errors are below 0.11 dB. The FEA data provided earlier in Fig. 9 and Fig. 10 appears consistent with this result, since the  $L_b^{Lin}$  plots do exhibit larger perturbations than their MG counterparts. Note that the function  $R_{b+r}$  generates  $R_b + R_r$ , in which case the respective rmse reported in Table 4 is computed using  $(L_b + L_r - R_{b+r})$ .

The following contour plots provide further insight to the loss factors observed through FEA, as well as the respective rational function fit. Each figure contains data only for a single dielectric constant, and  $\epsilon' = 2.8$  is chosen as a representative example. Furthermore, plots are shown for the Linear mixture model.

Figure 13 compares the FEA derived beam loss factor  $L_b^{Lin}$  with the fit equation  $R_b^{Lin}$ . The plot in Fig. 13 (a) is colored using the  $L_b^{Lin}$  data, and constant loss contours of  $L_b^{Lin}$  are shown using solid black lines and that of  $R_b^{Lin}$  with dashed white lines. Both sets of contours are displayed every 3 dB, with the highest extending to 42 dB. In Fig. 13 (b), the difference between  $L_b^{Lin}$  and  $R_b^{Lin}$  is shown. Although a peak residual of 0.4 dB is observed, this occurs at  $L_b^{Lin} \approx 39$  dB, which should be insignificant for most purposes. The rmse over the plot is 0.107 dB, which is slightly above the rmse reported in Table 4. This is understandable, since Table 4 accounts for all nine values of  $\epsilon'$  examined in this research.

Examination of any contour line in Fig. 13 (a) reveals that the product  $r_l \cdot \tan(\delta)$  is constant valued along the contour. Since the plot is generated with  $\epsilon'$  fixed at 2.8, then  $F_{Lin}(\epsilon')$  is obviously constant, and therefore  $r_l \cdot \tan(\delta)/F_{Lin}(\epsilon')$  must also equate to a constant along the contour. The later expression is defined in (32) as  $u_{Lin}$ , and  $R_b^{Lin}$  is a rational polynomial in terms of  $u_{Lin}$  given by (33). In a sense then,  $R_b^{Lin}$  maps the set of points on a given contour line to a scalar which is the loss associated with that contour line. It does so across all values of  $\epsilon'$  as well. Moreover, constant loss contour lines are rectangular hyperbolas, but are defined only for positive arguments. This is a common characteristic for all the loss factors addressed in this research, regardless of the mixture model.

Figure 14 (a) compares the FEA derived aperture loss factor  $L_a^{Lin}$  with the rational fit  $R_a^{Lin}$  and is drawn in the same fashion as Fig. 13 (a). The rmse for this fit is 0.102 dB, just slightly higher than the study wide value reported in Table 4. As with the beam loss factor, the contours are rectangular hyperbolas.

A curve fit for the lens gain in decibels is written directly using the rational function fit for the aperture loss factor as:

$$\check{G}_{Lin} = 10 \cdot \log_{10}(4\pi^2 r_l^2) - R_a^{Lin}, \quad (37)$$

and in Fig. 14 (b), it is compared with the FEA derived gain. Even though the gain and aperture loss factor contours are quite different, the rmse of the gain fit is identical to that of aperture loss factor. This must be so, since  $\check{G}_{Lin}$  is only dependent upon the lens radius  $r_l$  and  $R_a^{Lin}$ . Since  $r_l$  is known exactly, the error in the gain fit can only originate from  $R_a^{Lin}$ .

A distinguishing characteristic of the constant gain contours in Fig. 14 (b) is that they have a finite maximum. This implies that for a given  $\epsilon'$  and a  $\tan(\delta) > 0$ , there is a lens radius  $r_{peak}$ , at which the gain peaks and increasing  $r_l$  beyond  $r_{peak}$  can only result in a lower gain. Determination of  $r_{peak}$  is attained by solving the derivative of (37) in terms of  $r_l$  with the condition that  $d\check{G}_{Lin}/dr_l = 0$ . In doing so it is found that depending upon the mixture rule being modeled,  $r_{peak}$  must lie on

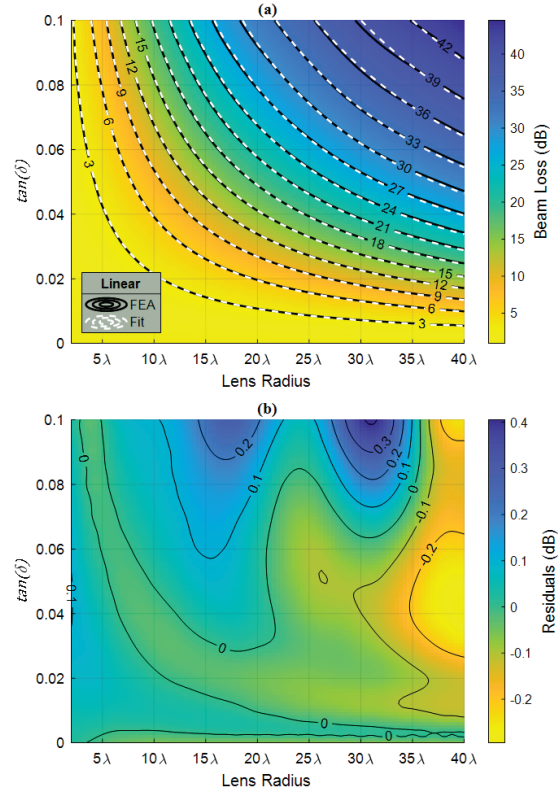


Fig. 13. (a) Illustrates a direct comparison of FEA results  $L_b^{Lin}$  and the rational function fit  $R_b^{Lin}$  using coefficients from Table 1 and Table 3. (b) Shows the residual difference,  $E_b^{Lin} = L_b^{Lin} - R_b^{Lin}$ . Printed material  $\epsilon' = 2.8$ .

either the  $R_a^{Lin} \approx 10.14$  dB contour or the  $R_a^{MG} \approx 10.39$  dB contour. For example, with  $\epsilon' = 2.8$  and  $\tan(\delta) = 0.04$  and linear mixing, then  $r_{peak} \approx 8.23\lambda$ . Upon reducing the loss tangent to 0.02, yields  $r_{peak} \approx 16.5\lambda$ . The product  $r_{peak} \cdot \tan(\delta)$  is a constant for a given  $\epsilon'$  and mixing rule. A red dashed trace in Fig. 14 indicates the respective contour.

Finally, in Fig. 15 is a comparison between the FEA derived radiation loss factor  $L_r^{Lin}$  and the fit equation  $R_r^{Lin}$ . The rmse for this fit is 0.028 dB, which is slightly below the study wide value provided in Table 4.

It is notable that the maximum radiation loss observed in Fig. 15 (a) is  $\approx 9.7$  dB, since the maximum beam loss seen in Fig. 13 (a) is  $\approx 44.5$  dB. For the lossless case, 100% of the power accepted by the lens is radiated, and between 78% to 80% of the radiated power is contained within the main lobe. As loss is introduced, the radiated power naturally decreases. For instance, along the 9 dB loss contour shown in Fig. 15 (a), only 13% of the accepted power is being radiated. Furthermore, the same combinations of  $r_l$  and  $\tan(\delta)$  that produce a 9 dB radiation loss, produce  $\approx 14.8$  dB beam loss in

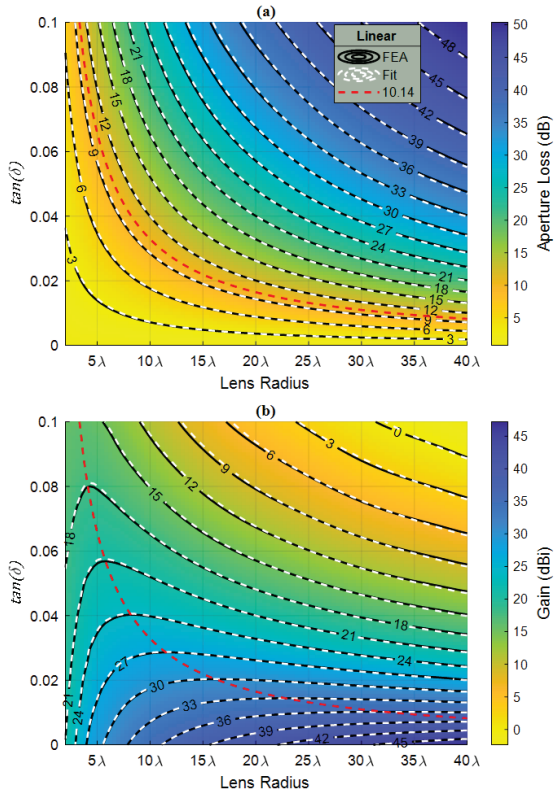


Fig. 14. (a) Illustrates a direct comparison of FEA results  $L_a^{Lin}$  and  $R_a^{Lin}$ . (b) Illustrates a direct comparison of FEA derived gain and the fit provided by  $\check{G}_{Lin}$ . Red trace is hyperbola marking locus of gain peaks.  $\epsilon' = 2.8$ .

Fig. 13 (a). This means that  $\approx 3\%$  of the radiated power is now contained in the main beam. At the severest point simulated, that being the top right corner of the contour plots, the radiation loss has only increased by another 0.7 dB, and therefore the radiated power is very nearly the same being  $\approx 11\%$  of accepted. However, the beam loss has increased by 29.7 dB, therefore reducing the power in the main beam to approximately 0.0035% of the radiated power.

### B. Maximum useful lens radius of common polymers

We have shown that for each loss factor  $L_x$ , and each mixing rule  $y$ , a rational function curve fit of an auxiliary variable  $u_y = r_l \cdot \tan(\delta) / F_y(\epsilon')$ , provides an accurate and wide range empirical model of that loss factor. We now further define the normalized loss tangent as being:

$$t_y = \frac{\tan(\delta)}{F_y(\epsilon')}, \quad (38)$$

thus:

$$u_y = r_l \cdot t_y, \quad (39)$$

and therefore:

$$L_x^y \approx R_x^y(r_l \cdot t_y). \quad (40)$$

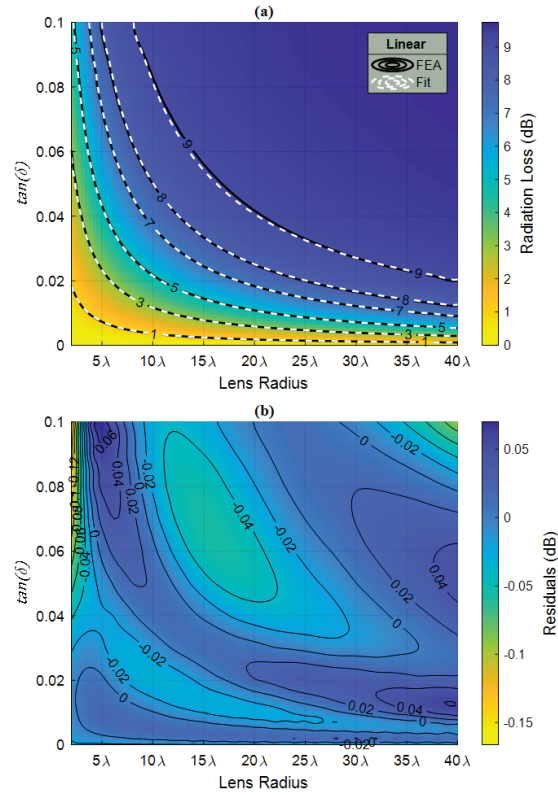


Fig. 15. (a) Illustrates a direct comparison of FEA results  $L_r^{Lin}$  and the rational function fit  $R_r^{Lin}$ . (b) Shows the residual difference,  $E_r^{Lin} = L_r^{Lin} - R_r^{Lin}$ .  $\epsilon' = 2.8$ .

The purpose of (38) is more than convenience and will be evident shortly. Up to now, we have been utilizing contour plots that visualize loss and gain by treating  $\epsilon'$  as a constant and  $r_l$  and  $\tan(\delta)$  as independent variables. This provides the most direct method to compare FEA results to the rational function approximations. As a comparative design aide though, it is cumbersome since a separate plot is needed for every  $\epsilon'$  being considered. Therefore, we now treat  $r_l$  and  $t_y$  as independent variables. Since  $t_y$  encapsulates the loss characteristics of a particular lens material, a single contour plot facilitates visualization of loss as  $r_l$  is varied across an infinite set of materials.

This is done in Fig. 16 for the rational function approximation of the input referred beam loss factor  $L_b^{MG} + L_r^{MG} = -10 \cdot \log_{10}(P_b/P_0)$ . This is an important performance metric, since  $P_b/P_0$  is the ratio of power radiated in the main beam to the power accepted by the lens. Logarithmic scales are used for both  $r_l$  and  $t_{MG}$  due to the relatively large range of values. The diagonal traces are constant  $L_b^{MG} + L_r^{MG}$  contours and are remarkably linear. The vertical red dashed lines show the locus of points that represent  $L_b^{MG} + L_r^{MG}$  associated with the

Table 5: Polymers considered in this research

ID	Material
A	High Density Polyethylene [19]
B	Low Density Polyethylene [19]
C	Polytetrafluoroethylene (PTFE) [19]
D	Polypropylene (PP) [20]
E	Polycarbonate (PC) [15]
F	Acrylonitrile butadiene styrene (ABS) [15]
G	DSM Somos NanoTool [15]
H	DSM Somos ProtoGen 18120 [16]
I	DSM Somos ProtoTherm 12120 [15]
J	DSM Somos Watershed 11122 [15]

Table 6: Polymer properties along with normalization factor and normalized loss tangent for MG mixing

ID	$\epsilon'$	$\tan(\delta)$	$F_{MG}(\epsilon')$	$t_{MG}$
A	2.35	$1.5 \times 10^{-4}$	1.03	$1.46 \times 10^{-4}$
B	2.28	$1.6 \times 10^{-4}$	0.989	$1.62 \times 10^{-4}$
C	2.05	$1.70 \times 10^{-4}$	0.865	$1.96 \times 10^{-4}$
D	2.23	$2.00 \times 10^{-3}$	0.963	$2.08 \times 10^{-3}$
E	2.59	$5.20 \times 10^{-3}$	1.15	$4.51 \times 10^{-3}$
F	2.54	$1.51 \times 10^{-2}$	1.13	$1.34 \times 10^{-2}$
G	3.2	$2.55 \times 10^{-2}$	1.46	$1.74 \times 10^{-2}$
H	3.16	$3.30 \times 10^{-2}$	1.44	$2.29 \times 10^{-2}$
I	2.88	$4.37 \times 10^{-2}$	1.30	$3.36 \times 10^{-2}$
J	2.62	$4.24 \times 10^{-2}$	1.17	$3.63 \times 10^{-2}$

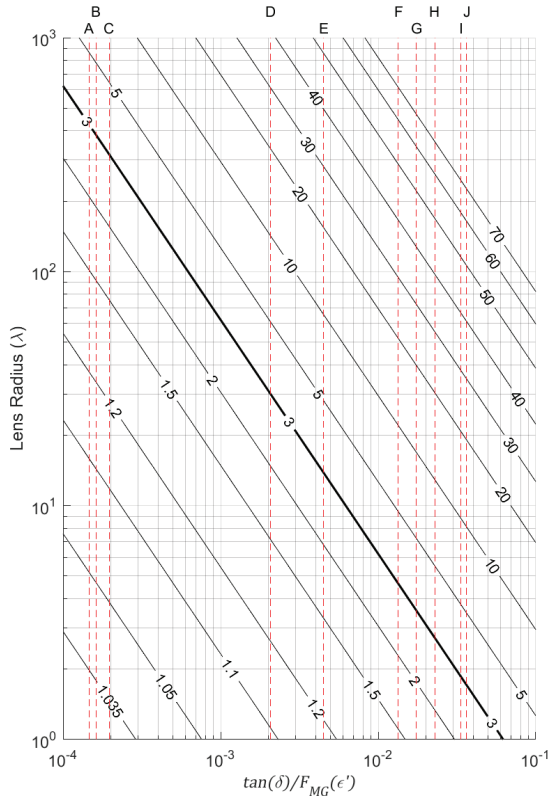


Fig. 16. Beam loss relative to  $P_0$  as lens radius  $r_l$  and the normalized loss tangent  $t_{MG}$  are varied. Contour labels are in dB.

constant  $t_{MG}$  for the material identified by the capital letter directly above the trace. These traces are labeled A through I and refer to the polymers listed in Table 5. In Table 6, the published dielectric constant and loss tangent of each polymer is listed, along with the respective normalization factor and normalized loss tangent computed for MG mixing.

The 3 dB contour in Fig. 16 is of particular interest since it identifies the combinations of material and lens radius that produce a radiation pattern in which half of the accepted power is contained in the main lobe, with the remaining half lost to heating and side lobes. Points to the right of the 3 dB contour have greater main lobe loss, and points to the left have less. Thus, for any point on the contour, increasing either  $r_l$ ,  $t_{MG}$  or both, results in a main lobe containing less than half of the accepted power. We solve for the intersection of each red trace with the 3 dB contour, and consider the associated  $r_l$  as the maximum useful lens radius for the respective material. The same procedure is repeated using the Linear mixing rule. Compared to MG mixing, the Linear rule always produces a smaller useful radius, i.e., it produces greater loss. Thus, the Linear mixture provides a lower bound and the MG mixture an upper. Taken together, the Linear and MG predictions are considered as a range of useful radii, with the actual value dependent upon the mixing model employed. This data is reported in the second column of Table 7. An interesting occurrence is that regardless of mixing rule or the material,  $L_b$  and  $L_r$  are fixed values along any constant  $L_b + L_r$  contour. For the 3 dB contour,  $L_b = 1.41$  dB and  $L_r = 1.59$  dB.

A similar contour plot of the the rational function approximation of lens gain  $G = 10 \cdot \log_{10}(4\pi^2 r_l^2) - L_a^{MG}$  is provided in Fig. 17. Additionally, the 3 dB contour from Fig. 16 is superimposed. We solve for the gain at the intersection of each red line with the overlaid  $L_b^{MG} + L_r^{MG}$  contour and consider this the maximum useful gain of the lens. This is also carried out for Linear mixing, which always results in lower gain. The two values are considered as the range that may occur depending upon the mixing model, and are reported in the third column of Table 7.

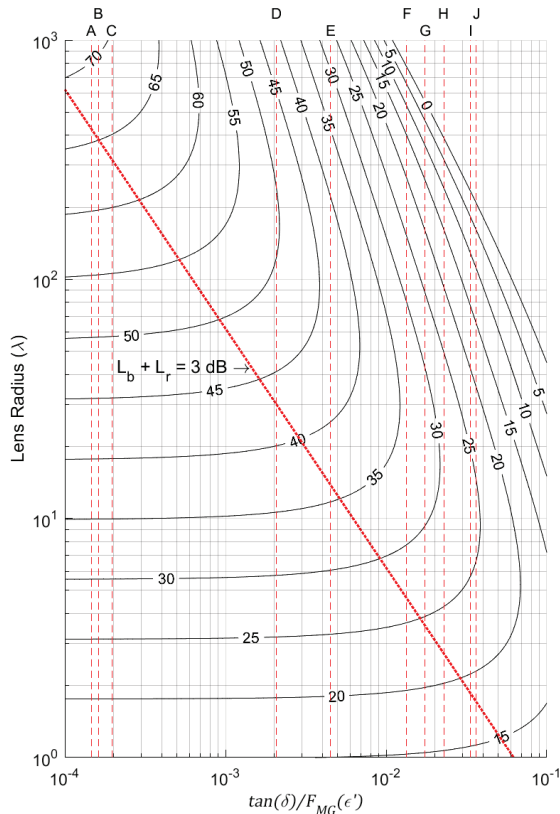


Fig. 17. Antenna gain as lens radius  $r_l$  and the normalized loss tangent  $t_{MG}$  are varied. Contour labels are in dB.

Table 7: Maximum useful lens radius and gain (Lin : MG)

ID	$r_{\max} (\lambda)$	$G_{\max} (\text{dBi})$
A	356 : 425	64.4 : 65.9
B	326 : 384	63.6 : 65.1
C	279 : 316	62.3 : 63.4
D	25.6 : 29.9	41.5 : 42.9
E	11.0 : 13.8	34.2 : 36.1
F	3.73 : 4.64	24.8 : 26.7
G	2.51 : 3.57	21.3 : 24.4
H	1.93 : 2.72	19.0 : 22.1
I	1.39 : 1.85	16.2 : 18.7
J	1.36 : 1.71	16.0 : 18.0

### C. The product $r_l \cdot t_y$

The product of the lens radius  $r_l$  in terms of  $\lambda$  and the normalized loss tangent  $t_y$  is a key metric in characterizing the radiation pattern of a LL with loss. This is because  $L_x^y \approx R_x^y(r_l \cdot t_y)$  as pointed out in the previous

Table 8: Thresholds of performance and associated  $r_l \cdot t_y$  products

Threshold Description	$r_l \cdot t_{\text{Lin}}$	$r_l \cdot t_{\text{MG}}$
50% of accepted power is contained within the main beam, i.e., $\eta_r \eta_b = 0.5$ . <b>Note:</b> $L_b = 1.41$ , $L_r = 1.59$ dB regardless of mixture.	0.0525	0.0622
Gain at peak value for given material and mixture. Increasing $r_l$ can only decrease the gain. <b>Note:</b> The aperture loss differs slightly with mixture: $L_a^{\text{Lin}} = 10.14$ , $L_a^{\text{MG}} = 10.39$ dB.	0.289	0.360
13% of accepted power is radiated, and $\approx 3\%$ of the radiated power is contained in the main beam. <b>Note:</b> The beam efficiency differs slightly with mixture: $\eta_b^{\text{Lin}} = 0.033$ , $\eta_b^{\text{MG}} = 0.028$ . Note that 13% accepted equates to an $L_r = 9$ dB.	0.715	0.922

section. The product  $r_l \cdot t_y$  therefore provides a succinct method to specify thresholds of operation for the LL with loss. This is done in Table 8 for the three thresholds that have been discussed earlier in Sections III-A and III-B.

## IV. CONCLUSION

This research has applied EMT and 3D FEA to model the transmissive loss through a waveguide fed additively manufactured Luneburg lens. It is found that rational function approximations accurately model antenna loss factors derived from this modeling. Using this empirical model of loss, the following conclusions are drawn.

For a given mixing rule  $y$ , it is the product of lens radius  $r_l$  and the polymers normalized loss tangent  $t_y$ , that ultimately determine the transmissive loss of the lens. The normalized loss tangent is itself, a function of the polymer's dielectric constant  $\epsilon'$  and its loss tangent  $\tan(\delta)$ . When comparing the relative merits of two different polymers, neither  $\epsilon'$  nor  $\tan(\delta)$  taken alone are sufficient to make the best choice. However, choosing the material with the lowest  $t_y$ , is guaranteed to result in the lowest transmissive loss.

Given that transmissive loss is dependent on the product  $r_l \cdot t_y$ , a maximum  $r_l$  exists for each combination of mixing rule, polymer and level of loss that is deemed tolerable. In this research, the threshold of useful operation occurs when half of the accepted power

by the antenna is radiated in the main lobe. Therefore, for a given mixing rule, once the polymer is chosen, the engineer can determine the maximum useful lens radius. In turn, this determines maximum gain achievable  $G_{max}$ , which is the value of  $G$  when the main lobe contains exactly 50% of the accepted power.

The product  $r_l \cdot t_y$  provides a concise method to specify thresholds of operation for the LL with loss. It is of course dependent upon the mixing rule, but even so, immediately indicates important aspects of the radiation pattern and thus the performance. Three thresholds have been identified and tabulated. Regardless of mixture rule, values below 0.05 result in greater than 50% of the accepted power being radiated in the main beam. Thus, this simple rule can guide material selection. Other factors being equal, the Linear mixing rule always produces greater loss than the MG rule. Taken together, the two EMT rules set lower and upper bounds of performance. Examining Table 7, it is observed that the difference in  $G_{max}$  predicted by these two theories ranges between 1.4 dB and 3.1 dB for practical size lenses. At present however, the unit cell structures used in AM graded index components do not seem to obey the MG mixing law [5]. Rather, they more closely follow the Bruggeman and Capacitive model, which are both better approximated by the Linear mixing rule [25]. To maximize gain, research into producing unit cell arrangements that follow the MG mixing law is therefore still needed.

## REFERENCES

- [1] R. K. Luneburg, *Mathematical Theory of Optics*. Brown University Press, Providence, RI, USA, 1944.
- [2] P. S. Hall and S. J. Vetterlein, "Review of radio frequency beamforming techniques for scanned and multiple beam antennas," *IEEE Proc. Microwaves, Antennas Propag.*, vol. 137, no. 5, pp. 293-303, 1990.
- [3] Y. Li, Lei G. M. Chen, Z. Zhang, Z. Li, and J. Wang, "Multibeam 3-D-printed Luneburg lens fed by magnetolectric dipole antennas for millimeter-wave MIMO applications," *IEEE Trans. Antennas Propag.*, vol. 67, no. 5, pp. 2923-2933, May 2019.
- [4] J. Deroba, A. Good, K. Sobczak, Z. Larimore, and M. S. Mirotznik, "Additively manufactured Luneburg retroreflector," *IEEE Trans. Aerospace Electronic Syst.*, Sep. 2019.
- [5] M. Liang, W.-R. Ng, K. Chang, K. Gbele, M. E. Gehm, and H. Xin, "A 3-D Luneburg lens antenna fabricated by polymer jetting rapid prototyping," *IEEE Trans. Antennas Propag.*, vol. 62, no. 4, pp. 1799-1807, 2014.
- [6] Z. Larimore, S. Jensen, P. Parsons, B. Good, K. Smith, and M. S. Mirotznik, "Use of space-filling curves for additive manufacturing of three dimensionally varying graded dielectric structures using fused deposition modeling," *Additive Manuf.*, vol. 15, pp. 48-56, 2017.
- [7] Z. Larimore, S. Jensen, A. Good, J. Suarez, and M. S. Mirotznik, "Additive manufacturing of Luneburg lens antennas using space-filling curves and fused filament fabrication," *IEEE Trans. Antennas Propag.*, vol. 66, no. 6, pp. 2818-2827, 2018.
- [8] S. Biswas, A. Lu, Z. Larimore, P. Parsons, A. Good, N. Hudak, B. Garrett, J. Suarez, and M. S. Mirotznik, "Realization of modified Luneburg lens antenna using quasi-conformal transformation optics and additive manufacturing," *Microwave Optical Technol. Lett.*, vol. 61, no. 4, pp. 1022-1029, 2019.
- [9] S. Biswas and M. S. Mirotznik, "High gain, wide-angle QCTO-enabled modified Luneburg lens antenna with broadband anti-reflective layer," *Nature: Sci. Rep.*, vol. 10, no. 1, pp. 1-13, 2020.
- [10] O. Bjorkqvist, O. Zetterstron, and O. Quevedo-Teruel, "Additive manufactured dielectric Gutman lens," *Electronic Lett.*, vol. 55, no. 25, pp. 1318-1320, 2019.
- [11] J. Poyanco, F. Pizarro, and E. Rajo-Iglesias, "3D-printing for transformation optics in electromagnetic high-frequency lens applications," *Materials*, vol. 13, pp. 1-11, 2020.
- [12] P. Liu, X. Zhu, Y. Zhang, J. Li, and Z. Jiang, "3D-printed cylindrical Luneburg lens antenna for millimeter wave applications," *Int. J. RF Microwave Comput.-Aided Eng.*, vol. 30, pp. 1-8, 2019.
- [13] C. Wang, J. Wu, and Y. Guo, "A 3-D printed multibeam dual circularly polarized Luneburg lens antenna based on quasi-icosahedron models for Ka-band wireless applications," *IEEE Trans. Antennas Propag.*, vol. 68, no. 8, pp. 5807-5815, 2020.
- [14] K. Hoel, S. Kristoffersen, M. Ignatenko, and D. Filipovic, "Half ellipsoid Luneburg GRIN dielectric lens loaded double ridged horn antenna," in *Proc. IET 12th Eur. Conf. Antennas Propag.*, London, UK, 2018.
- [15] P. I. Deffenbaugh, R. C. Rumpf, and K. H. Church, "Broadband microwave frequency characterization of 3-D printed materials," *IEEE Trans. Compon. Packaging Manuf. Technol.*, vol. 3, no. 12, pp. 2147-2155, 2013.
- [16] J. Monkevich and G. Le Sage, "Design and fabrication of a custom-dielectric Fresnel multi-zone plate lens antenna using additive manufacturing techniques," *IEEE Access*, vol. 7, 2019.

- [17] J. Zechmeister and J. Lacik, "Complex relative permittivity measurement of selected 3D-printed materials up to 10 GHz," in *Proc. IEEE Conf. Microwave Techn.*, Pardubice, Czech Republic, 2019.
- [18] Y. Li and Q. Zhu, "Luneburg lens with extended flat focal surface for electronic scan applications," *Optics Express*, vol. 24, no. 7, 2016.
- [19] J. Krupka, "Measurements of the complex permittivity of low loss polymers at frequency range from 5 GHz to 50 GHz," *IEEE Microwave Wireless Compon. Lett.*, vol. 26, no. 6, pp. 464-466, 2016.
- [20] J. K. Pakkathillam, B. T. Sivaprakasam, J. Poojali, C. V. Krishnamurthy, and K. Arunachalam, "Tailoring antenna focal plane characteristics for a compact free-space microwave complex dielectric permittivity measurement setup," *IEEE Trans. Instrum. Meas.*, vol. 70, 2021.
- [21] A. Sihvola, *Electromagnetic Mixing Formulas and Applications*. London, U.K.: The Institution of Engineering and Technology, 2008.
- [22] R. C. Johnson, *Antenna Engineering Handbook*. McGraw-Hill, New York, NY, USA, 1993.
- [23] COMSOL Multiphysics® v. 5.6. Stockholm, Sweden: COMSOL AB. Available: [www.comsol.com](http://www.comsol.com).
- [24] MATLAB, ver. 2021a. Natick, MA, USA: The Mathworks Inc., 2021.
- [25] E. Burden, Y. Oh, B. Mummareddy, D. Negro, P. Cortes, A. Du Plessis, E. MacDonald, J. Adams, F. Li, and R. Rojas, "Unit cell estimation of volumetrically-varying permittivity in additively manufactured ceramic lattices with X-ray computed tomography," *Mater. Des.*, vol. 210, Nov. 15, 2021.
- [26] G. Guo, Y. Xia, C. Wang, M. Nasir, and Q. Zhu, "Optimal radiation pattern of feed of Luneburg lens for high-gain application," *IEEE Trans. Antennas Propag.*, vol. 68, no. 12, pp. 8139-8143, Dec. 2020.
- [27] C. A. Balanis, *Antenna Theory - Analysis and Design*. Hoboken, NJ, USA: John Wiley & Sons Inc., 2005.
- [28] M. Dourado, J. Meireles, and A. Rocha, "A global optimization approach applied to structural dynamic updating," in *Proc. 14th Int. Conf. Comput. Sci. Its Appl. (ICCSA)*, vol. 8580, pp. 195-210, 2014.



**Brian F. LaRocca** received the B.S.E.E and M.S.E.E degrees from New Jersey Institute of Technology, Newark, NJ, USA in 1985 and 2000 respectively. From 1985 to 1996 he worked in industry, 1996 to 2004 as a government contractor, and 2004 to present as a civilian engineer with the Dept. of the Army at Ft. Monmouth, NJ, USA and Aberdeen Proving Ground, MD, USA. He received the Ph.D. degree in electrical engineering from the University of Delaware, Newark, DE, USA in the summer of 2022.



**Mark S. Mirotznik** (S'87–M'92–SM'11) received the B.S.E.E. degree from Bradley University, Peoria, IL, USA, in 1988, and the M.S.E.E. and the Ph.D. degrees from the University of Pennsylvania, Philadelphia, PA, USA, in 1991 and 1992, respectively. From 1992 to 2009, he was a Faculty Member with the Department of Electrical Engineering, The Catholic University of America, Washington, DC, USA. Since 2009, he has been a Professor and an Associate Chair for Undergraduate Programs with the Department of Electrical and Computer Engineering, University of Delaware, Newark, DE, USA. He holds the position of Senior Research Engineer with the Naval Surface Warfare Center, Carderock Division. His current research interests include applied electromagnetics and photonics, computational electromagnetics, multifunctional engineered materials, and additive manufacturing.

# A Parasitic Hat for Microstrip Antenna Design Based on Defected Structures for Multiband Applications

Faten F. Ismail, Mostafa A. El-Aasser, and Nasr H. Gad

Physics Department, Faculty of Science  
Ain Shams University, Cairo 11566, Egypt  
fatenfouad.p@sci.asu.edu.eg, elaasser@gmail.com,  
ngad@sci.asu.edu.eg

**Abstract** – In this article, a novel design of a quad-band parasitic hat microstrip antenna is proposed for multiband applications. The proposed antenna consists of a rectangular patch of dimensions 30 mm×11 mm cut with four L-shaped slots connected with a rectangular slot in the middle of the front side of the antenna to form a parasitic hat based upon defected microstrip structure. On the other side of the antenna, a defected ground structure is integrated as five rectangular slots embedded in the ground plane with the same width but with various lengths. The suggested antenna is designed and fabricated on a substrate material with an area of 45 × 40 mm<sup>2</sup> with a thickness of 1.52 mm to generate four frequency bands. The proposed antenna is fed by a microstrip transmission line. The simulated radiation patterns, return losses, maximum gains, and efficiencies of the antenna are carried out by using electromagnetic simulation software based on the finite element method. The measured return loss results validate that the suggested antenna can be designed to cover the frequency ranges from (3.8464 to 4.1456) GHz for sub-7GHz 5G applications, (6.7 to 7.162) GHz for ultra-wideband applications, (9.1616 to 9.5187) GHz for maritime radio-navigation positioning systems, and (11.5421 to 16.4085) GHz for radio-navigation satellite standards. The suggested antenna is based upon defected ground structure and defected microstrip structure techniques to improve the antenna performance.

**Index Terms** – Defected ground structure, defected microstrip structure, microstrip antenna, multiband, parasitic hat, slot antenna.

## I. INTRODUCTION

In the last two decades, the microstrip patch antenna has been widely used in multiband applications [1, 2], because of its small and compact size, low profile, lightweight, low volume, and low cost. Different techniques have been used to increase the bandwidth of

the microstrip antenna, such as the defected structures technique, which consists of two types; the first one is the defected ground structure (DGS). The second type is the defected microstrip structure (DMS). The DGS is a periodic or non-periodic cascading defect configuration embedded through the ground plane. The main structure used to create DGS is the electromagnetic band gap (EBG) [3]. The DGS is synthesized based on a single or many defects with periodic or aperiodic structures comparable to EBG. The DMS follows the DGS behavior but without any cutting inside the ground plane.

To enhance the microstrip antenna performance in multi-band applications either the DMS [4], or the DGS is used at the ground plane [5] or a combination of them [6]. In addition, other different techniques have been suggested to obtain multiband applications to enhance the bandwidth of the conventional patch antenna such as parasitic elements [7, 8]. With the increase of many different wireless communication systems, it is desirable to integrate a single wireless device to cover multiple wireless applications such as dual-band [9, 10], the triple band [11, 12], quad-band [13], and penta-band applications [14]. In reference [15], a dipole antenna and three microstrip slot antennas have been designed operating at 10 GHz in the X-band. In reference [16], a dual-slot radiating patch and a combination of L and U shape DGS were proposed to form a split ring structure and to get a tri-band DGS antenna for multiband applications resonating at (1.57, 2.47, and 0.926) GHz. In reference [17], two groups of five rectangular slots connected with each other by a small strip were etched in the ground plane acting as DGS to form a microstrip-fed printed slot antenna to generate five operating frequencies for multiband applications.

In this article, the main aim of the work is to use a parasitic element, which is a non-radiating element to be placed in front of the radiating patch to direct the EM wave towards its direction. The design of a

quad-band microstrip antenna with a parasitic hat element with a microstrip line feed for multiband applications is introduced. The designed antenna has an overall dimension of  $(45 \times 40 \times 1.52) \text{ mm}^3$ . The suggested antenna consists of four L-shaped slots connected with a rectangular slot cut from a rectangular shaped patch of dimensions  $(30 \times 11) \text{ mm}^2$ . The first two L-shaped slots on the right side of the patch are connected with the other two L-shaped slots on the left side of the patch with a rectangular slot in the middle with a dimension  $(8 \times 1) \text{ mm}^2$  to form a parasitic hat element in the front side of the antenna acting as DMS. On the backside of the antenna, there is a defected ground plane structure in the shape of five rectangular slots of lengths of (6, 18, 30, 18, and 6) mm respectively. All five rectangular slots have the same width of 3 mm to enhance the bandwidth. The proposed antenna radiates with four bandwidths for  $(S_{11} < -10 \text{ dB})$  and seven operating frequencies (4, 6.94, 9.39, 12, 12.93, 14, and 15.5) GHz suitable for multi-band applications to cover sub-7GHz 5G applications, ultra-wideband (UWB) applications, maritime radio-navigation positioning systems, and radio-navigation satellite standards.

## II. ANTENNA DESIGN AND ANALYSIS

### A. Antenna geometry

The geometry layout of the suggested parasitic hat antenna with DGS and DMS is shown in Fig. 1. The antenna uses RO4350B as a substrate material having a dielectric constant ( $\epsilon_r = 3.66$ ), a loss tangent ( $\tan \sigma = 0.004$ ), a dielectric thickness ( $h_s = 1.52 \text{ mm}$ ), and copper thickness ( $t = 0.035 \text{ mm}$ ).

As illustrated in Fig. 1, The overall area of the proposed antenna is  $(45 \times 40) \text{ mm}^2$ . The proposed parasitic hat antenna is composed of four L-shaped slots etched from a radiating rectangular shaped patch of a dimension  $(30 \times 11) \text{ mm}^2$ . Two L-shaped slots are on the right side of the patch, and the other two slots are on the left side of the patch. Four L-shaped slots are connected with a rectangular slot in the middle of a dimension  $(8 \times 1) \text{ mm}^2$ . The dimensions of the four L-shaped slots are the same,  $(6 \times 3) \text{ mm}^2$ . The parasitic hat patch antenna is located on the top of the substrate, while the DGS five rectangular slots are etched at the bottom. The width of the five rectangular slots is the same, ( $w=3\text{mm}$ ) but their lengths are different; the lengths of the first, second, third, fourth, and fifth rectangular slots are (6, 18, 30, 18, and 6) mm, respectively. The proposed antenna has a linearly polarized characteristic at all operating frequencies. The proposed parasitic hat microstrip antenna is investigated by electromagnetic simulator software (high-frequency

structure simulator (HFSS)) based on the finite element method (FEM) [18].

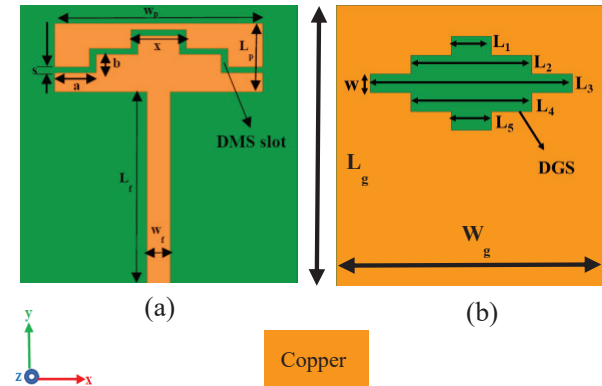


Fig. 1. The geometry of the proposed parasitic hat antenna (a) front view (patch) and (b) back view (ground).

All the parameters for the suggested antenna are given in Table 1.

Table 1: Optimized parameters of the proposed parasitic hat microstrip antenna

Parameter	Value (mm)	Parameter	Value (mm)	Parameter	Value (mm)
$W_g$	40	b	3	$L_2$	18
$L_g$	45	x	8	$L_3$	30
$h_s$	1.52	$L_p$	11	$L_4$	18
$W_f$	3.35	$W_p$	30	$L_5$	6
$L_f$	31	s	1	w	3
a	6	$L_1$	6	-	-

### B. Design procedure

DGS and DMS have an essential role in broadening the bandwidth of the microstrip antennas. In this section, they will be employed to choose the most suitable antenna structure to obtain a multiband antenna; four design configurations were carried out. Fig. 2 shows the design procedure of the ground plane, and patch by using the four configurations. Fig. 3 shows the return loss ( $S_{11}$ ) for the different configurations (from antenna 1 to antenna 4).

As illustrated in Fig. 2 (a), in the first configuration (antenna 1), five rectangular slots of the same width but having different lengths are embedded in the ground plane with a transmission line of length 36 mm. The resonance frequencies (3.2, 6.1, 11.2, 12.7, and 16.8) GHz were obtained. Fig. 2 (b), in the second configuration (antenna 2), (4.4, 6, 9.8, 11, 13.2,

and 14.8) GHz resonance frequencies are obtained by adding a rectangular radiating patch of a dimension  $(30 \times 11)$  mm<sup>2</sup> in the front side of the antenna. On the other side of the antenna 2, the five rectangular slots are etched in the ground plane. The length of the rectangular patch ( $L_p$ ) is chosen as approximately equal to half of the wavelength at the resonant frequency and can be calculated using the equations below [19]:

$$f_s = \frac{C}{2L_p \sqrt{\epsilon_{reff}}} \quad (1)$$

$$\epsilon_{reff} \approx \frac{\epsilon_r + 1}{2}, \quad (2)$$

where  $C$  is the speed of light in a vacuum,  $\epsilon_r$  is the relative permittivity,  $\epsilon_{reff}$  is the effective relative permittivity,  $L_p$  is the length of the rectangular patch, and  $f_s$  is the fundamental resonant frequency.

To achieve multiband operation for the proposed antenna, the lengths of DGS and DMS slots must be around  $\lambda_g/2$  for all operating frequencies ( $f$ ) based on the following equation:

$$\lambda_g = \frac{C}{f \sqrt{\epsilon_{reff}}}, \quad (3)$$

where  $\lambda_g$  is the guide wavelength [20].

The third configuration (antenna 3) of Fig. 2 (c) provides a wider bandwidth by employing a parasitic hat-shaped embedded in the radiating patch by etching four L-shaped slots of dimension  $(6 \times 3)$  mm<sup>2</sup>. Two rectangular slots, with the dimension  $(3.5 \times 1)$  mm<sup>2</sup>, are removed from the rectangular patch. There is an only individual rectangular strip with the dimension  $(1 \times 1)$  mm<sup>2</sup> that connects between the upper and lower parts of the radiating patch and acts as an inductively coupling. The obtained antenna provides the resonance frequencies (7.7, 9.4, 11.3, 15) GHz.

Finally, as shown in Fig. 2 (d) in the fourth configuration (antenna 4), the desired parasitic hat multi-band antenna is obtained by cutting a rectangular strip of a dimension  $(1 \times 1)$  mm<sup>2</sup> that connects the upper and lower parts of the antenna to form the proposed parasitic hat antenna. It acts as a capacitively coupling to obtain seven operating frequencies (4, 6.94, 9.39, 12, 12.93, 14, and 15.5) GHz with return losses (−21, −17, −15,

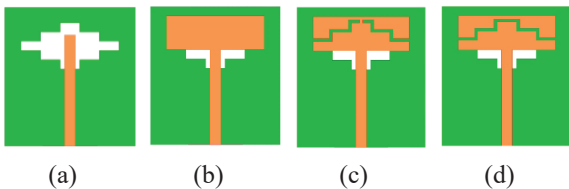


Fig. 2. DGS, DMS evolution configurations (a) antenna 1, (b) antenna 2, (c) antenna 3, and (d) antenna 4.

−16, −40, −22, and −43) dB, respectively for multi-band applications.

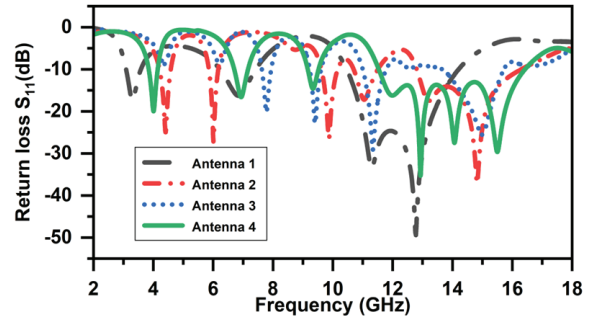


Fig. 3. Simulated return loss ( $S_{11}$ ) for different configurations (antenna 1 to antenna 4).

All the operating frequencies with the antenna configurations (antenna 1 to antenna 4) are given in Table 2.

Table 2: Antenna configurations (antenna 1 to antenna 4) with their operating frequencies

Antenna configurations	Frequency (GHz)
<b>Antenna 1</b>	3.2, 6.8, 11.3, 12.7
<b>Antenna 2</b>	4.4, 6, 9.8, 11, 13.2, 14.8
<b>Antenna 3</b>	7.7, 9.4, 11.3, 15
<b>Antenna 4 (proposed)</b>	4, 6.94, 9.39, 12, 12.93, 14, 15.5

### III. RESULTS AND DISCUSSION

#### A. Return loss ( $S_{11}$ )

The return loss is measured with Rohde and Schwarz ZVB20 vector network analyzer (VNA), which has a frequency range limited to 20 GHz. Fig. 4 displays

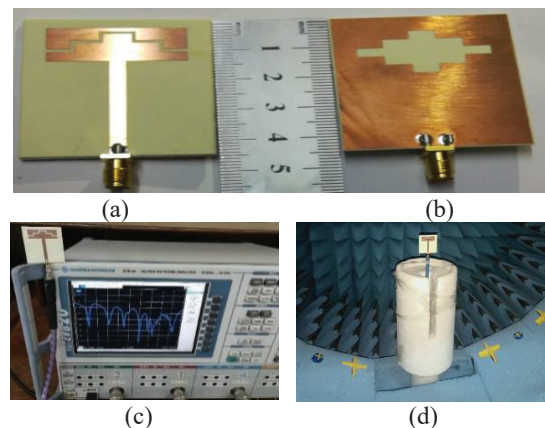


Fig. 4. Fabricated proposed parasitic hat antenna (a) front side (b) backside (c) return loss  $S_{11}$  observed in VNA (d) the antenna in the Anechoic Chamber.

the fabricated antenna frontside, backside, return loss  $S_{11}$  observed in VNA, and the antenna in the Anechoic Chamber. Fig. 5 shows the simulated and measured return loss  $S_{11}$  of the proposed multiband antenna. The simulated result shows a bandwidth from (3.8 to 16.4) GHz, whereas the obtained measured bandwidth is from (3.6 to 17.4) GHz.

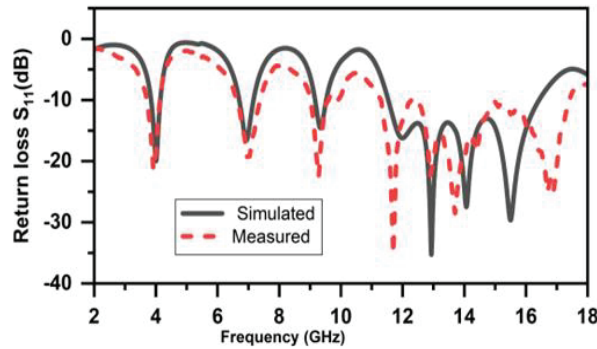


Fig. 5. The simulated and measured return loss  $S_{11}$  of the proposed parasitic hat antenna.

For verifying the full rectangular radiating patch antenna of dimension  $(30 \times 11) \text{ mm}^2$  with five rectangular slots as DGS is fabricated and shown in Fig. 6. The return loss results (measured and simulated) for the fabricated rectangular patch antenna are illustrated in Fig. 7.

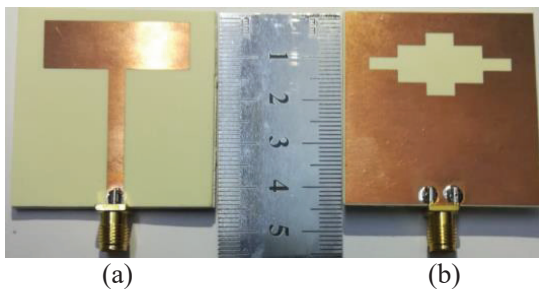


Fig. 6. Fabricated full rectangular patch antenna with DGS (a) top view (b) bottom view.

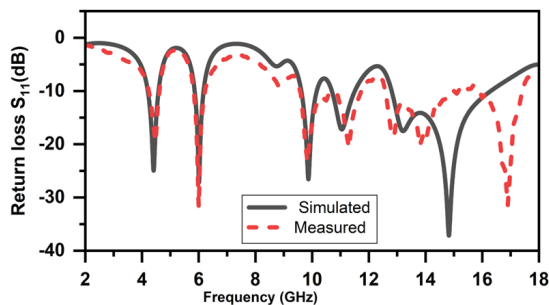


Fig. 7. The simulated and measured return loss  $S_{11}$  of the rectangular patch antenna with DGS.

## B. Parametric study for the effect of parasitic spacing

In this section, a parametric study for five different values for the spacing ( $s$ ) between the patch and the parasitic hat element is shown. Fig. 8 displays the simulated return loss  $S_{11}$  for different values for the spacing ( $s$ ) between the patch and the parasitic hat element.

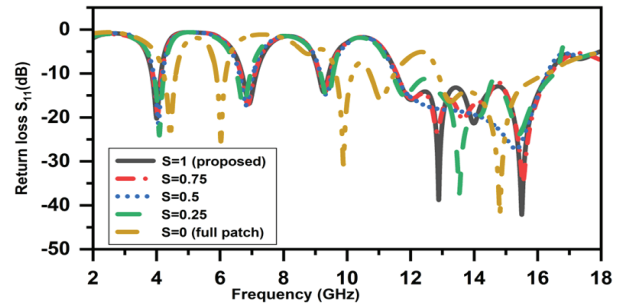


Fig. 8. The return loss  $S_{11}$  for five different values for spacing ( $s$ ) between the patch and the parasitic hat.

All five different values of the spacing ( $s$ ) with the resonating frequencies and their return losses are given in Table 3.

Table 3: Five different values of the spacing ( $s$ ) with their resonating frequencies, and return losses

Spacing ( $s$ )(mm)	Resonating frequency (GHz)	Return loss $S_{11}$ (dB)
1 (Proposed)	4, 6.94, 9.39, 12, 12.93, 14, 15.5	-21, -17, -15, -16, -40, -22, -43
0.75	4, 6.8, 9.2, 12, 12.8, 13.6, 15.5	-19, -17, -14, -15, -23, -20, -34
0.5	4, 6.8, 9.3, 15.3	-24, -18, -16, -15, -37, -23
0.25	4, 6.7, 9.3, 11.8, 13.5, 15.4	-24, -18, -16, -15, -37, -23
0 (Full patch)	4.4, 6, 9.8, 11, 13.2, 14.8	-25, -26, -31, -16, -16, -42

Table 3 shows that the proposed parasitic hat antenna ( $s = 1$ ) is the best result.

## C. Surface current distribution ( $J_{surf}$ )

The current density distribution across the proposed antenna lattice at multiple resonant frequencies is shown in Fig. 9 (a)-(g).

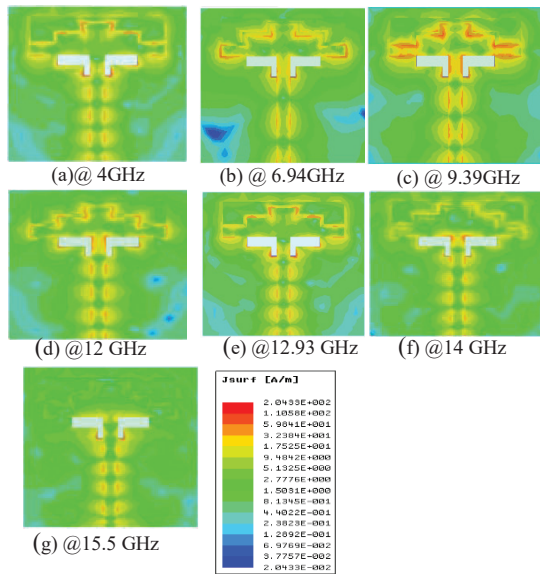


Fig. 9. Simulated surface current density distribution of the proposed antenna at (a) 4GHz, (b) 6.94 GHz, (c) 9.39 GHz, (d)12 GHz, (e) 12.93 GHz, (f) 14 GHz, and (g) 15.5 GHz.

**D. Antenna radiation patterns, gain, and efficiency**

The radiation patterns of the proposed omnidirectional antenna at different bands in E-plane (Y-Z plane) and H-plane (X-Z plane) areas at different resonance frequencies are simulated, measured, and illustrated in Fig. 10.

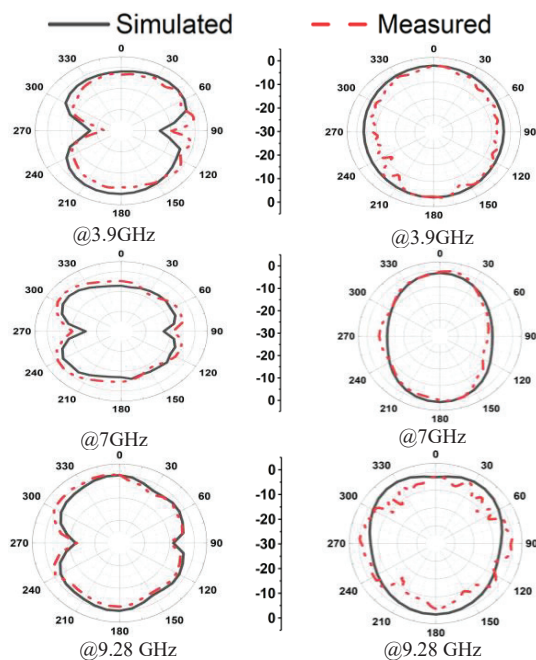
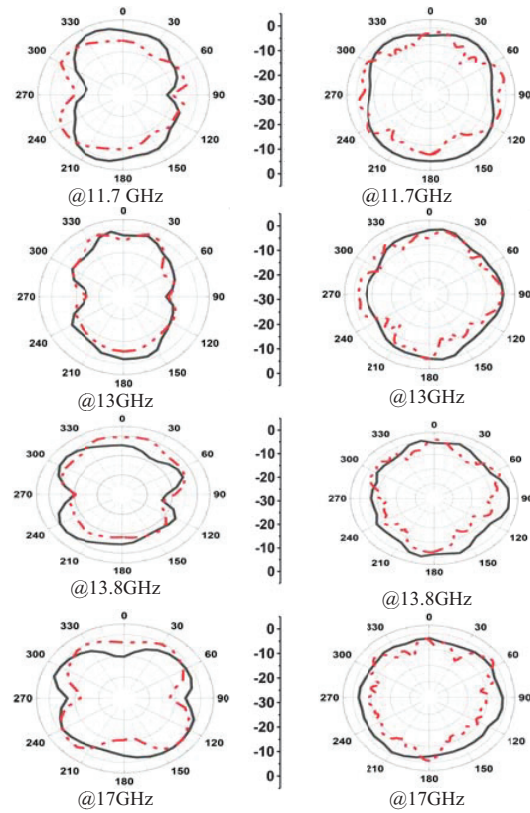


Fig. 10. Continued.



(a) E-plane at 3.9, 7, 9.28, 11.7, 13, 13.8, and 17 GHz. (b) H-plane antenna at 3.9, 7, 9.28, 11.7, 13, 13.8, and 17 GHz.

Fig. 10. Simulated and measured radiation pattern (E-plane and H-plane) of the proposed antenna at (3.9, 7, 9.28, 11.7, 13, 13.8, and 17) GHz.

Figures 11 (a), and (b) illustrate the simulated and measured maximum gain and radiation efficiency versus frequency (freq.) for the proposed multiband antenna, respectively.

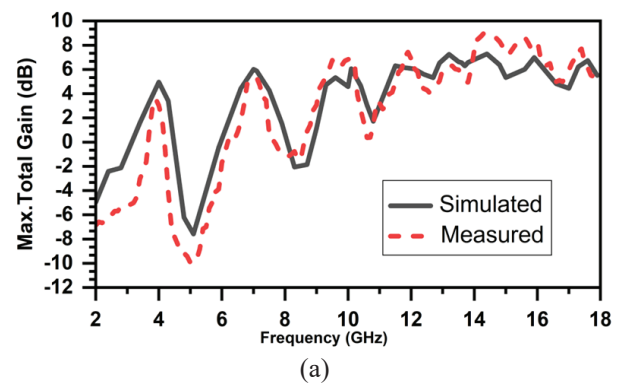


Fig. 11. Continued.

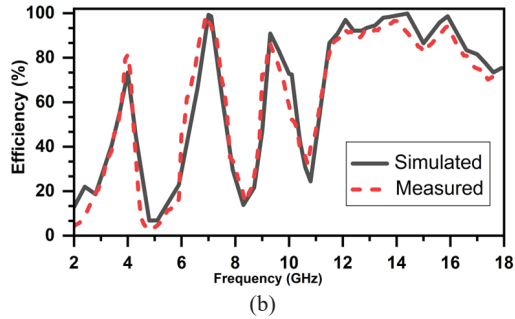


Fig. 11. (a) Simulated and measured maximum gain vs frequency, and (b) Simulated and measured radiation efficiency vs frequency for the proposed antenna.

All simulated and measured values of maximum gain and efficiency of the proposed antenna are shown in Table 4.

Table 4: The simulated and measured maximum gain, and efficiency of the proposed parasitic hat antenna

Resonant freq. (GHz)		Maximum Gain (dB)		Efficiency (%)	
Sim.	Meas.	Sim.	Meas.	Sim.	Meas.
4	3.9	4.9	3.6	73.32	79.29
6.49	7	6	5.5	95.2	86.11
9.39	9.28	4.7	5.4	89.88	87.48
12	11.7	6	6	94.94	91.75
12.39	13	6.53	6	93.61	93.61
14	13.8	6.57	4.9	98.97	95.43
15.5	17	6	5.9	94.28	75.11

A comparison of the obtained results of the proposed antenna with recently published work is given in Table 5.

Table 5: Comparison of the proposed parasitic hat antenna with recently published work

Ref. No.	Antenna size (mm <sup>3</sup> ), Material	Resonance freq. (GHz)	Techniques
[21]	45×45×1.6, FR4 epoxy	5,6,8,7,5,8,5	Parasitic element
[22]	20×30×1.6, FR4 epoxy	2.26,3.6,5.3	DGS, monopole
[23]	27.5×20×1.5, FR4 epoxy	2.44,3.55,5.6	DMS, monopole
[24]	58×48×0.8, FR4 epoxy	2.2,2.3,2.5	DGS, Parasitic
This work	45×40×1.52, RO4350	4, 6.94, 9.39, 12, 12.93, 14, 15.5	DGS, DMS, Parasitic element

## IV. CONCLUSION

In this article, a novel design of a microstrip patch antenna with a parasitic hat has been proposed for multi-band applications such as sub-7GHz 5G applications, ultra-wideband (UWB) applications, maritime radio-navigation positioning systems, and radio-navigation satellite standards. The presented antenna has multiple bandwidths starting from 3.8 to 16.4 GHz with less than  $-10$  dB return loss ( $S_{11}$ ) within the region. Three methods of enhancing the performance of the rectangular microstrip patch antenna were employed. The measured operating frequencies are (3.9, 7, 9.28, 11.7, 13, 13.8, and 17) GHz with return losses ( $-21.4$ ,  $-19.2$ ,  $-22.5$ ,  $-35.2$ ,  $-25.2$ ,  $-29.1$ , and  $-26.8$ ) dB, respectively. In conclusion, the antenna achieves stable radiation patterns, higher radiation on efficiency, and broad bandwidth around the operating frequencies 0.29 GHz with (7.48%) at 4 GHz, 0.462 GHz with (6.66 %) at 6.94 GHz, 0.3571 GHz with (3.823 %) at 9.39 GHz, 0.96 GHz with (7.99 %) at 12 GHz, 0.97GHz with (7.4 %) at 12.93GHz, 1.28GHz with (9.07 %) at 14 GHz, and 1.66 GHz with (10.66 %) at 15.5 GHz. The simulated results show that the DGS, DMS, and parasitic elements are critical factors for improving the bandwidth of the proposed antenna.

## REFERENCES

- [1] A. J. Khalilabadi and A. Zadehghol, "Multi-band antenna for wireless applications including GSM/UMTS/LTE and 5G bands," *Applied Computational Electromagnetic Society (ACES) Journal*, vol. 34, no. 2, pp. 270-271, Feb. 2019.
- [2] A. Ahmad, F. Arshad, S. I. Naqvi, Y. Amin, and H. Tenhunen, "Design, fabrication, and measurements of extended I-shaped multiband antenna for wireless applications," *Applied Computational Electromagnetic Society (ACES) Journal*, vol. 33, no. 4, pp. 388-393, Apr. 2018.
- [3] Md. Sh. Alam, N. Misran, B. Yatim, and M. T. Islam, "Development of electromagnetic band gap structures in the perspective of microstrip antenna design," *International Journal of Antennas and Propagation*, 2013.
- [4] K. Hossain, T. Sabapathy, M. Jusoh, P. J. Soh, R. B. Ahmad, M. I. Jais, and Q. H. Abbasi, "A frequency-reconfigurable microstrip antenna with constant dipole-like radiation patterns using single bias, triple varactor tuning with reduced complexity," *Wireless Personal Communications*, pp. 1-22, 2021.
- [5] M. A. Gaber, F. F. Ismail, A. Yahia, M. A. El-Aasser, and N. H. Gad, "A printed antenna design with defected ground structure for multiband

- applications,” *European Journal of Science and Technology*, no. 28, pp. 1528-1533, Nov. 2021.
- [6] F. F. Ismail, M. A. Gaber, M. A. El-Aasser, and N. H. Gad, “Design of a mirror dtairs multiband microstrip antenna using defected structures,” *In 38th National Radio Science Conference (NRSC)*, vol. 1, pp. 47-55. IEEE, 2021.
- [7] M. El-Sayed, A. Yossry, A. Yahia, M. A. El-Easser, and N. H. Gad, “Printed monopole antenna design with parasitic element for multi-band applications,” *In 2021 International Conference on Electronic Engineering (ICEEM)*, pp. 1-4. IEEE, 2021.
- [8] Y. Deng, X. F. Li, and J. S. Hong, “A compact tri-band miniaturized antenna with parasitic elements loading,” *Applied Computational Electromagnetic Society (ACES) Journal*, vol. 35, no. 7, pp. 829-836, Jul. 2020.
- [9] O. Amjad, S. W. Munir, S. T. Imeci, and A. O. Ercan, “Design and implementation of dual band microstrip patch antenna for WLAN energy harvesting system,” *Applied Computational Electromagnetic Society (ACES) Journal*, vol. 33, no. 7, pp. 746-751, Jul. 2018.
- [10] A. E. Farahat and K. F. A. Hussein, “Dual-band (28/38 GHz) MIMO antenna system for 5G mobile communications with efficient DoA estimation algorithm in noisy channels,” *Applied Computational Electromagnetics Society (ACES) Journal*, vol. 36, no. 3, Mar. 2021.
- [11] K. Fertas, H. Kimouche, M. Challal, H. Aksas, R. Aksas, and A. Azrar “ Design and optimization of a CPW-Fed tri-band patch antenna using genetic algorithms,” *Applied Computational Electromagnetic Society (ACES) Journal*, vol. 30, no. 7, Jul. 2015.
- [12] M. H. B. Ucar and Y. E. Erdemli, “Triple-band microstrip line-fed printed wide-slot antenna for WiMAX/WLAN operations,” *Applied Computational Electromagnetic Society (ACES) Journal*, vol. 29, no. 10, pp. 793-800, Oct. 2014.
- [13] E. W. Coetsee, J. W. Odendaal, and J. Joubert, “A quad-band antenna with AMC reflector for WLAN and WiMAX applications,” *Applied Computational Electromagnetic Society (ACES) Journal*, vol. 33, no. 10, pp. 1123-1128, Oct. 2018.
- [14] C. H. Chang and K. L. Wong, “Printed  $\lambda/8$ -PIFA for penta-band WWAN operation in the mobile phone,” *IEEE Trans. Antennas Propag.*, vol. 57, no. 5, pp. 1373-1381, May 2009.
- [15] A. A. Eldek, A. Z. Elsherbeni, C. E. Smith, and K. Lee, “Wideband planar slot antennas,” *Applied Computational Electromagnetic Society (ACES) Journal*, vol. 9, no. 1, 2004.
- [16] R. Patel, A. Desai, and T. K. Upadhyaya, “An electrically small antenna using defected ground structure for RFID, GPS and IEEE 802.11 a/b/g/s applications,” *Progress In Electromagnetics Research Letters*, vol. 75, pp. 75-81, 2018.
- [17] N. H. Gad and M. Vidmar, “Design of a microstrip fed printed-slot antenna using defected ground structures for multiband applications,” *Applied Computational Electromagnetic Society (ACES) Journal*, vol. 33, no. 8, pp. 854-860, Aug. 2018.
- [18] ANSYS® Electromagnetics Student, ver. 2.2.1. Online: Ansys | Engineering Simulation Software.
- [19] C. A. Balanis, *Antenna Theory: Analysis and Design*. John Wiley & Sons, 2016.
- [20] R. Garg, P. Bhartia, I. Bahl, and A. Ittipiboon, *Microstrip Antenna Design Handbook*, Artech House, Norwood, MA, 2001.
- [21] V. Sharma, N. Lakwar, N. Kumar, and T. Garg, “Multiband low-cost fractal antenna based on parasitic split ring resonators.” *IET Microwaves, Antennas & Propagation*, vol. 12, no. 6, pp. 913-919, 2018.
- [22] Wen-Ch. Liu, Chao-M. Wu, and Y. Dai, “Design of triple-frequency microstrip-fed monopole antenna using defected ground structure,” *IEEE Transactions on Antennas and Propagation*, vol. 59, no. 7, pp. 2457-2463, 2011.
- [23] M. Karthikeyan, R. Sitharthan, T. Ali, S. Pathan, J. Anguera, and D. Sh. Sundar, “Stacked T-shaped strips compact antenna for WLAN and WiMAX applications,” *Wireless Personal Communications*, pp. 1-14, 2021.
- [24] M. Sahal, V. Tiwari, and D. Bhatnagar. “Wideband CPW fed circularly polarized antenna using planar transmission line DGS,” *In 2020 7th International Conference on Signal Processing and Integrated Networks (SPIN)*, pp. 1100-1104. IEEE, 2020.



applications.

**Faten Fouad** received her B.Sc. degree in Electronics physics from Faculty of Science Ain Shams University, Cairo, Egypt in 2006 where she is currently pursuing the M.Sc. degree. Her current research interests include microstrip antenna designing for multiband



**Mostafa A. El-Aasser** received his B.Sc. (Honors) and M.Sc. in physics from Ain Shams University, Cairo, Egypt, in 1989 and 1995, respectively. He received his Ph.D. in 2002. Currently, he is a professor of physics at Ain Shams University, Cairo. His current research interests

include optoelectronics, electromagnetics, concentrated solar power systems, and photovoltaics.



**Nasr Gad** received his B.Sc. (Honors) and M.Sc. degrees in Electronics (Physics) from Faculty of Science, Ain Shams University, Cairo, Egypt, in 2005 and 2012 respectively. He received his Ph.D. degree in Electrical Engineering from the University of Ljubljana, Ljubljana, Slovenia in 2018. From 2018 till now, he is a lecturer of physics at Ain Shams University, Cairo. His current research interests include planar printed antenna design for multiband/wideband applications, microwave circuits, and solar energy.

# Solar Cell Integrated Wearable Patch Antenna on Artificial Magnetic Conductor for On-Body and In-Body Communications

Suresh Babu T. Naganathan<sup>1</sup> and Sivakumar Dhandapani<sup>2</sup>

<sup>1</sup>Department of Electronics and Communication Engineering  
Adhiparasakthi Engineering College, Melmaruvathur 603319, India  
sureshbabutns@gmail.com

<sup>2</sup>Department of Electronics and Communication Engineering  
Easwari Engineering College, Chennai 600089, India  
dgsivakumar@gmail.com

**Abstract** – This paper presents a patch antenna on a jeans textile with an artificial magnetic conductor (AMC) structure stacked on a solar cell for wearable applications in the Industrial, Scientific, and Medical (ISM) band. Meanwhile, the loading of the AMC reflector increases the radiation efficiency and antenna gain and also results in a reduction in specific absorption rate levels. As examination cases, two textile antenna designs loaded on  $7 \times 8$  patches of AMC plane with the ground plane of both fully copper conductor and partially copper aided with solar cells were fabricated and tested, presenting a strong agreement between simulation and measurement. Its measured impedance bandwidth is 13.79% (2.16 GHz–2.48 GHz) with good return loss and voltage standing wave ratio features in the operating band where it is being used. Besides being a source of electricity, the silicon solar cells are also used as a radio frequency ground plane for the AMC plane. They can produce 363.08 mW.

**Index Terms** – Artificial magnetic conductor (AMC), integrated antennas, patch antennas, solar cells, wearable antennas, wireless body area networks (WBAN).

## I. INTRODUCTION

The evolution of technology is important only when it is harmonized with our mother nature. So, while developing any technology, the environment should be the utmost priority. Wireless communication is the most emergent, prolific, and accepted area of the communication field. So far, research efforts focus on spectrum efficiency, transmission reliability, data rate, and services provided to users [1–3]. However, most of the recent research efforts have disregarded the implications of wireless networks' environmental responsibility, e.g., energy efficiency and environmental impact [4, 5]. Green energy may even require its surroundings to help gener-

ate power, making it mostly unpredictable. This is where smart technology and the internet of things (IoT) come into play [6–8].

Green wireless communication will provide energy-efficient communication. It will result in less radiation from devices as well as more economic solutions for service providers, and they will also strive to reduce their carbon footprint [9–11]. The integration of the solar cell with an antenna, called “green antennas,” can be used for advanced wireless technologies for energy-efficient green communication. As for renewable energy, solar cells are becoming an important source by virtue of their cleanliness and safety. Indeed, silicon solar cells can be utilized as both a radiating patch [12–15] and an antenna ground plane [16–21] due to its conducting properties.

The GaAs solar cell patches [12] were utilized to demonstrate the antenna structure, instead of copper patches. The authors demonstrated that the patch antenna is stacked with a solar cell [13–15] for wireless local area network (WLAN), worldwide interoperability for microwave access (Wi-Max) and wireless fidelity (Wi-Fi) applications, where the solar cell performs as an RF patch section notwithstanding its direct current (DC) generation. The variation of the reflection coefficient of the multiband patch antenna loaded in slots with and without solar cell stacking was addressed [13]. The influence of solar cell operation on RF antenna performance was investigated by combining a DC/RF isolation circuit [14]. The investigation into the performance of solar cell ground plane [16] for antenna design on FR4 substrate was discussed. Also presented were silicon solar cells used as microwave ground planes with patch antennas on the FR4 substrate for WLAN applications [17], thin film glass substrate for wireless communications [18], airborne communication nodes [19], Plexiglas substrate for remote area applications [20], and the FR4 substrate for future mobile communications [21]. Changes in solar

cell DC power production with and without antennas were also examined [20, 21].

Recently, advancements in technology in solar cell research have allowed their size to be reduced to such an extent that they can be easily sewn onto items of clothing without appearing presently bulky [22, 23]. Solar clothing uses photovoltaic cells in order to harness the sun's energy and use it to power electronic gadgets. Initially, copper and, after that, fabric-conducting materials are used as the conducting parts of the wearable antennas. For fabricating the wearable antennas, different types of non-conducting fabric dielectric materials are used. For high performance radio LAN (HIPER-LAN) applications, the radiation performance of copper-based and Zelt-based conductive fabric-based wearable patch antennas [24] aided by polyester fabric substrate was investigated. Under bending and crumpling conditions, the copper foil koch fractal wearable dipole antenna in the very high frequency (VHF) band (430 MHz–475 MHz) for military applications [25] and the ring resonator wearable patch antenna [27] at 5.8 GHz aided with a common jeans cotton substrate were investigated. A parametric study was demonstrated on the rectangular textile patch antenna [26], which was made from both copper and nickel-plated polyester fabric with a denim substrate for ISM band wireless body-area network applications. Wearable patch antennas with different electro-textile materials were fabricated, and their radiation performance was discussed [28, 30]. The performance of a new embroidered wearable antenna on a Felt substrate [29] was demonstrated and tested. A brief study on wearable antennas for dual-band operation [31–33], dual-mode single band operation [34] and ultra-wideband (UWB) operation [35] was also reported.

The electromagnetic band-gap (EBG) structure has captivated researchers due to its desirable unique band-gap features, which have been discovered to be used in suppressing surface waves and improving performance in wearable antenna designs [36, 37], such as bandwidth, gain, compactness, and so on, for wireless body area network applications. Furthermore, metasurfaces have inspired a wide range of applications in wearable antennas, where they are used not only to improve the properties of antennas, such as bandwidth and gain, but also to ensure the antenna will work at an appropriate frequency. Metasurface-based wearable antennas are presented and discussed for their performance in the dual-band [38, 39] operation, the ISM band [40], UWB [41], and also X-band [42] applications. The use of metamaterials for SAR reduction [43] is being investigated in the context of designing communication equipment for safety compliance.

An AMC is a metamaterial that imitates the attributes of a permanent magnetic conductor (PMC).

AMC can be useful in wireless body area networks (WBAN) because it allows for better transmission and less backward radiation [44, 45]. Additionally, the operating frequency range of the antenna is closely related to the bandwidth of the AMC. The dual-band wearable antenna loaded with AMC was presented for WLAN applications [46]. The ability of the AMC to reduce SAR for wearable antenna design [47–53] was discussed. The textile patch antenna associated with the solar cell has not been discussed in detail to date.

In this article, an AMC loaded textile patch antenna with and without integrated solar cells is demonstrated and its radiation performance is studied. This paper is organized as follows: Section II describes the proposed antenna design and its fabrication. Section III describes high-frequency structure simulator (HFSS) antenna simulation analysis compared with measurement results and also the solar cell parametric measurement with and without the antenna. Finally, Section IV shows the conclusion.

## II. ANTENNA DESIGN AND FABRICATION

The proposed textile antenna layout consists of two modules, and it is shown in Figure 1. One of them is the patch antenna module, and the other is the AMC reflector module.

In the upper module, there are three layers that are of focus: the patch, substrate, and ground plane. Similarly, in the lower module, there are three layers: the AMC reflector plane, substrate, and ground plane. In both modules, the conducting parts (patch, AMC plane, and ground plane) are made of copper foil with a thickness of 0.025 mm, whereas the substrate part is Jeans fabric with a relative permittivity ( $\epsilon_r$ ) of 1.67, a loss tangent ( $\delta$ ) of 0.02, and a thickness ( $h$ ) of 2 mm. The jeans fabric and copper foil have been cut manually. In this study, two designs of antenna models are demonstrated. The first model is an incorporated patch antenna (top module) with a fully copper-grounded AMC module (bottom module), and the second one is the same incorporation with a partially copper-grounded AMC module, aided with solar cells.

The top patch antenna module of the proposed model is designed by using a transmission line model and its geometry is shown in Figure 2(a). The patch antenna consists of a top copper patch with a size of 46 mm  $\times$  51 mm and a bottom copper ground with a size of 96 mm  $\times$  101 mm, which is glued using fabric glue onto a Jeans substrate with a size of 96 mm  $\times$  101 mm. The feed point is carefully chosen through HFSS V.15 of ANSYS for good impedance matching. As shown in Figure 2(b), the bottom AMC module is made up of a 7  $\times$  8 array of copper foil square unit patches, and each AMC unit cell measures 10 mm  $\times$  10 mm and is glued on the same size

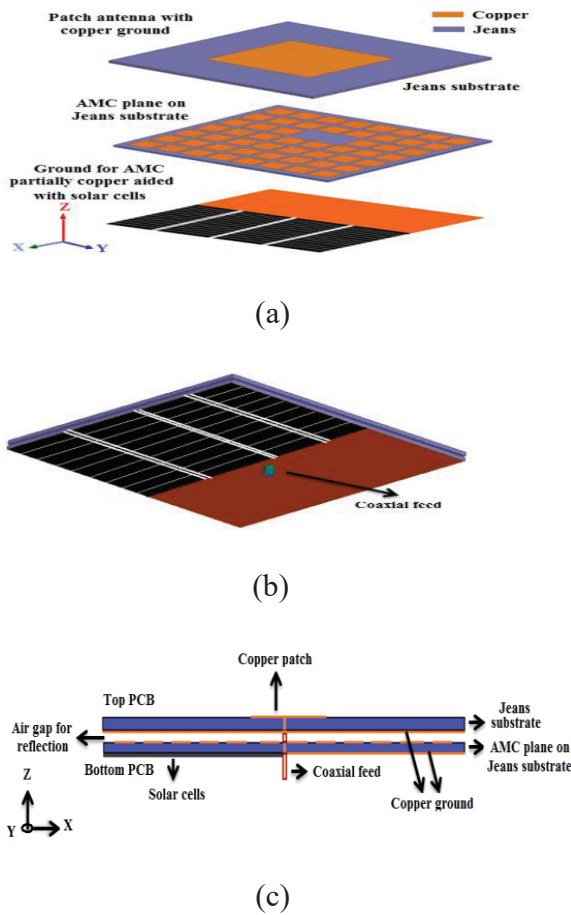


Fig. 1. Antenna layout: (a) 3D layout of the proposed patch antenna on the AMC plane with partially aided solar cells; (b) proposed antenna coaxial feed view; (c) proposed antenna side view.

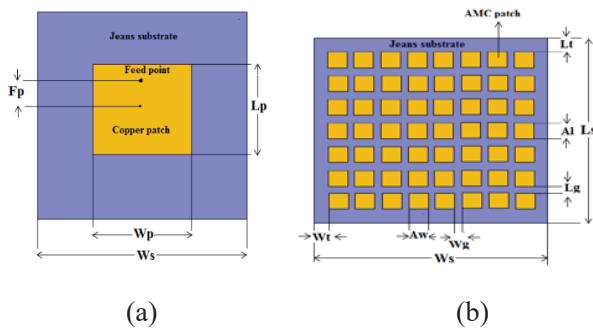


Fig. 2. Geometry of the proposed antenna: (a) patch antenna (top module); (b) AMC plane (bottom module).

as the top module of the Jeans substrate. Their optimized dimensions are summarized in Table 1.

The AMC unit cells are arranged periodically in equal spaces and cover the entire area of the substrate.

Table 1: Optimized dimensions of the proposed antenna

Parameters	Value (mm)	Parameters	Value (mm)
$L_p$	46	$L_t$	4
$W_p$	51	$W_t$	3.5
$L_s$	96	$A_l$	10
$W_s$	101	$A_w$	10
$F_p$	16	$L_g$	3
-	-	$W_g$	2

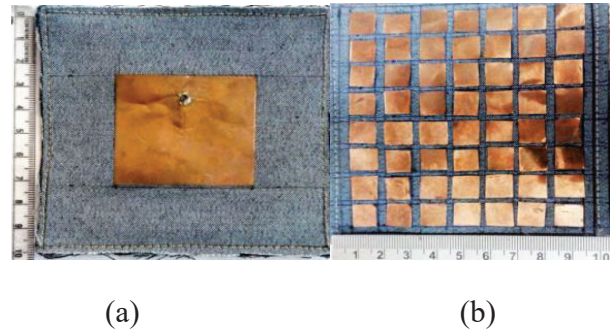


Fig. 3. Fabrication of the proposed antenna modules: (a) patch antenna; (b) AMC plane.

The fabricated modules are shown in Figure 3(a) and (b). The ground plane of the AMC module for the two proposed cases: the first one is glued with copper foil, and the second one is partially copper foil soldered with the solar cells under investigation.

In the first case, the fabricated AMC reflector plane with a copper ground plane is situated underneath the patch antenna, keeping an air gap of 1 mm between the assemblies. This is shown in Figure 4. The inner conductor of the coaxial RF connector is associated with the feed point of the upper patch module, which provides a good impedance match [54]. Therefore, the outer conductor is associated with the ground of the patch and the AMC reflector.

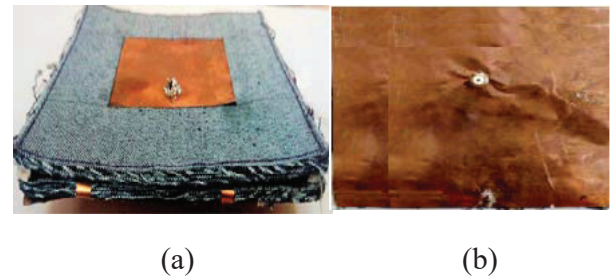


Fig. 4. Patch antenna integrated on the AMC plane with copper ground plane: (a) front side view; (b) back side view.

For the subsequent case, the second module is fabricated as in the first case; except the ground plane is modified by the half-done copper ground plane soldered with the negative terminal of the two series connected 4 V, 100 mA solar cells with dimensions of 60 mm  $\times$  60 mm  $\times$  1.5 mm. The front side and back side views of the fabricated subsequent modules are shown in Figure 5.

This section covers a key strategy for determining the dielectric constant of jeans, chosen for antenna fabrication under microwave frequencies. The exploratory arrangement of the microwave test bench and the dielectric constant measurement setup of jeans under test are indicated schematically in Figure 6. A standing wave pattern will be produced by turning on the klystron power supply and the klystron tube. The general procedure for the measurement of guide wave length ( $\lambda_g$ ) and frequency ( $f$ ) of the signal is reported [55].

The probe shall be kept at a minima position, and the reading on the bench shall be taken. The jeans under test will be put in the wave guide in contact with the short circuit plate and the position of the new displaced minima will be recorded. The difference between the two positions of the minima shall be the shift ( $\Delta$ ) caused by the inclusion of the jean dielectric. The dielectric constant will be determined utilizing the formulae detailed in [55, 56], and the measured value of the dielectric constant of the jeans under test is 1.67.

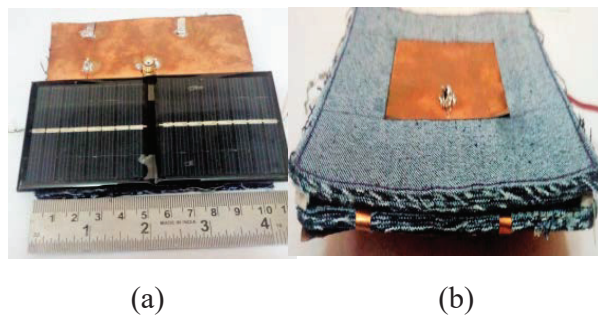


Fig. 5. Patch antenna integrated on the AMC plane aided with solar cell ground plane: (a) front side view; (b) back side view.

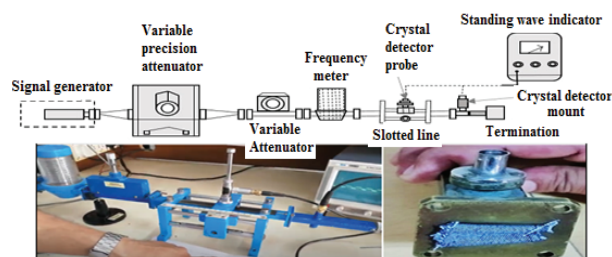


Fig. 6. Experimental setup of a microwave bench and dielectric constant measurement.

### III. SIMULATION AND MEASUREMENT RESULTS

The simulation process is carried out step-by-step using HFSS V.15. To compute the electrical behavior of complex components with arbitrary shapes and user-defined material properties, HFSS V.15 employs a 3D full-wave Finite Element Method (FEM) field solver. Initially, the top patch antenna module is simulated, and the result indicates that the return loss ( $S_{11}$ ) of better than -10 dB is attainable over the 2.38 GHz–2.48 GHz band with a center frequency of 2.42 GHz and an impedance bandwidth of 4.13%. The realized peak gain of the proposed patch antenna under simulation is 4.51 dBi.

Furthermore, a standardized model for a capacitive partially reflective surface screen and its equivalent circuit representation are employed here to facilitate the analysis of AMC. The geometry of the AMC unit cell and its equivalent circuit representation [57] are shown in Figure 7, where the conducting element is represented by the inductor and the inter-element capacitance by the capacitor. Subsequently, the reflection phase characteristic of the AMC unit cell against frequency with suitable boundary conditions [57, 58] was simulated. A single cell of the structure was studied using periodic boundary conditions on its sides to simulate an infinite structure [44]. The simulation setup and the resultant reflection phase characteristic of the AMC unit cell against frequency are shown in Figure 8(a) and (b). Meanwhile, the operating bandwidth of the proposed AMC unit is defined in the frequency range of 2.15 GHz to 2.55 GHz between  $\pm 90^\circ$ . After that, the proposed antenna on the AMC model is carried out, which is shown in Figure 8(c). The simulated result indicates that the  $S_{11}$  of better than -10 dB is attainable at the 2.38–2.46 GHz band.

Wearable antennas are explicitly designed to be worn close to the physical body, and the SAR is used to address the dangers posed to the human body by wearable specialized gadgets [47]. SAR is a critical boundary for determining the amount of electromagnetic field consumed by human tissues [48].

Figure 9 simulates the basic model of human tissues [53] with their electrical properties, relative permittivity

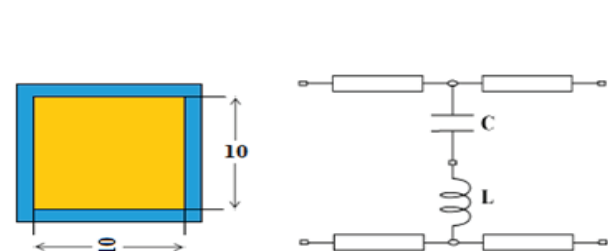


Fig. 7. Geometry of an AMC unit cell with its typical equivalent circuit.

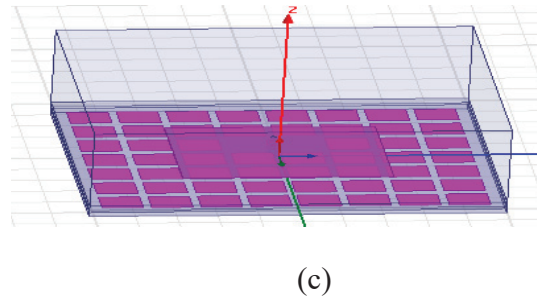
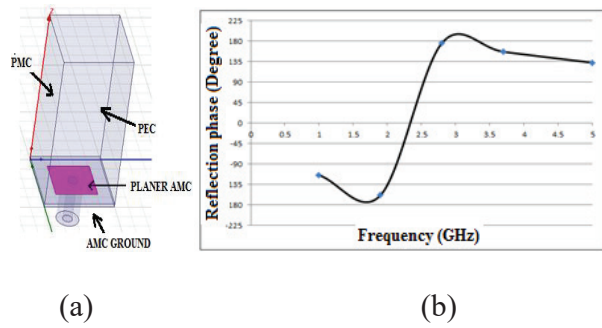


Fig. 8. AMC unit cell. (a) Simulation setup in HFSS. (b) Reflection phase characteristic. (c) Overall view of the proposed antenna on AMC in HFSS.

( $\epsilon_r$ ), conductivity ( $\sigma$ ), mass density ( $\rho$ ) and thickness ( $d$ ), consisting of skin ( $\epsilon_r = 38.0067$ ,  $\sigma = 1.184$ ,  $\rho = 1001$  kg/m<sup>3</sup>,  $d = 1$  mm), fat ( $\epsilon_r = 10.8205$ ,  $\sigma = 0.58521$ ,  $\rho = 900$  kg/m<sup>3</sup>,  $d = 2$  mm), and muscle ( $\epsilon_r = 55$ ,  $\sigma = 1.437$ ,  $\rho = 1006$  kg/m<sup>3</sup>,  $d = 10$  mm) with a size of 130 mm × 120 mm × 13 mm and SAR distributions at 2.4 GHz with an input power of 0.1 W. The antenna is positioned at a height of 2 mm from the tissue surface. From the simulated SAR distributions, the peak 1 g SAR value for patch alone is 4.08 W/kg. Then again, the peak 1 g SAR value for patches on AMC is 1.272 W/kg ( $3.4576e^{-1}$ ). From the outcome, it tends to be seen that the most extreme SAR regard diminishes essentially with the presentation of the AMC plane and, furthermore, the SAR constraint is fulfilled with a value that is well-below the acceptable limit. Both the patch and the substrate have been cut and stuck manually. Moreover, feeding cable losses were not considered in the simulation.

In this study, surveys for both free space and on-body surroundings are considered. The performance of the man-made proposed antenna placed on the flat surface of the physical body should be studied to demonstrate whether it meets the sensible application necessities or not. Each layer of the physical body has its own dielectric characteristics that additionally rely on the frequency. The proposed antennas are meant to be worn around the torso area; hence they are positioned on the abdomen. The proposed antenna was

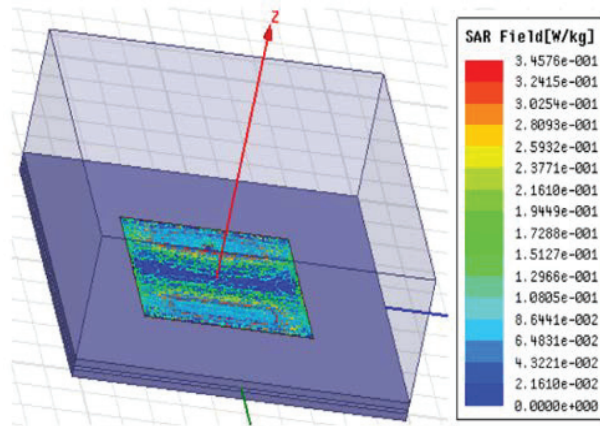


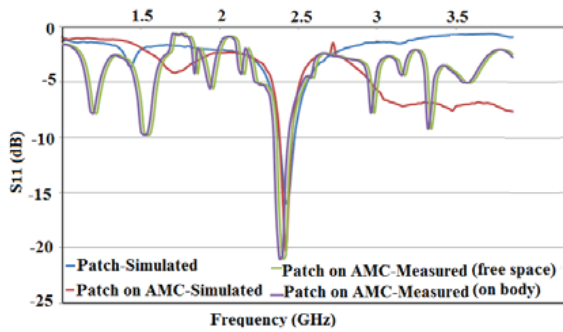
Fig. 9. SAR distributions of the proposed antenna on AMC in HFSS.



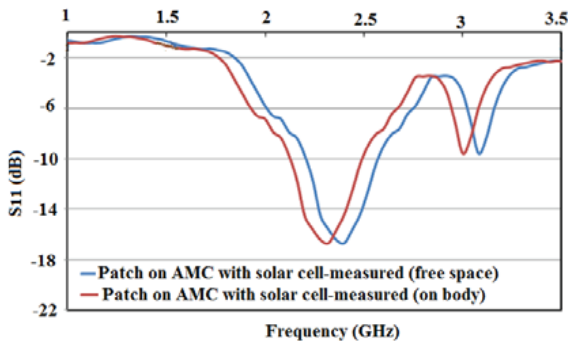
Fig. 10. Proposed wearable antenna measurement setup.

tested through an Agilent-N5230A vector network analyzer associated with the standard calibration, and the S-parameter measurement arrangement is displayed in Figure 10.

The simulated and measured values of the  $S_{11}$  and VSWR concerning the frequency are shown in Figures 11 and 12 in free space and in the body environment. The simulated  $S_{11}$  and VSWR of the patch antenna on the AMC plane with the copper ground at 2.42 GHz are  $-20.26$  dB and 1.23 with an impedance bandwidth of 3.3% from 2.38–2.46 GHz. By considering the free space environment, the measured  $S_{11}$  and VSWR of the patch



(a)



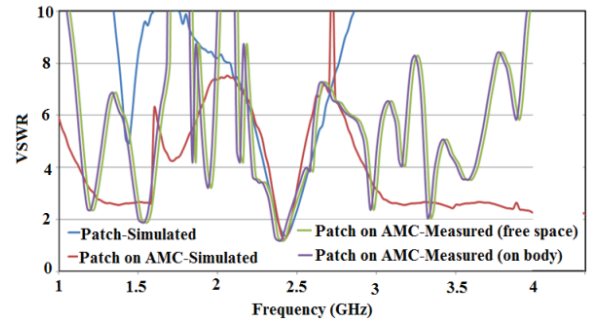
(b)

Fig. 11.  $S_{11}$  versus frequency: (a) free space environment; (b) on-body environment.

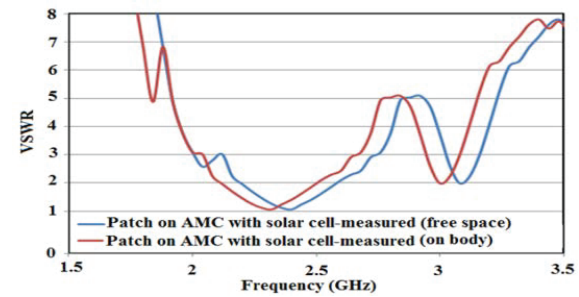
antenna on the AMC plane with the copper ground at 2.4 GHz are  $-21$  dB and 1.19 with an impedance bandwidth of 4.16% from 2.36–2.46 GHz. On the other hand, the measured  $S_{11}$  and VSWR of the same patch antenna on the AMC plane with partially copper-aided solar cells ground plane at 2.4 GHz is  $-16.695$  dB and 1.06 with an impedance bandwidth of 13.33% from 2.24–2.56 GHz.

For on-body consideration, the proposed patch antenna on the AMC plane with the copper ground plane resonates over the 2.34–2.44 GHz band (impedance bandwidth of 4.2%) and also the same patch antenna on the AMC plane with a partially copper-aided solar cell ground plane resonates over the 2.16–2.48 GHz band (impedance bandwidth of 13.79%) with VSWR less than 2. Figures 11 and 12 show that  $S_{11}$  of the antenna encompasses a slight deviation, whereas the general performance of the antenna is largely the same as with the original antenna. It is often seen that the designed wearable antenna suffers less from the electrical characteristics of human tissues, and its performance is comparatively stable.

The proposed antenna gain was measured over an anechoic chamber measurement setup and is shown in



(a)



(b)

Fig. 12. VSWR versus frequency: (a) free space environment; (b) on-body environment.

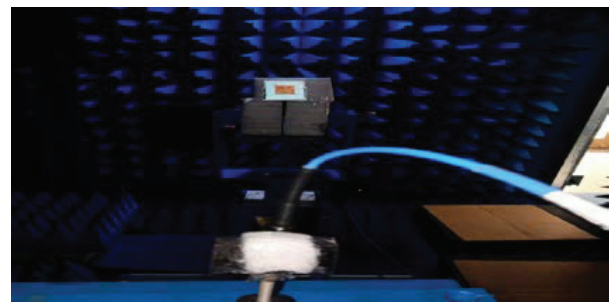


Fig. 13. Photograph of the measurement environment: the anechoic chamber with standard horn antenna and proposed antenna.

Figure 13. The radiation pattern of the simulated gains of the proposed antenna at 2.4 GHz is shown in Figure 14.

The realized peak gain of the proposed patch antenna loaded with AMC under simulation is 7.02 dBi. The simulated antenna gain was enhanced from 4.51 dBi for the patch antenna to 7.02 dBi for the patch on the AMC reflector. From an application point of view, an AMC reflector can be evaluated by comparing antenna radiation features in the presence of an AMC reflector with and without the aid of solar cell ground.

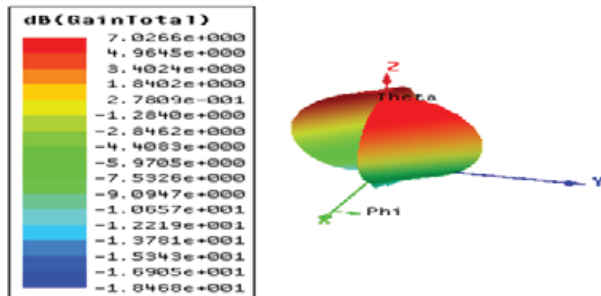
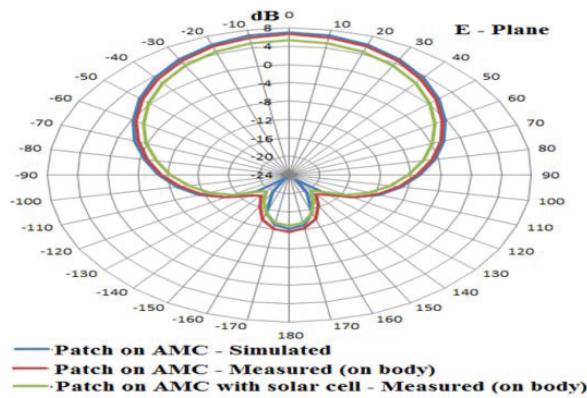
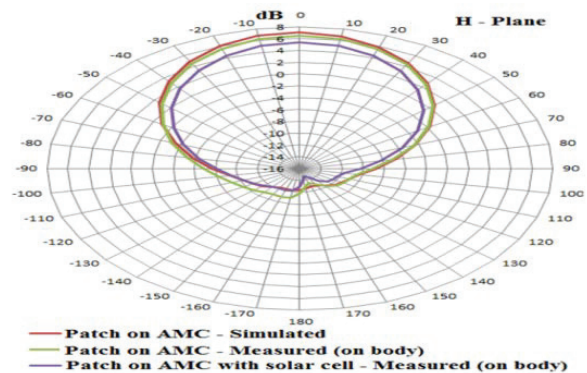


Fig. 14. Simulated 3D gain radiation pattern of the proposed antenna.



(a)



(b)

Fig. 15. 2D radiation patterns of simulated and measured gain: (a) E-plane; (b) H-plane.

The far-field E-plane (YZ-plane) and H-plane (XZ-plane) radiation patterns at 2.4 GHz are shown in Figure 15 (a) and (b) based on simulation and measurement results. In the physical body environment, the measured peak gain of the proposed antenna on the AMC plane

with copper ground and the same patch on the AMC with copper ground aided with solar cells is 6.53 dBi and 5.33 dBi, respectively.

The AMC loaded antennas have decreased side and back lobe radiation, as shown in Figure 15, and have good unidirectional radiation properties. When compared to the proposed antenna with copper ground, the proposed antenna with copper ground aided by solar cells emits the least amount of radiation in the broad-side direction and has a gain along the antenna plane that is only a few decibels below the maximum. When such an antenna is placed on the human body, the antenna's small rear lobe shows that very little energy is emitted into the tissue. Because of this property, the antenna is more robust to human body loading, making it an excellent fit for wearable applications.

On discussion of the effect of solar cells on AMC ground, the proposed antenna will not affect the radiation much and will only cause a minor deviation in gain due to the solar cells' semiconductor nature. Another limitation on the discussion about the operation of the proposed antenna in the body environment is that the solar cells are aided on the ground plane of the AMC, on the external body side, and the antenna patch on the internal body side. As a result, the maximum radiation is directed at the human body, and its radiation gain performance suffers slightly. This proposed design is useful for in-body and on-body communication. Meanwhile, the utilization of solar cells must be considered for its DC energy conversion performance when externally falling solar light hits the solar cells.

A small difference between the simulated and measured curves is examined. This is clarified by the vulnerability concerning the material substrate properties and the mechanical errors brought about by the manual manufacturing method with basic apparatuses. Note that utilizing machine dimensions or laser slicing does not lead to better outcomes because of the unavoidable irregularity of the antenna during practical operation. The most significant thing is that antenna performance, despite everything, satisfies the necessities for WLAN communication. SAR measurements and thermal impacts [48, 59] are used to examine the biological effects of the performing antenna. Due to lower permittivity at higher frequencies, there was a decline in biological effect as the resonant frequency increased. As a result, SAR is reduced, and the heat effect is also reduced. Electronic textiles, which are hybrid products that incorporate electrical functionality into textiles, must frequently resist washing operations in order to maintain textile usability. However, washability, which is critical for many electronic textile applications such as medical or sports due to cleanliness standards, is frequently insufficient. The elements that determine

Table 2: Comparison with previous works

Parameter/Ref.	Conducting parts	Substrate parts	Reflected plane/number of unit cells/size (mm <sup>2</sup> )	No. of band	Gain dBi	Band of operation (GHz)	1 g aver. SAR W/kg	Applications
[36]	Shieldex conductive metalized nylon (Zell)	Leather	EBG 8 circular periodic 100 × 100	1	0.75	5.7–5.87	1.21	ISM band for on-body communication
[37]	Copper	Poly Dimethyl siloxane	EBG 2 × 3 40 × 32	1	2.1–5.6	Center frequency 2.4	0.0536	WBAN applications
[38]	Copper	Rogers RT/Duroid 5880	Metasurface 2 × 2 –	2	4.54 4.71	3.2–3.5 3.9–4.3	0.174 0.207	WBAN communication
[40]	Copper	Rogers RO3003	Metasurface 2 × 2 62 × 40	1	6.2	2.36–2.4	0.66	Medical BAN devices
[41]	Nickel-copper-polyester	Felt	Metamaterial 7 × 7 100 × 100	1	6	4.55–13	0.067	UWB-WBAN application
[44]	ShieldIt Super	Felt	AMC 3 × 3 87 × 77	2	5.5 7.5	2.4–2.7 5.04–6.04	-	Wi-Fi on-body applications
[46]	ShieldIt Super	Felt	AMC 4 × 4 100 × 100	2	2.5 0–4	2.45 5.04–5.93	0.0464 0.0232	WLAN applications
[49]	ShieldIt	Fleece fabric	AMC 6 × 4 306 × 306	1	6.53	2.17–2.57	0.03 (for 10 g aver.)	Wearable applications
[50]	ShieldIt	Felt (antenna) Denim (AMC)	AMC 3 × 3 85 × 85	2	-	2.4–2.69 5.15–5.87	-	Wi-Fi and the 4G-LTE applications
[51]	Copper	Pellon (antenna) RO3003 (AMC)	AMC 4 × 4 124 × 124	1	4.6	2.2–2.6	0.33	ISM band applications
[52]	Zelt	Felt Jeans Cotton	AMC 2 × 3 42 × 63	2	7.14 9.9	Center frequency 2.45 & 5.8	0.34 0.27	Wi-Fi applications
[53]	Copper	Polyimide	AMC 2 × 2 66.8 × 66.8	1	7.47	2.27–2.76	0.15	Medical BAN devices
The proposed antenna	Copper	Jeans fabric	AMC 7 × 8 101 × 96	1	5.33	2.16–2.48	1.272	ISM band applications & DC energy conversion

Table 3: Evaluation results of the proposed antenna

Model	Band of operation (GHz)	Impedance bandwidth	VSWR	$S_{11}$ (dB)	Gain total (dBi)
Patch sim.	2.38–2.48	4.13%	1.38	−15.94	4.51
Patch on AMC sim.	2.38–2.46	3.3%	1.23	−20.26	7.02
Patch on AMC meas.	2.34–2.44	4.2%	1.19	−21	6.53
Patch on AMC with solar cells meas.	2.16–2.48	13.79%	1.272	−18.3	5.33

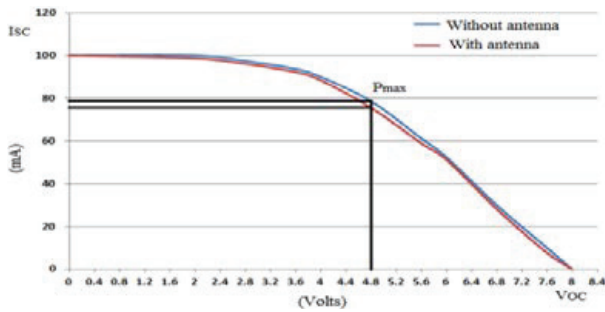


Fig. 16. Solar cell VI characteristics with and without antenna.

washing damage in textile integrated electronics, as well as common weak points, have not been substantially explored, making a targeted strategy to improve washability in electronic textiles problematic [60, 61].

The solar cell parameters, open circuit voltage ( $V_{OC}$ ) and short circuit current ( $I_{SC}$ ) were measured by concentrating the normal sun-based light on solar cells, embedding them with and without the antenna. From the measurements, the proposed solar cells carry a current of  $I_{SC} = 100$  mA with a voltage  $V_{OC} = 8$  V when none is integrated with the antenna. Nevertheless, the same solar cells are connected with an antenna; the measured  $I_{SC}$  current and  $V_{OC}$  voltage are 96 mA and 8 V, respectively. The voltage-current (VI) characteristics of solar cells integrated with and without antennas are shown in Figure 16. The power delivered by a solar cell is the product of current and voltage. If the multiplication is done point for point, for all voltages from short-circuit to open-circuit conditions, the power curve is obtained for a given radiation level. Of course, neither of these two conditions generates any electrical power, but there must be a point, called the “Knee” point, somewhere in between where the solar cells generate maximum power,  $P_{max}$ . The observed  $P_{max}$  of the solar cell without and with the antenna is 378 mW and 363.08 mW, which is a small decrease in maximum output DC power of 14.92 mW and is also commonly acceptable.

Table 2 shows the novelty of the proposed antenna compared with several reported wearable antennas. The

evaluation results in Table 3 indicate that the proposed antennas have a lower profile and operate in the ISM band used for green wearable wireless on-body and in-body communications with acceptable bandwidth.

#### IV. CONCLUSION

In this article, a textile patch antenna on the AMC surface stacked silicon solar cells partially with its copper ground is presented and tested for its performance. A technical viewpoint on the loading of the AMC with the antenna and also the RF behavior of solar cells by incorporating them into the AMC ground plane is elucidated. The improvement of radiation efficiency with a reduction in specific absorption rate levels is achieved over frequencies clustered around 2.4 GHz. The bending and crumbling tests on the proposed antenna are limited due to the brittle nature of solar cells stacked with the AMC ground plane. Currently, flexible solar cells are a research-level technology. In order for solar clothing to function at an optimal level, direct exposure to sunlight is required for very long periods. It is hoped that solar clothing will be able to charge phones, tablets, and GPS units for people who enjoy outdoor activities such as skiing, snowboarding, or hiking.

#### REFERENCES

- [1] A. Maskooki, G. Sabatino, and N. Mitton, “Analysis and performance evaluation of the next generation wireless networks,” *M. Simul. Comput. Netw. Syst. Methodol. Appl.*, vol. 21, pp. 601-627, Apr. 2015.
- [2] N. F. M. Aun, P. J. Soh, A. A. Al-Hadi, M. F. Jamlos, G. A. E. Vandebosch, and D. Schreurs, “Revolutionizing wearables for 5G: 5G technologies: Recent developments and future perspectives for wearable devices and antennas,” *IEEE Microw. Mag.*, vol. 18, no. 3, pp. 108-124, May 2017.
- [3] R. Dangi, P. Lalwani, G. Choudhary, I. You, and G. Pau, “Study and investigation on 5G technology: A systematic review,” *Sensors*, vol. 22, no. 1, Dec. 2021.
- [4] R. K. Kanth, P. Liljeberg, H. Tenhunen, Y. Amin, Q. Chen, L. Zheng, and H. Kumar, “Quantifying the environmental footprint of rigid substrate printed

- antenna," in *Proc. 2012 IEEE Conf. Technol. Soc. Asia (T&SA)*, Singapore, pp. 27-29, Oct. 2012.
- [5] R. K. Kanth, Q. Wan, H. Kumar, P. Liljeberg, Q. Chen, L. Zheng, and H. Tenhunen, "Evaluating sustainability, environment assessment and toxic emissions in life cycle stages of printed antenna," *Procedia Eng.*, vol. 30, pp. 508-513, Jan. 2012.
- [6] O. Boric-Lubecke, V. M. Lubecke, B. Jokanovic, A. Singh, E. Shahhaidar, and B. Padasdao, "Microwave and wearable technologies for 5G," in *Proc. 12th Int. Conf. Telecommun. Modern Satellite, Cable Broadcasting Services (TELSIKS)*, Nis, Serbia, pp. 183-188, 14-17, Oct. 2015.
- [7] O. Galinina, H. Tabassum, K. Mikhaylov, S. Andreev, E. Hossain, and Y. Koucheryavy, "On feasibility of 5G-grade dedicated RF charging technology for wireless-powered wearables," *IEEE Wireless Commun.*, vol. 23, no. 2, pp. 28-37, Apr. 2016.
- [8] K. N. Paracha, S. K. Abdul Rahim, P. J. Soh, and M. Khalily, "Wearable antennas: A review of materials, structures, and innovative features for autonomous communication and sensing," *IEEE Access*, vol. 7, pp. 56694-56712, Apr. 2019.
- [9] A. Desore and S. A. Narula, "An overview on corporate response towards sustainability issues in textile industry," in *Environment, Development and Sustainability: A Multidisciplinary Approach to the Theory and Practice of Sustainable Development*, vol. 20, no. 4. Berlin, Germany: Springer, pp. 1439-1459, Aug. 2018.
- [10] C. C. Zarakovitis, Q. Ni, and M.-A. Kourtis, "Enabling radioprotection capabilities in next generation wireless communication systems: An ecological green approach," *Trans. Emerging Telecommun. Technol.*, vol. 29, no. 10, pp. 1-21, Oct. 2018.
- [11] A. Srivastava, M. S. Gupta, and G. Kaur, "Energy efficient transmission trends towards future green cognitive radio networks (5G): Progress, taxonomy and open challenges," *J. Netw. Comput. Appl.*, vol. 168, Oct. 2020.
- [12] S. Vaccaro, J. R. Mosig, and P. de Maagt, "Making planar antennas out of solar cells," *Electron. Lett.*, vol. 38, no. 17, pp. 945-947, Aug. 2002.
- [13] O. Yurduseven, D. Smith, N. Pearsall, and I. Forbes, "A solar cell stacked slot-loaded suspended microstrip patch antenna with multiband resonance characteristics for WLAN and WiMAX systems," *Prog. Electromagn. Res.*, vol. 142, pp. 321-332, Sep. 2013.
- [14] O. Yurduseven and D. Smith, "Solar cell stacked dual-polarized patch antenna for 5.8 GHz band WiMAX network," *Electron. Lett.*, vol. 49, no. 24, pp. 1514-1515, Nov. 2013.
- [15] M. Elsdon, O. Yurduseven, and X. Dai, "Wideband metamaterial solar cell antenna for 5 GHz Wi-Fi communication," *Prog. Electromagn. Res. C*, vol. 71, pp. 123-131, Feb. 2017.
- [16] S. V. Shynu, M. J. R. Ons, P. Mcevoy, J. A. Max, J. M. Sarah, and B. Norton, "Integration of microstrip patch antenna with polycrystalline silicon solar cell," *IEEE Trans. Antennas Propag.*, vol. 57, no. 12, pp. 3969-3972, Jun. 2009.
- [17] S. V. Shynu, M. J. R. Ons, J. A. Max, and B. Norton, "Dual band a-Si:H solar-slot antenna for 2.4/5.2 GHz WLAN applications," in *Proc. IEEE 2009 3rd European Conference on Antennas and Propag.*, Berlin, Germany, pp. 408-410, Mar. 2009.
- [18] M. J. R. Ons, S. V. Shynu, M. J. Ammann, S. J. McCormack, and B. Norton, "Transparent patch antenna on a-Si thin-film glass solar module," *Electron. Lett.*, vol. 47, no. 2, pp. 85-86, Jan. 2011.
- [19] O. O'Conchubhair, A. Narbudowicz, P. Mcevoy, and M. J. Ammann, "Circularly polarised solar antenna for airborne communication nodes," *Electron. Lett.*, vol. 51, no. 9, pp. 667-669, Apr. 2015.
- [20] F. Nashad, S. Foti, D. Smith, M. Elsdon, and O. Yurduseven, "Ku-band suspended meshed patch antenna integrated with solar cells for remote area applications," *Prog. Electromagn. Res. C*, vol. 83, pp. 245-254, Apr. 2018.
- [21] T. N. S. Babu and D. Sivakumar, "Stepped slot patch antenna with copper ground plane and solar cell ground plane for future mobile communications," *Prog. Electromagn. Res. C*, vol. 98, pp. 187-198, Jan. 2020.
- [22] B. Naresh, V. K. Singh, and V. K. Sharma, "Integration of RF rectenna with thin film solar cell to power wearable electronics," *Int. J. Microw. Wireless Technol.*, vol. 13, no. 1, pp. 46-57, Feb. 2021.
- [23] T. N. S. Babu and D. Sivakumar, "Patch antenna integrated on solar cells for green wireless communication: A feature oriented survey and design issues," *Int. J. RF Microw. Comput.-Aid. Eng.*, vol. 32, no. 1, pp. 1-29, Sep. 2021.
- [24] S. Sankaralingam and B. Gupta, "Experimental results on HIPERLAN/2 antennas for wearable applications," *Prog. Electromagn. Res. C*, vol. 25, pp. 27-40, Oct. 2011.
- [25] R. Poonkuzhali, C. Alex Zachariah, and T. Balakrishnan, "Miniaturized wearable fractal antenna for military applications at VHF band," *Prog. Electromagn. Res. C*, vol. 62, pp. 179-190, Mar. 2016.
- [26] D. Ferreira, P. Pires, R. Rodrigues, and F. S. C. Rafael, "Wearable textile antennas-examining the effect of bending on their performance," *IEEE Antennas Propag. Mag.*, vol. 17, pp. 1045-9243, Jun. 2017.

- [27] I. A. Mohamed, F. A. Mai, and A. S. Abd-El, "Novel electro-textile patch antenna on jeans substrate for wearable applications," *Prog. Electromagn. Res. C*, vol. 83, pp. 255-265, Apr. 2018.
- [28] I. Agbor, K. B. Dipon, and I. Mahbub, "A comprehensive analysis of various electro-textile materials for wearable antenna applications," in *Proc. 2018 Texas Symp. Wireless Microw. Circuits Syst. (WMCS)*, Waco, TX, USA, pp. 1-4, Apr. 5-6, 2018.
- [29] S. Zhang, W. Whittow, R. Seager, A. Chauraya, and C. J. Vardaxoglou (Yiannis), "Non-uniform mesh for embroidered microstrip antennas," *IET Microw. Antennas Propag.*, vol. 11, no. 8, pp. 1086-1091, Feb. 2017.
- [30] F. N. Mohd Hussin Ezzaty, P. J. Soh, M. F. Jamlos, H. Lago, and A. Al-Hadi Azremi, "Wideband microstrip-based wearable antenna backed with full ground plane," *Int. J. RF Microw. Comput.-Aid. Eng.*, vol. 29, no. 7, pp. 1-12, Mar. 2019.
- [31] B. Sanz-Izquierdo, J. C. Batchelor, and M. I. Sobhy, "Button antenna on textiles for wireless local area network on body applications," *IET Microw. Antennas Propag.*, vol. 4, no. 11, pp. 1980-1987, Nov. 2010.
- [32] S. J. Boyes, P. J. Soh Boyes, Y. Huang, G. A. E. Vandenbosch, and N. Khiabani, "On-body performance of dual-band textile antennas," *IET Microw. Antennas Propag.*, vol. 6, no. 15, pp. 1696-1703, Dec. 2012.
- [33] E. F. Sundarsingh, S. Velan, M. Kanagasabai, K. S. Aswathy, C. Raviteja, and M. G. N. Alsath, "Polygon-shaped slotted dual-band antenna for wearable applications," *IEEE Antennas Wireless Propag. Lett.*, vol. 13, pp. 611-614, Mar. 2014.
- [34] C. Mendes and C. Peixeiro, "A dual-mode single-band wearable microstrip antenna for body area networks," *IEEE Antennas Wireless Propag. Lett.*, vol. 16, pp. 3055-3058, Oct. 2017.
- [35] S. Chilukuri and S. Gogikar, "A CPW-fed denim based wearable antenna with dual band-notched characteristics for UWB applications," *Prog. Electromagn. Res. C*, vol. 94, pp. 233-245, Aug. 2019.
- [36] J. Tak, Y. Hong, and J. Choi, "Textile antenna with EBG structure for body surface wave enhancement," *Electron. Lett.*, vol. 51, no. 15, pp. 1131-1132, Jul. 2015.
- [37] G. Gao, R. Zhang, C. Yang, H. Meng, W. Geng, and B. Hu, "Microstrip monopole antenna with a novel UC-EBG for 2.4 GHz WBAN applications," *IET Microw. Antennas Propag.*, vol. 13, no. 13, pp. 2319-2323, Oct. 2019.
- [38] B. Hazarika, B. Basu, and J. Kumar, "A multi-layered dual-band on-body conformal integrated antenna for WBAN communication," *AEU-Int. J. Electron. Commun.*, vol. 95, pp. 226-235, Oct. 2018.
- [39] C. Wang, L. Zhang, S. Wu, S. Huang, C. Liu, and X. Wu, "A dual-band monopole antenna with EBG for wearable wireless body area networks," *Appl. Comput. Electromagn. Soc. J.*, vol. 36, no. 1, pp. 48-54, Jan. 2021.
- [40] Z. H. Jiang, E. B. Donovan, E. S. Peter, and H. W. Douglas, "A compact, low-profile metasurface-enabled antenna for wearable medical body-area network devices," *IEEE Trans. Antennas Propag.*, vol. 62, no. 8, pp. 4021-4029, Aug. 2014.
- [41] H. Yalduz, T. E. Tabaru, V. T. Kilic, and M. Turkmen, "Design and analysis of low profile and low SAR full-textile UWB wearable antenna with metamaterial for WBAN applications," *AEU-Int. J. Electron. Commun.*, vol. 126, no. 153465, Sep. 2020.
- [42] E. Delihasanlar and A. H. Yuzer, "Wearable textile fabric based 3D metamaterials absorber in X-band," *Appl. Comput. Electromagn. Soc. J.*, vol. 35, no. 2, pp. 230-236, Feb. 2020.
- [43] M. R. I. Faruque, M. T. Islam, and N. Misran, "Influence of SAR reduction in muscle cube with metamaterial attachment," *J. Microelectron. Electron. Compon. Mater.*, vol. 41, no. 3, pp. 233-237, Aug. 2011.
- [44] M. Mantash, A. C. Tarot, S. Collardey, and K. Mahdjoubi, "Investigation of flexible textile antennas and AMC reflectors," *Int. J. Antennas Propag.*, vol. 2012, no. 236505, pp. 1-10, May 2012.
- [45] A. Alemaryeen and S. Noghianian, "AMC integrated textile monopole antenna for wearable applications," *Appl. Comput. Electromagn. Soc. J.*, vol. 31, no. 6, pp. 612-618, Jun. 2016.
- [46] S. Yan, P. J. Soh, and A. E. Vandenbosch Guy, "Low-profile dual-band textile antenna with artificial magnetic conductor plane," *IEEE Trans. Antennas Propag.*, vol. 62, no. 12, pp. 6487-6490, Dec. 2014.
- [47] C. K. Chou, H. Bassen, J. Osepchuk, Q. Balzano, R. Petersen, M. Meltz, R. Cleveland, J. C. Lin, and L. Heynick, "Radio frequency electromagnetic exposure: Tutorial review on experimental dosimetry," *Bioelectromagnetics*, vol. 17, no. 3, pp. 195-208, Jan. 1996.
- [48] V. Karthik and T. Rama Rao, "Investigations on SAR and thermal effects of a body wearable microstrip antenna," *Wireless Personal Commun.*, vol. 96, no. 7, Mar. 2017.

- [49] K. Kamardin, A. R. M. Kamal, S. H. Peter, S. N. Asmawati, M. E. Jalil, and M. F. A. Malek, "Textile diamond dipole and artificial magnetic conductor performance under bending, wetness and specific absorption rate measurements," *Radio Eng.*, vol. 24, no. 3, pp. 729-738, Sep. 2015.
- [50] M. Mantash, A. C. Tarot, S. Collardey, and K. Mahdjoubi, "Design methodology for wearable antenna on artificial magnetic conductor using stretch conductive fabric," *Electron. Lett.*, vol. 52, no. 2, pp. 95-96, Jan. 2016.
- [51] A. Alemaryeen and S. Noghianian, "Crumpling effects and specific absorption rates of flexible AMC integrated antennas," *IET Microw. Antennas Propag.*, vol. 12, no. 4, pp. 627-635, Feb. 2018.
- [52] A. Mersani, O. Lotfi, and J. M. Ribero, "Design of a textile antenna with artificial magnetic conductor for wearable applications," *Microw. Optical Technol. Lett.*, vol. 60, pp. 1343-1349, Jun. 2018.
- [53] B. Yin, J. Gu, X. Feng, B. Wang, Y. Yu, and W. Ruan, "A low SAR value wearable antenna for wireless body area network based on AMC structure," *Prog. Electromagn. Res. C*, vol. 95, pp. 119-129, Sep. 2019.
- [54] N. I. Zaidi, M. T. Ali, N. H. A. Rahman, M. S. A. Nordin, A. A. S. A. Shah, M. F. Yahya, and H. Yon, "Analysis of different feeding techniques on textile antenna," in *Proc. 2019 Int. Symp. Antennas Propagation (ISAP)*, Xi'an, China, pp. 1-3, 27-30, Oct. 2019.
- [55] S. K. Dargar and V. M. Srivastava, "Moisture content investigation in the soil samples using microwave dielectric constant measurement method," *Int. J. Elect. Comput. Eng.*, vol. 10, no. 1, pp. 704-710, Feb. 2020.
- [56] S. Sankaralingam and B. Gupta, "Determination of dielectric constant of fabric materials and their use as substrates for design and development of antennas for wearable applications," *IEEE Trans. Instrum. Meas.*, vol. 59, no. 12, pp. 3122-3130, Dec. 2010.
- [57] A. P. Feresidis, G. Goussetis, S. Wang, and J. C. Vardaxoglou, "Artificial magnetic conductor surfaces and their application to low-profile high-gain planar antennas," *IEEE Trans. Antennas Propag.*, vol. 53, no. 1, pp. 209-215, Jan. 2005.
- [58] G. A. Casula, G. Montisci, A. Fanti, G. Mazzarella, and P. Maxia, "Design of low-cost uniplanar AMC structures for UHF applications," in *Proc. IEEE Int. Symp. Antennas Propagation USNC/URSI National Radio Sci. Meeting*, Vancouver, BC, Canada, pp. 1598-1599, Jul. 19-24, 2015.
- [59] M. B. Lodi, G. Muntoni, A. Ruggeri, A. Fanti, G. Montisci, and G. Mazzarella, "Towards the robust and effective design of hyperthermic devices: Improvement of a patch antenna for the case study of abdominal rhabdomyosarcoma with 3D perfusion," *IEEE J. Electromagn., RF Microw. Med. Biol.*, vol. 5, no. 3, pp. 197-205, Sep. 2021.
- [60] F. Andriulli, "Washable Antennas? Be Careful While Doing Laundry! [Editor's Comments]," *IEEE Antennas Propagation Mag.*, vol. 63, no. 4, pp. 4-4, Aug. 2021.
- [61] J. Pei, J. Fan, and R. Zheng, "Protecting wearable UHF RFID tags with electro-textile antennas: The challenge of machine washability," *IEEE Antennas Propagation Mag.*, vol. 63, no. 4, pp. 43-50, Aug. 2021.



#### **Suresh Babu T. Naganathan**

received the B.E. degree in Electronics and Communication Engineering from Madurai Kamaraj University, India, in 1997 and the M.E. degree in Power Electronics and Drives from Anna University, India, in 2009, respectively. He is currently working as an Assistant Professor in the Department of Electronics and Communication Engineering at Adhiparasakthi Engineering College, Tamilnadu, India. His research interests include those in the areas of Electromagnetics, Antenna design and Wave Propagation.



#### **Sivakumar Dhandapani**

received the B.E. degree in Electronics and Communication Engineering from the University of Madras, India, in 1995, the M.E. degree in Process Control and Instrumentation from Annamalai University, India, in 2002, and the Ph.D. degree in Faculty of Information and Communication from Anna University, India, in 2010, respectively. He is now a Professor at Easwari Engineering College in Chennai, India, in the Department of Electronics and Communication Engineering. His research interests include those in the areas of MANET, Wireless Sensor Networks, Mobile Computing, and Network Security.

# Dual-Band Highly Isolated Eight-Element MIMO Antenna for 5G Mobile Phone

Yonghao Wang, Xin Wang\*, Junlin Wang\*, and Rui Shao

College of Electronic and Information Engineering  
Inner Mongolia University, Hohhot 010021, China

y.h.wang@mail.imu.edu.cn, wangxin219@imu.edu.cn, wangjunlin@imu.edu.cn, shaorui@mail.imu.edu.cn

**Abstract** – Based on the characteristic mode analysis (CMA) theory, a compact dual-band dual antenna pair with high element isolation function for 5G mobile terminal is proposed and designed in this paper. The antenna pair is composed of a pair of symmetrical stacked F-shaped radiators printed on the outside of the side frame, perpendicular to the main board. Based on the proposed decoupled antenna pairs, four pairs of antenna pairs are placed at both ends of two long side plates, and an 8-element MIMO antenna is proposed. High isolation in the operating frequency bands are achieved by using grounding branches and defective ground structure (DGS). All radiation elements are etched on a low-cost FR4 substrate with a total size of  $150 \times 75 \times 6.8 \text{ mm}^3$ . The prototype of the antenna array is fabricated and measured. The working range of the antenna pair can cover 3.4GHz-3.6GHz, 4.8GHz-5GHz 5G frequency bands and 5GHz-6GHz WLAN / WiFi / WiMax frequency bands. Besides, the isolation between any adjacent array elements are also  $> 15\text{dB}$  and  $> 16\text{dB}$  respectively, the total efficiency are 52%–75% and 58%–88% respectively, and the measured envelope correlation coefficients (ECC) are  $< 0.16$ . Furthermore, user's head effects are investigated and desirable results are obtained. The above results show that this proposed antenna array is a good candidate for MIMO applications in 5G smartphones.

**Index Terms** – Antenna pair, characteristic mode analysis (CMA), dual-band, high-isolation, MIMO, 5G smartphones.

## I. INTRODUCTION

As a combination of technology and fashion, smartphones have been developing towards the design concept of thinner body and higher screen proportion. In the 15th edition of 3GPP, two main NR 5G bands are defined: band 1 (FR1, 450MHz-6000MHz) and band 2 (FR2, 24.25GHz-52.6GHz). However, the design of millimeter wave antennas with bands above 24GHz must face the problems of serious spatial attenuation and high processing accuracy. At the same time, the 3.4GHz-3.6GHz and

4.8GHz-5GHz 5G bands have been supported by China, Russia and other countries, and the 5.15GHz-5.925GHz WLAN bands are also the indispensable bands in the design of 5G mobile phone MIMO antenna. At present, 5G antenna design under 6GHz band still faces the bottleneck of limited frequency coverage. Therefore, it is very necessary to use the same number of antennas inside a full screen mobile phone with a very small clearance area and cover 5G bands and WLAN bands at the same time. Several MIMO antenna designs have been reported with multi-band operation. On the one hand, [1–3] deformed the antenna by adding branches, and formed several current resonance paths by adding radiation branches, so as to realize the coverage of multiple frequency bands. On the other hand, coupling feed is a common way to increase bandwidth in antenna design. The coupling feeding method is used for energy transmission between the directly fed metal plane and the main radiation surface. Compared with the direct feeding, the coupling feeding can easily obtain a larger bandwidth [4–6].

With the continuous development of 5G communication system in the future, users' requirements for system capacity and signal quality are constantly improving, large-scale multiple input multiple output (MIMO) system with multiple antennas can achieve higher data rates, so it will become one of the core technologies of 5G communication [7]. However, placing multiple antennas in a limited design space may cause extreme deterioration of antenna system isolation and radiation efficiency. Therefore, it is a great challenge for antenna designers to realize the very effective isolation of each antenna in MIMO system. Several techniques have shown that isolation between antenna elements can be improved when they are closely spaced together. On the one hand, increasing the space distance between two antennas and reducing the number of antenna elements in a certain space are the most direct decoupling methods [8]. On the other hand, some researchers focus on improving the isolation between units by adding decoupling structure. For example,

researchers use the neutralization line compensation technology [9–11] to select one or several branches of appropriate size to connect the two antennas at the appropriate position, and these branches produce paths opposite to the original coupling path, so as to achieve the purpose of decoupling. Similarly, The defective ground structure (DGS) technology [12, 13] is simple and easy to implement. When there is a current distribution on the ground between two antenna units that can produce strong coupling between them, slotting on the ground can change the current distribution, block the current path and play a better decoupling effect. In this paper, a short-circuit branch connecting two antenna units with the ground is proposed, so that the energy should be radiated from the gap between the two antenna units and the ground to two opposite directions respectively, so as to improve the isolation of the antenna pair from the two units.

To sum up, it is very necessary to design a mobile phone antenna that can cover 5G bands and WLAN bands at the same time and achieve high isolation. In this paper, based on the characteristic mode analysis (CMA) theory, a dual-band decoupled dual antenna pair for 5G terminal application based on coupling feed is proposed. Four pairs of antennas are integrated on a mobile terminal, and a dual-band  $8 \times 8$  MIMO antenna is manufactured and tested. The size of the antenna is  $150 \times 75 \times 6.8 \text{ mm}^3$ , which is similar to the size of existing smart phones such as Huawei mate 40 and Xiaomi 11. The low band (LB) is 3.4GHz-3.6GHz and the high band (HB) is 4.8GHz-6GHz. This antenna operating band can cover 3.5GHz (3.4GHz-3.6GHz) 5G frequency band, 4.9GHz (4.8GHz-5GHz) 5G frequency band, and 5.5GHz (5.15GHz-5.925GHz) WLAN / WiMAX / WiFi frequency bands, which can effectively reduce the number of antennas specially covering WLAN frequency bands in 5G Mobile phones. Besides, in the low frequency band (LB) and high frequency band (HB), The isolation between any adjacent array elements are also  $> 15\text{dB}$  and  $> 16\text{dB}$ , respectively. Furthermore, The envelope correlation coefficients (ECCs), total efficiency, and specific absorption rate (SAR) all reach the expected values in the whole working frequency bands. The main achievements of this work are as follows: (1) High isolation (more than 15 dB) is achieved while supporting the multi-band operation. (2) Cover both the 5G and WLAN bands (3) Antenna design based on CMA that are rarely reported.

## II. ANTENNA PAIR DESIGN AND EVOLUTION

### A. Geometry of proposed antenna pair

The structure and size of the proposed antenna pair are shown in Figure 1. The main board size is 50mm

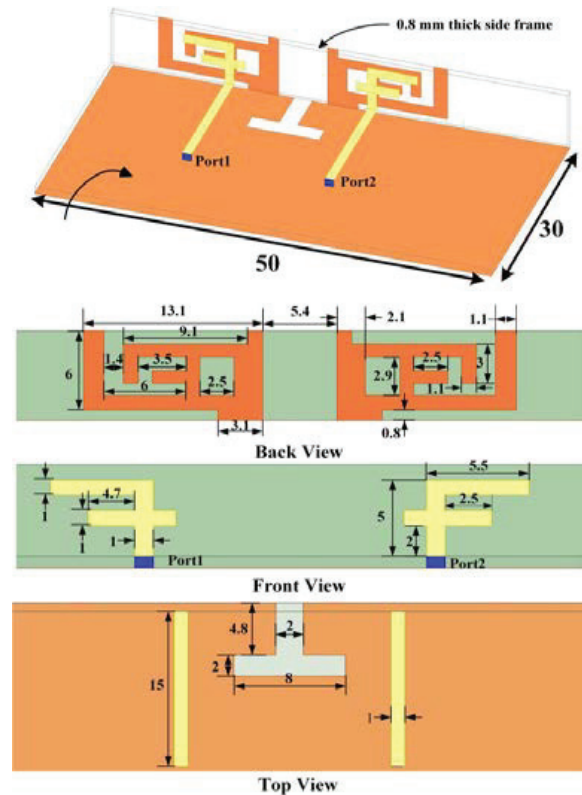


Fig. 1. Geometry and dimensions of the proposed antenna pair.

$\times 25\text{mm} \times 0.8\text{mm}$ . The antenna pair is composed of a pair of symmetrical stacked F-shaped radiators printed on the outside of the side frame, perpendicular to the main board, and the size is  $50\text{mm} \times 6\text{mm} \times 0.8\text{mm}$ . The main body of the stacked F-shaped radiator is mainly connected by two F-shaped branches with different sizes from top to bottom, and is connected with the ground on the back of the main board through a short-circuit branch. The stacked F-shaped radiator is coupled and fed by a pair of F-shaped branches printed on the inner side of the side frame. The substrate of the main board and side frame is FR-4, the relative dielectric constant is 4.4, and the loss tangent is 0.02. Between the two elements, a T-shaped slot is cut in the ground. The feed line, with a width of 1mm, is printed on the top layer of the main board and connected to the F-shaped branches.

### B. The theory of characteristic mode analysis

According to CMA [14–17], the characteristic mode fields form a weighted orthogonal set over a conductor surface and the sphere at infinity. The total surface field distribution of an antenna can be obtained by the superposition of each mode field. In CMA,  $\alpha_n$  is a weighting factor defined as modal weighting coefficient (MWC). The MWC reflects the mode contribution of the total

field density, and its expression is:

$$\alpha_n = \frac{V_n}{1 + j\lambda_n} = \frac{\langle J_n, E^i \rangle}{1 + j\lambda_n}, \quad (1)$$

where  $V_n$  reflects the coupling of external excitation and characteristic current, which is defined as the mode excitation coefficient (MEC).

Each CM corresponds to a characteristic value  $\lambda_n$ , which represents the ratio of reactive power to radiated power. Modal significance (MS) is closely related to  $\lambda_n$ , which is denoted as:

$$MS_n = \frac{1}{|1 + j\lambda_n|}. \quad (2)$$

$MS_n$  is independent of the excitation source, and only related to the shape of the conductor. It indicates the potential ability of a CM working in certain bands.

### C. Design process and analysis

Characteristic mode theory, which was first proposed in 1971 [14], is widely used in antenna design because it can reveal the intrinsic properties of the antenna geometry structure. CMA is used in the design process in our work, with the goal of optimizing the geometrical structure of the antenna pair. The modal significance (MS) is introduced to indicate the potential of each mode in the absence of an external source. Besides, we also observe the surface current of the antenna structure through simulation to guide the design of the antenna structure and adjust the frequency coverage of the antenna. The simulation software are ANSYS HFSS 2020R1 and CST 2020. Due to the symmetry of the structure, only port 1 needs to be simulated and analyzed. In order to clearly show the continuous changes of our design, Figure 2 (a) shows the structural evolution process in four different cases.

Since the coupled feed antenna includes a feed branch and a short-circuit branch connected to the ground. The gap between the two branches is used to couple energy to the short-circuit branch, which essentially adds capacitive component to the antenna. The short-circuit branch can add inductive component to the antenna. So, the antenna is more possible to produce dual-band resonance and a wider bandwidth. Therefore, we propose a coupled loop element, which is composed of section of feed line, a direct fed F-patch, and a coupled grounded stacked F-patch.

In case 1, two grounded F-shaped patches are placed symmetrically to form an initial antenna pair. The design MS and modal current of case 1 are shown in the Figure 4 (a) and Figure 5 (a). According to the characteristic mode analysis, the current path and current length of 3.5GHz modal current (About 3.5GHz quarter wavelength: 23mm), it can be inferred that the grounded F-shaped patch can effectively excite 3.5GHz resonance. By observing the simulated  $S_{11}$  curve and surface

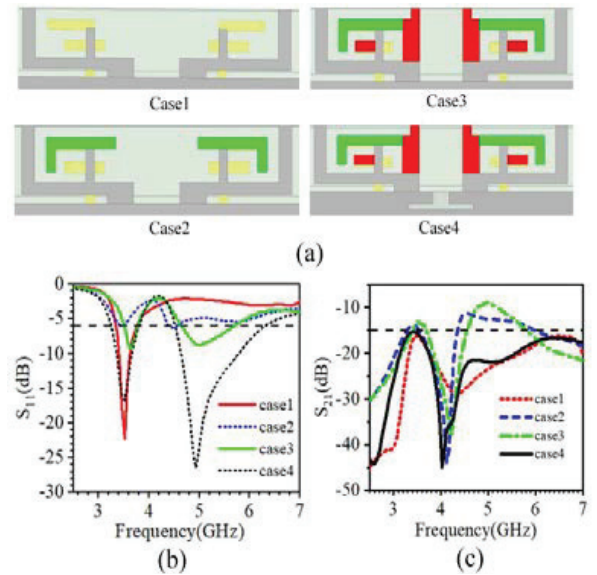


Fig. 2. Antenna pair design process. (a) Evolution process of the antenna pair. (b) Comparison of  $S_{11}$  in four cases. (c) Comparison of  $S_{21}$  in four cases.

current distribution, it is found that it is highly consistent with the results of characteristic mode analysis, as shown in Figures 2 (b) and 5 (b). It is worth noting that the distance between the two antenna elements in the antenna pair is only 5.4mm ( $0.065\lambda_g$ ,  $\lambda_g = v/f$ . Where  $\lambda_g$  is the free space wavelength of 3.5GHz. Where  $v$  is the speed of light and  $f$  is the value of frequency.), but the isolation is still greater than 15dB, as shown in Figure 2 (c). The main reason is that the two elements of the antenna pair are grounded and symmetrical, their 3.5GHz current paths are symmetrical and in opposite directions, and the energy is radiated in two opposite directions from the gap between the two antenna units and the ground, as shown in Figure 3, so the isolation is very high. Although the resonant frequency and isolation of this antenna pair are very satisfactory, a single frequency band is far from meeting the needs of 5G mobile phones. We also need to modify the antenna pair to generate new resonant modes and cover as many useful frequency bands as possible.

Next, on the basis of the coupled grounding F-shaped patch, L-shaped branches (Figure 2 (a), green part) are added to form case2 to generate a new mode. Through the analysis of its characteristic mode, it can be seen that two modes of 3.5GHz and 5.5GHz can be excited, as shown in Figure 4 (b). However, from the simulation  $S_{11}$  curve of case 2, as shown in Figure 2 (b), it can be seen that the center frequency, bandwidth and impedance matching of the newly generated high frequency band are not very ideal, so case 2 needs

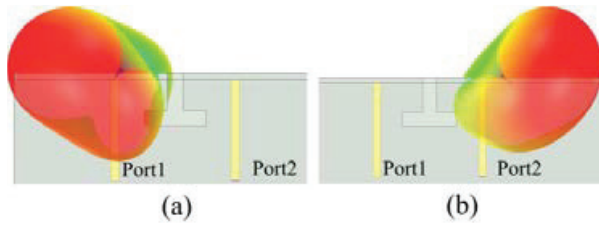


Fig. 3. Comparison of radiation directions of port 1 and port 2. (a) Port 1. (b) Port 2.

to be modified. Then, on the basis of case 2, the red part in Figure 2 (a) is added to form a stacked F-patch (case3) to adjust the high-frequency resonance point, expand the bandwidth and increase the matching. As shown in Figure 4 (c), the characteristic mode analysis shows that the stacked F-patch has three modes, and three resonances are generated near 3.5GHz, 4.8GHz and 5.5GHz respectively. The three effective modes realize dual frequency resonance and expand the bandwidth of high frequency band. The newly generated modal current of 5.5GHz is shown in Figure 5 (c). From the path of modal current and simulated surface current (Figure 5 (c) and (d)), it can be observed that the antenna is a quarter wavelength resonant mode at 5.5GHz. As shown in Figure 2 (b) and (c), we can roughly observe from the S11 and S21 curves of case2 and case3 that the antenna pair has two working frequency bands and the high-frequency band bandwidth is wide, but the return loss and isolation of the antenna pair are not satisfactory. We also need to improve the structure of the antenna pair to make the return loss of the antenna pair lower and the isolation better than 15dB.

Finally, the defective ground structure (DGS) is introduced, which is mainly used for impedance matching and reducing the mutual coupling between two units of antenna pair in the high frequency band, so as to further improve its performance. We open a T-shaped slot on the ground of case 3, as shown in Figure 2 (a) case 4. By changing the ground current, the resonant bandwidth can be adjusted and the current coupling between two adjacent ports can be reduced. In Figure 6 (b), we can see that when the antenna is in 5.5 GHz mode, there is a strong ground current (black circle) on the ground. Due to the existence of a strong ground current, there is a strong coupling between the two units of the antenna pair. As can be seen from the comparison between Figure 6 (a) and (b), when we add the DGS structure, the coupling of the ground current is obviously weakened, thus reducing the coupling between the two units. As shown in Figure 2 (b) and (c), after a series of improvements, the impedance matching, isolation and frequency band coverage of the antenna pair corresponding to case 4 have achieved very satisfactory results.

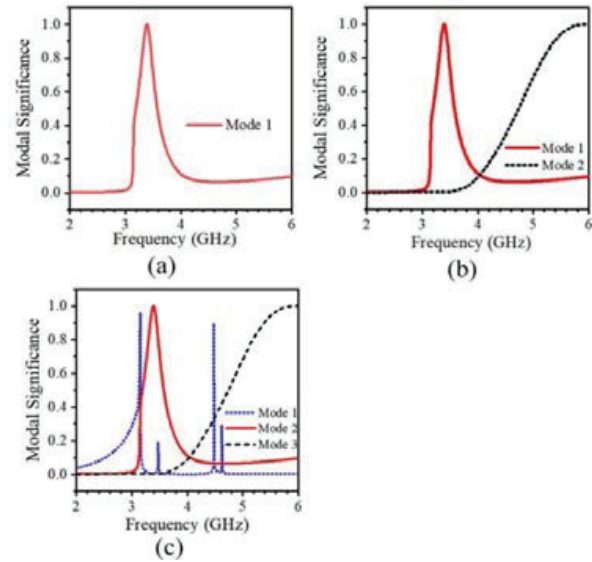


Fig. 4. Modal significance. (a) MS of case 1. (b) MS of case 2. (c) MS of case 3.

### III. EIGHT-ELEMENT ANTENNA DESIGN AND RESULTS

#### A. Geometry of eight-element antenna array

We use the proposed antenna pair to construct a MIMO antenna array to further improve the capacity of the communication system. As shown in the Figure 7, the overall dimensions of the antenna is  $150 \times 75 \times 6.8 \text{ mm}^3$ , which is similar to the size of existing smart phones such as Huawei mate 40 and Xiaomi 11. Four pairs of antenna pairs are placed along the two long frames, and an 8-element antenna array is proposed. Impedance matching and isolation may deteriorate due to changes in the size of the metal ground plane during the composition of the antenna array. We

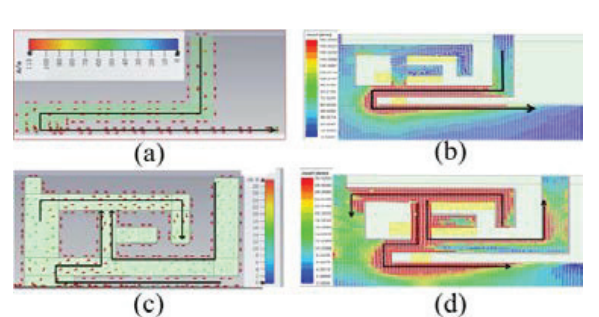


Fig. 5. Modal current and simulated surface current distribution at 3.5 and 5.5 GHz. (a) 3.5 GHz modal current in case 1. (b) 3.5 GHz simulated surface current distribution. (c) 5.5 GHz modal current in case 2. (d) 5.5 GHz simulated surface current distribution.

will fine tune the size of the two elements in the proposed antenna pair to reduce the impact of the expansion of the metal ground plane. The distance between antenna pairs on the same side frame is 76.6mm, allowing for future millimeter wave antenna design. To separate the coupling current from one antenna pair to the other and decrease mutual interference between antenna pairs, a 15mm×2mm gap is etched on the long side of the ground and a 13mm×2mm gap is etched on the short side of the ground. To test the proposed 8-element MIMO antenna array, a prototype is fabricated and measured.

### B. Performance of antenna array

The reflection coefficient, transmission coefficient, ECC and total efficiency of the eight element MIMO antenna were measured by using vector network analyzer (VNA) instrument keysight E5071C and microwave anechoic chamber. The measured results can fully meet the engineering application. The pictures taken during measurement are shown in Figure 8.

Due to the symmetry of the structure, only half of the elements are selected for discussion. In the Figure 9, the simulated and measured reflection and transmission coefficients are shown respectively. The slight difference between them is due to SMA connector and manufacturing errors. The results show that the working bandwidth of -6dB includes two frequency bands: 3.4GHz-3.6GHz and 4.8GHz-6GHz, which can cover 3.5GHz (3.4GHz-3.6GHz) 5G frequency band, 4.9GHz (4.8GHz-5GHz) 5G frequency band and 5.5GHz (5GHz-6GHz) 5.2GHz WLAN / 5.5GHz WiMAX / 5.8GHz WiFi frequency bands. It can be observed that 15dB iso-

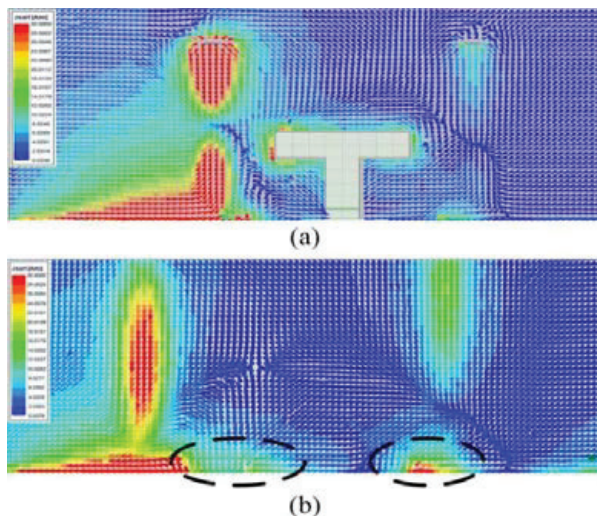


Fig. 6. Ground current at 5.5 GHz. (a) With T-shaped slot. (b) Without T-shaped slot.

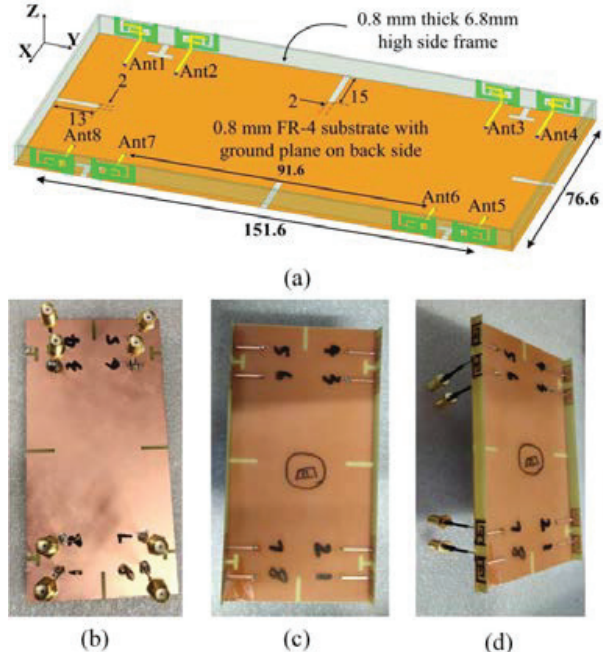


Fig. 7. The dimensions and fabrication of the eight-element antenna array (unit: mm). (a) General view. (b) Bottom view. (c) Top view. (d) Side view.

lation is achieved between elements on the same side and on the opposite side.

We measured the total efficiency and ECCs of the antenna through the microwave anechoic chamber. As shown in Figure 10 (a), the measured total efficiency of each element of the antenna is basically better than 50%, and the maximum value can reach 88%. In addition, the envelope correlation coefficients (ECCs) are employed as the metric to evaluate the MIMO performance of the proposed antenna, which are also provided in Figure 10 (b). Obviously, the ECC between any two ports is less than 0.16 (basically <0.1), which reveals the well interference suppressing ability.

The ECC describes the correlation between any two antenna elements in a MIMO antenna array. The lower ECC values lead to higher the diversity gain, which are highly expected in the MIMO antenna array. The ECC between antenna  $i$  and  $j$  can be calculated using the following formula [18]:

$$ECC_{ij} = \frac{\left| \iint_{4\pi} \vec{F}_i(\theta, \varphi) \cdot \vec{F}_j^*(\theta, \varphi) d\Omega \right|^2}{\iint_{4\pi} \left| \vec{F}_i(\theta, \varphi) \right|^2 d\Omega \cdot \iint_{4\pi} \left| \vec{F}_j(\theta, \varphi) \right|^2 d\Omega}, \quad (3)$$

where  $ECC_{ij}$  denotes the ECC between antenna  $i$  and antenna  $j$ ,  $F_i(\theta, \varphi)$  and  $F_j(\theta, \varphi)$  are the field pattern of two radiating elements with respect to  $\theta$  and  $\varphi$  components, \* denotes the complex conjugate operator.

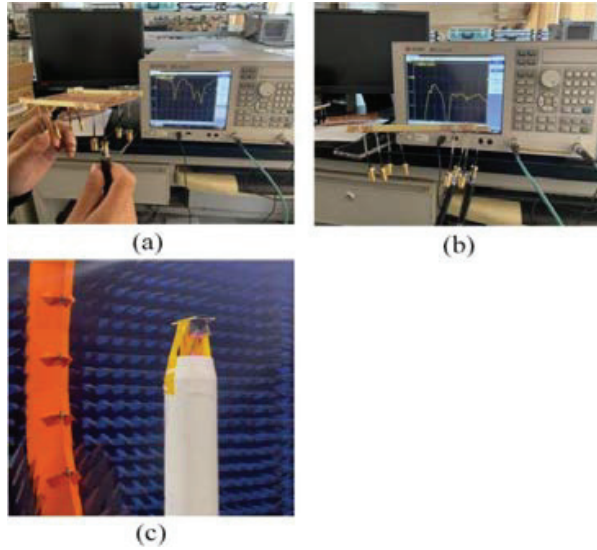


Fig. 8. The pictures taken during measurement.

Table 1: Comparison between the proposed and the referenced antennas

Ref.	Operating band (GHz)	Isolation (dB)	Efficiency (%)	Size (mm <sup>2</sup> )
[20]	3.25–3.65	12	58–72	14 × 6
[21]	3.4–3.6 4.8–4.9	11.8	Not given	15 × 6
[22]	3.3–4.2 4.8–5.0	12.5	53.8–79.1	18.6 × 7
[23]	3.4–3.6	17.5	62–76	25 × 3
Proposed	3.4–3.6 4.8–6.0	15	52–88	13.1 × 6.8

As shown in Figure 11, the radiation pattern of the antenna is analyzed. When the port 1 is excited, the overall radiation of the 8-element MIMO antenna presents omnidirectivity. At 3.5GHz and 5.5GHz, the maximum gain can reach 4.6dB and 8.7dB respectively. It can fully meet the signal quality requirements of 5G mobile phones in the future.

The specific absorption rate (SAR) [18] is the measure of the intensity of backward radiation on per unit mass of the human body. In order to investigate safety concerns of the user, the SAR intensity must be verified. Therefore, the energy absorbed (SAR) by user's head tissue need not to cross the value of 1.6W/Kg of 1-g tissue, according to American regulator, and 2W/Kg of 10-g tissue, according to European regulator. Full wave electromagnetic simulator can be used to extract SAR values directly. The full wave electromagnetic simulator ANSYS HFSS 2020R1 is used to estimate the SAR

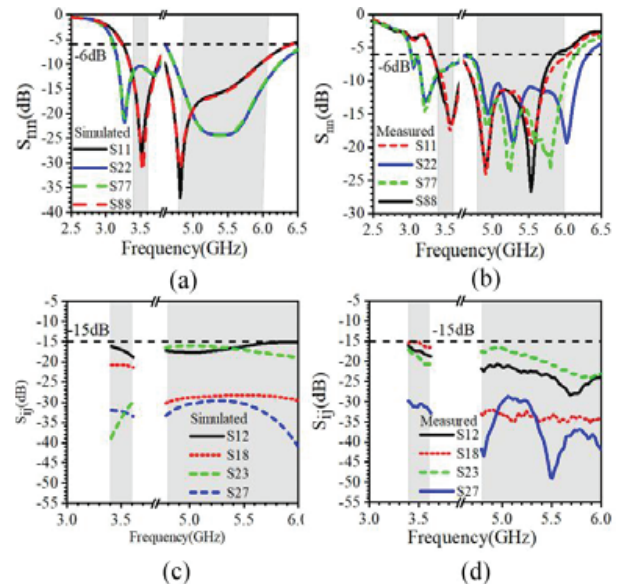


Fig. 9. Simulated and measured S-parameters of the proposed antenna. (a) Simulated  $S_{mn}$ . (b) Measured  $S_{mn}$ . (c) Simulated  $S_{ij}$ . (d) Measured  $S_{ij}$ .

of the model. The antenna is placed near the head of a realistic human model. In the simulation, the antenna is placed 2mm away from the human head [19]. The input power of each unit of the antenna is 25mW, so the total input power is 200mW. Figure 12 shows the SAR results of the antenna for 1-g tissue. The SAR peak values at 3.5GHz, 4.8GHz, and 5.75GHz are 0.54W/Kg, 0.49W/Kg, and 0.65W/Kg respectively, as shown in the Figure 13. It can be seen that the antenna is safe for operation in vicinity of the human body.

Table 1 shows the comparison between the proposed antenna and other recently reported smartphone 5G MIMO antennas. It can be seen that most eight-element antennas can only cover a single frequency

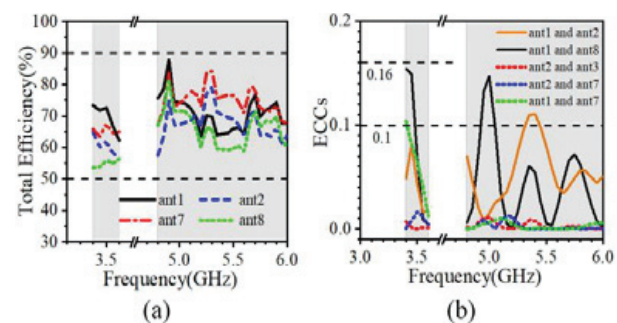


Fig. 10. Measured total efficiency and ECCs of the proposed antenna. (a) Measured total efficiency. (b) Measured ECCs.

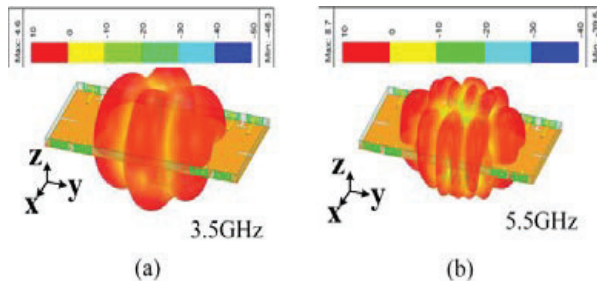


Fig. 11. Radiation pattern (Port 1 is excited). (a) 3.5 GHz. (b) 5.5 GHz.

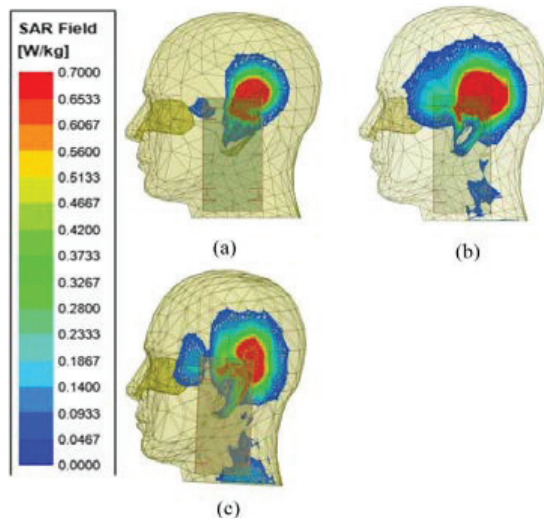


Fig. 12. SAR analysis. (a) 3.5 GHz. (b) 4.8 GHz. (c) 5.75 GHz.

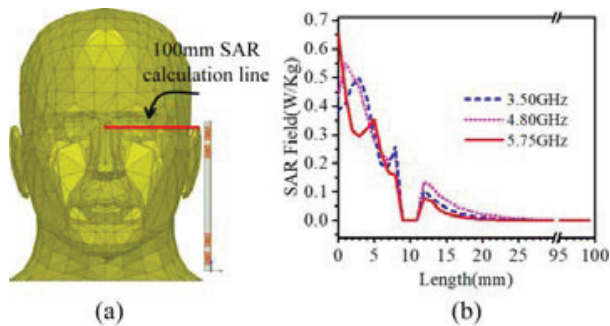


Fig. 13. Method of SAR calculation. (a) SAR calculation line. (b) SAR field.

band, and a few antennas that can cover dual frequency bands have the problems of small number of antenna units and low isolation. However, our proposed antenna can not only cover multiple useful frequency bands, but also achieve high isolation ( $> 15\text{dB}$ ).

## IV. CONCLUSION

In this work, we propose a compact dual-band dual-antenna pair and form an eight elements MIMO system, which resonates in the frequency bands of 3.4GHz-3.6GHz and 4.8GHz-6GHz, and realizes the impedance bandwidth of 200MHz and 1200MHz respectively based on  $v_{\text{swr}}3:1$  criteria. Also, the isolation between the ports is below  $-15\text{dB}$  and ECC is basically less than 0.1 for the whole band of interest. Moreover, the SAR study is conducted to understand the interaction of the system with the human body and it is found that it is safe to use within the vicinity of human body. The proposed antenna pairs were placed at the sides of the chassis with two antenna pairs on each side. Sufficient space is reserved for future millimeter wave antenna design and various sensor installation. The proposed antenna system can be termed as potential candidate for future 5G smart phone terminals.

## ACKNOWLEDGMENT

The authors extend appreciation to the support of the National Natural Science Foundation of China (Grant No. 51965047), the Natural Science Foundation of Inner Mongolia (Grant No. 2021MS06012) and the Key Scientific and Technological Project of Inner Mongolia (Grant No. 2020GG0185) for this project.

## REFERENCES

- [1] H. Zhu, X. Guan, B. Ren, and C. Wang, "Dual-band eight-element MIMO antenna consisted of tightly arranged hybrid antenna pairs for 5G smartphone," *Int. J. RF Microwave Comput.-Aided Eng.*, vol. 31, no. 12, Art. no. e22886, 2021.
- [2] W. Wang, Y. Wu, W. Wang, and Y. Yang, "Isolation enhancement in dual-band monopole antenna for 5G applications," *IEEE Trans. Circuits Syst. II: Express Briefs*, vol. 68, no. 6, pp. 1867-1871, 2021.
- [3] A. S. Elkorany, A. N. Mousa, S. Ahmad, D. A. Saleeb, A. Ghaffar, M. Soruri, M. Dalarsson, M. Alibakhshikenari, and E. Limiti, "Implementation of a miniaturized planar tri-band microstrip patch antenna for wireless sensors in mobile applications," *Sensors*, vol. 22, no. 2, 2022.
- [4] P. Mathur, R. Augustine, M. Gopikrishna, and S. Raman, "Dual MIMO antenna system for 5G mobile phones, 5.2 GHz WLAN, 5.5 GHz WiMAX and 5.8/6 GHz WiFi applications," *IEEE Access*, vol. 9, pp. 106734-106742, 2021.
- [5] H. D. Chen, Y. C. Tsai, C. Y. D. Sim, and C. Kuo, "Broadband eight-antenna array design for sub-6 GHz 5G NR bands metal-frame smartphone applications," *IEEE Antennas Wireless Propag. Lett.*, vol. 19, no. 7, pp. 1078-1082, 2020.
- [6] X. T. Yuan, Z. Chen, T. Gu, and T. Yuan, "A wideband PIFA-pair-based MIMO antenna for 5G

- smartphones,” *IEEE Antennas Wireless Propag. Lett.*, vol. 20, no. 3, pp. 371-375, 2021.
- [7] M. Shafi, A. F. Molisch, P. J. Smith, T. Haustein, P. Zhu, P. De Silva, F. Tufvesson, A. Benjebbour, and G. Wunder, “5G: A tutorial overview of standards, trials, challenges, deployment, and practice,” *IEEE J. Selected Areas Commun.*, vol. 35, no. 6, pp. 1201-1221, 2017.
- [8] H. Zou, Y. Li, B. Xu, Y. Chen, H. Jin, G. Yang, and Y. Luo, “Dual-functional MIMO antenna array with high isolation for 5G/WLAN applications in smartphones,” *IEEE Access*, vol. 7, pp. 167470-167480, 2019.
- [9] D. Serghiou, M. Khalily, V. Singh, A. Araghi, and R. Tafazolli, “Sub-6 GHz dual-band  $8 \times 8$  MIMO antenna for 5G smartphones,” *IEEE Antennas Wireless Propag. Lett.*, vol. 19, no. 9, pp. 1546-1550, 2020.
- [10] L. Sun, H. Feng, Y. Li, and Z. Zhang, “Compact 5G MIMO mobile phone antennas with tightly arranged orthogonal-mode pairs,” *IEEE Trans. Antennas Propag.*, vol. 66, no. 11, pp. 6364-6369, 2018.
- [11] W. Jiang, B. Liu, Y. Cui, and W. Hu, “High-isolation eight-element MIMO array for 5G smartphone applications,” *IEEE Access*, vol. 7, pp. 34104-34112, 2019.
- [12] X. T. Yuan, W. He, K. D. Hong, C. Z. Han, Z. Chen, and T. Yuan, “Ultra-wideband MIMO antenna system with high element-isolation for 5G smartphone application,” *IEEE Access*, vol. 8, pp. 56281-56289, 2020.
- [13] H. F. Abutarboush, W. Li, and A. Shamim, “Flexible-screen-printed antenna with enhanced bandwidth by employing defected ground structure,” *IEEE Antennas Wireless Propag. Lett.*, vol. 19, no. 10, pp. 1803-1807, 2020.
- [14] D. Gao, Z. X. Cao, S. D. Fu, X. Quan, and P. Chen, “A novel slot-array defected ground structure for decoupling microstrip antenna array,” *IEEE Trans. Antennas Propag.*, vol. 68, no. 10, pp. 622-628, 1971.
- [15] R. Harrington and J. Mautz, “Theory of characteristic modes for conducting bodies,” *IEEE Trans. Antennas Propag.*, vol. 19, no. 5, pp. 7027-7038, 2020.
- [16] J. Dong, S. Wang, and J. Mo, “Design of a twelve-port MIMO antenna system for multi-mode 4G/5G smartphone applications based on characteristic mode analysis,” *IEEE Access*, vol. 8, pp. 90751-90759, 2020.
- [17] Y. Q. Hei, J. G. He, and W. T. Li, “Wideband decoupled 8-element MIMO antenna for 5G mobile terminal applications,” *IEEE Antennas Wireless Propag. Lett.*, vol. 20, no. 8, pp. 1448-1452, 2021.
- [18] H. Arai, *Measurement of Mobile Antenna Systems*. London, U.K.: Artech House, 2001.
- [19] *IEEE Recommended Practice for Determining the Peak Spatial-Average Specific Absorption Rate (SAR) in the Human Head from Wireless Communications Devices: Measurement Techniques*, IEEE Standard-1528, Dec. 2003.
- [20] S. H. Kiani, A. Altaf, M. Abdullah, F. Muhammad, N. Shoaib, M. R. Anjum, R. Damaševičius, and T. Blažauskas, “Eight element side edged framed MIMO antenna array for future 5G smart phones,” *Micromachines*, vol. 11, no. 11, 2020.
- [21] L. Chang, G. Zhang, and H. Wang, “Dual-band antenna pair with lumped filters for 5G MIMO terminals,” *IEEE Trans. Antennas Propag.*, vol. 69, no. 9, pp. 5413-5423, 2021.
- [22] L. Cui, J. L. Guo, Y. Liu, and C. Y. D. Sim, “An 8-element dual-band MIMO antenna with decoupling stub for 5G smartphone applications,” *IEEE Antennas Wireless Propag. Lett.*, vol. 18, no. 10, pp. 2095-2099, 2019.
- [23] Y. Li, C. Y. D. Sim, Y. Luo, and G. Yang, “High-isolation 3.5 GHz eight-antenna MIMO array using balanced open-slot antenna element for 5G smartphones,” *IEEE Trans. Antennas Propag.*, vol. 67, no. 6, pp. 3820-3830, 2019.



**Yonghao Wang** received his bachelor's degree in communication engineering from Shandong University of Science and Technology in Qingdao, China in July 2020. From September 2020, he studies for a master's degree in electronic and communication engineering at Inner Mongolia University, Hohhot. China. His research interests are to research and design 5G miniaturized high isolation dual band MIMO antenna for mobile phone.



**Xin Wang** received a doctor's degree in engineering in Instrument Science and technology of Zhong-bei University, she is currently working in the College of Electronic Information engineering, Inner Mongolia University, Hohhot. China. Her research interests are micro nano RF devices (antennas, filters, couplers, etc.), metamaterial antenna.



**Junlin Wang** received a doctor's degree in engineering in Instrument Science and technology of Zhong-bei University. He is currently working in the College of electronic information engineering, Inner Mongolia University, Hohhot, China. His research interests are micro nano RF devices (antennas, filters, couplers, etc.), metamaterial antenna.



**Rui Shao** received a bachelor's degree in communication engineering from Shandong University of Technology, Zibo, China, in July 2020. From September 2020, she studies for the master's degree of Information and Communication Engineering at Inner Mongolia University, Hohhot, China. Her research interests are to research and design 5G high isolation MIMO antenna.

# Triple Bands UWB Antenna with Minimum Printed Area for Power Harvesting Applications

Nourhan D. Sehsah<sup>1</sup>, Tamer G. Abouelnaga<sup>1,2</sup>, and Hamdi A. Elmikati<sup>3</sup>

<sup>1</sup>Higher Institute of Engineering and Technology, Kafr Elsheikh, Egypt  
nourdiab1010@gmail.com, tamer@eri.sci.eg

<sup>2</sup>Microstrip Circuits Department  
Electronics Research Institute, Cairo 4473221, Egypt

<sup>3</sup>Faculty of Electronic Engineering, Mansoura University, Mansoura 35516, Egypt  
h.elmikati@gmail.com

**Abstract** – In this paper, a triple-band ultra-wideband UWB eight elements monopole antenna array is proposed. This antenna array is designed with the minimum printed area and is prepared for wireless local area network (WLANs) power harvesting applications. It covers the bands of 2.4 GHz and 5 GHz, which makes it suitable for Wi-Fi frequencies to harvest their power. The eight-element antenna array dimensions are 28.5 cm by 15 cm. These dimensions are chosen for the mini-solar cell integration process. Low-cost FR4 material is used as a substrate. The proposed antenna's measured reflection coefficient is compared with its simulated counterpart and is founded in good harmony.

**Index Terms** – Antenna, monopole, power harvesting, WLAN.

## I. INTRODUCTION

In previous research, several antennas are proposed for energy harvesting applications. Wi-Fi technology is commonly used in homes, offices, cafes, etc. 2.4 GHz and 5 GHz are used by the Wi-Fi networks. Upper and lower WLAN frequency bands are extended to (5.725 - 5.825) GHz and (5.15 - 5.35) GHz, respectively [1]. Radio-frequency RF energy can be harvested by A novel broadband CPW-fed fractal [2] and promoted to harvest energy at WiMAX, LTE 2600, Wi-Fi 2.4 GHz, WLAN, ISM, and 5G frequency bands [3, 4], a dual-band rectifier with broad-band  $1 \times 4$  quasi-Yagi antenna that used in same application of harvesting has printed area of 9814 mm<sup>2</sup> [5]. In [6] the antenna was increased Front to a Back (F/B) ratio with a printed area of 2471.38 mm<sup>2</sup>, but the DSRMA [7] with a printed area of 4775 mm<sup>2</sup>, and in [8] is 1476 mm<sup>2</sup>. The radiation patterns of omnidirectional antennas have a good performance when three pairs of dipole radiators are located back-to-back [9], also preferable to harvesting RF energy from ambient sources effi-

ciently [10]. Decent RF-to-DC conversion efficiency was achieved between 40%–60% at 0 dBm by a double-sided Printed monopole antenna that has a printed area of 9053 mm<sup>2</sup> [11]. The energy harvester's main elements are the rectifier array and antenna array. The first was responsible for converting the RF energy to DC and the last was for capturing the RF waves. The energy harvester can be combined with a dual-band microstrip patch antenna and DC voltage measured at the output [12].

The main challenge is to obtain a high-efficiency and miniature-zed antenna array [13]. Table 1 shows a comparison among different proposed antenna structures that were used in RF energy harvesting. According to the equation of Friis transmission, the harvested power can be estimated by [14–16] as

$$\frac{P_r}{P_t} = \left(\frac{\lambda}{4\pi D}\right)^2 G_t G_r, \quad (1)$$

where  $G_r$  is the gain of the receiver antenna,  $G_t$  is the gain of the transmitter antenna,  $P_t$  is the transmitted power,  $P_r$  is the received Power,  $\lambda$  is the wavelength of the electromagnetic signal, and  $D$  is the distance between the transmitter and receiver antennas. This paper aims to introduce a UWB antenna with a minimum printed area for power harvesting applications without losing the omnidirectional radiation properties. Three designs are introduced and compared with each other. These designs are circular patch monopole antenna, triple UWBs monopole antenna, and triple UWBs monopole antenna with the minimum printed area. Minimum printed area of 1624.56 mm<sup>2</sup> is obtained based on the current distribution investigation. The proposed antennas are compared with each other for their suitability for power harvesting operation and visibility to be integrated with a solar cell unit. The candidate antenna structure is used to develop an eight elements antenna array. The array dimensions are designed to be

Table 1: Previous power harvesting antennas structures and parameters

Ref. [5]		
Printed area (mm <sup>2</sup> )	9814	
Frequency bands (GHz)	1.8–2.2 GHz	
Gain (dBi)	10.9 dB at 1.85 GHz and 13.3 dB at 2.15 GHz	
Directivity (dBi)	Unspecified	
3 dB BW	E-plane	30.0 deg at 1.85 GHz and 20.0 deg at 2.15 GHz
	H-plane	100.0 deg at 1.85 GHz and 82.0 deg at 2.15 GHz
Ref. [6]		
Printed area (mm <sup>2</sup> )	2471.38	
Frequency bands (GHz)	1.95–2.45 GHz	
Gain (dBi)	8.3 dB at 1.95 GHz and 7.8 dB at 2.45 GHz	
Directivity (dBi)	Unspecified	
3 dB BW	E-plane	65.9 deg at 1.95 GHz and 83.9 deg at 2.45 GHz .
	H-plane	81.5 deg at 1.95 GHz and 75.1 deg at 2.45 GHz.
Ref. [7]		
Printed area (mm <sup>2</sup> )	4775	
Frequency bands (GHz)	(0.8–1.05) GHz, (1.6–2.2) GHz, and (2.4–3) GHz	
Gain (dBi)	15.8 dB at 1.6 GHz	
Directivity (dBi)	Unspecified	
3 dB BW	E-plane	110 deg
	H-plane	Unspecified
Ref. [8]		
Printed area (mm <sup>2</sup> )	1476	
Frequency bands (GHz)	2.4–2.5 GHz	
Gain (dBi)	Unspecified	
Directivity (dBi)	Unspecified	
3 dB BW	E-plane	89.0 deg
	H-plane	98.0 deg
Ref. [11]		
Printed area (mm <sup>2</sup> )	9053	
Frequency bands (GHz)	0.85–5.5 GHz	
Gain (dB)	5.3 dBi	
Directivity (dBi)	Unspecified	
3 dB BW	E-plane	39.0 deg
	H-plane	Omni direction

integrated with a solar cell unit to improve its efficiency and to maintain its transparency as much as possible. Our goal is to harvest the greatest power from the Wi-Fi bands (2.4 to 2.5) GHz and (5.1 to 5.8) GHz [17]. The antenna reflection coefficient is measured and compared with its simulated counterpart. Also, the radiation properties of the proposed antenna array are investigated for their power harvesting application suitability.

Table 1 shows the difficulty to cover the Wi-Fi bands with the minimum printed area and omnidirectional characteristics.

## II. MONOPOLE ANTENNA DIFFERENT STRUCTURES, DESIGN, AND SIMULATION

For Wi-Fi RF power harvesting purposes, a three different antenna structures are designed and investigated. The same FR4 substrate with a dielectric constant of 4.4, loss tangent of 0.02, and thickness of 1.6 mm at a frequency of 1 GHz is used for all antennas. The proposed three structures are compared to each other and the most candidate one is used to be integrated with a solar cell unit.

### A. Circular disk monopole antenna

Figure 1 shows the printed monopole antenna that is proposed to collect Wi-Fi RF power, efficiently. The radius of radiating patch can be calculated by [18] as

$$R = \left( \frac{3.2 \text{ GHz}}{f_L \times k} \right) - \left( \frac{4 \times P}{9} \right), \quad (2)$$

where  $P$  is the gap between the feedline length and ground plane length,  $K = 1.15$  constant, and  $f_L$  is lower

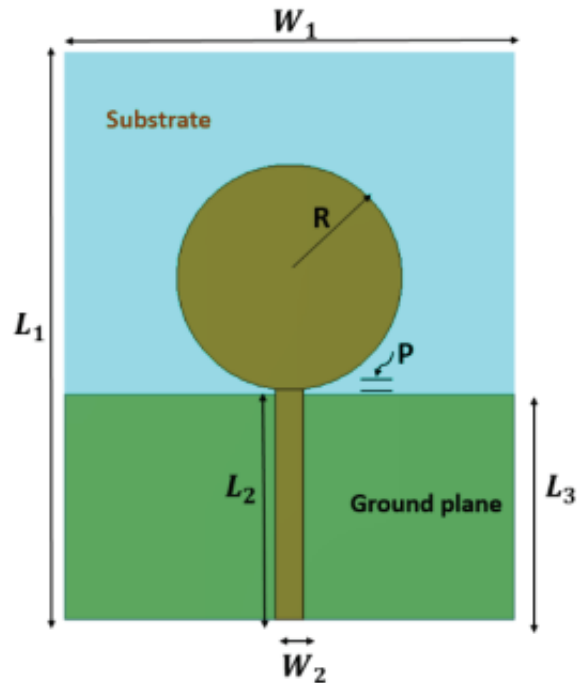


Fig. 1. Circular monopole antenna.

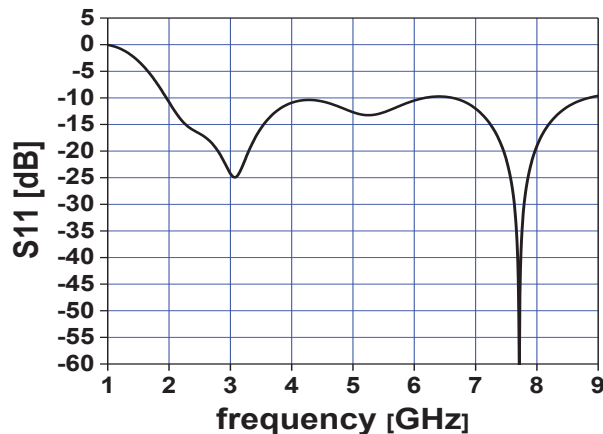


Fig. 2. (a) Circular patch monopole antenna reflection coefficient versus frequency.

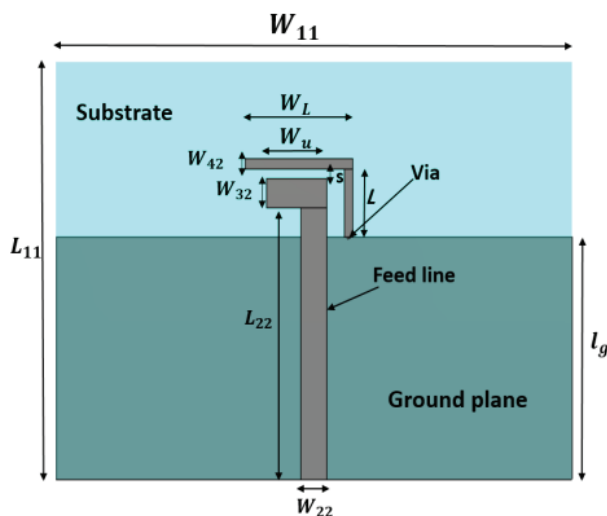


Fig. 2. (b) Circular patch monopole antenna current distribution at 3.1 and 7.7 GHz.

cut-off frequency. Considering  $F_L$  of 2 GHz, the patch radius is found to be 11.8 mm. The feed line width is calculated using [19] and found to be 3 mm. Other dimensions are optimized using the CST simulator and are found to be  $L_1 = 60.4$  mm (substrate length),  $W_1 = 48$  mm (Substrate width),  $L_2 = 24$  mm (ground plane length),  $L_3 = 24.5$  mm (feed line length),  $W_2 = 3$  mm (feed line width), and  $R = 12$  mm (circular patch radius). This type of monopole antenna suffers from a large occupation area which reaches  $525.89 \text{ mm}^2$  at the top and  $1152 \text{ mm}^2$  at the bottom. Figure 2 (a) shows the simulated return loss ( $S_{11}$ ) and it is observed that the bandwidth is extended from 2 GHz to 9 GHz, also current distribution and radiation pattern appear in Figures 2 (b) and (c) at frequencies 3.1 GHz and 7.7 GHz

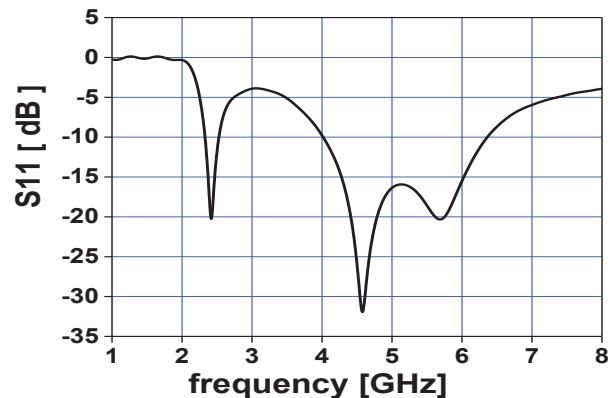


Fig. 2. (c) Circular patch monopole antenna radiation pattern at 3.1 and 7.7 GHz.

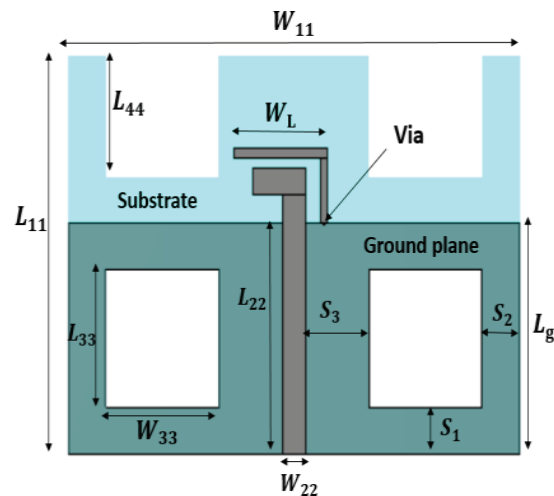


Fig. 3. Triple bands monopole antenna.

## B. Triple bands planar monopole antennas

Based on [20], a triple-band monopole antenna with a shorted parasitic inverted  $-L$  wire is designed to cover RF frequency bands at 2.4 GHz, 5.2 GHz, and 5.8 GHz, Figure 3. The reflection coefficient is shown in Figure 4 (a), while the current distribution and radiation pattern at resonant frequencies of 2.43 GHz, 4.6 GHz, and 5.7 GHz are shown in Figures 4 (b) and (c). Table 2 shows the dimensions of the proposed antenna in mm, and a radius equal to 0.2 mm.

Table 3 shows the effect of varying the length of the ground plane  $L_g$  on the lower (2.4 - 2.5) GHz and the

Table 2: Proposed triple-band antenna geometry

$W_{11}$	$L_{11}$	$W_{22}$	$L_{22}$	$W_L$	$W_u$	$L_g$	$L$	$W_{32}$	$W_{42}$	$s$
60	43	3	28	12.5	7	25	7	3	1	1

Table 3: Different dimensions for  $L_g$  and B.W at each dimension  $w_L = 12.5$  mm and  $w_U = 7$  mm

$L_g$	B.W
27 mm	(2.52–2.62) GHz
26 mm	(2.48–2.59) and (4.73–6.64) GHz
25 mm	(2.41–2.55) and (3.84–6.55) GHz

Table 4: Different dimensions for  $w_L$  and B.W at each dimension  $L_g = 25$  mm and  $w_U = 7$  mm

$w_L$	B.W
12.3 mm	(2.45–2.57) and (3.86–6.56) GHz
12.5 mm	(2.42–2.55) and (3.84–6.55) GHz
13 mm	(2.35–2.48) and (3.83–6.53) GHz

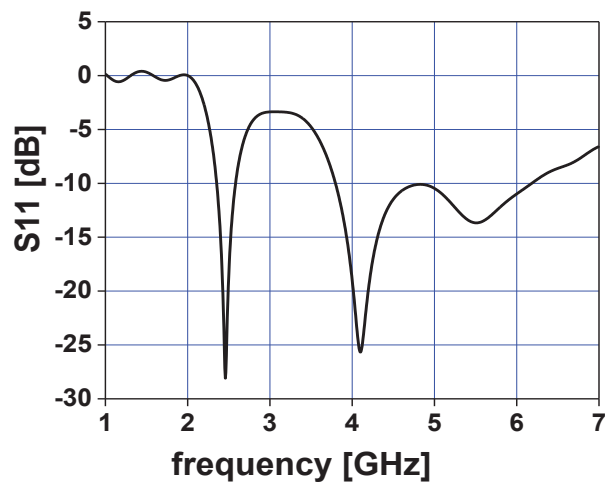


Fig. 4. (a) Triple bands monopole antenna reflection coefficient versus frequency.

higher (5.1-5.8) GHz frequency bands. Tables 4 and 5 show the effect of varying  $W_u$  and  $W_L$  on the lower and higher frequency bands. Bandwidth of 127 MHz (2.418-2.545) GHz and 2.702 GHz are obtained when  $L_g$ ,  $W_L$ , and  $W_u$  are chosen to be 25 mm, 12.5 mm, and 7 mm respectively

**C. Triple bands planar monopole antennas rectangular slots**

Based on Section II-B, the above elements with  $W_L = 12.5$  mm is the main radiator that contributor to the frequency 2.43 GHz and 4.6 GHz and there is a strong cur-

Table 5: Different dimensions for  $w_U$  and B.W at each dimension  $w_L = 12.5$  mm and  $L_g = 25$  mm

$w_u$	B.W
6.7 mm	(2.41–2.54) and (3.87–6.66) GHz
7 mm	(2.41–2.55) and (3.84–6.56) GHz
7.5 mm	(2.43–2.56) and (3.82–6.39) GHz

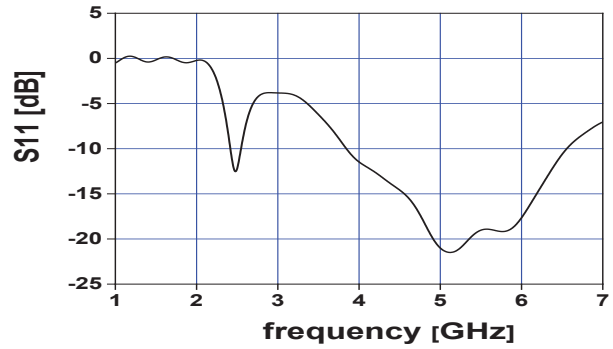


Fig. 4. (b) Triple bands monopole antenna current distribution at (1) 2.43, (2) 4.6, and (3) 5.7 GHz.

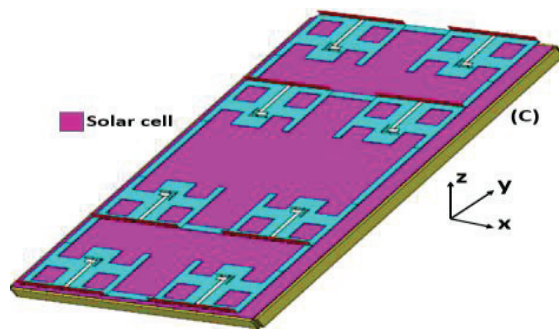
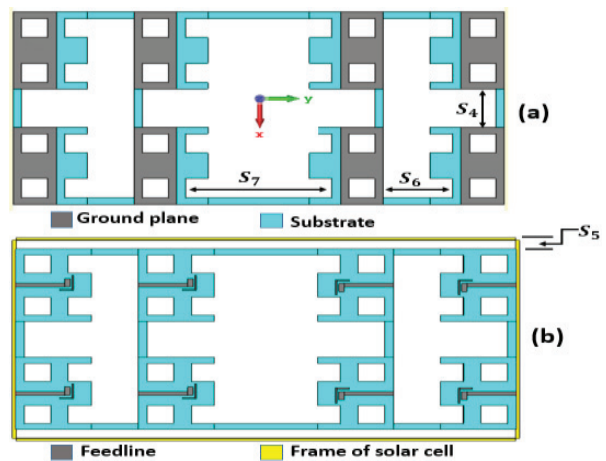


Fig. 4. (c) Triple bands monopole antenna radiation pattern at 2.43, 4.6, and 5.7 GHz, respectively.

rent at the via, but at 5.7 GHz the main radiator is the bottom element with  $W_u = 7$  mm, after that we removed the emptied places from the ground plane where there are no currents as shown in (Figure 5).

The resonant frequencies were shifted from (2.43 to 4.1) GHz, (4.6 to 4.1) GHz, and (5.7 to 5.5) GHz. The dimensions of the rectangular slots are  $L_{33} = 15$  mm and

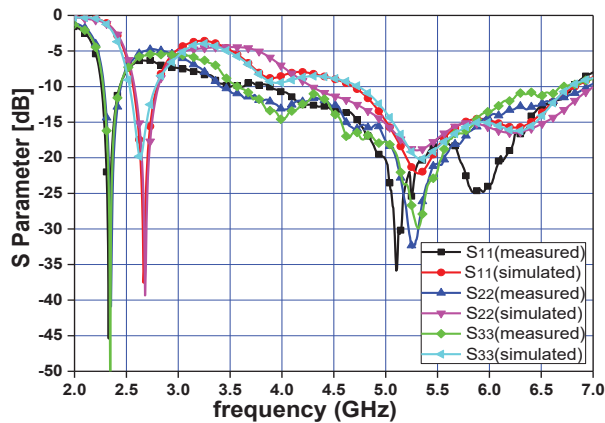


Fig. 5. Triple bands planar monopole antennas with rectangular slots.

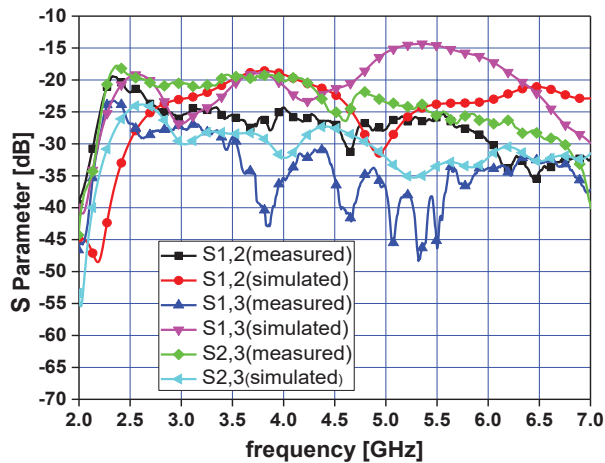


Fig. 6. (a) Triple bands monopole antenna with rectangular slots reflection coefficient versus frequency.

$W_{33}=15$  mm,  $L_{44}=13$  mm and spaced by  $S_3=10$  mm from the center of the feed line. The rectangular slot is also Separated by  $s_1=5$  mm and  $s_2=5$  mm from the substrate edges. Figure 6 shows the reflection coefficient, current distribution, and radiation pattern at 2.46, 4.1, and 5.5 GHz.

#### D. Comparison among the proposed structures

It's observed that the printed area of the triple bands' monopole antenna is less than that of the circular monopole by 3.2% as compared to 30% for the proposed triple bands with rectangular slots. Thus, the antenna turned to mini-transparent and overcome its main problem which is represented in a large area, Table 6.

Referring to Tables 1 and 6, it is observed the proposed triple bands with two slots monopole antenna present the minimum printed area with an almost omnidirectional radiation H-plane pattern.

Table 6: Comparison among proposed structure

Circular monopole antenna		
Printed area (mm <sup>2</sup> )	1677.89	
Frequency bands (GHz)	From 1.96 to 6.15 GHz and 6.64 to 8.83 GHz	
Gain (dB)	2.86 dB at 3.1 GHz and 6.218 dB at 7.7 GHz	
Directivity (dB)	3.4 dB at 3.1 GHz and 6.44 dB at 7.7 GHz	
3 dB BW	E-plane	98.4 deg at 3.1 GHz and 34.9 deg at 7.7 GHz
	H-plane	216.9 deg at 3.1 GHz and 71.9 deg at 7.7 GHz
Triple bands monopole antenna		
Printed area (mm <sup>2</sup> )	1624.56	
Frequency bands (GHz)	From 2.33 to 2.53 and 4.02 to 6.36	
Gain (dB)	2.32 dB at 2.43 GHz, 3.86 dB at 4.6 GHz, and 3.83 dB at 5.7 GHz	
Directivity (dB)	2.9 dB at 2.43 GHz, 4.05 dB at 4.6 GHz, and 4.156 dB at 5.7 GHz	
3 dB BW	E-plane	95.1 deg at 2.43 GHz, 125.6 deg at 4.6 GHz, and 146.0 deg at 5.7 GHz
	H-plane	285.8 deg at 2.43 GHz, 56.9 deg at 4.6 GHz, and 47.0 deg at 5.7 GHz
Triple bands monopole antenna with rectangular slots		
Printed area (mm <sup>2</sup> )	1174.56	
Frequency bands (GHz)	From 2.35 to 2.58 GHz and 3.79 to 6.14 GHz	
Gain (dB)	0.5 dB at 2.46 GHz, 2.467 dB at 4.1 GHz, and 2.915 dB at 5.5 GHz.	
Directivity (dB)	2.94 dB at 2.46 GHz, 3.9 dB at 4.1 GHz, and 4.167 dB at 5.5 GHz	
3 dB BW	E-plane	257.3 deg at 2.46 GHz, 124.0 deg at 4.1 GHz, and 50.5 deg at 5.5 GHz
	H-plane	95.2 deg at 2.46 GHz, 80.4 deg at 4.1 GHz, and 56.3 deg at 5.5 GHz

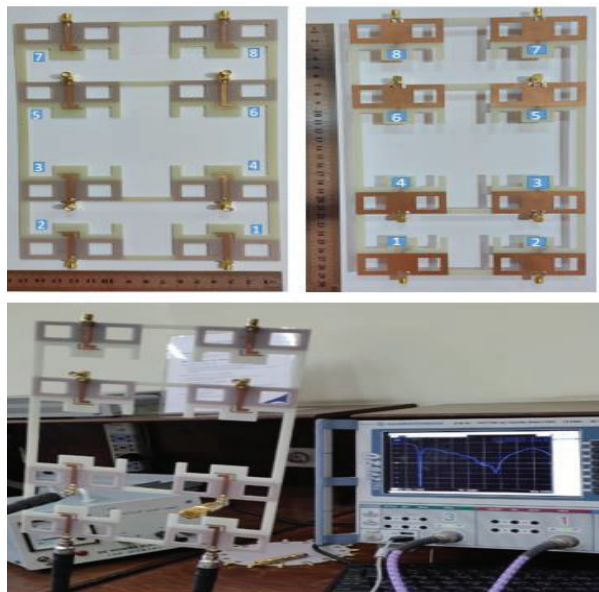


Fig. 6. (b) Triple bands monopole antenna with rectangular slots current distribution at (1) 2.46, (2) 4.1, and (3) 5.5 GHz.

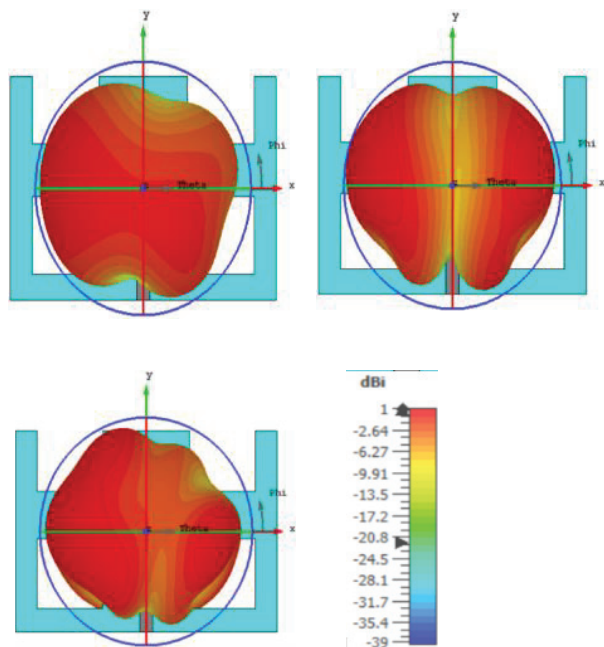


Fig. 6. (c) Triple bands monopole with rectangular slots radiation pattern at 2.46, 4.1, and 5.5 GHz, respectively.

### III. PROPOSED EIGHT-ELEMENT ANTENNA

The developed antenna (Section II-C) is used as an element of the 8-element antenna array. The dimensions of the array are set to be  $(165 \times 285) \text{ mm}^2$  which is the

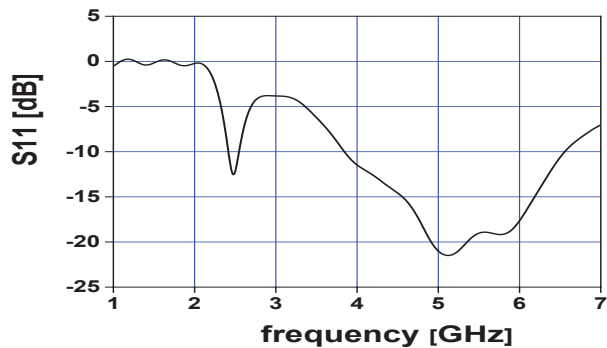


Fig. 7. Triple bands monopole antenna with rectangular slots integrated with the aforementioned mini-solar cell reflection coefficient.

same as the mini-solar cell unit which will be used to test the presence of the mini-solar cell material on antenna performance. The antenna array element is separated by the horizontal distance  $S_4=30 \text{ mm}$  and vertical distance  $S_6=27 \text{ mm}$ . Each four elements group is separated by a vertical distance  $S_7=59 \text{ mm}$ , and  $S_5=7.5 \text{ mm}$ , Figure 8.

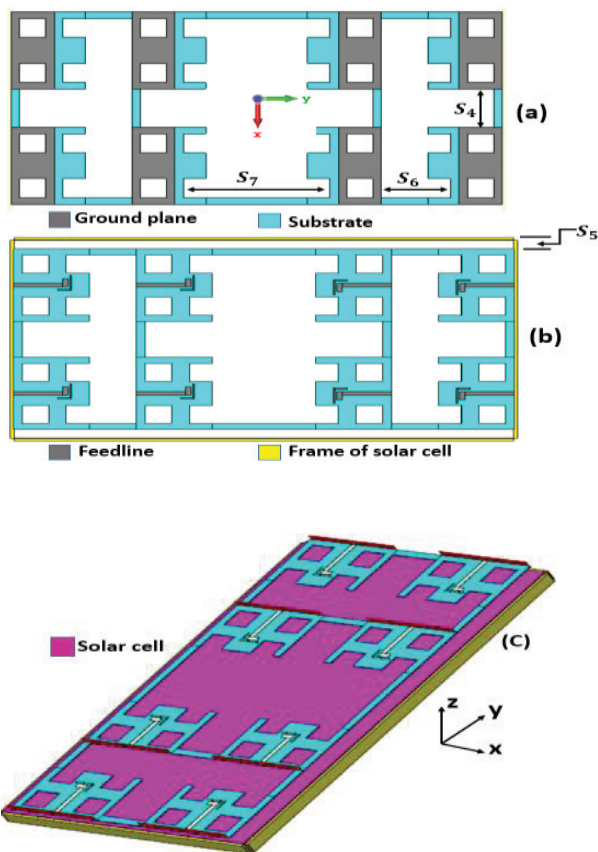


Fig. 8. Structure of proposed antennas: (a) bottom view; (b) top view; (c) antennas with eight-element.

Table 7: Gain, directivity, and efficiency at 2.44 GHz

At 2.44 GHz			
Ant. No.	G (dBi)	D (dBi)	Efficiency %
1	4.660	5.316	85.99
2	5.569	6.285	84.79
3	5.052	5.629	87.55
4	4.702	5.336	86.42
5	4.659	5.317	85.95
6	5.569	6.286	84.79
7	5.053	5.632	87.52
8	4.702	5.336	86.42

The solar cell material is considered to be glass with  $\epsilon_r=3.9$  and  $\tan\delta=0.0054$ . An aluminum metal frame is also considered.

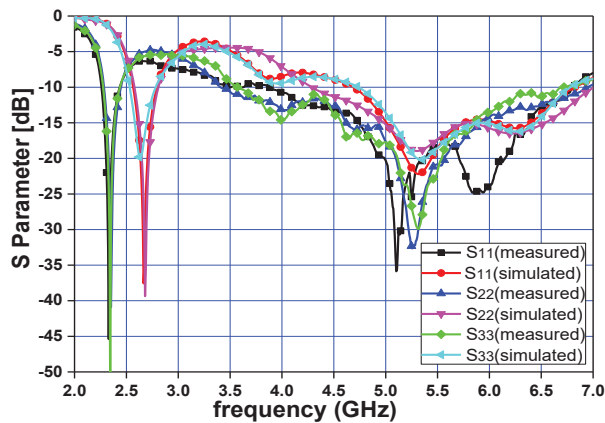


Fig. 9. Simulated and measured reflection coefficient of the proposed array.

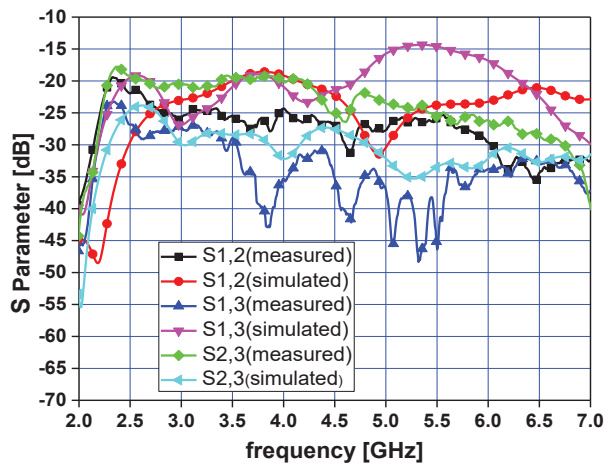


Fig. 10. Simulated and measured coupling of proposed antenna array.

Table 8: Gain, directivity, and efficiency at 5.44 GHz

At 5.44 GHz			
Ant. No.	G (dBi)	D (dBi)	Efficiency %
1	5.719	6.334	86.80
2	7.047	7.737	85.30
3	6.388	7.054	85.80
4	6.353	7.093	84.34
5	5.727	6.342	86.80
6	7.045	7.736	85.30
7	6.379	7.045	85.79
8	6.354	7.093	84.34

Figure 7 shows a bandwidth that extends from 2.35 GHz to 2.58 GHz and from 3.79 GHz to 6.14 GHz is achieved when the antenna is integrated with the aforementioned mini-solar cell. The simulated and measured reflection and coupling coefficients are shown in Figures 9 and 10, respectively.

The simulated bandwidth extends from 2.35 GHz to 2.58 GHz and 3.79 GHz to 6.14 GHz as compared with the measured counterpart which extends from 2.26 GHz to 2.42 GHz. and from .4.18 GHz to 6.8GHz. A minimum isolation of  $-20$  dB is obtained over the operating frequency lower and higher bands.

R&S ZVB 20 Vector Network Analyzer is used to measure the reflection coefficient of the proposed antenna array elements, Figure 11. The radiation pattern of the proposed antenna array when integrated with the solar cell unit is investigated shown in Figure 12

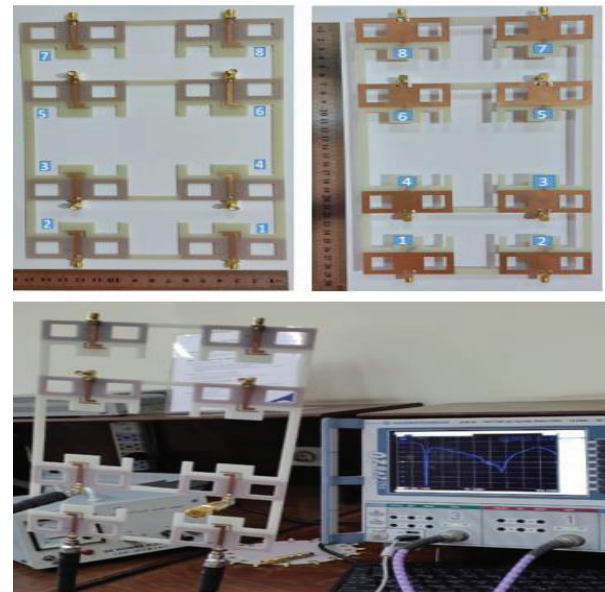


Fig. 11. Fabricated antenna array elements with VNA.

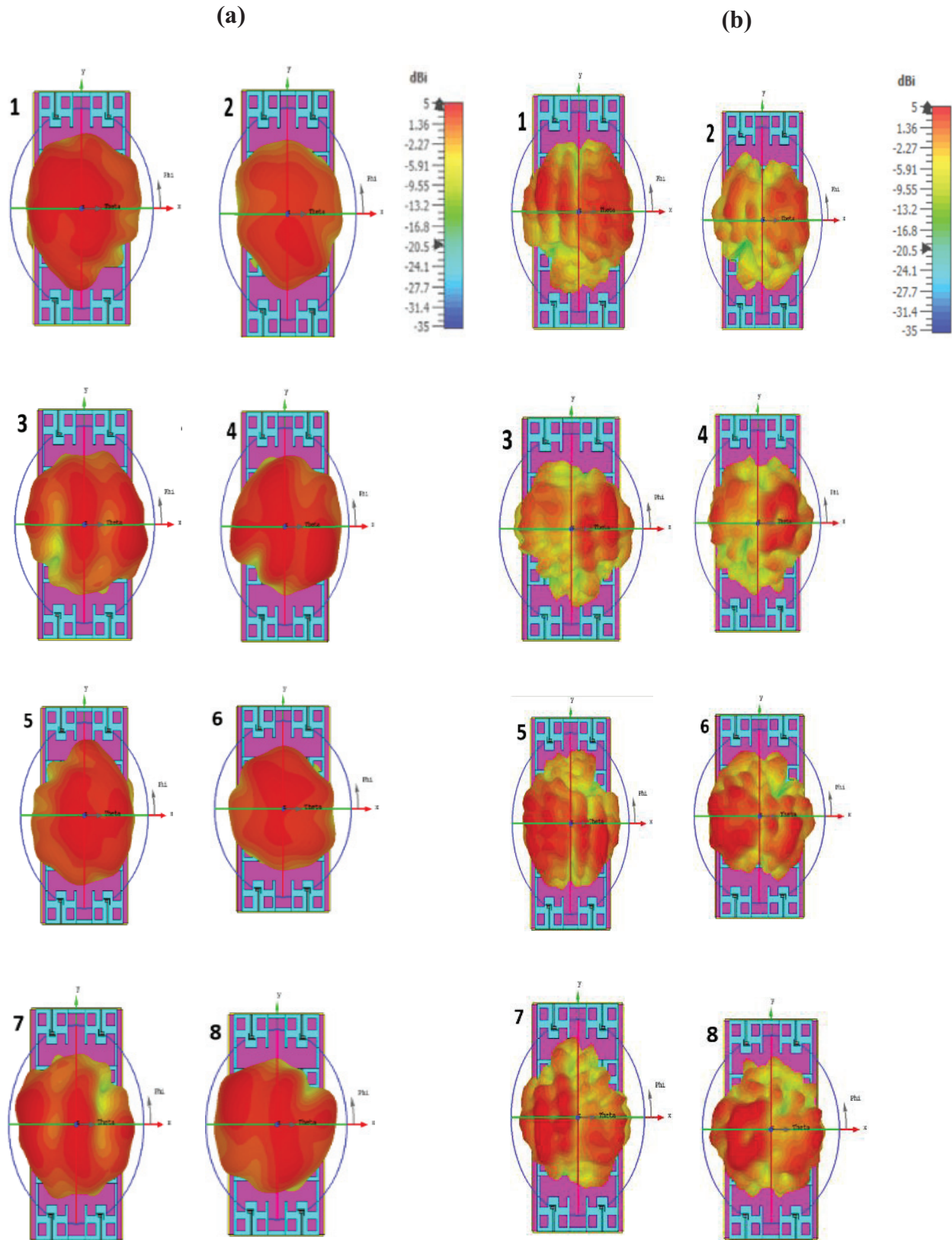


Fig. 12. (a) Radiation pattern at 2.44 GHz.

Fig. 12. (b) Radiation pattern at 5.44 GHz.

at resonance frequencies of 2.44 GHz and 5.44 GHz. Tables 7 and 8 show the gain, directivity, and efficiency of each antenna element at 2.44 GHz and 5.44 GHz, respectively.

#### IV. CONCLUSION

This paper presented a transparent 8- elements antenna array that is ready to be merged with solar cell units. It is designed to be operated at the Wi fi bands of 2.4 GHz and 5 GHz. Two frequency bands of 2.4 GHz to 2.5 GHz and 5.1 GHz to 5.8 GHz with acceptable reflection coefficients below  $-10$  dB are obtained. Good agreement between experimental and simulated results is obtained. This antenna array is intended for collecting the largest amount of power from several wireless communication bands by using eight antenna elements with suitable parameters in terms of Gain and radiation pattern.

#### REFERENCES

- [1] K. S. Ryu and A. A. Kishk, "UWB antenna with single or dual band notches for lower WLAN," *Antennas Propagat.*, vol. 57, no. 12, pp. 3942-3950, Dec. 2009.
- [2] X. Bai, J.-W. Zhang, L.-J. Xu, and B.-H. Zhao, "A broadband CPW fractal antenna for RF energy harvesting," *Applied Computational Electromagnetic Society (ACES) Journal*, vol. 33, no. 5, pp. 482-487, May 2018.
- [3] T. Hamza, B. Adel, and B. M. Reda, "A low-cost elliptical triple-band antenna for RF energy harvesting applications," in *Proc. Int. Conf. Renewable Energies Developing Countries*, Marrakech, Morocco, pp. 29-30, Jun. 2020.
- [4] N. A. Eltresy, A. M. Abd Elhamid, D. M. Elsheakh, H. M. Elshennawy, and E. A. Abdallah, "Silver sandwiched ITO based transparent antenna array for RF energy harvesting in 5G mid-range of frequencies," *IEEE Access*, vol. 9, pp. 49476-49486, Mar. 2021.
- [5] H. Sun, Y. X. Guo, M. He, and Z. Zhong, "A dual-band rectenna using broad-band yagi antenna array for ambient RF power harvesting," *IEEE*, vol. 12, pp. 918-921, Jul. 2013.
- [6] M. Aboulalaa, A. B. Abdel-Rahman, A. Allam, and H. Elsadek, "Design of dual band microstrip antenna with enhanced gain for energy harvesting applications," *IEEE, Antennas Wirel. Propag. Lett.*, vol. 16, pp. 1622-1626, Jan. 2017.
- [7] M. Kurvey and A. Kunte, "Design and optimization of stepped rectangular antenna for RF energy harvesting," in *Proc. IEEE Int. Conf. Commun. Inform. Comput. Technol.*, Mumbai, India, pp. 2-3, Feb. 2018.
- [8] E. L. Chuma, L. T. Rodriguez, Y. Lano, L. L. B. Roger, and M. A. S. Soriano, "Compact rectenna based on a fractal geometry with a high conversion energy efficiency per area," *IEEE, IET Microwaves, Antennas Propag.*, vol. 12, pp. 173-178, 2018.
- [9] Y. J. Wu, B. H. Sun, J. F. Li, and Q. Z. Liu, "Triple-band omni-directional antenna for WLAN application," *Progress Electromagn. Res. PIER*, vol. 76, pp. 477-484, Aug. 2007.
- [10] N. Mao, D. Yang, and Y. Tang, "A dual circularly polarized rectenna with wide-beam," in *Proc. IEEE, Int. Symp. Antennas Propag. (ISAP)*, Hangzhou, China, pp. 3-6, Dec. 2018.
- [11] S. Agrawal, M. S. Parihar, and P. N. Kondekar, "Broadband rectenna for radio frequency energy harvesting application," *IETE J. Res.*, vol. 64, pp. 347-353, Aug. 2017.
- [12] O. Amjad, S. W. Munir, S. T. Imeci, and A. Ö. Ercan, "Design and implementation of dual band microstrip patch antenna for WLAN energy harvesting system," *Applied Computational Electromagnetic Society (ACES) Journal*, vol. 33, no. 7, pp. 746-751, Jul. 2018.
- [13] U. Olgun, C. C. Chen, and J. L. Volakis, "Design an efficient ambient Wi-Fi energy harvesting system," *IET Microwaves, Antennas Propag.*, vol. 6, pp. 1200-1206, Mar. 2012.
- [14] S. Manavalan and P. Anumuthu, "Design of tri-band microstrip patch rectenna for radio frequency energy harvesting system," *IETE, J. Res.*, pp. 1-6, 2019.
- [15] J. A. Shaw, "Radiometry and the Friis transmission equation," *AAPT, Amer. J. Phys.*, vol. 81, no. 1, pp. 33-37, Jan. 2013.
- [16] G. A. Thiele, "Friis transmission over a ground-plane," *IEEE, Antennas Propag. Mag.*, vol. 61, pp. 72-76, Feb. 2019.
- [17] A. Desai, T. Upadhyaya, M. Palandoken, R. Patel, and U. Patel, "Dual band optically transparent antenna for wireless application," in *IEEE, Proc. Asia Pacific Microwave Conf.*, Kuala Lumpur, Malaysia, pp. 960-963, 13-16, Nov. 2017.
- [18] N. Anveshkumar and A. S. Gandhi, "Design and performance analysis of a modified circular planar monopole UWB antenna," in *Proc. IEEE, Int. Conf. Comput. Commun. Netw. Technol. (ICCCNT)*, Delhi, India, pp. 3-5, Jul. 2017.
- [19] R. Garg, I. Bahl, and M. Bozzi, *Microstrip Lines and Slotlines*. Norwood, MA, USA: Artech House, 2013.
- [20] J. Y. Jan and L. C. Tseng, "Small planar monopole antenna with a shorted parasitic inverted-L wire for wireless communications in the 2.4-, 5.2-, and 5.8 GHz bands," *IEEE Trans. Antennas Propag.*, vol. 52, no. 7, pp. 1903-1905, Jul. 2004.



**Tamer G. Abouelnaga** was born in Nov. 1976. He received his B.Sc. degree (1994–1999, honors degree) in Electronics Engineering from Menofiya University, Egypt, M.Sc. degree (2002–2007), and Ph.D. degree (2007–2012) in Electronics and Communications from Ain Shams University. He works as a Researcher (2012–2017) and an Associate Professor (2018 till now) in Microstrip Circuits Department, Electronics Research Institute, Egypt. He works as Students Affairs Vice Dean (2018–2019) and Community Service and Environmental Development Vice Dean (2019 till now) – Higher Institute of Engineering and Technology – Kafr Elsheikh City. He had published 37 papers, 26 papers in peer-refereed journals, and 11 papers in international conferences in the area of RFID, horn, MIMO, 5G, and DRA antennas. His current research interests are in hyperthermia breast cancer therapy and human body implanted antennas.



**Nourhan D. Sehsah** is a Post Graduate Student (master), at Mansoura University, Egypt. She was born in Kafr El-Shiekh, Egypt in Mar, 1988. She received a B.Sc. degree in Electronics and Communication Engineering from HIET, Kafr El-Shiekh, Egypt in May 2012. She is a demonstrator at the Higher Institute of Engineering

and Technology (HIET) in Kafr El-Shiekh, Egypt in the period from 2013 to 2022. Her current research interest on Harvesting power applications with the minimum transparent printed area.



**Hamdi A. Elmikati** was born in January 1943, he is an Emeritus Professor of Electromagnetic Waves at the Department of Communications and Electronics Engineering, Mansoura University - Egypt. He received the BSc and MSc degrees in Electrical Engineering from Alexandria University - Egypt in 1964 and 1969 respectively and the Ph.D. degree in Electrical Engineering from Leningrad Polytechnic Institute - Russia in 1974. He is a Life Senior Member of the IEEE, a Member of the Institute of Physics – the USA, and a Member of the Optical Society of America (OSA). Professor Elmikati has held several positions: Full-Time Professor of Electromagnetic Waves and Head of the Department of Communications and Electronics Engineering, Mansoura University, Vice Dean and Dean of the Faculty of Engineering, Mansoura University. His research interests include: Computational Electromagnetics, numerical analysis, modelling and design of antennas, microwave passive devices, optical fibres and photonics. He has co-authored more than 90 research papers in international conferences and journals in the fields of microwave and optical communications engineering. He has supervised more than 60 PhD and MSc students.

# Design of a Novel Circularly Polarized MIMO Antenna with Enhanced Isolation for Ultra-wideband Communication

Lei Zhang, Quanyuan Feng, and Muhammad K. Khan

School of Information Science and Technology  
Southwest Jiaotong University, Chengdu 610031, China  
leizhang\_swjtu@163.com, fengquanyuan@163.com, Kabirawab@my.swjtu.edu.cn

**Abstract** – In this paper, we propose a circularly polarized (CP) ultra-wideband (UWB) MIMO antenna. Compared with common linearly polarized (LP) UWB antenna, the proposed antenna can excite circular polarization (CP) mode for WLAN communication and its impedance bandwidth can also fully cover UWB spectrum. It consists of identical circularly polarized antennas. Each unit adopts circular monopole with extended orthogonal rectangle patch to realize broadband and symmetrical rectangular ground with slot in the diagonal of each antenna unit to achieve circular polarization for WLAN band. It has a very compact size and the dimension is  $25 \times 51 \times 0.8 \text{ mm}^3$ . The impedance bandwidth of the proposed antenna is from 3.1 GHz to 13.5 GHz, with average gain of 4 dBi, fully covering UWB bandwidth and enhanced by 38%. At the same time, circular polarization is achieved by embedding two symmetrical rectangular slot structures in the two opposite corners of every antenna unit. The extended orthogonal rectangle patch is introduced to enhance impedance bandwidth and broaden axial ratio (AR) bandwidth. The measured 3 dB axial ratio (AR) bandwidth is 1.8 GHz (4.7-6.5 GHz), fully covering WLAN band. Meanwhile, the slit slot between antenna units and rectangular openings are introduced to achieve high isolation. The proposed antenna keeps ECC (envelope correlation coefficient) below 0.01, which showing good isolation and diversity characteristics. The proposed antenna can simultaneously operate in the UWB spectrum and exhibit circularly polarized (CP) radiation characteristic in WLAN.

**Index Terms** – Circular polarization (CP), compact, enhanced bandwidth, high isolation, multiple input and multiple output (MIMO), ultra-wideband (UWB).

## I. INTRODUCTION

In 2002, the FCC allowed the commercialization of 3.1-10.6 GHz band [1], then the ultra-wideband communication technology attracted the attention of many researchers and companies. UWB communication technology was first used in the military field, but nowadays

it is widely used in cell phone mobile communication, high-speed wireless communication in vehicle internet, high-precision radar and other fields [2, 3]. Ultra-wideband communication technology has the advantages of ultra-wide bandwidth, high transmission rate, large system capacity, low power consumption, high positioning accuracy, and anti-multipath interference [4]. In recent years, it has been rapidly developed and become one of the most popular wireless communication technologies.

Many researches studied on how to implement UWB technology. [5–9] reported various UWB monopole antennas. [5–7] achieved ultra-wideband in the 3.1-10.6 GHz band by using ring, circular, and rectangular patches, respectively. [8, 9] utilized inverted L-strip and fork shape structure to cover the UWB band. In most of the designs, ultra-wideband antennas in the frequency band are linear polarization (LP) propagation, and linearly polarized (LP) transceiver has high requirements for antenna placement, which usually must ensure that the polarization direction of the transmitter and receiver is the same, in order to avoid the impact of polarization mismatch. Therefore, the linearly polarized (LP) antenna is extremely susceptible to polarization mismatch and multipath interference in actual communication, which greatly reduces the reliability and quality of communication. Circular polarization (CP) can effectively reduce these deficiencies of linear polarization and improve the stability of the system. Some of the papers proposed design methods to achieve broadband or ultra-wideband circular polarization [10–17]. [10, 11] utilized open slot etched on the side of the coplanar ground to achieve wideband circular polarization in 3.3-3.8 GHz and 3.1-7.2 GHz separately. By embedding two symmetrical rectangular ground planes with L-shaped slots in diagonal corners of the slot, [12, 13] realized wideband circular polarization. In [14] and [15], structures of sequential phase network were adopted to achieve 5-6 GHz CP. [16] introduced an antipodal structure of four different strips with a microstrip line to excite two orthogonal modes and produced circular polarization in

a wide band of 4.4-7.7 GHz. Similarly, double-Y-shape coupling slots were introduced to achieve 3 dB axial ratio bandwidth (ARBW) of 3.58-6 GHz [17]. Although the bandwidth of circular polarization of many antennas has been improved a lot, most of -10 dB impedance bandwidth (IBW) still can not fully meet the UWB band.

Meanwhile, in practice, the permitted power spectral density is very low in the whole wide band, less than  $-41.3$  dBm/MHz [18]. So UWB system is vulnerable to multipath interference, leading to deterioration of the performance of the actual communication system. With the requirement of fast and stable high throughput of modern communication, MIMO technology has received a wide attention and been widely used. MIMO technology utilizes the diversity of multiple antenna transceivers, allowing the signal to be transmitted in multiple channels, which significantly reduces multipath fading and increases transmission capacity. Thus MIMO technology can improve the channel capacity, suppress multipath fading, and enhance the reliability of the system. The combination of ultra-wideband and MIMO technology can be a good solution to the problem of multipath fading and improve the capability of anti-interference and the robustness of system. Some papers combine ultra-wideband technology with MIMO technology to obtain a more high-speed and stable communication transmission process. [19–28] show relevant research progress but most of them are linearly polarized (LP). Some papers combine ultra-wideband technology with MIMO technology to obtain more high-speed and stable communication transmission but most of them are linearly polarized (LP) [19–23]. [19] utilized stub and Y-type defective ground structure to achieve linearly polarized UWB MIMO antenna. [20, 21] placed the antenna units orthogonally to enhance isolation to realize MIMO. [22, 23] introduced fence-type structure and utilized extended T-shaped stub separately to achieve compact MIMO UWB antenna. Currently, several recent papers are beginning to investigate how to achieve partial circular polarization in wideband or UWB band [24–28]. [24] utilized asymmetrical ground planes along the longitudinal axis of the microstrip line to achieve circular polarization in UWB band. Better isolation was achieved by increasing the spatial distance of the antenna unit, and resulted in a larger size. [25] incorporated hexagonal wide slot with a vertical arm and L-shaped radiators in the rectangular feeds to enhance isolation. [26] utilized circular-arc-shaped antenna with asymmetric ground plane to excite CP mode in the range of 1.75–4.75 GHz and orthogonal placement weakened the coupling of the antenna unit. Truncated corner square patches and parasitic periodic metallic plates were introduced to achieve CP radiation ranging from 5.08 GHz to 5.92 GHz and high isolation in [27]. [28] added rectangular inverted L-

type microstrip to support circular polarization and used defected ground structure to enhance isolation.

Some design methods for MIMO antennas have been discussed above, and methods for enhancing isolation have also been briefly mentioned. The following is a summary of currently used decoupling methods [29–39]. [29–31] utilized slots in the middle of ground to form defective ground to reduce mutual coupling. [32] placed the antenna units orthogonally and effectively improved isolation. [33–35] used open-stubs to enhance isolation. And [36] used neutralization line to enhance isolation. [37] placed the antenna units in the far-field region at the expense of size. H-shaped and meander-line electromagnetic band gap (EBG) structure were used for mutual coupling reduction [38, 39].

In this paper, we proposed a novel circularly polarized (CP) UWB MIMO antenna. The impedance bandwidth of the proposed antenna is 3.1-13.5 GHz, and achieve polarization radiation from 4.7 GHz to 6.1 GHz, completely covering the WLAN band. The prototype of the proposed antenna is  $25 \times 51 \times 0.8$  mm<sup>3</sup> and is compact compared with previous works. Common UWB MIMO antennas works in the way of linear polarization. The proposed antenna adopts extended orthogonal rectangle units and symmetrical rectangular ground with slot in the diagonal of each antenna unit to achieve circular polarization (CP) for WLAN band. And the AR bandwidth is wider than many current designs. To reduce coupling between antenna units, the slot in the middle of the ground and rectangular openings at both ends are utilized to decouple. The isolation of the proposed antenna is below -18 dB and in most of operating band less than -20 dB, showing high isolation overall. Meanwhile, ECC is below 0.01, showing excellent diversity characteristic compared with related designs. This paper presents the analysis and data results related to the antenna simulation and far-field test, including the S-parameter, current distribution, gain, ECC (envelope correlation coefficient), and DG (diversity gain). Antenna design and related analysis are discussed in the following sections. The results indicate the proposed antenna can excite circular polarization (CP) in WLAN band and is suitable for UWB wireless communication system.

## II. PROPOSED ANTENNA DESIGN AND ANALYSIS

### A. Circularly polarized antenna design

Figure 1 shows the design process of the circularly polarized ultra-wideband antenna, and the entire process of simulation design is carried out in HFSS (V18.0).

$$2 \times \pi \times r_{eff} \times L = \pi \times r^2, \quad (1)$$

$$f_L = \frac{c}{\lambda} = \frac{72}{L + r_{eff} + p}, \quad (2)$$

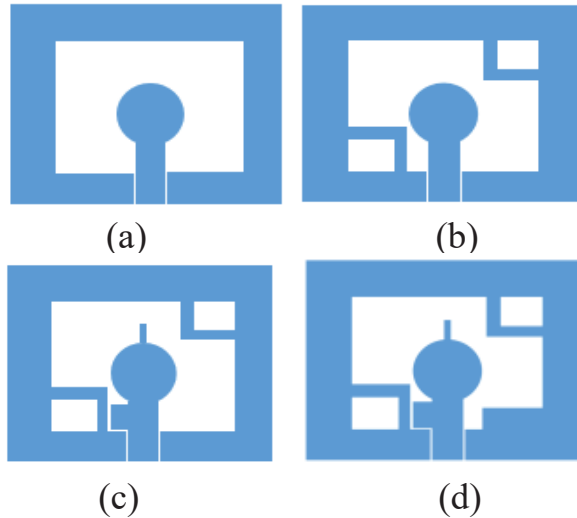


Fig. 1. The evolution of CP UWB antenna.

where  $f_L$  is the lowest radiation frequency,  $L$  is the diameter of the circular monopole,  $r_{eff}$  is the effective radius of an equivalent cylindrical monopole antenna,  $p$  is spacing between circular patch and floor (frequency is in GHz and size is in mm).

First, we adopt CPW fed circular patch with rectangular slot as the basis. The size of a circular patch can be estimated using the above formula. The introduced two symmetrical rectangular grounds with slot in the diagonal of the square slot help to converge to the 3-dB. The extended orthogonal rectangular branches of the circular can achieve the CP characteristic. And finally rectangular cell in the lower right corner further improves the current distribution to achieve circular polarization in WLAN. Figures 1 (a)–(d) show the iteration process of the antenna.

The original antenna consists of a rectangular slot and circular radiating patch fed by CPW. From Figure 2, we can see clearly that, in the initial design,  $S_{11}$  below  $-10$  dB ranges from 2.9 to 4.1 GHz, which is far from meeting the impedance bandwidth of UWB. And from Figure 3, we can see that ARBW deteriorates in the whole band, far greater than 3 dB. As shown in Figure 1 (b), although the impedance bandwidth is only expanded to the right by 1 GHz, the overall AR is improved to below 10 dB, when two symmetrical rectangular slot structures in the two opposite corners of every antenna unit is introduced. Further, two orthogonal rectangular branches extend from the top and side of the circular radiator and the impedance bandwidth and 3 dB ARBW are subsequently broaden and enhanced. As illustrated in Figures 2 and 3, the impedance bandwidth is broaden to 8.5 GHz and CP is realized from 4.9 GHz to 5.8 GHz. Finally, a rectangular patch is embedded in

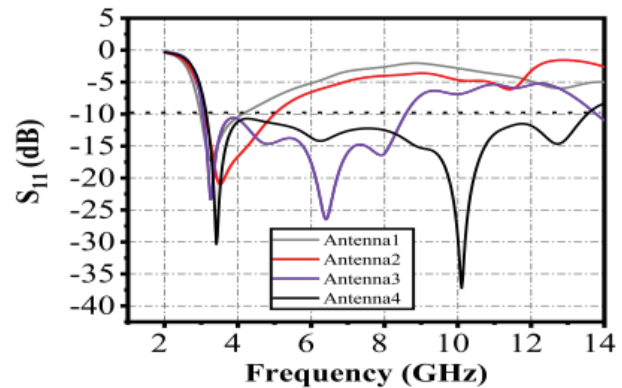


Fig. 2. Simulated  $S_{11}$ .

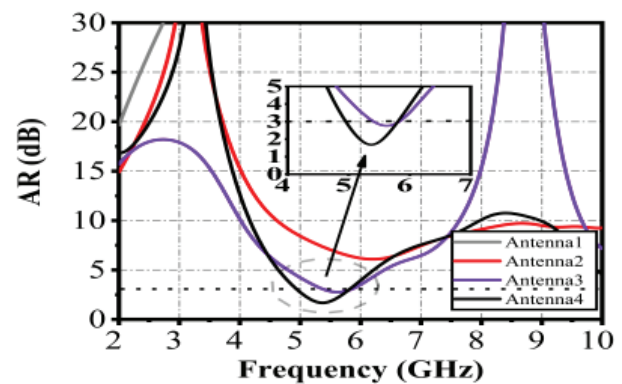


Fig. 3. Simulated axial ratio (AR).

lower right of the square slot.  $S_{11}$  is expanded to 13.5 GHz, from 3.1–13.5 GHz, which fully meets the UWB spectrum. And the AR bandwidth is further improved to cover the entire WLAN band.

To illustrate how the 3 dB ARBW increases with the design process, Figure 4 gives the amplitude ratio and phase difference between the horizontal and vertical components of the electric field in the major axis direction for Ant. 1–Ant. 4, respectively. Ideally, CP waves are generated by exciting two orthogonal modes with equal amplitude and a phase difference of  $90^\circ$ . For Ant.1, the amplitude ratio of the two electric field components is much greater than 10 in the entire frequency band, which does not satisfy the circular polarization and also the phase difference does not meet the requirement of  $90^\circ$  degree phase difference. As shown in Figure 4, with the symmetrical rectangular ground with slot in the diagonal of each antenna unit introduced, the amplitude ratio of the antenna drops considerably below 10 throughout the band, and below 5 around 5 GHz, while the phase relationship stabilizes between  $80^\circ$  and  $90^\circ$ . As can be seen from Figure 3, the antenna axis ratio has been improved considerably, indicating that the introduced structure can help well in achieving circular polarization characteris-

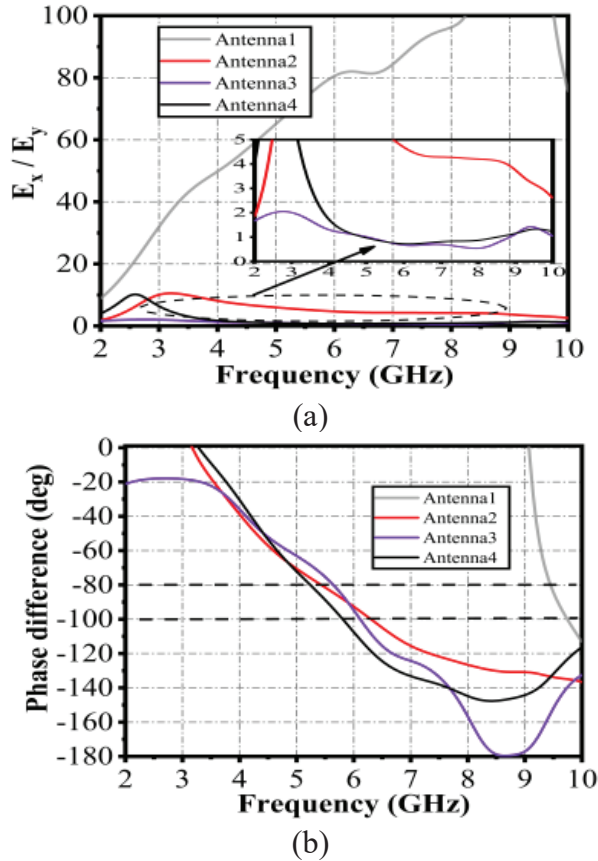


Fig. 4. Amplitude ratio and phase difference of the electric field. (a) Amplitude ratio. (b) Phase difference.

tics. With the introduction of the extended orthogonal rectangle patch, the amplitude ratio of the antenna is close to 1, showing that the magnitude of the horizontal and vertical components of the electric field antenna are nearly equal at this time. At the same time, the slope of the phase in 4.5-6 GHz is further decreased, resulting in an enhanced axial ratio bandwidth. Finally, the proposed antenna, shown in Figure 3, achieves 3 dB ARBW in 4.9-5.8 GHz with full coverage of the WLAN (5.2-5.8 GHz) band, and the phase difference and amplitude ratio are in accordance with the theoretical excitation of CP.

### B. Design of MIMO antenna

Based on the CP antenna above, the circularly polarized MIMO UWB antenna is proposed as shown in Figure 5. The dimension of the proposed antenna is  $25 \times 51 \times 0.8 \text{ mm}^3$ . The substrate of the proposed antenna is FR4 material with relative permittivity ( $\epsilon_r$ ) of 4.4 and loss tangent ( $\tan\delta$ ) of 0.02. And the antenna is fed by coplanar waveguide and connected to a SMA connector with  $50 \Omega$  characteristic impedance in the

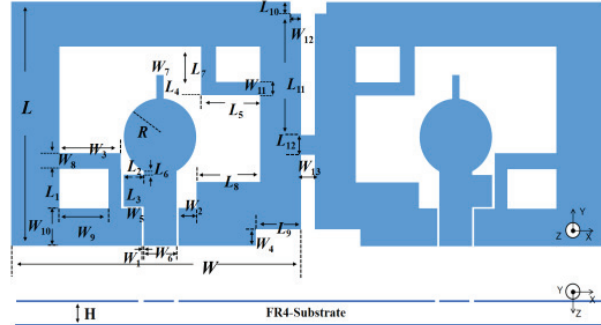


Fig. 5. Geometry of circularly polarized UWB MIMO antenna.

Table 1: Dimensions of the proposed antenna (unit: mm)

Parameter	Size	Parameter	Size
$L$	25	$W_2$	1.2
$L_1$	3.8	$W_3$	5
$L_2$	2.3	$W_4$	2
$L_3$	3.4	$W_5$	0.1
$L_4$	2.7	$W_6$	3.1
$L_5$	5.5	$W_7$	0.9
$L_6$	0.7	$W_8$	1.3
$L_7$	5.5	$W_9$	4
$L_8$	6	$W_{10}$	3.5
$L_9$	4	$W_{11}$	1.7
$L_{10}$	0.9	$W_{12}$	0.9
$L_{11}$	12.1	$W_{13}$	1
$L_{12}$	2	$W_8$	1.3
$W$	25	$H$	0.8

simulation. To enhance the isolation and realize good diversity performance, the slit slot between antenna units and rectangular openings are introduced to achieve high isolation. As illustrated in Figures 6 and 7,  $S_{12}$  is below  $-18 \text{ dB}$  and  $-20 \text{ dB}$  in the most cases. By introducing the slit slot in the middle of the ground and rectangular openings at the top and bottom of ground to form a defective ground structure, the coupling between the antenna units is reduced to below  $-15 \text{ dB}$  without the need to reserve extra large space. The AR band-width is 4.7-6.1 GHz, completely covering the WLAN band. Thereby, it can work in WLAN band in circular polarization. Meanwhile, impedance band-width also keeps wide (3.1-13.5 GHz). Table 1 shows the specific size parameters of the optimized antenna.

To illustrate the CP radiation mechanism, the current distribution of the antenna surface is plotted to analyze the generation of polarization. As shown in Figure 8, current distribution of the CP antenna in different phases of  $0^\circ$ ,  $90^\circ$ ,  $180^\circ$ , and  $270^\circ$  at 5.6 GHz is presented. From Figure 8 (a), we can see that the current flows mainly

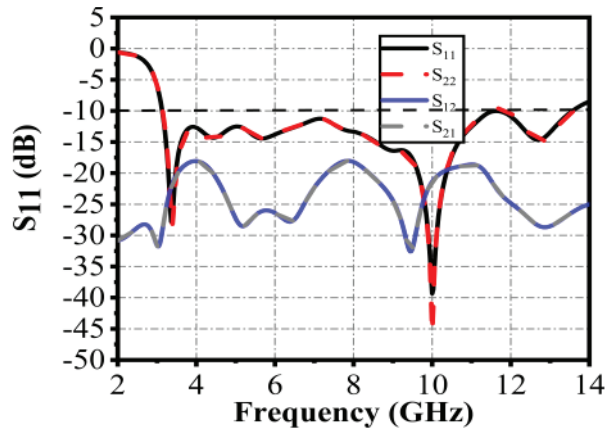


Fig. 6. Simulated  $S$ -parameter.

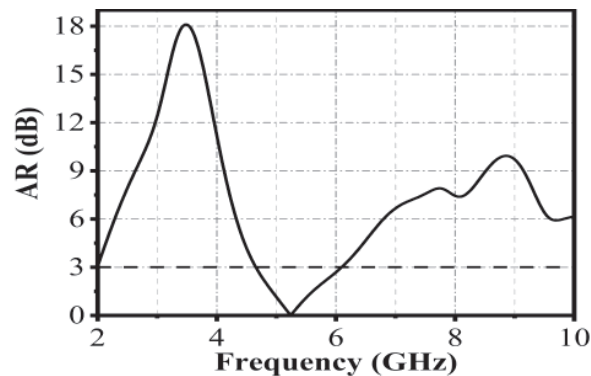


Fig. 7. Simulated axial ratio (AR).

along the  $-x$  and  $y$  axes, so the direction of the synthetic current vector points to the second quadrant. When the phase is changed by  $90^\circ$ , the current direction is along the  $x$  and  $y$  axes, and the current vector points to the first quadrant, which is orthogonal to the  $0^\circ$  phase direction. Similarly, after changing the phase to  $180^\circ$  and  $270^\circ$ , the vector points to the forth and second quadrants in turn. As can be seen from the Figure 8, the current direction rotates in the clockwise direction as phase increases. Thus, the proposed antenna can excite a left-handed circular polarization (LHCP) along the  $z$ -axis.

### III. PARAMETERS OPTIMIZATION AND DISCUSSION

The width of the symmetrical ground slot, the length of the extended rectangular branch, and the spacing between introduced rectangular branch and circular radiating unit affect the performance of this antenna. So the effect of the variation of these critical parameters on the antenna performance is studied to obtain the optimal results. In the following, the effect of the corresponding structure of the antenna on the 3 dB ARBW

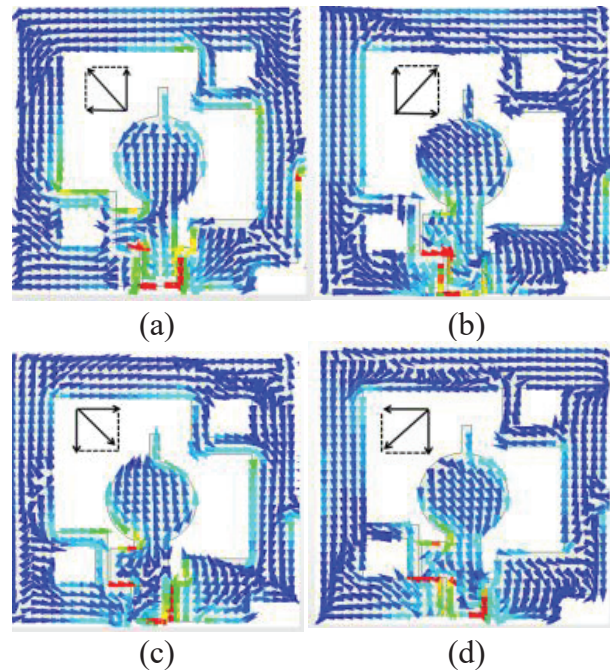


Fig. 8. Surface current distributions at 5.6 GHz for four phase angles. (a)  $0^\circ$ . (b)  $90^\circ$ . (c)  $180^\circ$ . (d)  $270^\circ$ .

and impedance bandwidth is analyzed to achieve better performance of the antenna. In the process of optimizing and analyzing the parameters, we adopt the control variable method, where the other parameters are kept fixed and the relevant variables of interest are changed.

#### A. The influence of length of side extended rectangular ranch $L_2$

Figures 9 (a) and (b) give the effect of the length of the extended rectangular branch on the side of the circular radiating patch ( $L_2$ ) on the antenna impedance bandwidth and AR bandwidth, respectively. From Figure 9 (a), it can be seen that  $L_2$  has a large impact on the impedance bandwidth, when  $L_2 = 0.3$  mm,  $S_{11}$  is almost greater than  $-10$  dB in the entire band, and can not meet the bandwidth of UWB. With the increase of  $L_2$ , the impedance bandwidth is optimized. As shown in Figure 9 (b), the AR bandwidth is greater than 5 dB in 5-6 GHz when  $L_2 = 0.3$  mm. As  $L_2$  increases, CP is achieved and the AR bandwidth is expanded. When  $L_2 = 1.3$  mm, the CP is achieved in 5.4-5.8 GHz, but the impedance bandwidth of 5-7 GHz cannot meet the requirement.

From Figure 9, we can see that the parameter  $L_2$  has a large impact on the performance of the antenna on AR bandwidth and impedance bandwidth. Finally,  $L_2$  is chosen as 2.3 mm as the best value, and the AR bandwidth can cover the WLAN band.

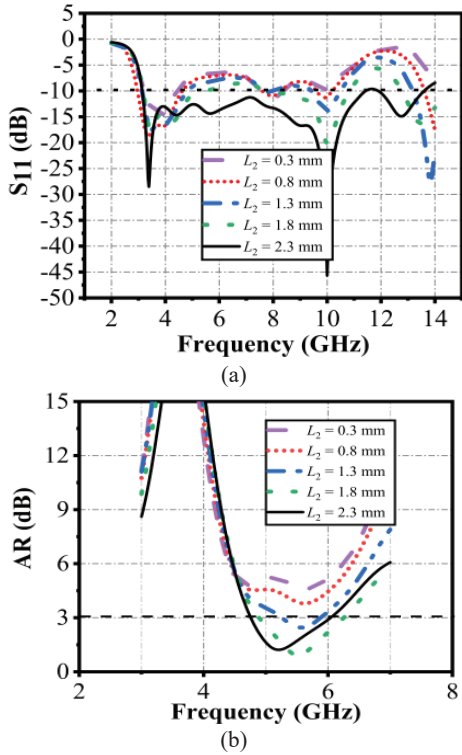


Fig. 9. Simulated results of different  $L_2$ . (a)  $S_{11}$ . (b) AR.

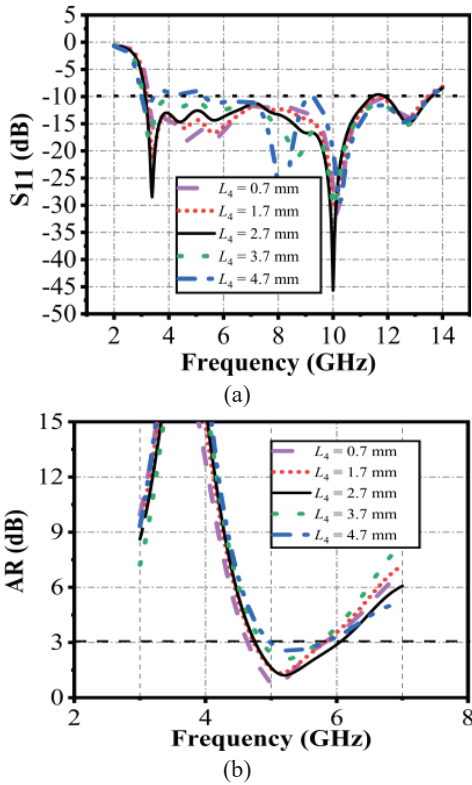


Fig. 10. Simulated results of different  $L_4$ . (a)  $S_{11}$ . (b) AR.

**B. The influence of length of top extended rectangular branch  $L_4$**

The effect of the top extended rectangular patch on the antenna is further investigated. Fixing other parameters, the effect on the antenna performance is shown below when  $L_4$  is taken to different values. From Figures 10 (a) and (b), it can be seen that when varying  $L_4$  has a small effect on the impedance bandwidth. Only when  $L_4= 4.7$  mm,  $S_{11}$  is greater than -10 dB in around 3.7-5 GHz. With increase of  $L_4$  the AR is shifted to the left and bandwidth is broadened. When  $L_4 = 2.7$  mm, the impedance bandwidth is 3.1- 13.5 GHz, with AR bandwidth of 4.6-6.1 GHz.

**C. The influence of width of rectangular ground with slot  $W_8$**

Figures 11 (a) and (b) show the effect of variation in  $W_8$  on the impedance bandwidth and AR bandwidth. As  $W_8$  increases, the antenna  $S_{11}$  parameters shift slightly towards the left overall, and covers the entire UWB band. Meanwhile, the AR bandwidth remains almost constant, indicating the AR and impedance bandwidth is not sensitive to the variations of  $W_8$ .

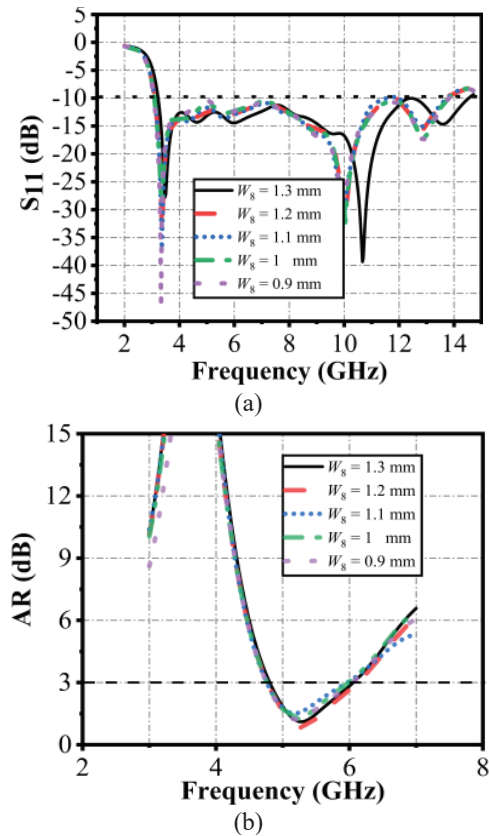


Fig. 11. Simulated results of different  $W_8$ . (a)  $S_{11}$ . (b) AR.

#### D. The influence of length of internal rectangular patch $L_8$

The effect of the parameter  $L_8$  on the impedance bandwidth is mainly concentrated in the high frequency band. When  $L_8 = 3$  mm, the impedance bandwidth deteriorates in 10-13 GHz. As  $L_8$  increases, the high frequency band gradually eases, whereas  $S_{11}$  exceeds -10 dB in 6-10 GHz when  $L_8 = 7$  mm. Although the AR gradually shifts to the left with the increase of  $L_8$ , it can be seen that the effect of this parameter on AR is much less than the effect on the impedance bandwidth. Ultimately,  $L_8$  is chosen as 6 mm.

#### IV. RESULT AND DISCUSSION

The fabrication of the proposed antenna is shown in Figure 13 with dimensions of  $25 \times 51 \times 0.8$  mm<sup>3</sup>. The proposed antenna was fabricated on FR4 substrate with dielectric constant of 4.4 and loss tangent of 0.02. The antenna feed line was connected to a 50  $\Omega$  SMA. In the test, the scattering parameters were measured by

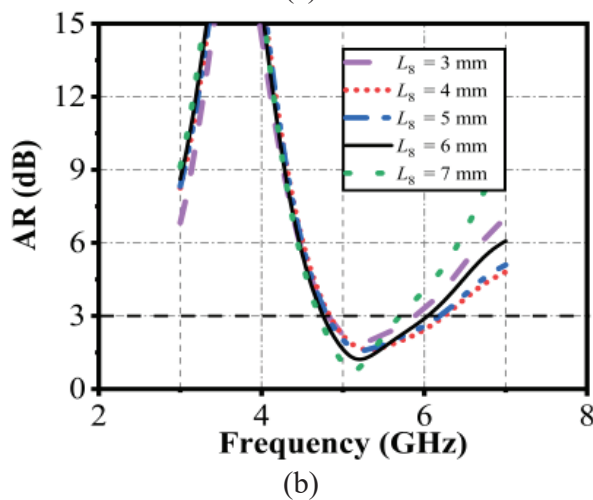
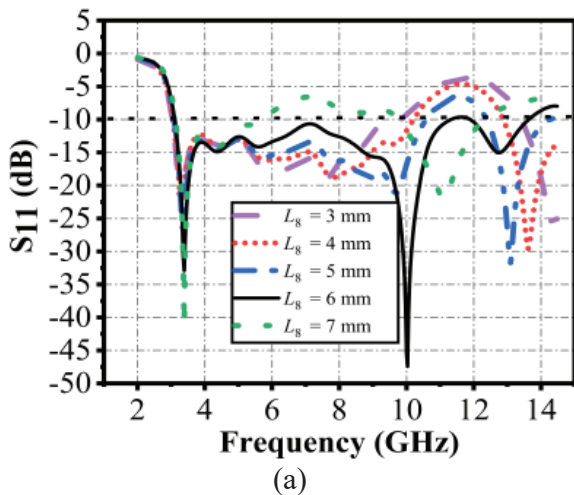


Fig. 12. Simulated results of different  $L_8$ . (a)  $S_{11}$ . (b) AR.

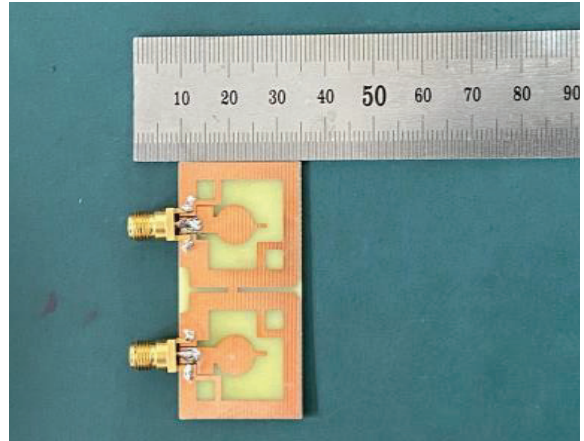


Fig. 13. Photograph of the fabricated antenna.



Fig. 14. Measured by Agilent NE5071C.

Agilent vector network analyzer NE5071C in Figure 14. And the far-field parameters, like gain, radiation pattern were measured in SATIMO anechoic chamber as shown in Figure 18.

Figure 15 shows the measured S-parameter of the proposed antenna compared with the simulated. It can

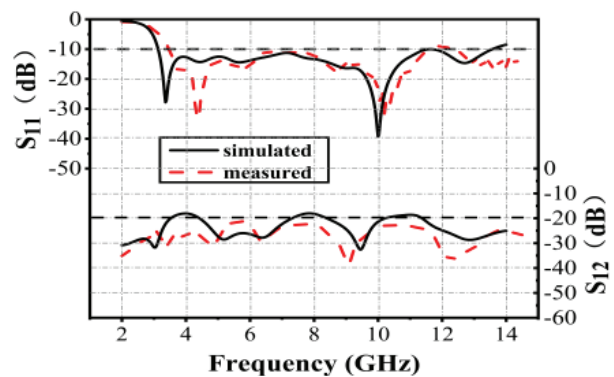


Fig. 15. Simulated and measured S-parameter.

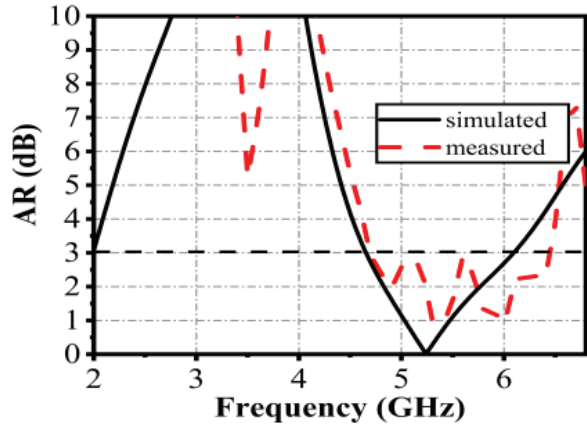


Fig. 16. Simulated and measured AR.

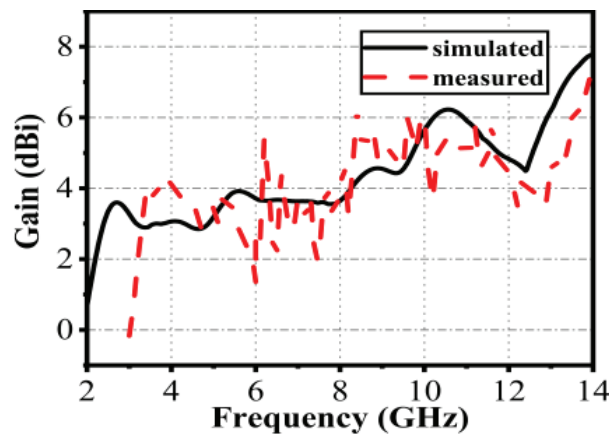


Fig. 17. Simulated and measured peak gain.

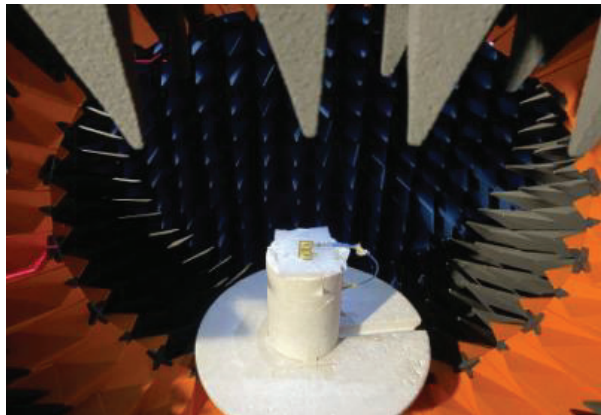


Fig. 18. Measured in SATIMO chamber room.

be seen that, from 3.2 GHz to 13.5 GHz,  $S_{11}$  is below -10 dB, showing that the impedance bandwidth is more than 10 GHz. Although the starting frequency is slightly shifted to the right, it is acceptable and consistent with

simulated results. Figure 16 shows that the measured 3 dB ARBW is 4.7-6.5 GHz, covering the entire WLAN band. And the average peak gain is around 4 dBi as shown in Figure 17. At the same time, in the entire operating band, the MIMO antenna shows good isolation.  $S_{12}$  reflects the degree of isolation. We can see, in Figure 15,  $S_{12}$  is below -20 dB in most cases, which shows that the proposed antenna has high isolation. Due to the toleration of manufacturing and welding, there are some deviations between the measured and simulated data. In general, the proposed antenna achieves wide bandwidth and CP as expected.

Figure 19 shows the radiation patterns of the proposed antenna in the X-Z and Y-Z planes, respectively at 4.8 GHz, 5.6GHz, and 8 GHz. As shown in the Figures 19 (a) and 19 (b), the proposed antenna generates LHCP radiation mode in the bore-sight direction. And Figure 19 (c) shows the radiation pattern of the proposed antenna in LP mode and it shows quasi-omnidirectional characteristic. Although there are some discrepancies

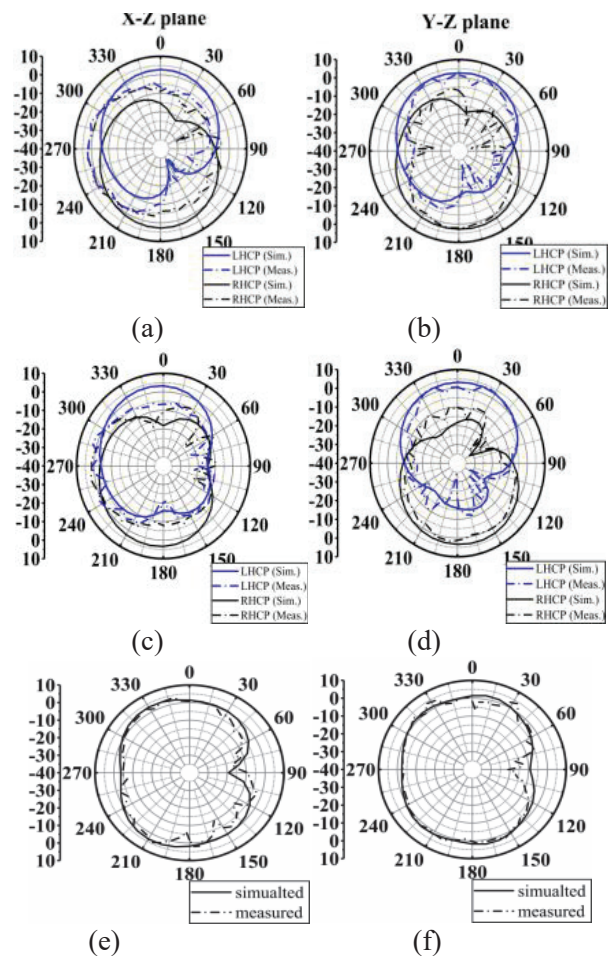


Fig. 19. Radiation patterns at different frequencies. (a and b) 4.8 GHz. (c and d) 5.6 GHz. (e and f) 8 GHz.

Table 2: Comparison with related antennas

Ref.	Overall geometry (mm <sup>3</sup> )	-10 dB IBW (GHz)	3 dB ARBW (GHz)	Isolation (dB)	ECC	Decoupling method
[20]	40 × 40 × 1.524	3.1-10.6	linear	< -16	0.13	modified ground and orthogonal arrangement
[21]	48 × 28 × 1.6	3-11.5	linear	< -18	0.039	vertical placement
[22]	50 × 35 × 1	3-11	linear	< -25	0.004	fence-type decoupling structure
[23]	80 × 40 × 1.6	2.13-11.03	linear	< -20	N/A	decoupling stubs
[24]	99.7 × 33.5 × 0.8	2.9-7.1	3.1-6.35	< -20	0.003	extended array element interval
[25]	25 × 25 × 1.6	3-11	4-5.5	< -17	0.15	modified ground
[26]	130 × 130 × 1	1.175-5.79	1.75-4.46	N/A	N/A	N/A
[27]	56 × 32 × 3	5-6.6	5.1-5.85	< -20	0.02	parasitic periodic metallic plates
[31]	32.5 × 42 × 1	3.6-13	5.2-7.1	< -18	0.02	defective ground structure
[34]	150 × 100 × 0.8	2.5-2.55	2.5-2.55	< -20	0.003	decoupling stubs
[36]	35 × 16 × 0.8	3.1-5	linear	< -22	N/A	neutralization line
[39]	32 × 64 × 1.6	3.1-10.6	linear	< -17	0.02	meander-line EBG
Proposed	25 × 51 × 0.8	3.1-13.5	4.7-6.1	< -18	0.01	defective ground structure

which may be due to processing errors, measured results is consistent with the analysis results above.

The diversity performance of MIMO antenna can be measured in terms of ECC (envelop correlation coefficient) and DG (diversity gain). ECC is a vital diversity parameter that depicts the correlation or isolation of related channels. ECC can be calculated by considering the impact of all S-parameters. Formula (3) is a quick way to calculate ECC. Usually, ECC below 0.5 is widely adopted criterion for engineering [18].

$$\rho_e = \frac{|S_{11}^* S_{12} + S_{21}^* S_{22}|^2}{(1 - |S_{11}|^2 - |S_{21}|^2)(1 - |S_{22}|^2 - |S_{12}|^2)}. \quad (3)$$

DG is described as an increment in signal to interference level and can be calculated by formula (4).

$$DG = 10\sqrt{1 - |\rho_e|}. \quad (4)$$

As shown in Figure 20, the ECC value of the antenna is less than 0.01 and DG more than 9.95. Hence, the low ECC and high DG indicate that the MIMO antenna has favorable diversity characteristics to combat multipath fading.

Table 2 shows the comparison between the proposed antenna and antennas in the relevant papers. And it can be seen that, the proposed CP antenna has excellent performance parameters with more compact size, larger bandwidth, and high isolation.

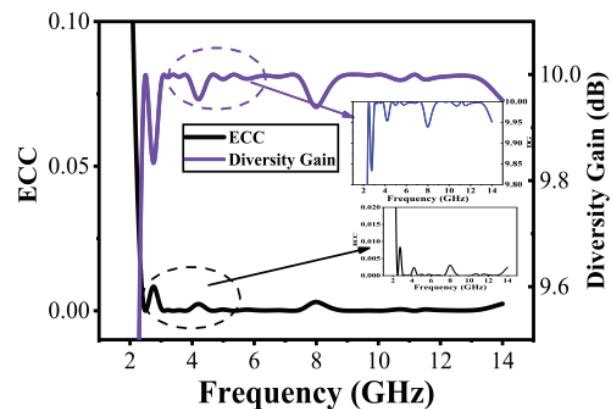


Fig. 20. ECC and diversity gain.

## V. CONCLUSION

In this paper, we propose a novel compact circularly polarized ultra-wideband MIMO antenna. Compared with common linearly polarized antennas, the proposed antenna can excite CP mode for WLAN communication and its impedance bandwidth can also fully cover UWB spectrum. It has a very compact size and the dimension is 25 × 51 × 0.8 mm<sup>3</sup>. The impedance bandwidth is 3.1-13.5 GHz, with average peak gain of 4 dBi, fully covering UWB bandwidth and enhanced by 38%. At the same time, CP is achieved by embedding two symmetrical rectangular slot structures in the two opposite corners

of every antenna unit and measured 3 dB ARBW is 4.7-6.5GHz (1.8 GHz), fully covering WLAN band. Meanwhile, the MIMO antenna keeps high isolation, the diversity characteristic  $\text{ecc}$  is lower than 0.01 and shows very good isolation diversity characteristics. It can simultaneously operate in the UWB spectrum and exhibit CP radiation characteristic in the band of WLAN. Research on how to broaden the AR bandwidth in the entire UWB spectrum is still very difficult. Currently, most can only achieve circular polarization in some frequency bands. And this will be the next step in our work. Overall, the proposed antenna has the advantage of compact size, broadband circularly polarization, enhanced isolation, and easy fabrication.

### ACKNOWLEDGMENT

This work was supported by Key Project of the National Natural Science Foundation of China under Grant 62090012, 62031016 and 61831017, the Project under Grant 19-163-21-TS-001-062-01, and the Sichuan Provincial Science and Technology Important Projects under Grant 2019YFG0498, 2020YFG0282, 2020YFG0452 and 2020YFG0028.

### REFERENCES

- [1] Federal Communication Commission, "First report and order revision of part 15 of the Commission's rules regarding ultra-wideband transmission system," Tech. Rep. ET 98-153, FCC, Washington, DC, USA, 2002.
- [2] K. S. Ryu and A. A. Kishk, "UWB antenna with single or dual band-notches for lower WLAN band and upper WLAN band," *IEEE Trans. Antennas Propag.*, vol. 57, no. 12, pp. 3942-3950, 2009.
- [3] M. Rahman and J. D. Park, "The smallest form factor UWB antenna with quintuple rejection bands for IoT applications utilizing RSRR and RCSRR," *Sensors*, vol. 18, no. 3, p. 911, 2018.
- [4] Z. N. Chen, "UWB antennas: From hype, promise to reality," in *Proc. 2007 Loughborough Antennas Propag. Conf.*, Loughborough, UK, pp. 19-22, 2007.
- [5] T. Ali, A. W. Mohammad Saadh, R. C. Biradar, A. Andújar, and J. Anguera, "A miniaturized slotted ground structure UWB antenna for multiband applications," *Microw. Opt. Technol. Lett.*, vol. 60, pp. 2060-2068, 2018.
- [6] J. Y. Siddiqui, C. Saha, and Y. M. M. Antar, "Compact dual-SRR-loaded UWB monopole antenna with dual frequency and wideband notch characteristics," *IEEE Antennas Wirel. Propag. Lett.*, vol. 14, pp. 100-103, 2015.
- [7] K. Kaur, A. Kumar, and N. Sharma, "Split ring slot loaded compact CPW-fed printed monopole antennas for ultra-wideband applications with band notch characteristics," *Progress Electromagn. Res. C*, vol. 110, pp. 39-54, 2021.
- [8] A. K. Gautam, S. Yadav, and B. K. Kanaujia, "A CPW-fed compact UWB microstrip antenna," *IEEE Antennas Wirel. Propag. Lett.*, vol. 12, pp. 151-154, 2013.
- [9] B. Yang and S. Qu, "A compact integrated Bluetooth UWB dual-band notch antenna for automotive communications," *AEU Int. J. Electronics Commun.*, vol. 80, pp. 104-113, Oct. 2017.
- [10] J. Jan, C. Pan, K. Chiu, and H. Chen, "Broadband CPW-fed circularly-polarized slot antenna with an open slot," *IEEE Trans. Antennas Propag.*, vol. 61, no. 3, pp. 1418-1422, Mar. 2013.
- [11] U. Ullah, S. Koziel, and I. B. Mabrouk, "A simple-topology compact broadband circularly polarized antenna with unidirectional radiation pattern," *IEEE Antennas Wirel. Propag. Lett.*, vol. 18, no. 12, pp. 2612-2616, Dec. 2019.
- [12] S. Zhou, P. Li, Y. Wang, W. Feng, and Z. Liu, "A CPW-fed broadband circularly polarized regular-hexagonal slot antenna with L-shape monopole," *IEEE Antennas Wirel. Propag. Lett.*, vol. 10, pp. 1182-1185, 2011.
- [13] G. Li, H. Zhai, T. Li, L. Li, and C. Liang, "CPW-fed S-shaped slot antenna for broadband circular polarization," *IEEE Antennas Wirel. Propag. Lett.*, vol. 12, pp. 619-622, 2013.
- [14] S. Maddio, "A compact wideband circularly polarized antenna array for C-band applications," *IEEE Antennas Wirel. Propag. Lett.*, vol. 14, pp. 1081-1084, Dec. 2015.
- [15] K. Ding, R. Hong, D. Guan, L. Liu, and Y. Wu, "Broadband circularly polarised stacked antenna with sequential-phase feed technique," *IET Microw. Antennas Propag.*, vol. 14, pp. 779-784, 2020.
- [16] N. Rasool, K. Huang, A. B. Muhammad, and Y. A. Liu, "Wideband circularly polarized slot antenna with antipodal strips for WLAN and C-band applications," *Int. J. RF Microw. Comput. Aided Eng.*, vol. 29, no. 11, 2019.
- [17] J. Wei, X. Jiang, and L. Peng, "Ultrawideband and high-gain circularly polarized antenna with double-Y-shape slot," *IEEE Antennas Wirel. Propag. Lett.*, vol. 16, pp. 1508-1511, 2017.
- [18] C. Luo, J. Hong, and L. Zhong, "Isolation enhancement of a very compact UWB-MIMO slot antenna with two defected ground structures," *IEEE Antennas Wirel. Propag. Lett.*, vol. 14, pp. 1766-1769, Apr. 2015.
- [19] J. Tao and Q. Feng, "Compact ultrawideband MIMO antenna with half-slot structure," *IEEE Antennas Wirel. Propag. Lett.*, vol. 16, pp. 792-795, 2017.

- [20] D. Singh, A. A. Khan, S. A. Naqvi, M. Saeed Khan, A. D. Capobianco, S. Boscolo, M. Midrio, and R. M. Shubair, "Inverted-c ground MIMO antenna for compact UWB applications," *J. Electromagn. Waves Appl.*, vol. 35, no. 15, pp. 2078-2091, May 2021.
- [21] A. A. Ibrahim, J. Machac, and R. M. Shubair, "UWB MIMO antenna for high speed wireless applications," *Applied Computational Electromagnetic Society (ACES) Journal*, vol. 34, no. 9, pp. 1294-1299, Sep. 2019.
- [22] L. Wang, Z. Du, H. Yang, R. Ma, Y. Zhao, X. Cui, and X. Xi, "Compact UWB MIMO antenna with high isolation using fence-type decoupling structure," *IEEE Antennas Wirel. Propag. Lett.*, vol. 18, no. 8, pp. 1641-1645, Aug. 2019.
- [23] Y. Yu, S. Mao, M. Li, and D. He, "Isolation enhancement between ports of a compact ultrawideband MIMO antenna," *Applied Computational Electromagnetic Society (ACES) Journal*, vol. 36, no. 1, pp. 61-66, Jan. 2021.
- [24] U. Ullah, I. B. Mabrouk, S. Koziel, and M. Al-Hasan, "Implementation of spatial/polarization diversity for improved-performance circularly polarized multiple-input-multiple-output ultrawideband antenna," *IEEE Access*, vol. 8, pp. 64112-64119, 2020.
- [25] S. Saxena, B. K. Kanaujia, S. Dwari, S. Kumar, and R. Tiwari, "A compact dual-polarized MIMO antenna with distinct diversity performance for UWB applications," *IEEE Antennas Wirel. Propag. Lett.*, vol. 16, pp. 3096-3099, 2017.
- [26] R. Xu, S. S. Gao, J. Liu, J.-Y. Li, Q. Luo, W. Hu, L. Wen, X.-X. Yang, and J. T. Sumantyo, "Analysis and design of ultrawideband circularly polarized antenna and array," *IEEE Trans. Antennas Propag.*, vol. 68, no. 12, pp. 7842-7853, Dec. 2020.
- [27] H. H. Tran, N. Hussain, and T. T. Le, "Low-profile wideband circularly polarized MIMO antenna with polarization diversity for WLAN applications," *AEU-Int. J. Electron. Commun.*, vol. 108, 2019.
- [28] P. Laxman and A. Jain, "Wideband circularly polarised antenna 'multi-input-multi-output' for wireless UWB applications," *IET Wireless Sensor Syst.*, vol. 11, no. 6, pp. 259-274, 2021.
- [29] I. Khan, Q. Wu, I. Ullah, S. U. Rahman, H. Ullah, and K. Zhang, "Designed circularly polarized two-port microstrip MIMO antenna for WLAN applications," *Appl. Sci.*, vol. 12, no. 3, 2022.
- [30] Jaiverdhan, M. M. Sharma, and R. P. Yadav, "Broadband circularly polarized compact MIMO slot antenna based on strip and stubs for UWB applications," *Electromagnetics*, vol. 41, no. 3, pp. 292-302, 2021.
- [31] S. Kumar, D. Nandan, K. Srivastava, S. Kumar, H. Singh, M. Marey, H. Mostafa, and B. K. Kanaujia, "Wideband circularly polarized textile MIMO antenna for wearable applications," *IEEE Access*, vol. 9, pp. 108601-108613, 2021.
- [32] A. Kumar and T. Agrawal, "High performance circularly polarized MIMO antenna with polarization independent metamaterial," *Wirel. Personal Commun.*, vol. 116, pp. 3205-3216, 2021.
- [33] A. Kumar, A. De, and R. K. Jain, "Circular polarized two-element textile antenna with high isolation and polarization diversity for wearable applications," *Int. J. Microw. Wirel. Technol.*, pp. 1-9, 2022.
- [34] M. Y. Jamal, M. Li, and K. L. Yeung, "Isolation enhancement of closely packed dual circularly polarized MIMO antenna using hybrid technique," *IEEE Access*, vol. 8, pp. 11241-11247, 2020.
- [35] S. Kumar, G. Lee, D. Kim, W. Mohyuddin, H. Choi, and K. Kim, "A compact four-port UWB MIMO antenna with connected ground and wide axial ratio bandwidth," *Int. J. Microw. Wirel. Technol.*, vol. 12, no. 1, pp. 75-85, 2020.
- [36] S. Zhang and G. F. Pedersen, "Mutual coupling reduction for UWB MIMO antennas with a wideband neutralization line," *IEEE Antennas Wirel. Propag. Lett.*, vol. 15, pp. 166-169, 2016.
- [37] U. Ullah, I. B. Mabrouk, and S. Koziel, "Enhanced-performance circularly polarized MIMO antenna with polarization/pattern diversity," *IEEE Access*, vol. 8, pp. 11887-11895, 2020.
- [38] A. Kumar, A. De, and R. K. Jain, "Novel H-shaped EBG in E-plane for isolation enhancement of compact CPW-fed two-port UWB MIMO antenna," *IETE J. Res.*, pp. 1-7, 2022.
- [39] N. Kumar and K. U. Kiran, "Meander-line electromagnetic bandgap structure for UWB MIMO antenna mutual coupling reduction in E-plane," *Int. J. Electron. Commun.*, vol. 127, 2020.



**Lei Zhang** was born in Jiangsu, China. He received his B.S. degree in Electronic Information Engineering from Yanshan University, Qinghuangdao, China, in 2020. Now, he is pursuing his M.S. degree in Information and Communication Engineering at Southwest Jiaotong University, Chengdu, China. His major research is in miniaturized antenna, RFID technology, ultra-wideband communication, and MIMO technology.



**Quanyuan Feng** (M'06–SM'08) received the M.S. degree in Microelectronics and Solid Electronics from the University of Electronic Science and Technology of China, Chengdu, China, in 1991, and the Ph.D. degree in EM Field and Microwave Technology from Southwest Jiaotong University, Chengdu, China, in 2000. He is the Head of Institute of Microelectronics, Southwest Jiaotong University, Chengdu, China. He has been honored as the “Excellent Expert” and the “Leader of Science and Technology” of Sichuan Province owing

to his outstanding contribution. To date, more than 500 papers have been published on IEEE Transactions on Antennas and Propagation, IEEE Transactions on Microwave Theory and Techniques, IEEE Antennas and Wireless Propagation Letters, etc., among which more than 300 were registered by SCI and EI. His research interests include integrated circuits design, RFID technology, embedded system, wireless communications, antennas and propagation, microwave & millimeter wave technology, smart information processing, electromagnetic compatibility and RF/ microwave devices & materials, etc.



**Muhammad K. Khan** has received his BS and Master degree from the COMSATS University Pakistan in 2011 and 2016 respectively. Now he is pursuing his PhD in Information and Communication engineering from Southwest Jiaotong University China. His research interests include electromagnetics and antennas especially in the design and optimization of antenna array, microstrip patch antennas, and ultra wideband antennas.

# Multi-Mode Excitation by Interleaved EBG Structure for Suppression of Power/Ground Noise in Multi-Layer PCBs

Ding-Bing Lin<sup>1</sup>, Yen-Hao Chen<sup>1</sup>, and Min-Hung Hsieh<sup>2</sup>

<sup>1</sup>Department of Electronic and Computer Engineering  
National Taiwan University of Science and Technology, Taipei, Taiwan  
dblin@mail.ntust.edu.tw, chen.ian@inventec.com

<sup>2</sup>Signal Integrity Engineering Department  
Inventec Corporation, Taoyuan, Taiwan  
hsieh.tony@inventec.com

**Abstract** – Signal line transition with layer transition via is inevitable in multi-layer PCB. The return current can generate voltage noise between the cavities due to the discontinuity of the return current path. Other layer transition vias passing through the cavity can pick up the voltage noise and result in problems of signal integrity. In this paper, an electromagnetic bandgap (EBG) structure is proposed for suppression of the broadband cavity noise. The impedance discontinuity between layers of interleaved EBG cell enhances the efficiency of noise suppression, and the slots embedded in the EBG cell excite multi-mode resonances for extending the bandwidth of noise suppression. The dispersion diagram is utilized to preliminarily analyze the characteristic of the proposed EBG cell, and a  $5 \times 5$  cells EBG board is further analyzed for characterizing the efficiency of noise suppression. Both simulation and measurement results prove the proposed structure can effectively suppress the cavity noise under  $-35$  dB over the frequency range from 0.56 GHz to the highest measurement frequency, 20 GHz.

**Index Terms** – Electromagnetic bandgap, microwave filter, power/ground noise, signal integrity.

## I. INTRODUCTION

With increasing data rate of high-speed digital signal, the nonideal return current path can result in severe power integrity as well as signal integrity problems. The return current with low impedance path is required for the layer transition via passing through multiple layers, as the return current flows through the impedance of the cavity made up of two planes can create a voltage between the planes [1]. The created voltage can propagate in the cavity and should be minimized and suppressed because other layer transition vias passing through the cavity can pick up this voltage noise. To provide a low impedance path for the return current of the

layer transition via is an effective approach to suppress the cavity noise and can be achieved by placing decoupling capacitors between power and ground planes [2]. However, the effective inductance (ESL) of the capacitor component limits the bandwidth of the low impedance path of return current. For suppressing the propagation of cavity noise over the effective frequencies limited by the decoupling capacitor, a lot of electromagnetic bandgap(EBG) structures have been proposed to isolate the cavity noise for the GHz application [3–5]. Due to the demand for high density design, an EBG structure with double stacked patches has been proposed for achieving compact size and broadband isolation [6]. That structure is designed with the mushroom-like EBG structure so that it can be practically integrated into existing PCB designs without the issue of IR drop.

In order to further reduce the size and extend the effective bandwidth of the EBG structure, an interleaved EBG structure with double-stacked patches has been proposed [7]. The miniaturization is achieved by shunt capacitance of the interleaved patches, and the bandwidth is optimized by the location of vias connected to the patches. However, not only the layer transition via that carries high frequency components of high speed digital signals but also the layer transition via that connects to input node or switching node of switched-mode power supplies (SMPS) can inject noise into the cavity [8]. The switching power noise is typically lower than 1 GHz and the Nyquist frequency of the high-speed digital signal can be 28 GHz for 112 Gbps application with PAM4 signaling. These cavity noises can simultaneously couple to any signal passing through the cavity [9]. The signal that picks up cavity noise can be a severe problem of signal integrity and then further results in radiated emission, so that the EBG structure with wider stopband bandwidth and high isolation for suppression of cavity noise is needed.

An EBG structure based on the mushroom-like EBG structure with interleaved and double stacked patches in a four-layer stack-up is proposed in this paper. The impedance discontinuity between layers of interleaved EBG cell enhances the isolation for suppression of the noise propagation. The slots embedded in the EBG cell are induced to further extend the stopband bandwidth. The characteristic of the proposed EBG structure is measured by vector network analyzer and simulated by commercial field solvers. Both simulation and measurement present excellent results of suppression of noise propagation by improved stopband bandwidth and isolation. The design concept and procedure will be described in Section II. The simulation and measurement results of the proposed structure are shown in Section III. Finally, the conclusion is presented in Section IV.

## II. DESIGN CONCEPT AND PROCEDURE

### A. Suppression of propagation mode by discontinuity of impedance between plane pairs

The reference design shown in Figure 1 is based on the EBG cell [7] with geometrical parameters  $(a, b, d, h_1, h_2) = (12 \text{ mm}, 11.8 \text{ mm}, 0.8 \text{ mm}, 0.1 \text{ mm}, 0.1 \text{ mm})$  for the PCB made of FR-4 material with relative permittivity  $\epsilon_r = 4.4$ . The interleaved patches are double stacked in a four-layer stack-up. All the thicknesses of dielectric as well as the capacitance between adjacent planes are the same in the reference design. In order to extend the stopband bandwidth to lower frequency, the thickness

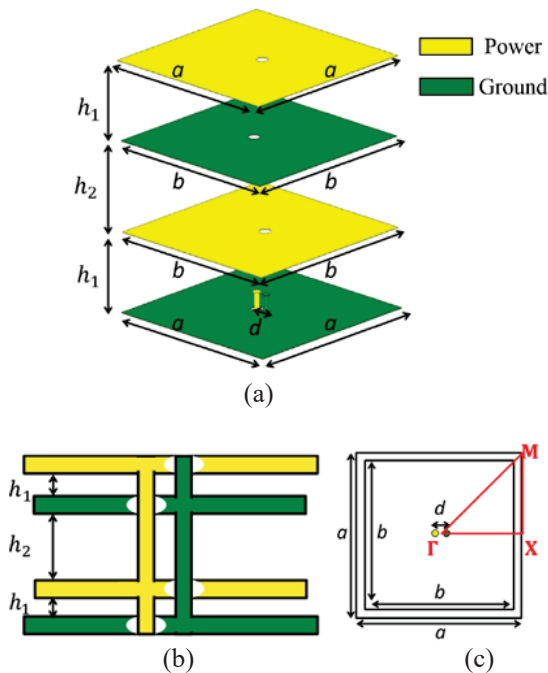


Fig. 1. (a) The unit cell of the referenced EBG structure with (b) side view and (c) top view.

of the dielectric,  $h_2$ , between the second and the third layers is increased from 0.1 to 0.8 mm. Therefore, the via barrel is lengthened and the inductance of the via is increased accordingly. As the capacitances between the first and second layers and the third and fourth layers remain the same, the increased inductance shifts the resonant frequency to lower frequency for extending the stopband bandwidth. The thickened dielectric between the second and the third layers also decreases the capacitance and results in the impedance discontinuities, so that the isolation for suppression of the noise propagation is enhanced. Figure 2 shows dispersion diagrams of the EBG cells of the reference design and that with thickened dielectric, respectively. For the result of the reference design, the bandgap is over the frequency range from 0.87 to 2.82 GHz except a propagating mode at 2.06 GHz. The bandgap of the design with thickened dielectric is from 0.59 to 2.95 GHz and its propagation mode is moved from 2.06 to 1.14 GHz. A  $5 \times 5$  cells EBG board shown in Figure 3 is used to further analyze the effectiveness of isolation for the practicality. The cavity noise is excited at (18 mm, 3 mm) and the observation point is at (42 mm, 51 mm). Figure 4 shows that the design with thickened dielectric not only moves the propagation mode from 2.06 to 1.14 GHz but also enhances the isolation for suppression of the noise propagation. The cavity noise is suppressed under  $-35 \text{ dB}$  from 0.53 to 5.77 GHz.

### B. Suppression of propagation mode by patches with slots

In order to suppress propagation modes for frequencies higher than 5.77 GHz, a novel EBG cell shown in Figure 5 is proposed for extending stopband bandwidth by excited multiple modes. The patches for the design shown in Figure 1 with geometrical parameters  $(a, b, d, h_1, h_2) = (12 \text{ mm}, 11.8 \text{ mm}, 0.8 \text{ mm}, 0.1 \text{ mm}, 0.1 \text{ mm})$  are replaced by the proposed EBG cells with geometrical parameters  $(g, w) = (0.1 \text{ mm}, 0.2 \text{ mm})$ . The slots need to be located at the edges of the patch as the resonances are created by the inductance of the slot and the capacitance

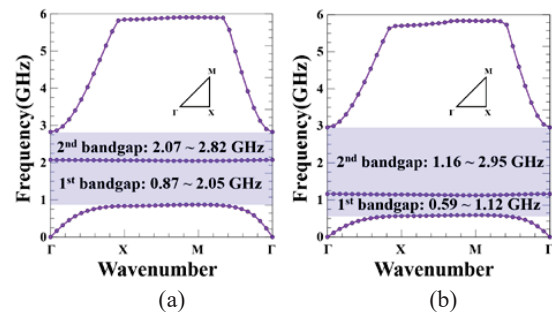


Fig. 2. (a) The dispersion diagrams of the EBG cell of reference design and (b) that with thickened dielectric.

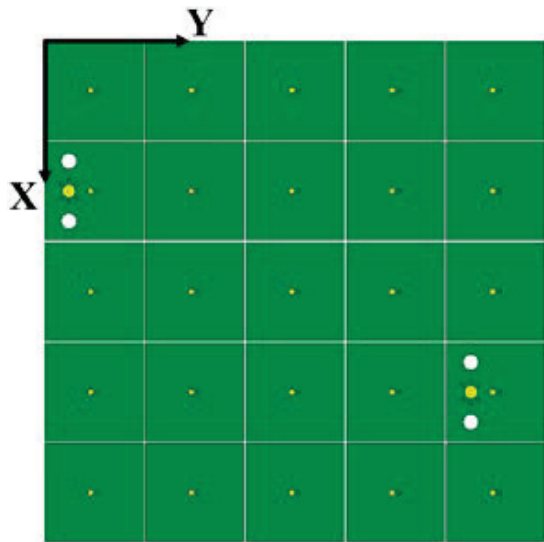


Fig. 3. The structure with  $5 \times 5$  EBG cells.

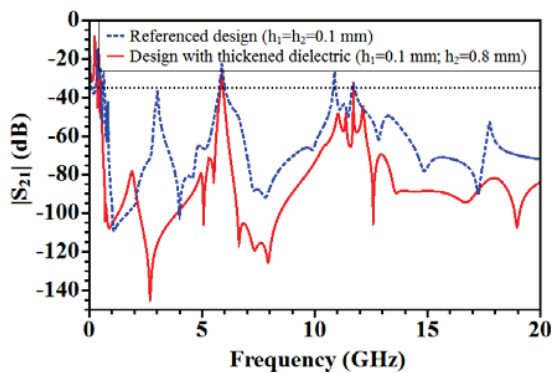


Fig. 4.  $|S_{21}|$  of the structure with  $5 \times 5$  EBG cells.

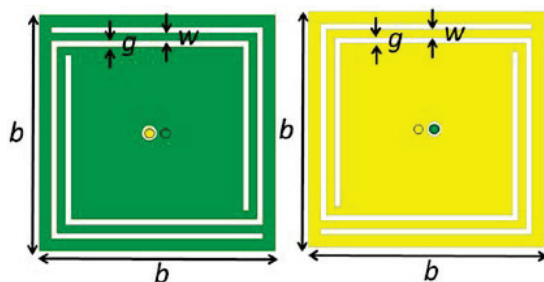


Fig. 5. Patches of the EBG cell with slots.

between patches. If the slots are close to the center of the patch, currents on the patch will directly flow through the via and the resonant modes will not be excited. Figure 6 shows the dispersion diagram of the EBG cells with slots. The bandgaps of the design with slots and that of reference design shown in Section II-A are alike, but multi-

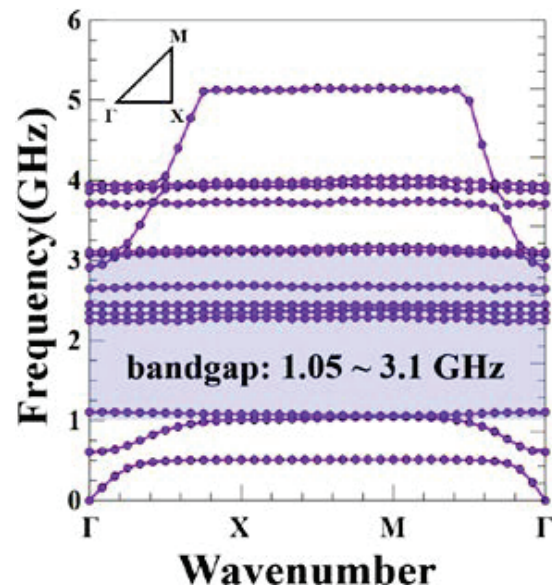


Fig. 6. The dispersion diagrams of the EBG cell with slots.

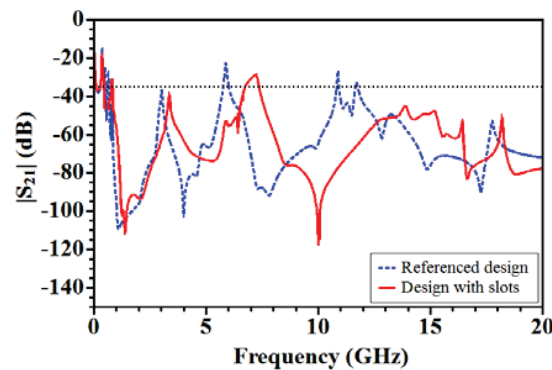


Fig. 7.  $|S_{21}|$  of the structure made of  $5 \times 5$  EBG cells with slots.

ple modes excited between 2 and 4 GHz shift the propagation mode from 5.9 to 7.2 GHz as Figure 7. As the propagation mode at 7.2 GHz still limits the stopband bandwidth, the structure comprises EBG cells with slots and the design of discontinuity of impedance between plane pairs is proposed in Section III.

### III. SUPPRESSION OF NOISE PROPAGATION BY THE PROPOSED EBG STRUCTURE

The proposed structure is composed of slots on patches with thickened dielectric design for broadband suppression of noise propagation. The thickened dielectric is intended for the enhancement of noise isolation at low frequencies and the slots are responsible for the suppression of high frequency noise by excited

multiple modes. Figure 8 shows the proposed structure can effectively suppress the cavity noise under  $-35$  dB over the frequency range from 0.56 to 20 GHz. An experiment board shown in Figure 9 is designed for the validation of the proposed structure.  $5 \times 5$  EBG cells are placed on a four-layer PCB with  $6 \text{ cm} \times 6 \text{ cm}$  substrate. The cavity noise is injected and picked by two compression-mount SMA connectors, respectively. Figure 10 shows excellent correlation result between simulation and measurement. The measurement result

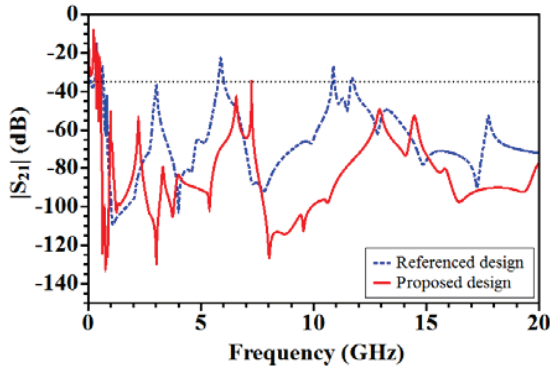


Fig. 8.  $|S_{21}|$  of the proposed structure with  $5 \times 5$  EBG cells.

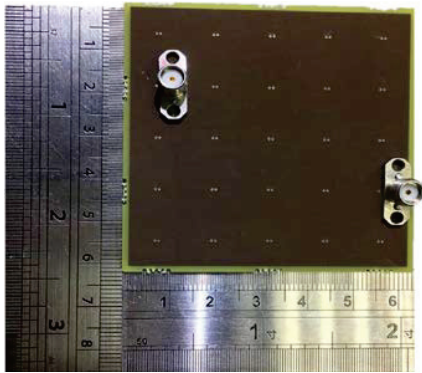


Fig. 9. Top side of the experiment board.

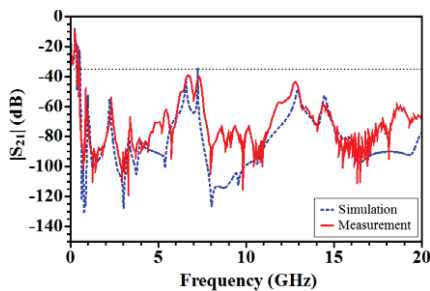


Fig. 10.  $|S_{21}|$  correlation between simulation and measurement.

proves the cavity noise can be suppressed under  $-35$  dB from 0.56 GHz to the highest measurement frequency, 20 GHz.

#### IV. CONCLUSION

The cavity noise propagating between two planes can be picked by layer transition vias passing through the cavity. In this paper, an EBG structure based on interleaved and double stacked patches is proposed to suppress the cavity noise. The increased inductance of the proposed EBG cell shifts the resonant frequency to lower frequency and the multiple modes excited by additional slots shift propagation mode to higher frequency. The stopband bandwidth is then extended for the broadband suppression of the cavity noise. The simulation and measurement results indicate that the cavity noise is suppressed under  $-35$  dB from 0.56 GHz to the highest measurement frequency, 20 GHz.

#### ACKNOWLEDGMENT

This work was supported in part by the Ministry of Science and Technology of Taiwan, and in part by the Inventec Corporation.

#### REFERENCES

- [1] L. D. Smith and E. Bogatin, "Taming signal integrity problems when signals change return planes," *Principles of Power Integrity for PDN Design, 1st ed.*, Prentice Hall, Boston, Massachusetts, USA, pp. 363-426, 2017.
- [2] K. Koo, L. G. Romo, T. Wang, T. Michalka, and J. Drewniak, "Fast decap assignment algorithm for optimization of power distribution networks," *2017 IEEE International Symposium on Electromagnetic Compatibility & Signal/Power Integrity (EMCSI)*, Washington, DC, pp. 573-578, 2017.
- [3] T. Wu, Y. Lin, and S. Chen, "A novel power planes with low radiation and broadband suppression of ground bounce noise using photonic bandgap structures," *IEEE Microwave and Wireless Components Letters*, vol. 14, no. 7, pp. 337-339, Jul. 2004.
- [4] C. Wang, G. Shiue, W. Guo, and R. Wu, "A systematic design to suppress wideband ground bounce noise in high-speed circuits by electromagnetic-bandgap-enhanced split powers," *IEEE Transactions on Microwave Theory and Techniques*, vol. 54, no. 12, pp. 4209-4217, Dec. 2006.
- [5] F. de Paulis, L. Raimondo, and A. Orlandi, "IR-DROP analysis and thermal assessment of planar electromagnetic bandgap structures for power integrity applications," *IEEE Transactions on Advanced Packaging*, vol. 33, no. 3, pp. 617-622, Aug. 2010.
- [6] J. Park, A. C. W. Lu, K. M. Chua, L. L. Wai, J. Lee, and J. Kim, "Double-stacked EBG structure

for wideband suppression of simultaneous switching noise in LTCC-based SiP applications,” *IEEE Microwave and Wireless Components Letters*, vol. 16, no. 9, pp. 481-483, Sep. 2006.

- [7] C. Wang and T. Wu, “Model and mechanism of miniaturized and stopband-enhanced interleaved EBG structure for power/ground noise suppression,” *IEEE Transactions on Electromagnetic Compatibility*, vol. 55, no. 1, pp. 159-167, Feb. 2013.
- [8] G. Ouyang, X. Ye, and T. Nguyen, “Switching voltage regulator noise coupling to signal lines in a server system,” *2010 IEEE International Symposium on Electromagnetic Compatibility*, Fort Lauderdale, FL, pp. 72-78, 2010.
- [9] V. S. Pandit, W. H. Ryu, and M. Choi, “Signal/power integrity interactions,” *Power Integrity for I/O Interfaces: With Signal Integrity/Power Integrity Co-Design, 1st ed.*, Prentice Hall, Boston, Massachusetts, USA, pp. 233-284, 2011.



**Ding-Bing Lin** received the M.S. and Ph.D. degrees in electrical engineering from National Taiwan University, Taipei, Taiwan, in 1989 and 1993, respectively.

From 1993 to 2016, he was a Faculty Member with the Department of Electronic Engineering, National

Taipei University of Technology, Taipei, Taiwan, where he was an Associate Professor, Professor, and Distinguished Professor in 1993, 2005, and 2014, respectively. Since August 2016, he has been a Professor with the Department of Electronic and Computer Engineering, National Taiwan University of Science and Technology.

Dr. Lin was the Chair of the Taipei Chapter, IEEE Broadcasting Society, from 2010 to 2014, the Technical Program Committee Chair of the 2015 Asia-Pacific International EMC Symposium, and the Chair of the Taipei Chapter, IEEE EMC Society from 2015 to 2018. He has been an Associate Editor for the *IEEE Transactions on EMC* since 2019 and in the Editorial Board of

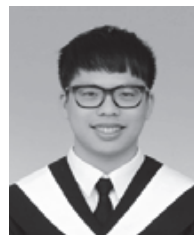
the *International Journal of Antennas and Propagation* since 2014. He is currently directing a human resources cultivation program named the Promotion Center for 5G Antennas and Radio Frequency Techniques Consortium. He has authored or coauthored more than 200 papers in international journals and at international conferences, respectively. His research interests include wireless communication, radio multipath fading channel modeling, mobile antennas, high-speed digital transmission, and microwave engineering.



**Yen-Hao Chen** received the M.S. degree in computer, communication, and control engineering from the National Taipei University of Technology, Taipei, Taiwan, in 2003. He is currently working toward the Ph.D. degree in electronic and computer engineering with the National

Taiwan University of Science and Technology, Taipei, Taiwan.

He has been working with Inventec Corporation since 2003 where his responsibilities include the design and analysis of signal and power integrity for products of servers, network switches, and storage equipment. His research interests include SI/PI simulations and noise modeling of switched-mode power supply.



**Min-Hung Hsieh** received the M.S. degree in electronic and computer engineering from the National Taiwan University of Science and Technology, Taipei, Taiwan, in 2018.

He has been working with Inventec Corporation since 2019 where his responsibilities include the design and analysis of signal integrity for industrial servers. His current interests include SI/PI simulations for PCIe and DDR signals.

# Calculation and Characteristics Analysis for Radiated Electromagnetic Field of High Voltage Converter Valve

Hongsen Zou<sup>1,3</sup>, Lin Zheng<sup>2</sup>, Yuan Zhang<sup>1</sup>, Jianan Zhang<sup>2</sup>, Yajie Wang<sup>2</sup>,  
and Huafeng Wang<sup>2</sup>

<sup>1</sup>State Grid Ningxia Electric Power CO., LTD. Ultrahigh Voltage Company  
hs-zou@qq.com, 18408673777@163.com

<sup>2</sup>State Key Laboratory of Advanced Power Transmission Technology  
(State Grid Smart Grid Research Institute CO., LTD.)

<sup>3</sup>School of Telecommunication Engineering  
Xidian University, Xi'an 710071, China  
zhenglin@geiri.sgcc.com.cn, zjnde@126.com, wangyajie@geiri.sgcc.com.cn, wanghuafeng@geiri.sgcc.com.cn

**Abstract** – Calculation and analysis of the radiated electromagnetic field by the high voltage converter valve are very important for the electromagnetic compatibility analysis between the various components of the converter system. First, the electromagnetic radiation calculation process of the converter valve is proposed. Then, according to the actual engineering application, a DC transmission simulation system of the converter system was built, and the current of the converter valve tower arm was obtained. Subsequently, according to the actual size, a 3D calculation model of the converter valve tower was established, and an MoM-based calculation method for the electromagnetic field of the converter valve tower was proposed. Finally, the attenuation characteristics and azimuth characteristics of the converter valve tower are analyzed, and the distribution rules of the radiated electromagnetic field inside the high voltage converter valve hall are clarified, which provide a theoretical foundation for the evaluation of the electromagnetic compatibility of the converter system.

**Index Terms** – A 3D calculation model, converter valve, DC transmission simulation system, MoM, radiated electromagnetic field.

## I. INTRODUCTION

High voltage direct current (HVDC) transmission has become the best choice for power transmission due to its large transmission capacity, long transmission distance, and high stability [1]. Among them, the HVDC transmission grid can not only realize large-scale and long-distance transmission of electric energy but also can greatly improve the safety, reliability, flexibility, and

economy of the grid, and it has significant social and economic benefits. HVDC transmission technology is the new peak of direct current (DC) transmission technology in the world, and it will play an irreplaceable role in long-distance power transmission projects [2].

The converter station is the center of AC and DC power exchange. It realizes the energy transfer from the AC system to the DC system [3]. It is the core of HVDC transmission technology. Its operation status directly affects the safety and stability of the entire DC transmission system and even the AC system. However, in the converter valve hall, the switching transient of the converter valve will generate a broadband current inside the valve tower, thereby deteriorating the surrounding electromagnetic environment [4]. At the same time, the online monitoring unit, communication system, and protection and control system of the converter valve are very close to the valve hall and are in a strong electromagnetic radiation field, which seriously affects its normal operation [5]. For this reason, it is necessary to carry out the calculation of the electromagnetic radiation of the converter valve and the research its attenuation characteristics.

In 1971, Harrold conducted experimental research, analyzed the frequency of power line radiofrequency electromagnetic noise, and used a spectrum analyzer to analyze the interference characteristics of radio frequency (RF) noise [5]. Afterward, Annstrand studied the radio interference generated when the converter valve was turned on [6], analyzed the factors affecting the level of radio interference, and proposed corresponding suppression methods. Maruvada and Gilsing proposed a calculation method for analyzing and calculating the RF interference level of converter stations, which was

verified based on the Vancouver Island converter station [7]. Morse measured the electromagnetic interference of the Nelson River DC transmission line in Canada [8, 9]. Melvolil *et al.* analyzed the electromagnetic noise voltage within the carrier frequency range of the HVDC converter station [10]. Bacon *et al.* measured the electromagnetic noise of AC lines near HVDC transmission lines. The measurement results are helpful to analyze the interference propagation mechanism between AC and DC transmission lines [11]. The International Special Committee on Radio Interference proposed a calculation formula suitable for the calculation and analysis of the radio interference of the bipolar DC line based on the large amount of measurement data obtained by the test line and the actual line in operation [12]. In addition, funded by the Canadian Electric Power Association, Maruvada, Malewki, Wong, etc., carried out electromagnetic disturbance measurements on two 400-kV converter stations in Canada and gave the electromagnetic field inside the station and 500 m outside the station 0.1. Measurement results of radio interference and RF interference in the M-5MHz frequency band [15]. Tatso and others in New England analyzed in detail the power carrier problem of a 450-kV, 1800-MW converter station through measurement and calculation [16]. Japanese Yuichirou Murata and Shinji Tanabe used the method of moments to calculate the RF noise generated by the transmission line of the HVDC converter station and produced a 400:1 scaling model. The measurement results are in good agreement with the calculation results [17]. With the development of HVDC transmission technology, the issue of electromagnetic compatibility in converter stations has been paid more attention, but almost all research works are concentrated in the field of RF interference, and research works are conducted on the basis of experiments.

To this end, this paper proposes a calculation method for the electromagnetic disturbance radiated by the high-pressure converter valve and analyzes the frequency characteristics and attenuation characteristics of the electromagnetic disturbance radiated by the high-pressure converter valve to provide theoretical guidance for the electromagnetic compatibility design of the high-pressure converter system.

## II. CALCULATION METHOD

### A. Calculation process of radiated electromagnetic field of converter valve

For the analysis of the electromagnetic radiation level of the valve of the flexible DC converter station, it is necessary to first obtain the current of all the wires at any moment by measurement or calculation; then for the spatial point where the electromagnetic field strength needs to be calculated, calculate the field

strength of each section of current at the same moment at this point and superimpose. Combined with the existing commonly used calculation software FEKO belongs to the characteristics of the frequency domain method, the time domain current obtained in the first step needs to be Fourier transformed to obtain its frequency domain response, and then calculate the response at different frequency points in the space point and superimposed to obtain the electric field strength at any point in space. The specific calculation steps are as follows.

- (1) The establishment of the 3D model of the valve tower. For 3D models of components without current inflow, such as shields, metal scatterers are modeled according to the actual dimensions. For 3D models of components with current flow, such as the converter valve unit and its internal power modules, a simplified unit model is built using a metal plate instead of the power units, considering the electrical connection of each power module inside the unit.
- (2) Setting of the excitation source. The excitation source is in the form of a single current source at the point of connection to the DC bus with the excitation source injected from one end and withdrawn from the other.
- (3) The calculation area is designated. Through the setting of boundary conditions, calculate the radiation field generated by the single excitation source considering the case of metal scatterers in the valve hall.
- (4) The calculation of valve tower electromagnetic radiation. The DC bus current obtained from the PSCAD calculation is Fourier transformed to obtain the amplitude-frequency characteristics at different frequencies. The frequency points of interest are multiplied with the radiation field results obtained in step (4) to obtain the electromagnetic radiation of the valve tower.

### B. Radiation source analysis of converter valve hall

From the generation mechanism distinction, the flexible DC converter valve electromagnetic disturbance sources can be divided into the following three kinds: (1) the operation of the converter valve caused by continuous electromagnetic disturbance; (2) the converter station high-voltage equipment corona generated electromagnetic disturbance; (3) the converter station high-voltage equipment discharge generated electromagnetic disturbance. Among them, corona and interference generated by the discharge of equipment are similar to the general AC high-voltage field station interference phenomenon. A basic assumption of the study converter station design can meet the immunity requirements corresponding to this phenomenon. In the occurrence of the above phenomenon, it can be ensured that the converter

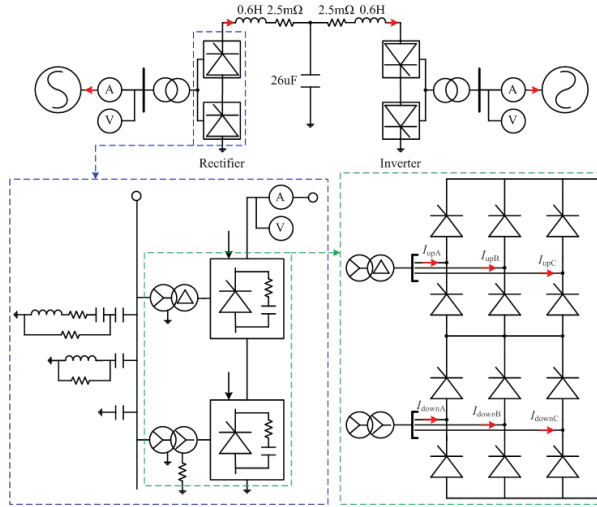


Fig. 1. The commutation simulation system of DC transmission.

station equipment is not affected and is a normal operation; so the analysis in this paper is no longer considered.

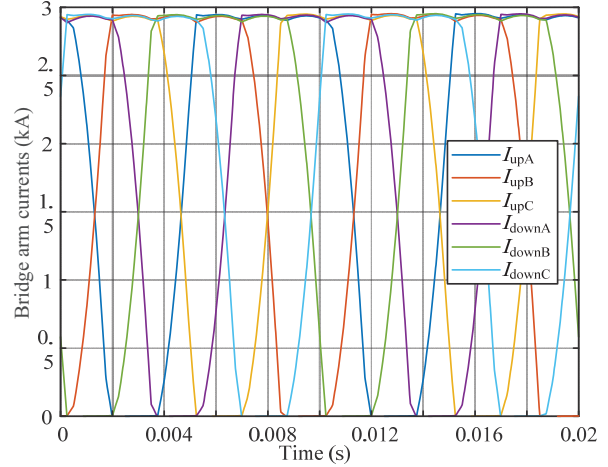
Establish a DC transmission commutation simulation system in actual engineering applications, as shown in Figure 1.

This paper mainly analyzes the electromagnetic radiation disturbance of the converter valve hall on the rectifier side, and the pulse current of the upper and lower three-phase bridge arms is shown in Figure 2(a). Furthermore, the frequency domain analysis method is used to obtain the amplitude-frequency characteristics of the bridge arm current, as shown in Figure 2(b). It can be seen that the currents of the three phases all exhibit periodic square-wave characteristics in the time domain, and only small differences appear in the high-frequency band in the frequency domain. In the third step calculation, the single radiation field is usually multiplied by the envelope parameter.

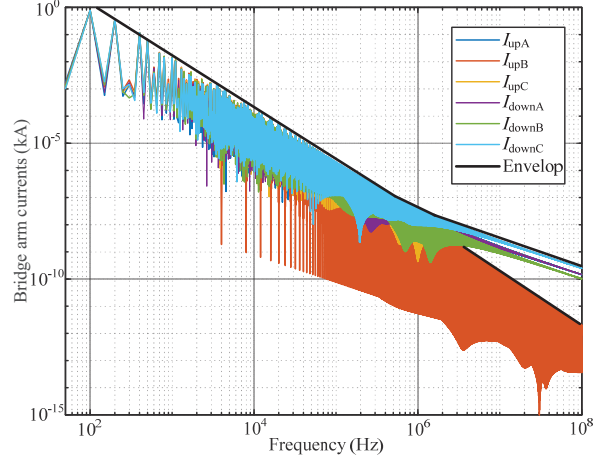
To facilitate the accuracy of the calculation of the radiated electromagnetic field, the amplitude-frequency envelope is used as the disturbance source, and the current excitation source is set at the corresponding bridge arm position.

### C. 3D models and calculation method of converter valve tower

Due to the existence of valve towers and a large number of metal conductor structures such as pole conductors in the valve hall, while the converter valve reflects different impedance characteristics under different operating conditions and frequencies, only the use of electromagnetic field numerical calculation methods to solve such complex electromagnetic field problems more accurately. In this paper, FEKO, a numerical calculation



(a) Time domain waveform diagram of bridge arm current



(b) Frequency domain waveform diagram of bridge arm current

Fig. 2. Time-frequency parameters of three-phase bridge arm current.

software developed based on the method of moments, is used to model and calculate in the valve hall.

For the electric field  $\mathbf{E}$ , the expression is

$$\mathbf{E} = \frac{\nabla}{4\pi\epsilon_0} \int_s \nabla \cdot \mathbf{J} \frac{e^{-jkR}}{R} dS - \frac{j\omega\mu}{4\pi} \int_s \mathbf{J} \frac{e^{-jkR}}{R} dS. \quad (1)$$

To solve for the current  $\mathbf{J}$ , a triangular section is made of the metal surface, as shown in Figure 3. After the triangular section, each side of the triangle is numbered and the positive and negative numbers of the two triangles connected to the side are defined.

Introduce the current basis function as

$$\mathbf{f}_n = \begin{cases} -\frac{\boldsymbol{\rho}_n^-}{\mathbf{h}_n^-}, & \boldsymbol{\rho}_n \text{ and } \mathbf{h}_n \text{ are marked } - \\ +\frac{\boldsymbol{\rho}_n^+}{\mathbf{h}_n^+}, & \boldsymbol{\rho}_n \text{ and } \mathbf{h}_n \text{ are marked } + \\ 0, & \text{else} \end{cases}, \quad (2)$$

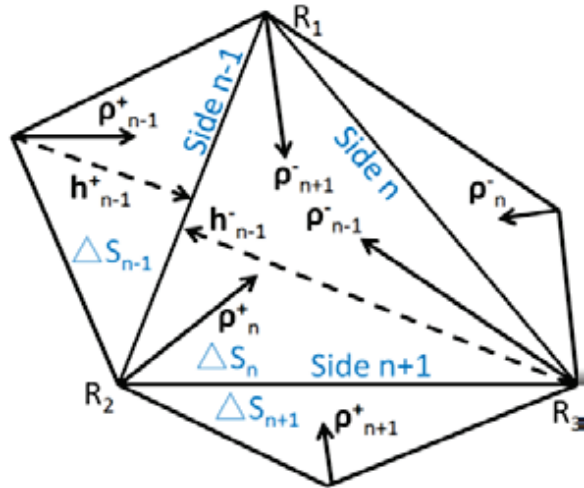


Fig. 3. Definition of the parameters of a triangular surface element.

where  $h_{n-1}^{\pm}$  denotes the distance from the vertex corresponding to the  $n-1$ th edge to the  $n-1$ th edge, and  $\rho_n^+$  denotes the vector from the vertex within  $S_n$  corresponding to the  $n$ th edge to the field point within triangle  $S_n$ .  $\rho_n^-$  denotes the vector from the vertex of the other triangle corresponding to the  $n$ th edge to the field point.

The current  $\mathbf{J}$  at any point in the triangle can be expanded by the vector from that point to the three vertices

$$\mathbf{J} = \sum_{n=1}^3 J_n \mathbf{f}_n. \quad (3)$$

Therefore, the electric field  $\mathbf{E}$  can be further expressed as

$$\mathbf{E} = \sum_{n=1}^N \frac{J_n}{h_n^{\pm}} \left( \frac{\nabla}{4\pi\epsilon j\omega} \int_{\Delta S_n} \pm 2 \cdot \frac{e^{-jkR}}{R} dS - \frac{j\omega\mu}{4\pi} \int_{\Delta S_n} \pm \rho_n^+ \frac{e^{-jkR}}{R} dS \right). \quad (4)$$

Taking the power function  $g_m = f_m$ ,  $m$  being the triangle number, and making the inner product of the power function and  $\mathbf{E}$

$$\begin{aligned} \langle \mathbf{g}_m^{\pm}, \mathbf{E} \rangle &= \sum_{n=1}^N J_n \left\langle -\nabla \cdot \mathbf{g}_m^{\pm}, \frac{\nabla}{4\pi\epsilon j\omega} \int_{\Delta S_n} \pm \frac{2}{h_n^{\pm}} \cdot \frac{e^{-jkR}}{R} dS \right\rangle \\ &+ \sum_{n=1}^N J_n \left\langle \mathbf{g}_m^{\pm}, -\frac{j\omega\mu}{4\pi} \int_{\Delta S_n} \pm \frac{\rho_n^+}{h_n^{\pm}} \cdot \frac{e^{-jkR}}{R} dS \right\rangle. \end{aligned} \quad (5)$$

Define each part of the above equation as follows:

$$\begin{cases} \Phi_{mn} = -\langle \nabla \cdot \mathbf{g}_m^{\pm}, \Phi_m \rangle \\ \mathbf{A}_{mn} = \langle \mathbf{g}_m^{\pm}, \mathbf{A}_m \rangle \\ \mathbf{Z}_{mn} = \Phi_{mn} + \mathbf{A}_{mn} \end{cases}. \quad (6)$$

$\Phi_{mn}$  and  $\mathbf{A}_{mn}$  are the scalar and vector bits between  $\Delta S_n$  and  $\Delta S_m$ .  $\mathbf{Z}_{mn}$  is the equivalent impedance between  $\Delta S_n$  and  $\Delta S_m$ . The matrix equation above can be

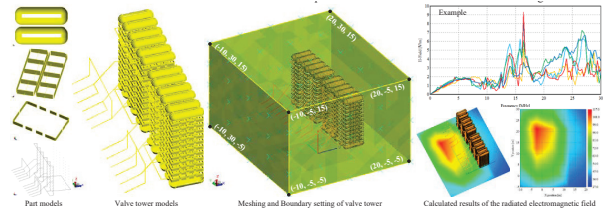


Fig. 4. Calculation process for electromagnetic radiation harassment from converter towers.

organized as

$$[\mathbf{Z}_{mn}][\mathbf{J}_n] = [\mathbf{V}_n]. \quad (7)$$

$\mathbf{V}$  is the conductor potential distribution and can be obtained by measuring the voltage.  $\mathbf{J}$  is calculated and substituted into the electric field equation to find  $\mathbf{E}$ .

To simplify the analysis, the conductors in this project were all modeled using conductors with a radius of 0.01 m (it was verified by comparison that changes in the radius of the conductors when calculating the radiation field had little effect on the calculation results). The metal frame is modeled using metal-faced conductors, without regard to the thickness of the metal frame, which is assumed to be a thin conductor plate made up of perfectly pure conductors. The final calculation process for the commutator tower is shown in Figure 4.

In the part models in Figure 4, the equalizer cover is insulated from the valve tower. The interior of the converter module can be simplified to 10 thyristors in series. The equalizer frame is connected to the valve tower at both the front and the rear, with the middle section insulated from the tower. The electrical connection contains all the wiring of the converter tower inside the converter valve hall. In this case, the current source is at the terminals of the converter transformer. When setting the boundaries, the coordinates of the rectangular boundary vertices are given, which is the basis information for the later analysis of the radiation properties.

### III. ANALYSIS OF ELECTROMAGNETIC RADIATION

#### A. Variation characteristics with frequency

As shown in Figure 5, it is the calculation result of the radiated electromagnetic field of the converter valve tower at  $(-10, 12.5, 5)$  in the 150 kHz to 30 MHz frequency band. Among them, Figure 5 (a) is the amplitude-frequency characteristic of the radiated electric field, and Figure 5 (b) is the amplitude-frequency characteristic of the radiated magnetic field.

It can be seen that the value of the radiated electric field is much larger than the value of the radiated magnetic field, which is about 1000 times. Therefore, when assessing the electromagnetic compatibility of converter valve towers, the radiated electric field should be the first

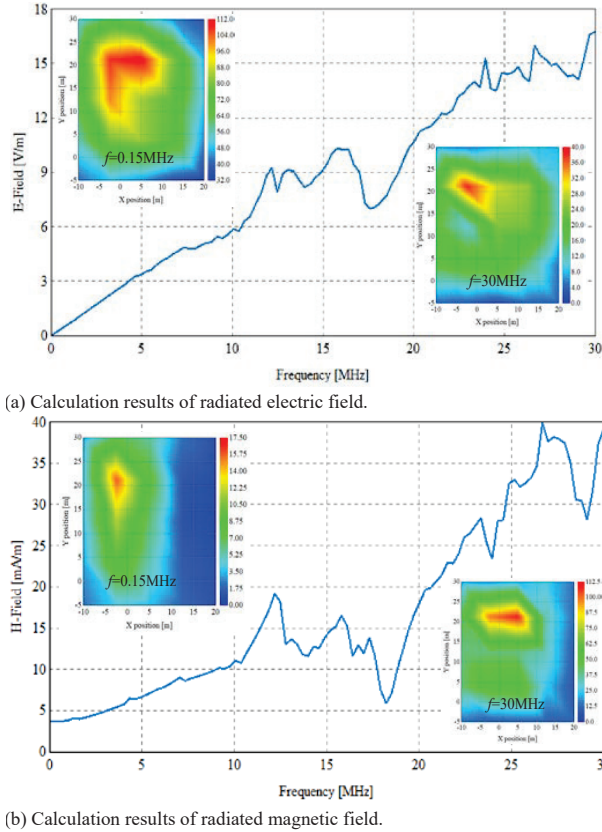


Fig. 5. Calculation results of the converter valve tower at (-10, 12.5, 5).

choice to be assessed. In addition, through the electromagnetic field cloud diagrams at  $f = 0.15$  MHz and  $f = 30$  MHz, it can be seen that on the plane of  $Z = 5$  m, the positions of the maximum radiation of the electric field and the magnetic field appear close. Therefore, if the communication facilities are placed in the air of the converter valve hall, the right side should be considered as much as possible, and the radiated electric field and radiated magnetic field in this direction are relatively small.

**B. Attenuation characteristics**

As shown in Figure 6, it is the calculation result of the radiated electromagnetic field of the converter valve tower at point  $(X, -5, 15)$ . It can be seen that in the  $X$ -axis direction, the calculated values of electromagnetic fields at different frequency points all show an attenuation trend on the  $X$ -axis. On this straight line, the attenuation characteristics of the electromagnetic field are almost identical.

As shown in Figure 7, it is the calculation result of the radiated electromagnetic field of the converter valve tower at point  $(-10, Y, 15)$ . It can be seen that on the  $Y$ -axis, the calculated electromagnetic field values all show

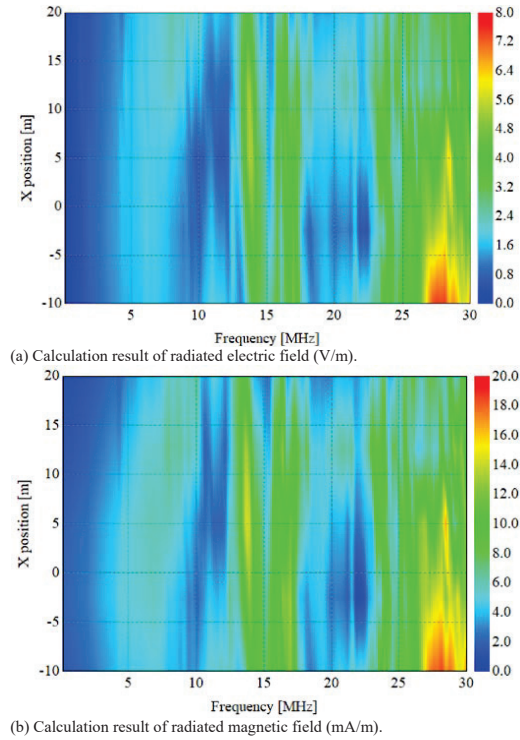


Fig. 6. The attenuation characteristics in the  $X$ -axis direction.

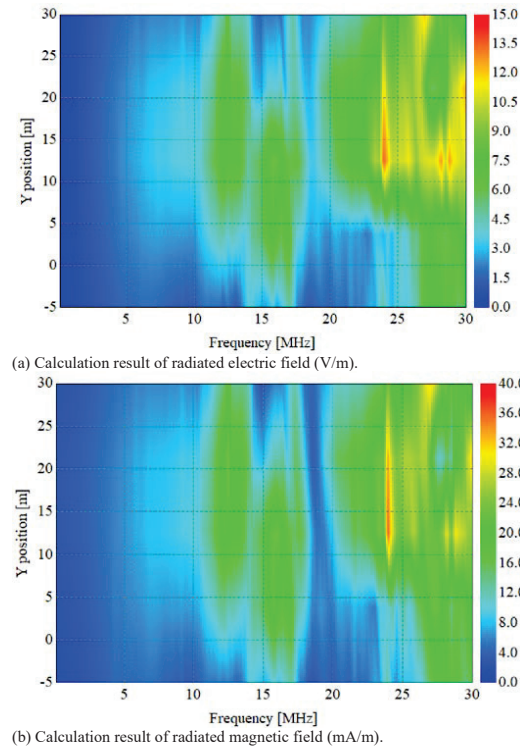


Fig. 7. The attenuation characteristics in the  $Y$ -axis direction.

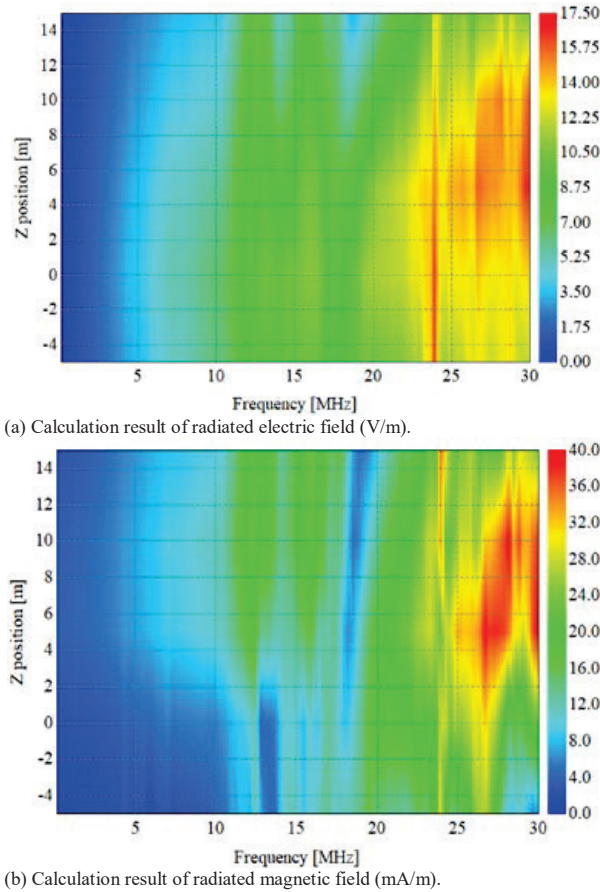


Fig. 8. The attenuation characteristics in the Z-axis direction.

a trend of first increasing and then decreasing, and the radiated electromagnetic field is the largest in the middle of the Y-axis.

As shown in Figure 8, it is the calculation result of the radiated electromagnetic field of the converter valve tower at point  $(-10, 12.5, Z)$ . It can be seen that the attenuation characteristic of the electric field value in the Z-axis direction is not obvious and can be approximately regarded as unchanged; the attenuation characteristic of the magnetic field value in the Z-axis direction is related to the frequency point. Among them, the higher the frequency is, the greater the electromagnetic field value.

### C. Azimuthal characteristics

To further demonstrate the azimuthal characteristics of the radiated electromagnetic field of the converter tower, the electromagnetic field values at eight near-field boundary points were calculated, as shown in Figure 9. It can be seen that within the 25-30 MHz band, the electromagnetic field values are greatest at points  $(-10, 30, 15)$  and smallest at points  $(20, -5, -5)$ . Therefore, when placing communication equipment inside the con-

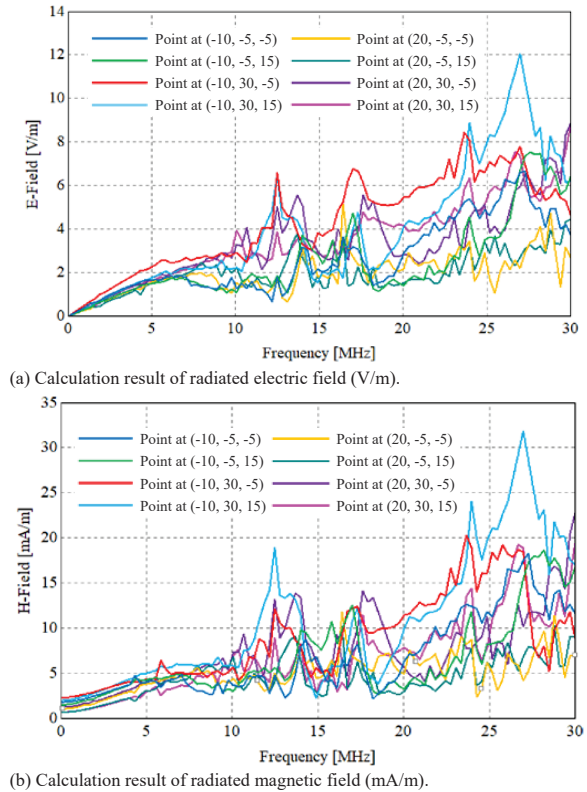


Fig. 9. Azimuthal characteristics of the radiated electromagnetic field.

verter hall, it should be placed at point  $(20, -5, -5)$  as far as possible, so that it receives less electromagnetic disturbance.

## IV. CONCLUSION

In this paper, the calculation method of electromagnetic radiation of high-voltage converter valve tower is proposed, and the attenuation characteristics of radiation field in space are analyzed, and the strongest and weakest positions of radiation electromagnetic field in the converter valve hall are clarified. It is suggested that when placing communication equipment in the converter valve hall, it should be placed in the lower right corner of the converter valve hall as far as possible. The proposed method can determine the spatial distribution of the radiation field inside the converter valve hall, and, based on this, the immunity requirements for communication equipment are proposed. In the future, combined with the experimental measurement method, the electromagnetic compatibility measures between the communication equipment and the converter valve are formulated.

## ACKNOWLEDGEMENT

This work was supported by the Technical Project of State Grid Ningxia Electric Power Co., Ltd. 5229CG21000D.

## REFERENCES

- [1] M. Wang, T. An, H. Ergun, Y. Lan, B. Andersen, M. Szechtman, and W. Leterm, "Review and outlook of HVDC grids as backbone of transmission system," *CSEE Journal of Power and Energy Systems*, vol. 7, no. 4, pp. 797-810, Jul. 2021.
- [2] B. Gao, F. Yang, M. Chen, P. Duan, Q.-J. Peng, and Y. Yang, "An improved mlpq method and application in the calculation Of electro-thermal field Of transmission line," *Applied Computational Electromagnetics Society (ACES) Journal*, vol. 30, no. 02, pp. 157-166, Aug. 2021.
- [3] H. Lee, M. Asif, K. Park, and B. Lee, "Feasible application study of several types of superconducting fault current limiters in HVDC grids," *IEEE Transactions on Applied Superconductivity*, vol. 28, no. 4, pp. 1-5, Jun. 2018.
- [4] E. Jin, Z. Song, X. Yang, and X. Yu, "Improved thevenin equivalent model of MMC considering pre-charge conditions and DC side fault conditions," *Applied Computational Electromagnetics Society (ACES) Journal*, vol. 36, no. 6, pp. 796-805, Nov. 2021.
- [5] S. M. M. Mirtalaei, S. H. H. Sadeghi, and R. Moini, "A method-of-moments model for determination of radiated magnetic field from switch-mode power supplies components using near-field measurement data," *Applied Computational Electromagnetics Society (ACES) Journal*, vol. 28, no. 08, pp. 672-679, Oct. 2021.
- [6] R. T. Harrold, "The spectrum analyzer to the measurement of EHV power line noise," *IEEE Transactions on Power Apparatus and Systems*, vol. 90, no. 2, pp. 1837-1847, 1971.
- [7] S. A. Annestrand, "Radio interference from HVDC converter stations," *IEEE Transactions on Power Apparatus and Systems*, PAS-90(3), pp. 874-882, 1972.
- [8] P. S. Maruvada and T. Gilsig, "A method of calculating the RI from HVDC converter stations," *IEEE Transactions on Power Apparatus and Systems*, vol. 92, no. 3, pp. 1009-1018, 1973.
- [9] A. R. Morse, "Field measurements on the Nelson River HVDC line including comparisons with test line data and calculated profiles," *Proceedings of the Canadian PowerConference*, Montreal, Canada, pp. 437-440, 1976.
- [10] A. R. Morse, "Field measurements of station-generated RI on the Nelson River HVDC line," *Proceedings of the International Electrical and Electronics Conference*, Toronto, Canada, pp. 78-79, 1976.
- [11] D. J. Melvolil, L. Haglof, and P. Degen, "Carrier frequency harmonics generated by HVDC conversion," *IEEE Transactions on Power Apparatus and Systems*, vol. 99, no. 2, pp. 564-575, 1980.
- [12] G. H. Bacon, D. L. Hedrick, and J. J. Fiedler, "Power line carrier application considerations involving HVDC transmission," *IEEE Transactions on Power Apparatus and System*, vol. 99, no. 3, pp. 1089-1096, 1980.
- [13] B. W. Jakel and Q.-B. Tu, "Electromagnetic environment near HVDC thyristor valves // 11th international symposium on high voltage engineering," vol. 2, no. 2, pp. 47-50, 1999.
- [14] Y. Liu, S. A. Sebo, and R. Caldecott, "Modeling of converter transformer using frequency domain terminal impedance measurements," *IEEE Transactions on Power Delivery*, vol. 8, no. 1, pp. 66-72, 1993.
- [15] D. G. Kasten, R. Caldecott, S. A. Sebo, and Y. Liu, "A computer program for HVDC Converter station RF noise calculations," *IEEE Transactions on Power Delivery*, vol. 9, no. 2, pp. 750-755, Apr. 1994.
- [16] P. S. Maruvada, R. A. Malewski, and P. S. Wong, "Measurement of the electromagnetic environment of HVDC converter stations," *IEEE Power Engineering Review*, vol. 9, no. 4, pp. 73-74, 2007.
- [17] R. Caldecott, R. V. Devore, and D. G. Kasten, "HVDC converter station tests in the 0.1 to 5MHz frequency," *IEEE Transactions on Power Delivery*, vol. 3, no. 3, pp. 971-977, 1988.
- [18] Y. Murata, S. Tanabe, and M. Tadokoroetc, "3D-MoM analysis of radio frequency noise radiation from HVDC converter station," *IEEE International Symposium*, pp. 980-985, 1999.



**Hong Sen Zou** is currently working with the State Grid Ningxia Electric Power Co., Ltd. Maintenance Company. His research interest includes power electronics and power system automation.



**Lin Zheng** is currently working with the State Key Laboratory of Advanced Power Transmission Technology (Global Energy Interconnection Research Institute Co., Ltd.). His research interest includes the development and engineering of control and protection system for HVDC and DC grid applications.



**Yuan Zhang** is currently working with the State Grid Ningxia Electric Power Co., Ltd. Maintenance Company. His research interest includes power electronics and power system automation.



**Yajie Wang** is currently working with the State Key Laboratory of Advanced Power Transmission Technology (Global Energy Interconnection Research Institute Co., Ltd.). Her research interest includes the development and engineering of control and protection system for HVDC and DC grid applications.



**Jianan Zhang** is currently working with the State Key Laboratory of Advanced Power Transmission Technology (Global Energy Interconnection Research Institute Co., Ltd.). Her research interest includes the development and engineering of control and protection system for HVDC and DC grid applications.



**Huafeng Wang** is currently working with the State Key Laboratory of Advanced Power Transmission Technology (Global Energy Interconnection Research Institute Co., Ltd.). His research interest includes the HVDC control and protection and valve control system of converter valves.

# Model of Ferrite-cored Driver-pickup Coil Probe Application of TREE Method for Eddy Current Nondestructive Evaluation

Siquan Zhang and Chengkai Ye

Department of Electrical and Automation  
Shanghai Maritime University, Shanghai 201306, China  
sqzhang@shmtu.edu.cn

**Abstract** – An analytical model of a driver-pickup coil probe, consists of a cylindrical ferrite core, located above a layered conductor is presented. The truncated region eigenfunction expansion (TREE) method is used and the solution region is truncated with a certain radius around  $z$  axis. First, the magnetic vector potential of each region of filamentary coil problem is derived and solved with variables separation method using boundary and interface conditions, and then the rectangular cross-section coil problem is solved with superposition method. The expression of induced voltage in pickup coil is obtained and can be calculated with software such as Matlab or Mathematica. Using the proposed analytical model, the influence of the excitation frequency and excitation current in the driver coil on the responses of the pickup coil is examined. Experiments are performed, and the changes of voltage induced in the pickup coil due to the conductor are measured at different excitation frequencies and excitation currents. The analytical calculation results agree with the experimental results very well, verifying the correctness of the proposed analytical model.

**Index Terms** – Eddy current testing, ferrite cored driver-pickup probe, induced voltage, magnetic vector potential, truncated region eigenfunction expansion method.

## I. INTRODUCTION

Eddy current testing (ECT) is one of the conventional methods used to evaluate the characteristics and defects of conductive materials. Due to its extremely high sensitivity and no contact need with test pieces, ECT is widely used in the safety assessment of critical components in industry and manufacturing.

Generally, an absolute ECT probe has one single coil, which is excited by a sinusoidal current and generates an eddy current in the conductor under test, the magnetic field reflected from the eddy current causes the impedance change of the coil. The signal of this impedance change can be measured and used to evaluate the conductive material [1–3].

In addition to single-coil probes, the differential ECT probes have two or more coils. Each coil has excitation and sensing functions, the coils are usually wound in opposite directions. When they are located on the same conductor, no signal is generated. When one coil is over the defective material and the other coil is over the good material, a very distinct differential signal can be observed [4, 5].

There are also probes in which excitation and sensing are performed by separate coils. For example, the widely used ECT driver-pickup probe consists of one or more driver coils and pickup coils. The detection process can be achieved by measuring the change of the induced voltage of the pickup coil close to the excitation coil [6, 7].

Many analytical methods have been developed for calculation the response of air-cored pickup coil for driver-pickup coil probe. Using the Fourier transform method, the expression of induced voltage in pickup coil above conductor was presented, both coils were air-cored, and the final expression of induced voltage was presented in integral form [8]. For an arbitrary pair of air-cored coils located above a conducting plate, the expression of change in mutual impedance due to eddy current induction was provided and discussed [9]. An inductive coupled circuit model was proposed and exact solutions for electromagnetic responses in several situations were developed, such as a coaxial driver-pickup probe without conductor and a coaxial driver-pickup probe encircling a long ferromagnetic conducting rod [10, 11].

The signal of air-cored probe is easily affected by external noise. The researchers have emphasized improving the sensitivity and signal-to-noise ratio of ECT probes. The ferrite core has high permeability and poor conductivity, which provides a convenient path for the magnetic field. The eddy current loss in the ferrite core is small, performing a considerable role in concentrating magnetic flux or shielding external noise. Various ferrite cores, such as I-core, T-core and E-core are used in ECT probes and have achieved good results in improving sensitivity [12–16].

However, the ferrite cores mentioned above are seldom used and discussed in driver-pickup probes. Therefore, it is necessary to further investigate the possibility of introducing ferrite core into the driver-pickup probe to improve the sensitivity of the pickup coil.

A driver-pickup self-nulling eddy current probe was developed in [17], in which a ferromagnetic shield was inserted between the driver coil and the sensor coil. The probe does not require calibration and can detect surface flaws and interlayer corrosion with a high probability of success. The probe also has advantages of simplifying nondestructive testing and reducing testing times without sacrificing defect resolution. However this study only contains experimental results, without theoretical analysis. An analytical model is needed to understand the underlying relationship of the parameters.

Many solutions of unbounded domain problems were obtained in the form of integrals, which have the disadvantage of long computation time. The TREE method truncates the infinite domain into a finite solution domain, which speeds up the calculation while maintaining the accuracy of calculation [18–20].

In this paper, as shown in Figure 1, an ECT probe is composed of a driver and a pickup coil, both of which surround the same ferromagnetic core, and the probe is placed above two-layered conductor. The TREE method is used to deduce the analytical model, and the final expression of the induced voltage of the pick-up coil is derived and expressed in matrix form. The correctness of the proposed analytical model is verified by experiments.

## II. SOLUTION

The geometry shown in Figure 2 (a) was analyzed first, where a sinusoidal current excited filamentary driver coil of radius  $r_0$  and a filamentary pickup coil of radius  $r_c$  encircle a ferrite cylinder with relative magnetic permeability  $\mu_f$ . The probe is placed above a two-layer conductor with conductivities  $\sigma_5$  and  $\sigma_6$  respectively.

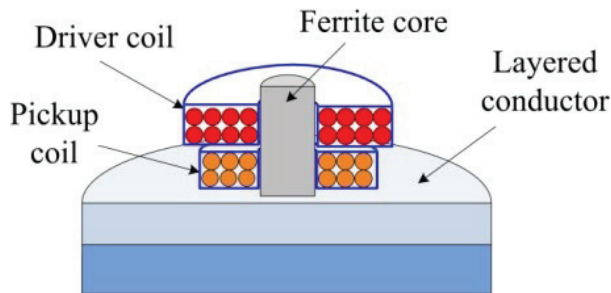


Fig. 1. Cross-sectional view of a driver and a pick-up coils encircling an I-core above layered conductor.

The plane  $z = 0$  coincides with the top surface of the conductor. The infinite solution domain is truncated by a cylindrical surface of radius  $b$ , and the whole problem geometry is divided into six regions along the axial direction.

Using the separation of variables method, the general form of the magnetic vector potential in all these regions can be written as a series of first kind Bessel functions of one order and solved with the boundary and interface conditions [13].

In Figure 2 (a), regions 1, 4, 5 and 6 contain only air or a conductor, the eigenvalues  $q_i$  are the positive real roots of the equation:

$$J_1(\mathbf{q}_i b) = 0 \quad i = 0, 1, 2, \dots, N_s, \quad (1)$$

where  $N_s$  is the number of summation terms.

Because regions 2 and 3 comprise two sub-regions, the ferrite core and the air, so the radial dependence in the expressions for  $A_\phi$  of these two sub-regions can be written as below.

For region 2:

$$A_{2core} = A_E J_1(p_i r) \quad 0 \leq r \leq a_1, \quad (2)$$

$$A_{2air} = A_E B_{1F} J_1(p_i r) + A_E C_{1F} Y_1(p_i r) \quad a_1 \leq r \leq b, \quad (3)$$

where  $J_n$  and  $Y_n$  are first kind Bessel functions of  $n$  order, and  $p_i$  are the corresponding discrete eigenvalues.

In regions 2 and 3, by using the continuity of  $B_r$  and  $H_z$  on the interface  $r = a_1$  gives

$$B_{1F} = \frac{\pi p_i a_1}{2} \left[ J_1(p_i a_1) Y_0(p_i a_1) - \frac{J_0(p_i a_1) Y_1(p_i a_1)}{\mu_f} \right] \quad (4)$$

$$C_{1F} = \frac{\pi p_i a_1}{2} J_1(p_i a_1) J_0(p_i a_1) \left( \frac{1}{\mu_f} - 1 \right). \quad (5)$$

Since at the boundary  $r = b$ ,  $A_\phi(b, z) = 0$  must also hold, the following equation is formed:

$$R_1(p_i b) = B_{1F} J_1(p_i b) + C_{1F} Y_1(p_i b) = 0, \quad (6)$$

where

$$R_1(p_i r) = B_{1F} J_1(p_i r) + C_{1F} Y_1(p_i r). \quad (7)$$

The eigenvalues  $p_i$  can be calculated using numerical procedures, such as FindRoot() in Mathematica or fzero() in Matlab to find real roots of eqn (6). Following the method of variables separation, the expressions for  $A_\phi$  in various regions of the problem in Figure 2 (a) have the following forms, which are expressed in matrix notation:

$$A_1(r, z) = J_1(\mathbf{q}^T r) \mathbf{q}^{-1} e^{-\mathbf{q}z} \mathbf{C}_1, \quad (8)$$

$$A_2(r, z) = \begin{matrix} J_1(\mathbf{p}^T r) \\ R_1(\mathbf{p}^T r) \end{matrix} \mathbf{p}^{-1} (e^{-\mathbf{p}z} \mathbf{C}_2 - e^{\mathbf{p}z} \mathbf{B}_2) \quad \begin{matrix} 0 \leq r \leq a_1 \\ a_1 \leq r \leq b \end{matrix}, \quad (9)$$

$$A_3(r, z) = \begin{matrix} J_1(\mathbf{p}^T r) \\ R_1(\mathbf{p}^T r) \end{matrix} \mathbf{p}^{-1} (e^{-\mathbf{p}z} \mathbf{C}_3 - e^{\mathbf{p}z} \mathbf{B}_3) \quad \begin{matrix} 0 \leq r \leq a_1 \\ a_1 \leq r \leq b \end{matrix}, \quad (10)$$

$$A_4(r, z) = J_1(\mathbf{q}^T r) \mathbf{q}^{-1} (e^{-\mathbf{q}z} \mathbf{C}_4 - e^{\mathbf{q}z} \mathbf{B}_4) \quad (11)$$

$$A_5(r, z) = J_1(\mathbf{q}^T r) \mathbf{s}_5^{-1} (e^{-\mathbf{s}_5 z} \mathbf{C}_5 - e^{\mathbf{s}_5 z} \mathbf{B}_5) \quad (12)$$

$$A_6(r, z) = -J_1(\mathbf{q}^T r) \mathbf{s}_6^{-1} e^{\mathbf{s}_6 z} \mathbf{B}_6, \quad (13)$$

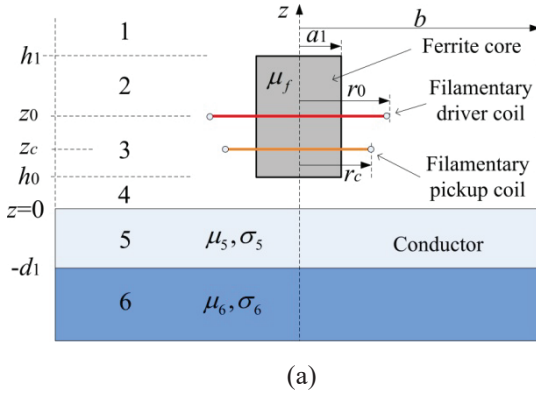
where

$$\mathbf{s}_5 = \sqrt{\mathbf{q}^2 + j\omega\mu_0\mu_5\sigma_5} \quad (14)$$

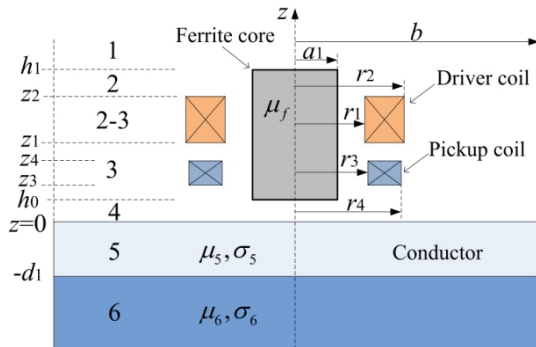
$$\mathbf{s}_6 = \sqrt{\mathbf{q}^2 + j\omega\mu_0\mu_6\sigma_6}. \quad (15)$$

In eqn (8)–(13),  $J_1(\mathbf{q}^T r)$ ,  $J_1(\mathbf{p}^T r)$ ,  $R_1(\mathbf{p}^T r)$  are row vectors;  $\mathbf{q}^{-1}$ ,  $\mathbf{p}^{-1}$ ,  $\mathbf{s}_5^{-1}$ ,  $\mathbf{s}_6^{-1}$  and exponentials  $e^{\pm\mathbf{q}z}$ ,  $e^{\pm\mathbf{p}z}$ ,  $e^{\pm\mathbf{s}_5 z}$ ,  $e^{\mathbf{s}_6 z}$  are diagonal matrices.  $\mathbf{C}_i$  and  $\mathbf{B}_i$  are column vectors of unknown coefficients.

The interface conditions, continuity of  $B_z$  and  $H_r$  between the six regions of the problem have to be satisfied. These unknown coefficients and the discrete eigenvalues are to be determined from the boundary and interface conditions. The magnetic vector potential of region 3 in Figure 2 (a) excited by filamentary



(a)



(b)

Fig. 2. (a) Filamentary and (b) rectangular cross-section driver and pickup coils encircling an I-core above layered conductor.

driver coil is obtained:

$$A_{3\text{filamentary}}(r, z) = \frac{1}{2} \mu I \mathbf{D}^{-1} R_1(\mathbf{p}r) \mathbf{p}^{-1} r_0 R_1(\mathbf{p}r_0) \cdot (e^{-\mathbf{p}z} \mathbf{C}_{36} - e^{\mathbf{p}z} \mathbf{B}_{36}) \cdot \frac{[(\mathbf{T}+\mathbf{U})e^{\mathbf{p}(h_1-z_0)} - (\mathbf{T}-\mathbf{U})e^{\mathbf{p}(z_0-h_1)}]}{[(\mathbf{T}-\mathbf{U})e^{-\mathbf{p}h_1} \mathbf{C}_{36} - (\mathbf{U}+\mathbf{T})e^{\mathbf{p}h_1} \mathbf{B}_{36}]}. \quad (16)$$

By using superposition method, the magnetic vector potential in region 3 excited by rectangular cross-section coil with rectangular cross section shown in Figure 2 (b) can be derived:

$$A_3(r, z) = \frac{\mu I}{2} \mathbf{D}^{-1} \mathbf{p}^{-1} R_1(\mathbf{p}r) \times \left[ \mathbf{p}^{-3} \int_{\mathbf{p}r_1}^{\mathbf{p}r_2} \mathbf{p}r_0 R_1(\mathbf{p}r_0) d(\mathbf{p}r_0) \right] (e^{-\mathbf{p}z} \mathbf{C}_{36} - e^{\mathbf{p}z} \mathbf{B}_{36}) \cdot \frac{(\mathbf{T}+\mathbf{U})(e^{\mathbf{p}(h_1-z_1)} - e^{\mathbf{p}(h_1-z_2)}) - (\mathbf{T}-\mathbf{U})(e^{\mathbf{p}(z_2-h_1)} - e^{\mathbf{p}(z_1-h_1)})}{(\mathbf{T}-\mathbf{U})e^{-\mathbf{p}h_1} \mathbf{C}_{36} - (\mathbf{T}+\mathbf{U})e^{\mathbf{p}h_1} \mathbf{B}_{36}}. \quad (17)$$

The  $z$  direction magnetic flux density  $B_z$  in region 3 excited by driver coil of  $N_1$  turns can be obtained as follows:

$$B_{z3} = \frac{\mu_0 N_1 I}{2(r_2 - r_1)(z_2 - z_1)} R_0(\mathbf{p}r) \mathbf{D}^{-1} (e^{-\mathbf{p}z} \mathbf{C}_{36} - e^{\mathbf{p}z} \mathbf{B}_{36}) \cdot \frac{(\mathbf{T}+\mathbf{U})(e^{\mathbf{p}(h_1-z_1)} - e^{\mathbf{p}(h_1-z_2)}) - (\mathbf{T}-\mathbf{U})(e^{\mathbf{p}(z_2-h_1)} - e^{\mathbf{p}(z_1-h_1)})}{(\mathbf{T}-\mathbf{U})e^{-\mathbf{p}h_1} \mathbf{C}_{36} - (\mathbf{T}+\mathbf{U})e^{\mathbf{p}h_1} \mathbf{B}_{36}} \cdot [\mathbf{p}^{-3} \int_{\mathbf{p}r_1}^{\mathbf{p}r_2} \mathbf{p}r_0 R_1(\mathbf{p}r_0) d(\mathbf{p}r_0)]. \quad (18)$$

The magnetic flux penetrated through a filamentary pick-up coil with radius  $r_c$  can be expressed as

$$\phi_r = \int_0^{2\pi} d\theta \int_0^{r_c} B_{z3}|_{z=z_c} r dr = \frac{\pi \mu_0 N_1 I}{(r_2 - r_1)(z_2 - z_1)} [\mathbf{p}^{-1} r_c R_1(\mathbf{p}r_c)] \mathbf{D}^{-1} (e^{-\mathbf{p}z_c} \mathbf{C}_{36} - e^{\mathbf{p}z_c} \mathbf{B}_{36}) \cdot \frac{(\mathbf{T}+\mathbf{U})(e^{\mathbf{p}(h_1-z_1)} - e^{\mathbf{p}(h_1-z_2)}) - (\mathbf{T}-\mathbf{U})(e^{\mathbf{p}(z_2-h_1)} - e^{\mathbf{p}(z_1-h_1)})}{(\mathbf{T}-\mathbf{U})e^{-\mathbf{p}h_1} \mathbf{C}_{36} - (\mathbf{T}+\mathbf{U})e^{\mathbf{p}h_1} \mathbf{B}_{36}} \cdot [\mathbf{p}^{-3} \int_{\mathbf{p}r_1}^{\mathbf{p}r_2} \mathbf{p}r_0 R_1(\mathbf{p}r_0) d(\mathbf{p}r_0)]. \quad (19)$$

The magnetic flux penetrated through  $N_2$  turns of pick-up coil with rectangular cross section can be derived as:

$$\phi = \frac{N_2}{(r_4 - r_3)(z_4 - z_3)} \int_{r_3}^{r_4} dr_c \int_{z_3}^{z_4} \phi_r dz_c = \frac{\pi \mu_0 N_1 N_2 I}{(r_2 - r_1)(r_4 - r_3)(z_2 - z_1)(z_4 - z_3)} \times [\mathbf{p}^{-4} \int_{\mathbf{p}r_3}^{\mathbf{p}r_4} \mathbf{p}r_c R_1(\mathbf{p}r_c) d\mathbf{p}r_c] \cdot [(e^{-\mathbf{p}z_3} - e^{-\mathbf{p}z_4}) \mathbf{C}_{36} + (e^{\mathbf{p}z_3} - e^{\mathbf{p}z_4}) \mathbf{B}_{36}] \cdot \frac{(\mathbf{T}+\mathbf{U})(e^{\mathbf{p}(h_1-z_1)} - e^{\mathbf{p}(h_1-z_2)}) - (\mathbf{T}-\mathbf{U})(e^{\mathbf{p}(z_2-h_1)} - e^{\mathbf{p}(z_1-h_1)})}{(\mathbf{T}-\mathbf{U})e^{-\mathbf{p}h_1} \mathbf{C}_{36} - (\mathbf{T}+\mathbf{U})e^{\mathbf{p}h_1} \mathbf{B}_{36}} \cdot \mathbf{D}^{-1} [\mathbf{p}^{-3} \int_{\mathbf{p}r_1}^{\mathbf{p}r_2} \mathbf{p}r_0 R_1(\mathbf{p}r_0) d(\mathbf{p}r_0)]. \quad (20)$$

The induced voltage in pick-up coil can be expressed as:

$$V = V_{co} \cdot \mathbf{p}^{-4} \text{Int}(\mathbf{p}^T r_3, \mathbf{p}^T r_4) \mathbf{W}_1 \mathbf{W}_2^{-1} \mathbf{W}_3 \mathbf{D}^{-1} \mathbf{p}^{-3} \text{Int}(\mathbf{p}r_1, \mathbf{p}r_2), \quad (21)$$

where

$$V_{co} = \frac{-j\omega\pi\mu_0 N_1 N_2 I}{(r_2 - r_1)(r_4 - r_3)(z_2 - z_1)(z_4 - z_3)} \quad (22)$$

$$\mathbf{W}_1 = (e^{-\mathbf{P}z_3} - e^{-\mathbf{P}z_4})\mathbf{C}_{36} + (e^{\mathbf{P}z_3} - e^{\mathbf{P}z_4})\mathbf{B}_{36} \quad (23)$$

$$\mathbf{W}_2 = (\mathbf{T} - \mathbf{U})e^{-\mathbf{P}h_1}\mathbf{C}_{36} - (\mathbf{T} + \mathbf{U})e^{\mathbf{P}h_1}\mathbf{B}_{36} \quad (24)$$

$$\mathbf{W}_3 = (\mathbf{T} + \mathbf{U})(e^{\mathbf{P}(h_1 - z_1)} - e^{\mathbf{P}(h_1 - z_2)}) - (\mathbf{T} - \mathbf{U})(e^{\mathbf{P}(z_2 - h_1)} - e^{\mathbf{P}(z_1 - h_1)}) \quad (25)$$

$$\text{Int}(\mathbf{p}^T r_3, \mathbf{p}^T r_4) = \int_{\mathbf{p}r_3}^{\mathbf{p}r_4} \mathbf{p}r_c R_1(\mathbf{p}r_c) d\mathbf{p}r_c \quad (26)$$

$$\text{Int}(\mathbf{p}r_1, \mathbf{p}r_2) = \int_{\mathbf{p}r_1}^{\mathbf{p}r_2} \mathbf{p}r_0 R_1(\mathbf{p}r_0) d\mathbf{p}r_0 \quad (27)$$

$$\mathbf{C}_{36} = \frac{1}{2}e^{\pm\mathbf{P}h_0}[(\mathbf{T}^{-1} \pm \mathbf{U}^{-1})\mathbf{E}e^{-\mathbf{q}h_0}\mathbf{C}_{46} + (\mathbf{T}^{-1} \mp \mathbf{U}^{-1})\mathbf{E}e^{\mathbf{q}h_0}\mathbf{B}_{46}] \quad (28)$$

$$\mathbf{C}_{46} = \frac{1}{2}[(1 \pm \mathbf{q}\mathbf{s}_5^{-1})\mathbf{C}_{56} + (1 \mp \mathbf{q}\mathbf{s}_5^{-1})\mathbf{B}_{56}] \quad (29)$$

$$\mathbf{C}_{56} = \frac{1}{2}e^{\mp\mathbf{s}_5 d_1}(1 \mp \mathbf{s}_5 \mathbf{s}_6^{-1})e^{-\mathbf{s}_6 d_1}, \quad (30)$$

where  $j$  is imaginary unit,  $N_1$  and  $N_2$  are the number of turns in the driver and pickup coils respectively,  $\mu_0$  is the permeability of vacuum,  $\omega$  and  $I$  are the angular frequency and effective value of the excitation current. The negative sign in eqn (22) states that the direction of induced voltage in pickup coil is always such that it will oppose the change in flux which produced it. The matrices  $\mathbf{D}$ ,  $\mathbf{T}$  and  $\mathbf{U}$  are defined in [13].

### III. SPECIAL CASES

The expression of voltage induced in the pick-up coil of an I-cored driver-pickup probe located above layered conductor has been derived and can be calculated with eqn (21). When the layered conductor is absent, the voltage induced in the pick-up coil is expressed as  $V_0$  and can also be calculated with eqn (21) by setting  $\sigma_5=0$  and  $\sigma_6=0$ . The change of induced voltage in pickup coil due to the conductor can be obtained as  $\Delta V=V-V_0$ .

When the I-core in Figure 2 was absent, the configuration changed into an air-cored probe with driver and pickup coils as shown in Figure 3. In this case, the expressions for  $A_\phi$  in various regions of Figure 3 (a) have the following forms which are also given in the form of matrix:

$$A_1(r, z) = J_1(\mathbf{q}^T r) e^{-\mathbf{q}z} \mathbf{K}_1 \quad (31)$$

$$A_2(r, z) = J_1(\mathbf{q}^T r) (e^{\mathbf{q}z} \mathbf{V}_2 + e^{-\mathbf{q}z} \mathbf{K}_2) \quad (32)$$

$$A_3(r, z) = J_1(\mathbf{q}^T r) (e^{\mathbf{s}_3 z} \mathbf{V}_3 + e^{-\mathbf{s}_3 z} \mathbf{K}_3) \quad (33)$$

$$A_4(r, z) = J_1(\mathbf{q}^T r) e^{\mathbf{s}_4 z} \mathbf{V}_4, \quad (34)$$

where

$$\mathbf{s}_3 = \sqrt{\mathbf{q}^2 + j\omega\mu_3\mu_0\sigma_3} \quad (35)$$

$$\mathbf{s}_4 = \sqrt{\mathbf{q}^2 + j\omega\mu_4\mu_0\sigma_4}. \quad (36)$$

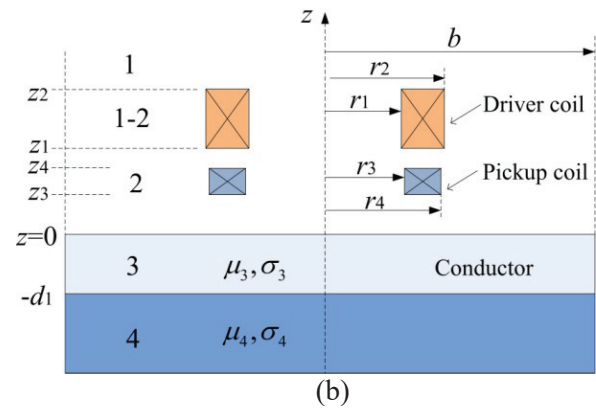
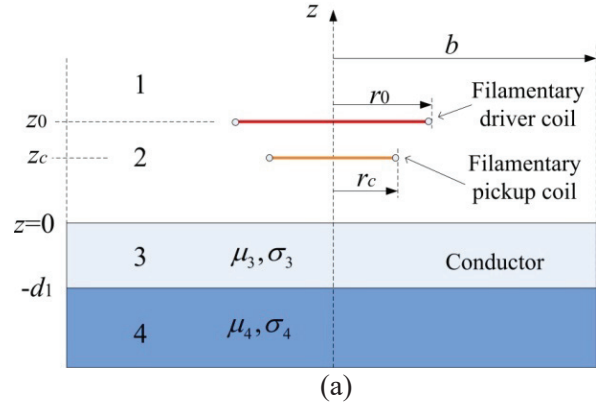


Fig. 3. (a) Filamentary and (b) rectangular cross-section exciting and pick-up coil of air-core probe located above layered conductor.

$J_1(\mathbf{q}^T r)$  is row vector; exponentials  $e^{\pm\mathbf{q}z}$ ,  $e^{\pm\mathbf{s}_3 z}$ ,  $e^{\mathbf{s}_4 z}$  are diagonal matrices.  $\mathbf{V}_i$  and  $\mathbf{K}_i$  are column vectors of unknown coefficients.

Using same method as cored probe, the expression of induced voltage in the pick-up coil of an air-cored probe can be obtained as follow.

$$V = V_{co} \cdot \mathbf{q}^{-4} \text{Int}(\mathbf{q}^T r_3, \mathbf{q}^T r_4) \mathbf{E}^{-1} \mathbf{W}_4 \mathbf{W}_5^{-1} \mathbf{W}_6 \times \mathbf{q}^{-3} \text{Int}(\mathbf{q}r_1, \mathbf{q}r_2), \quad (37)$$

where

$$\mathbf{W}_4 = (e^{\mathbf{q}z_4} - e^{\mathbf{q}z_3})\mathbf{V}_{24} - (e^{-\mathbf{q}z_4} - e^{-\mathbf{q}z_3})\mathbf{K}_{24} \quad (38)$$

$$\mathbf{W}_5 = (1 + \mathbf{q}^{-1}\mathbf{s}_3)\mathbf{V}_{34} + (1 - \mathbf{q}^{-1}\mathbf{s}_3)\mathbf{K}_{34} \quad (39)$$

$$\mathbf{W}_6 = e^{-\mathbf{q}z_1} - e^{-\mathbf{q}z_2} \quad (40)$$

$$\text{Int}(\mathbf{q}^T r_3, \mathbf{q}^T r_4) = \int_{\mathbf{q}r_3}^{\mathbf{q}r_4} \mathbf{q}r_c J_1(\mathbf{q}r_c) d\mathbf{q}r_c \quad (41)$$

$$\text{Int}(\mathbf{q}r_1, \mathbf{q}r_2) = \int_{\mathbf{q}r_1}^{\mathbf{q}r_2} \mathbf{q}r_0 J_1(\mathbf{q}r_0) d\mathbf{q}r_0 \quad (42)$$

$$\mathbf{V}_{34} = \frac{1}{2}e^{\pm\mathbf{s}_3 d_1}(1 \pm \mathbf{s}_3^{-1}\mathbf{s}_4)e^{-\mathbf{s}_4 d_1} \quad (43)$$

$$\mathbf{K}_{24} = \frac{1}{2}[(1 \pm \mathbf{q}^{-1}\mathbf{s}_3)\mathbf{V}_{34} + (1 \mp \mathbf{q}^{-1}\mathbf{s}_3)\mathbf{K}_{34}]. \quad (44)$$

In the case where an air-cored driver-pickup coil probe is above layered conductor, when the conductor



Fig. 4. Experimental setup.

is absent, the induced voltage in pickup coil can also be calculated with eqn (37) by setting  $\sigma_3=0$  and  $\sigma_4=0$ . The change of induced voltage in pickup coil due to conductor can also be obtained easily.

#### IV. EXPERIMENTAL VERIFICATION

The correctness of the proposed ferrite-cored driver-pickup probe model is verified by experimental measurements. The responses of pickup coil calculated by the model are compared with measured results. The experimental configuration is shown in Figure 4. The sinusoidal excitation signal of a frequency generated by a function generator is magnified by a power amplifier, and then transmitted to the driver coil. The amplitude of the sine wave and the magnification of the power amplifier are adjusted to ensure a 100 mA effective value current generated in the driver coil, the current was measured with a multimeter connected in series with the driver coil. Finally the voltage induced in the pickup coil is measured by a millivoltmeter parallel connection with the pickup coil. The responses of the induced voltage in the pickup coil are measured at different excitation frequencies range from 100 Hz to 30 kHz.

When the excitation frequency is fixed at 10 kHz, the responses of the pickup coil are also measured with different excitation currents.

#### V. RESULTS AND DISCUSSION

The voltages induced in the pick-up coil of an I-cored driver-pickup probe and an air-cored driver-pickup probe located above layered conductor can be calculated by eqn (21) and (37) respectively using Matlab or Mathematica, the parameters used in analytical calculation are shown in Table 1, which are the same as those used in experiments.

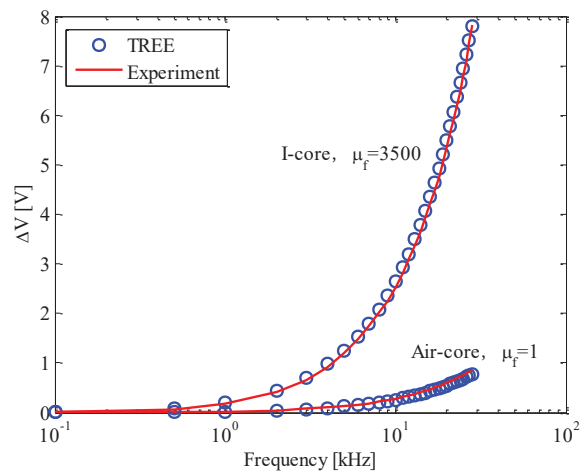
The calculated results are compared with the measurements. Figure 5 shows the induced voltage change of the pickup coil for an air-cored probe with  $\mu_f=1$  and a ferrite-cored probe with  $\mu_f=3500$ , due to the layered conductor, as a function of frequency. The calculations are performed by setting the summation terms  $N_s=60$  and truncation radius  $b=90$  mm, more than ten times the outer radius of the pickup coil.

Table 1: Parameters of the coils, I-core, and conductor used in experiments and analytical calculation

Inner radius	$r_1$	5.2 mm
Outer radius	$r_2$	7.2 mm
Parameter	$z_1$	7.3 mm
Parameter	$z_2$	16 mm
Number of turns	$N_1$	430
Inner radius	$r_3$	5.1 mm
Outer radius	$r_4$	7.8 mm
Parameter	$z_3$	1.1 mm
Parameter	$z_4$	5.1 mm
Number of turns	$N_2$	150
Core radius	$a_1$	4 mm
Parameter	$h_1$	18.1 mm
Relative permeability	$\mu_f$	3500
Liftoff	$h_0$	0.1 mm
Thickness	$d_1$	2 mm
Relative permeability	$\mu_3, \mu_4, \mu_5, \mu_6$	1
Conductivity	$\sigma_3, \sigma_4, \sigma_5, \sigma_6$	38 MS/m

When keeping the exciting currents at 100 mA, the change of induced voltage in the pickup coil increases with frequency. Excited with same frequency, the I-cored probe obtained a larger voltage change than that of the air-cored probe. The analytical results agree with the experimental results very well.

The influence of the excitation current on the responses of the pickup coil is also examined with pro-


 Fig. 5. Induced voltage change of the pickup coil for an air-cored probe ( $\mu_f=1$ ) and an I-cored probe ( $\mu_f=3500$ ) as a function of frequency due to the conductor.

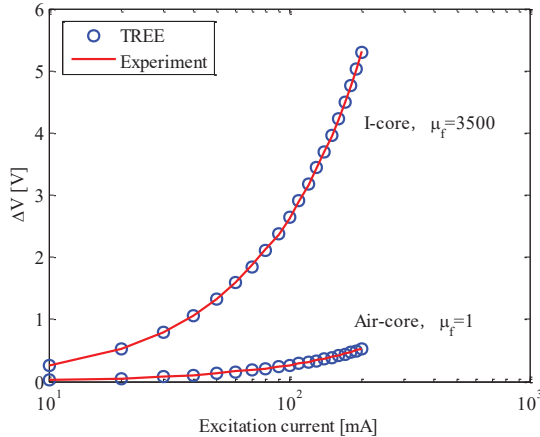


Fig. 6. Induced voltage change of the pickup coil for an air-cored probe ( $\mu_f = 1$ ) and an I-cored probe ( $\mu_f = 3500$ ) as a function of excitation current due to the conductor.

posed analytical model, and the analytical results are compared with experiments. Figure 6 shows the induced voltage change of the pickup coil for an air-cored probe with  $\mu_f = 1$  and an I-cored probe with  $\mu_f = 3500$ , as a function of excitation current, due to the layered conductor.

When the excitation frequency is maintained at 10 kHz, the change of induced voltage in the pickup coil are calculated and measured at different excitation currents. The results are shown in Figure 6, the change of induced voltage in the pickup coil increases with the current. Excited with same current, the I-cored probe obtains a larger voltage change than that of the air-cored probe. The results of analytical calculation are in good agreement with the experiment. In all cases, the relative error between analytical calculation and experiment is less than 3%.

## VI. CONCLUSION

An analytical model of ferrite-cored probe containing a driver coil and a pickup coil located over layered conductor was presented. The expression of induced voltage in the pickup coil was derived. The change of induced voltage in pickup coil due to layered conductor was calculated and measured. The factors affecting the responses of pickup coil, such as the excitation frequency and excitation current in the driver coil were examined. The proposed analytical model can be used in simulation of eddy current testing, coating thickness measurement, or directly used in eddy current probe design.

## REFERENCES

[1] G. Tytko and L. Dzikowski, "Fast calculation of the filamentary coil impedance using the truncated region eigenfunction expansion method,"

*Applied Computational Electromagnetics Society (ACES) Journal*, vol. 33, no. 12, pp. 1461-1466, 2018.

- [2] T. Theodoulidis and J. R. Bowler, "Impedance of a coil at an arbitrary position and orientation inside a conductive borehole or tube," *IEEE Trans. Magnetism*, vol. 51, no. 4, pp. 1-6, 2015.
- [3] C. V. Dodd and W. E. Deeds, "Analytical solutions to eddy-current probe-coil problems," *J. Appl. Phys.*, vol. 39, no. 6, pp. 2829-2838, 1968.
- [4] T. P. Theodoulidis and J. R. Bowler, "Bobbin coil signal variation due to an axisymmetric circumferential groove in a tube," *AIP Conf. Proc.*, vol. 1096, no. 1, pp. 1922-1929, 2009.
- [5] S. R. Luis, G. S. Telmo, M. R. Pedro, V. Pedro, and M. Piedade, "A differential planar eddy currents probe: Fundamentals, modeling and experimental evaluation," *NDT E Int.*, vol. 51, pp. 85-93, 2012.
- [6] T. P. Theodoulidis, "Developments in calculating the transient eddy-current response from a conductive plate," *IEEE Trans. Magnetism*, vol. 44, no. 7, pp. 1894-1896, 2008.
- [7] H. Huang and T. Takagi, "Inverse analyses for natural and multicracks using signals from a differential transmit-receive ECT probe," *IEEE Trans. Magnetism*, vol. 38, no. 2, pp. 1009-1012, 2002.
- [8] S. Zhang and N. Ida, "Analytical calculation of induced voltages of uniform eddy current probes above a moving conductor," *Lecture Notes Electr. Eng.*, vol. 506, pp. 177-193, 2019.
- [9] S. K. Burke and M. E. Ibrahim, "Mutual impedance of air-cored coils above a conducting plate," *J. Phys. D: Appl. Phys.*, vol. 37, no. 13, pp. 1857-1868, 2004.
- [10] D. R. Desjardins, T. W. Krause, A. Tetervak, and L. Clapham, "Concerning the derivation of exact solutions to inductive circuit problems for eddy current testing," *NDT E Int.*, vol. 68, pp. 128-135, 2014.
- [11] D. R. Desjardins, L. Clapham, and T. W. Krause, "Transient response of a driver-pickup coil probe in transient eddy current testing," *NDT E Int.*, vol. 75, pp. 8-14, 2015.
- [12] S. Zhang, "An analytical model of a new T-cored coil used for eddy current nondestructive evaluation," *Applied Computational Electromagnetics Society (ACES) Journal*, vol. 35, no. 9, pp. 1099-1104, 2020.
- [13] T. P. Theodoulidis, "Model of ferrite-cored probes for eddy current nondestructive evaluation," *J. Appl. Phys.*, vol. 93, no. 5, pp. 3071-3078, 2003.

- [14] S. Zhang, "Analytical model of an I-core coil for nondestructive evaluation of a conducting cylinder below an infinite plane conductor," *Meas. Sci. Rev.*, vol. 21, no. 4, pp. 99-105, 2021.
- [15] S. Zhang, "Analytical model of a T-core coil above a multi-layer conductor with hidden hole using the TREE method for nondestructive evaluation," *COMPEL - Int. J. Comput. Math. Electr. Electron. Eng.*, vol. 40, no. 6, pp. 1104-1117, 2021.
- [16] G. Tytko and L. Dziczkowski, "E-cored coil with a circular air gap inside the core column used in eddy current testing," *IEEE Trans. Magnetics*, vol. 51, no. 9, pp. 1-4, 2015.
- [17] B. Wincheski, J. P. Fulton, S. Nath, M. Namkung, and J. W. Simpson, "Self-nulling eddy current probe for surface and subsurface flaw detection," *Mater. Eval.*, vol. 52, no. 1, pp. 22-26, 1994.
- [18] F. Jiang and S. Liu, "Calculation and analysis of an analytical model for magnetic field monitoring based on TREE in eddy current testing," *Applied Computational Electromagnetics Society (ACES) Journal*, vol. 33, no. 12, pp. 1489-1497, 2018.
- [19] T. P. Theodoulidis and E. E. Kriezis, "Series expansions in eddy current nondestructive evaluation models," *J. Mater. Process. Technol.*, vol. 161, no. 1-2, pp. 343-347, 2005.
- [20] F. Sakkaki and H. Bayani, "Solution to the problem of E-cored coil above a layered half-space using the method of truncated region eigenfunction expansion," *J. Appl. Phys.*, vol. 111, no. 7, pp. 2829-2864, 2012.



**Siqian Zhang** received the Ph.D. degree in Material Processing Engineering from the South China University of Technology, Guangzhou, China. His current research interests include eddy current testing, analytical model in Non-destructive testing.



**Chengkai Ye** received the B.S. degree from Shanghai Maritime University. He is currently working towards the M.S. degree in Control Theory and Control Engineering. His current research interests include eddy current testing and the application of finite element method

in NDT.

# Research on the Characteristics of the Pantograph Arc and Analyzing its Influence on the ILS

Yingchun Xiao<sup>1,2</sup>, Feng Zhu<sup>1</sup>, Nan Lu<sup>1</sup>, Zixuan Wang<sup>1</sup>, and Shengxan Zhuang<sup>1</sup>

<sup>1</sup>Department of Electrical Engineering  
Southwest Jiaotong University, Chengdu 611756, China  
1134748712@qq.com, zhufeng@swjtu.cn, LuNan946@qq.com, 942043313@qq.com

<sup>2</sup>Lanzhou City University, Lanzhou 730070, China

**Abstract** – In this article, a radiation model is proposed to estimate the emission of the pantograph arc. An improved least-square regression analysis method is given for studying the pantograph arc characteristics at various sites on electrified railways and at various train speeds. The radiation model and the improved least-square method were both validated using the test data. The impact of arc on the airport instrument landing system (ILS) was investigated using electromagnetic wave propagation theory and the signal-to-noise ratio requirement of the ILS. We deduced the position limit of the articulated neutral section (ANS) and verified it through experiments. This research provides a theoretical foundation and technological methodology for civil aviation and high-speed railway electromagnetic compatibility studies as well as helps for airport site selection and high-speed railway route planning.

**Index Terms** – Airport instrument landing system, electromagnetic emission, electromagnetic interference, improved leastsquare method, pantograph arc.

## I. INTRODUCTION

With the development of high-speed electrified railways, more and more high-speed electrified railways are built near the airport to facilitate people's travel and transportation. When the pantograph of the high-speed train is not in good contact with the contact wire, it will produce a pantograph arc [1, 2]. Especially when the high-speed train passes through the articulated neutral section (ANS), the contact wire voltage magnitude and phase will change greatly, and a large number of arcs will be produced, which last for hundreds of milliseconds [3, 4]. If the electrified railway ANS is located near the airport beacon, the transient pantograph arc may interfere with the communication between the airport beacon and the aircraft. Therefore, it is necessary to study the emission characteristics of the pantograph arc and their influence on the airport's instrument landing system (ILS).

Different methods have been proposed to study the characteristics of the pantograph arc. Mayr [5], Habedank [6], and Cassie [7] each proposed three different theoretical models of the arc. Wang *et al.* [8] proposed an extended model EMTP based on Habedank's equation and Liu *et al.* [9] proposed an extended black-box model considering the dynamic separation process of pantograph and contact wire. Some experimental methods have been proposed to study the relationship between the pantograph arc and train speed, pantograph gap, voltage, current, weather, measurement methods, etc. [10–12]. However, the theoretical models are limited by certain assumptions. For the experiments established in the laboratory, the train speed and power are not as high as that in the real railway environment, and there are some safety risks. It is also possible to study electromagnetic radiation through actual tests [13, 14]. China's first national electromagnetic radiation test for electrified railways was conducted in the 1980s. However, the electrical characteristics of the contact wire are completely different from those in the early 1980s. The train speed has increased by five times, and the test equipment is also very different. These differences will inevitably affect the pantograph arc characteristics. In addition, the previous test was aimed at the pantograph arc of the ordinary position (OP) of the contact network, but the pantograph arc generated as the ANS was larger than that at the OP. Therefore, it is necessary to retest and analyze the electromagnetic emission (EME) of high-speed electrified railways. Some studies have shown that the emission from the pantograph arc may interfere with airport communication systems [15–17]. However, these studies have not verified the effect of pantograph arc on ILS signal through experiments.

To address the above issues, we proposed a radiation model for the pantograph arc and an improved least-square (LS) regression method. Based on the test data, the pantograph arc characteristics of different positions of the electrified railway and different train speeds are

analyzed. The position limit of the railway ANS under the condition that the airport ILS signal is not disturbed is deduced and verified by experiments.

## II. THE RADIATION MODEL OF THE PANTOGRAPH ARC

We build the radiation model based on electric dipoles. For a unit electric dipole of length  $l$ ,  $l$  is very small and its current is  $\dot{I} = Ie^{j\phi}$ . Due to the limitation of test conditions, the test distance is generally tens of meters away, and the test location is in the far field. So the  $E$ -field strength of the unit dipoles is

$$\dot{E}_\theta = \sqrt{\frac{\mu_0}{\epsilon_0}} j \frac{\dot{I} l \sin \theta}{2\lambda r} e^{-j\frac{2\pi r}{\lambda}}. \quad (1)$$

Here,  $\theta$  is the angle between the arc radiation direction and the vertical direction. It is a spherical wave, which continuously radiates energy along the direction of  $r$ . The pantograph arc radiation model can be expressed as shown in Figure 1.  $L_1$  is the upper arm and  $L_2$  is the lower arm of the pantograph, and the angles to the  $Z$ -axis are  $\alpha_1$  and  $\alpha_2$ , respectively.  $r$  is the distance between the arc and the field, and the angles to  $L_1$  and  $L_2$  are  $\theta_1$  and  $\theta_2$ , respectively. Suppose the current on  $L_1$  is  $i_1(t)$ , and the current on  $L_2$  is  $i_2(t)e^{-jkL_1}$ . If the  $E$ -field strength generated by  $L_1$  and  $L_2$  in the far field are  $\vec{E}_1$  and  $\vec{E}_2$ , the induced current of contact wire is  $I_3$ , the length is  $L_3$ , and the  $E$ -field strength is  $\vec{E}_3$ . So, the  $E$ -field strength  $\vec{E}$  generated by the pantograph arc is the superposition of  $\vec{E}_1$ ,  $\vec{E}_2$ , and  $\vec{E}_3$  in space. So,

$$\vec{E} = \sum_{i=1}^3 \vec{\theta}_i \frac{60\pi I_i}{\lambda r} \sin \theta_i e^{-j\frac{2\pi r}{\lambda}} \frac{1 - e^{-jkL_i(1 - \cos \theta_i)}}{k(1 - \cos \theta_i)}. \quad (2)$$

As reported in [18],  $I_3$  can be calculated by

$$I_3 = \frac{I_0}{1 + \rho} (e^{-\gamma y} + \rho e^{-\gamma y}). \quad (3)$$

Here,  $\rho$  is the reflection coefficient of the contact wire. If the projection of  $r$  on the  $YOZ$  is  $r'$ , and the angles of  $r'$  to  $r$  and  $Z$ -axis are  $\phi$  and  $\varphi$ , respectively, then

$$\begin{cases} \cos \theta_3 = \cos \phi \cos(\varphi - 90^\circ) \\ \vec{\theta}_3 = \frac{\vec{\phi} \sin \phi \cos(\varphi - 90^\circ) + \vec{\varphi} \sin(\varphi - 90^\circ)}{\sin \theta_3} \end{cases}. \quad (4)$$

The  $E$ -field strength of the pantograph arc calculated by this model is related to the contact line current, the structure of the pantograph, and the relative position of the pantograph arc and the receiving point. This model does not take into account the influence of train speed. So, we also want to use test data and regression analysis methods to study the pantograph arc characteristics.

## III. THE IMPROVED LEAST-SQUARES METHOD

Regression analysis is an effective tool to analyze the statistical characteristics of the test data. The basic process of regression analysis includes the model

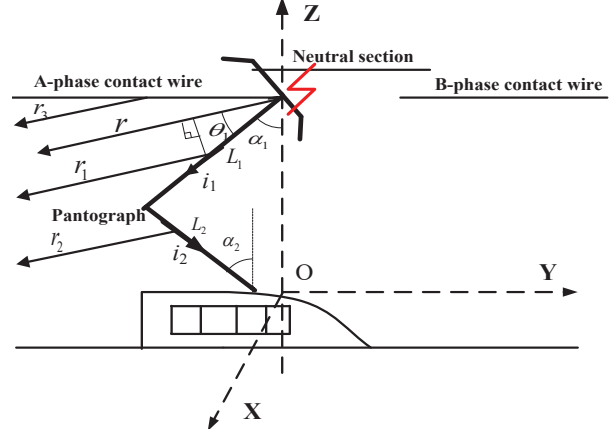


Fig. 1. Pantograph arc radiation model.

assumption, parameter calculation, and the rationality of the assumed model. The LS method is an existing linear regression method. It has been used to fit the test data [19–21]. The LS model is

$$E = a + b \lg f, \quad (5)$$

where  $E$  is the  $E$ -field strength, and  $f$  is the frequency.  $a$  and  $b$  can be calculated through the frequency domain test data.

$$\begin{cases} b = \frac{N \sum_{i=1}^N (E_i \lg f_i) - \sum_{i=1}^N (\lg f_i) \sum_{i=1}^N E_i}{N \sum_{i=1}^N (\lg f_i)^2 - (\sum_{i=1}^N \lg f_i)^2} \\ a = \frac{\sum_{i=1}^N E_i - b \sum_{i=1}^N \lg f_i}{N} \end{cases}, \quad (6)$$

where  $N$  is the number of test frequencies.

However, the error between different samples corresponding to the same frequency point is usually different, called the heteroscedasticity of the data. Therefore, the LS method cannot be used directly. We presented an improved LS model as

$$\hat{E}_{ij} = \hat{a} + \hat{b} \cdot f_j + e_{ij}, i = 1, \dots, m, j = 1, \dots, 1001, \quad (7)$$

where  $m$  is the number of samples, and each sample contains 1001 data.  $E_{ij}$  is the tested value of  $E$ -field strength.  $\hat{E}_{ij}$  is the estimated value of the  $E_{ij}$ , and obtained by model fitting.  $\hat{a}$  and  $\hat{b}$  are called regression coefficients, and  $e_{ij}$  is the error. The variance of the error is  $\text{Var}(e_{ij}) = \sigma_j^2$ . Only when  $\sigma_j^2$  is a constant, the regression coefficient can be directly calculated using the LS method. To make  $\sigma_j^2$  equal to the constant  $\sigma^2$ , we supposed  $\omega_{ij}^2$  is a variable and let  $\text{Var}(e_{ij}) = \omega_{ij}^2 \cdot \sigma^2$ . So,

$$\frac{\hat{E}_{ij}}{\omega_{ij}} = \hat{a} \frac{1}{\omega_{ij}} + \hat{b} \frac{f_j}{\omega_{ij}} + \frac{e_{ij}}{\omega_{ij}}, \quad (8)$$

where  $\hat{a}$  is the coefficient of  $1/\omega_{ij}$ , and  $\hat{b}$  is the coefficient of  $f_j/\omega_{ij}$ . Since  $\text{Var}(e_{ij}/\omega_{ij})$  is a constant,  $\hat{a}$  and  $\hat{b}$  can be directly estimated by (6). Therefore, according to (7), the fitted relationship of  $E$ -field strength and frequency can be represented by  $\hat{a}$  and  $\hat{b}$ .

In the process of calculating  $\hat{a}$  and  $\hat{b}$ , if the resid-

ual calculated is outside of the range  $(-2, 2)$ , the sample should be discarded. The residual  $r_{ij}$  is

$$r_{ij} = E_{ij} - \hat{E}_{ij} = (E_{ij} - \bar{E}_j) + (\bar{E}_j - \hat{E}_{ij}), \quad (9)$$

where  $\bar{E}_j$  is the average  $E$ -field strength of  $E_{ij}$  corresponding to  $f_j$ . Let the estimate of the variance at  $f_j$  be  $s_j^2$ ; then

$$\omega_{ij} = \frac{1}{s_j^2} = \frac{m-1}{\sum_{i=1}^m (E_{ij} - \bar{E}_j)^2}. \quad (10)$$

There are two parameters for investigating the rationality of the regression analysis model, the definition coefficient and the standard residual. The definition of coefficient  $K$  is defined as follows:

$$K^2 = 1 - \frac{\sum (E_{ij} - \hat{E}_{ij})^2}{\sum (E_{ij} - \bar{E}_j)^2}. \quad (11)$$

When  $K$  is close to 1, it means that most of the changes of  $E_{ij}$  can be explained by  $f_j$ , which shows that the assumption model is reasonable.

The standardized residual is

$$z_{ij} = \frac{r_{ij}}{\sqrt{\text{Var}(r_{ij})}}. \quad (12)$$

It can be seen that the more concentrated the value of  $Z_{ij}$  is, the closer  $\hat{E}_{ij}$  is to  $E_{ij}$ . When  $Z_{ij} \in (-2, 2)$ , which can explain the rationality of the assumption model.

#### IV. THE CHARACTERISTICS OF THE PANTOGRAPH ARC

In this section, the improved LS method is compared with the LS method and the radiation model. The improved LS method is used to analyze the pantograph arc characteristics when the train passes through different positions of the railway at different speeds.

##### A. Measurement

The airport ILS includes localizer (LOC), glideslope (GS), and marker beacon (MB). The corresponding working frequencies are 108.1-111.975, 328.6-335.4, and 75 MHz, respectively. Only arc emissions of the same or similar frequency to the ILS will affect its operation. So, we only measured the EME of the pantograph arc at the frequencies of 108-350 and 75 MHz. It is hard to test every frequency during the short time that the train passes. Therefore, we used the frequency sweeping technique of the electromagnetic interference receiver to test the emission of 108-350 MHz.

On the other hand, the electrified railway is generally provided with an ANS every 15–35 km, and the length of each ANS is about 300 m. The speed of the high-speed rail is about 200–380 km/h; so the train passes through an ANS every 140–630 s, which takes 2.8–5.4 s each time. The arc duration is about several hundred milliseconds. So, the measurement time must be greater than the time it takes for the train to pass through the ANS. During this time, the receiver scans several times to obtain the test results.

The EMI test receiver of R&S is used to test the electric field ( $E$ -field) strength, which works in the frequency range of 9 kHz to 3 GHz. The Log periodic antenna is used to receive the  $E$ -field, whose operating frequency ranges from 30 MHz to 2 GHz. The parameters of the test instrument should be set in strict accordance with IEC Standard 62236-2 [22].

The test layout is shown in Figure 2 (a). The height of the ANS is  $h$  and  $r$  away from the antenna, and  $h = 6.5$  m and  $r = 21$  m. The height of the antenna is  $h_0$ , and  $h_0 = 1.8$  m. The test distance is 10 m. The antenna is on the  $X$ -axis; so  $\varphi = 0^\circ$ . Therefore, based on these parameters and the radiation model proposed above, the  $E$ -field strength of the pantograph arc can be calculated.

We put the experimental equipment next to the OP and ANS of different speed railway lines for multiple tests. The test method strictly follows the regulations of the standard. First, place the test instrument in an open area near the location to be tested. Second, connect the antenna to the EMI test receiver. Then, turn on the receiver and set the parameters. Set up two traces, one to record the maximum value (Max/Hold) and the other to record the instantaneous value (Clear/Write). When the train passes, the pantograph arc is generated and the recording starts. When the train leaves, pause the recording and save the data. Figure 2 (c) is an example of the measurement data that was tested next to ANS. The upper blue curve is the Max/Hold of multiple sweeps. The lower curve is the Clear/Write of a single sweep result.

The measurement data includes the background noise and the EME when the train passes through the OP and ANS of the railway at different speeds. The train speeds are 120, 250, and 350 km/h, respectively. The test data plus the antenna coefficients are converted into the  $E$ -field strength values. Each sample has 1001 data points. According to these samples, the model parameters of the LS method and the improved LS method can be calculated.

#### V. COMPARISON OF DIFFERENT METHODS

According to the previous introduction, the  $E$ -field strength at different frequencies can be calculated based on the radiation model of the pantograph arc. Based on the test data, the fitting relationship between the  $E$ -field strength and the frequency can be obtained through the LS method and the improved LS method. For example, when the train passes through the ANS at a speed of 120 km/s, we use 16 sample data to calculate the parameters of the LS model and the improved LS model. The test data and the EME of some frequencies calculated by different methods are shown in Table 1. The frequency

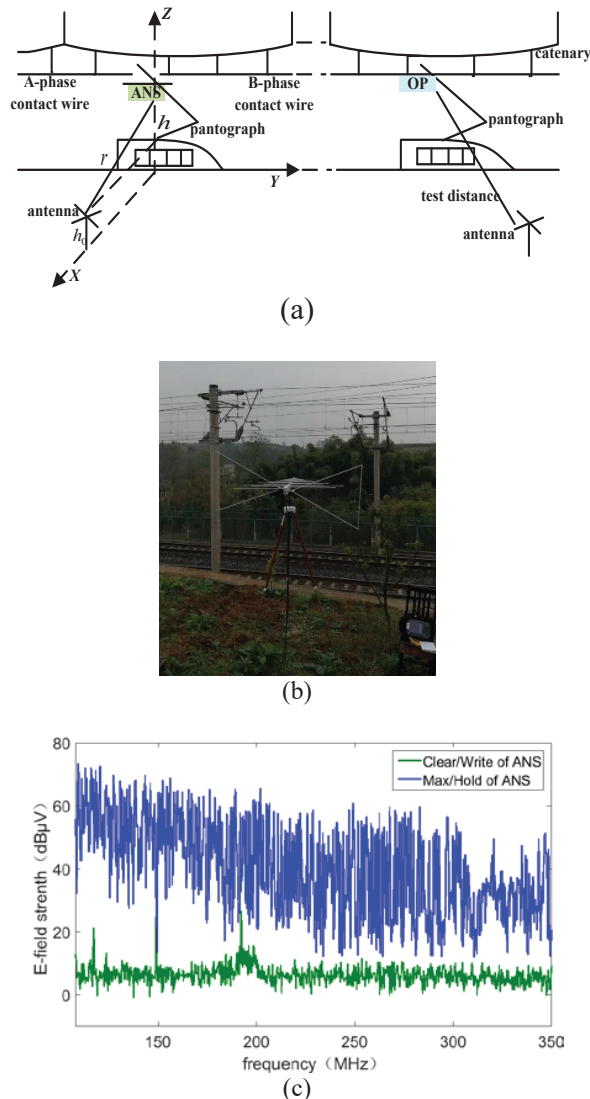


Fig. 2. Test layout. (a) Test diagram. (b) Test site. (c) Measurement data when a train passes through ANS.

in Table 1 belongs to the working frequency band of airport ILS.

From Table 1, the LS method, the radiation model, and the improved LS method from the test data had mean errors of 5.33, 1.18, and 0.89, respectively. The  $E$ -field strength obtained by the radiation model and the improved LS method proposed in this article has fewer errors with the test data, and both are better than the LS method. However, the radiation model does not consider the influence of train speed, which has limitations. It is not suitable for analyzing the influence of different train speeds on pantograph arc emission. So, the improved LS model is more general. We use the improved LS method to analyze the emission characteristics of the pantograph arc based on the test data.

Table 1: The test data and the EME are calculated by different methods ( $\text{dB}\mu\text{V}/\text{m}$ )

Frequency (MHz)	Radiation model	LS method	Improved LS method	Test data
75	80.23	76.04	78.60	79.75
108	76.14	75.20	76.21	76.56
110	76.30	74.65	76.07	75.97
112	76.16	74.12	75.93	74.16
328	62.17	52.17	60.33	61.40
330	61.99	51.99	60.19	58.90
332	59.63	51.81	60.04	60.76
334	61.46	51.63	59.90	60.62
336	60.48	51.46	59.75	58.95

### A. Emission characteristics of the pantograph arc

We analyzed the emission characteristics of the pantograph arc when trains with the same speed pass through the OP and ANS of the same railway. When the train speed is about 120 km/h, calculate the parameters of the improved LS model using 16 sample data. Calculate the definition coefficient  $K$  and the standard residual. If the standardized residuals of one sample data are not concentrated in  $(-2, 2)$ , remove the sample data and re-fit until  $K$  is close to 1 and all standard residuals are concentrated in  $(-2, 2)$ . Among them, the standard residual of one sample is shown in Figure 3.

We call the pantograph arc of the train passing ANS of the ANS arc and the pantograph arc of the train passing OP of the OP arc. The curves of  $E$ -field strength and frequency under different positions of the railway are shown in Figure 4. The  $E$ -field strength of the background is small and the value is the same in the entire frequency band. When the train passes the ANS, the maximum  $E$ -field strength of the EME is about 37 dB higher than when it passes the OP and is about 45 dB higher than the background. The average  $E$ -field strength of the ANS arc is 31 dB greater than the OP arc and about 37 dB higher than that of the background.

We analyzed the emission characteristics of the pantograph arc when trains of different speeds pass through the ANS. The train speeds are 120, 250, and 350 km/h, respectively. Like the above method, the parameters of the improved LS model are calculated.  $E$ -field strength and frequency curves of ANS arc at different train speeds are shown in Figure 5. It can be seen that the maximum  $E$ -field strength of the ANS arc can reach 91  $\text{dB}\mu\text{V}/\text{m}$ . The three background noises are similar, and the average EME of the ANS arc generated by 350 km/h train is about 3.5 dB higher than that of 250 km/h train and about 9 dB higher than that of 120 km/h train. In addition, as the frequency increases, the speed has less influence on EME.

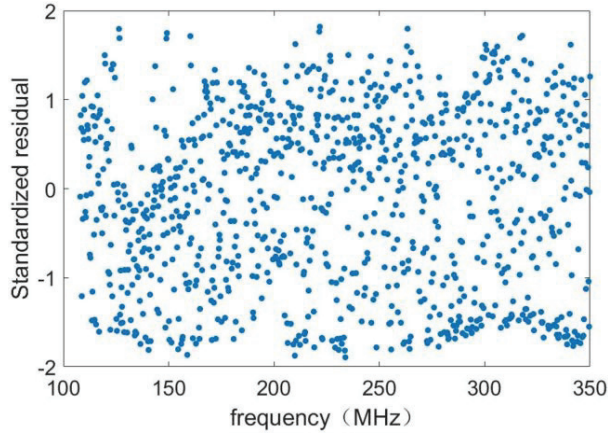


Fig. 3. Standardized residual of one ANS sample data.

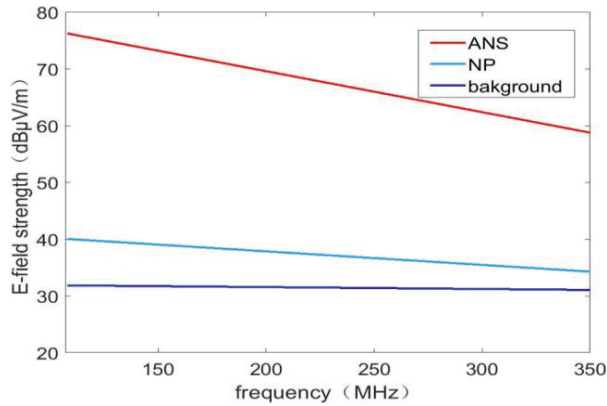


Fig. 4.  $E$ -field strength and frequency curves of pantograph arc at different positions of the railway.

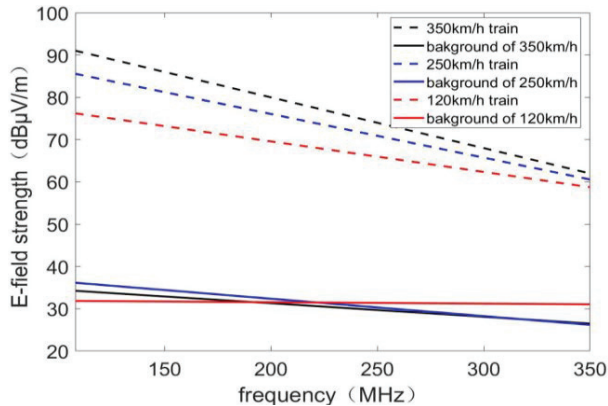


Fig. 5. The  $E$ -field strength and frequency curves of the ANS arc at different train speeds.

## VI. THE EFFECT OF THE ANS ARC ON AIRPORT ILS

The ILS cooperates with aircraft receivers to provide a virtual path to make the aircraft land safely. The LOC guides the runway entrance horizontal position by transmitting fan-shaped radio signals; the GS guides the vertical position of the runway entrance through the radio signal beam with an elevation angle of  $2.5^{\circ}$ - $3.5^{\circ}$ ; the MB provides the rough distance information relative to the runway entrance. The airborne ILS receiver receives the signal transmitted by the LOC, GS, and MB on the ground. The ANS arc generated by the high-speed train may affect the quality of the ILS signal received by the aircraft. Take one Chinese airport as an example to analyze the influence of EME on airport ILS when the high-speed train passes through the ANS.

### A. Airport ILS electromagnetic environment requirements

The LOC signal and the GS signal have similar signal formats, and both adopt the composite amplitude modulation system of 90 and 150 Hz audio amplitude modulation, which is a combination of carrier with sideband (CSB) signal and sideband only (SBO) signal in space. The airborne receiver receives the signal transmitted by the beacon, detects the 90 and 150 Hz audio components from it, and outputs the difference of depth of modulation (DDM). The DDM value can reflect the degree of deviation from the centerline of the runway and the GS, and equal to 0 on the centerline of the runway and the GS. The DDM on both sides of them are symmetrical. The International Civil Aviation Organization (ICAO) stipulates the deviation limit of DDM; the minimum deviation error of LOC is  $\pm 0.004$  DDM and that of GS is  $\pm 0.006$  DDM. To ensure the ILS signal does not interfere, the ground ILS signal received by the airborne ILS receiver must meet its signal-to-noise ratio requirements for the interference signal. One Chinese airport's ILS parameters are shown in Table 2.

### B. Analysis on the EMI of ANS arc to ILS

The locations of the ILS and the ANS are shown in Figure 6. The height of the aircraft is  $H$ , the distance from the ANS is  $d_n$ , and the glide angle is  $\beta$  which is equal to  $3^{\circ}$ . The landing point is 300 m away from the runway entrance. Take the landing point as the origin of the coordinates, assuming that the coordinates of ANS are  $(x, y)$ .  $d_S$ ,  $d_{S1}$ , and  $d_{S2}$  are the distances of the aircraft from LOC, GS, and MB, respectively.

From Figure 5, the EME maximum of the ANS arc at 10 m is about  $91 \text{ dB}\mu\text{V/m}$ . We can deduce that the EME of the ANS arc received by the airborne ILS receiver is

$$E_n = 91 - 20 \lg \frac{d_n}{10}, \quad (13)$$

Table 2: The ILS parameters

Beacon station	MB	LOC	GS
Working frequency, $f$ (MHz)	75	108.1-111.975	328.6-335.4
Antenna transmit power, $P$ (W)	2	15	9.5
Antenna gain, $G$ (dB)	10	9.5	14.3
Signal-to-noise ratio, $R$ (dB)	23	20	20

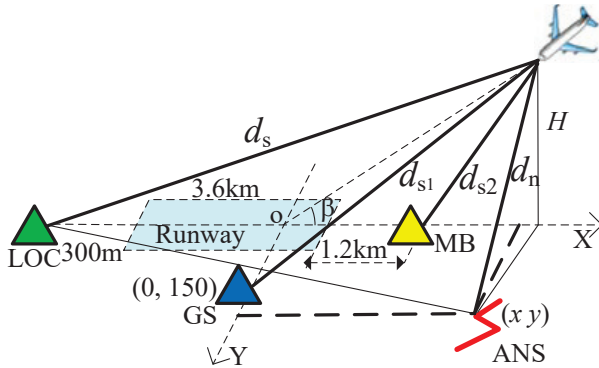


Fig. 6. Schematic diagram of the ILS and the ANS.

where  $d_n$  is related to  $H$ ,  $\beta$ ,  $x$ , and  $y$ . It can be expressed as

$$d_n = \sqrt{H^2 + y^2 + (H \cdot \cot \beta - x)^2}. \quad (14)$$

According to the theory of radio wave transmission, we can deduce that the ILS signal received by the airborne ILS receiver is

$$E_S = 10 \lg P + G - 20 \lg d + 134.8, \quad (15)$$

where  $d$  is the distance between the ILS beacon on the ground and the aircraft.  $d_s$ ,  $d_{s1}$ , and  $d_{s2}$  are all related to  $H$  and  $\beta$ .

According to (11), (13), and the ILS parameters in Table 2, we got the curve of various signals received by the aircraft to distance, as shown in Figure 7. During an aircraft landing, the various signals received by the aircraft increase as the distance decreases. The EME of the ANS arc changes more obviously with distance.

To make the aircraft communicate with the beacon on the ground normally, the signal-to-noise ratio must satisfy

$$E_S - E_n \geq R. \quad (16)$$

The LOC transmit power is 15 W and the antenna gain is 9.5 dB. The distance between aircraft and LOC is  $d_s$ ,

$$d_s = \sqrt{H^2 + (H \cdot \cot \beta + 3.6)^2}. \quad (17)$$

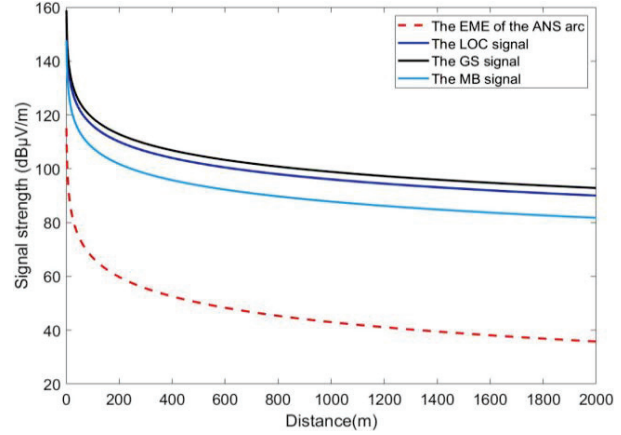


Fig. 7. Signals received by the airborne ILS receiver.

It can be deduced that the position of the ANS must meet the following conditions:

$$\begin{cases} (x - 19H)^2 + y^2 \geq 0.135H^2 + 0.424H + 0.04 \\ |y| > \sqrt{0.135H^2 + 0.424H + 0.04} \end{cases}. \quad (18)$$

When the aircraft is about to land at a height of 1.5 km, the vertical distance between the ANS and the runway must be greater than 990 m, and the horizontal distance from the runway entrance must be greater than 29.49 km. Otherwise, the ANS arc will affect the communication of the airport LOC.

The GS transmit power is 9.5 W and the antenna gain is 14.3 dB. The distance between aircraft and GS is  $d_{s1}$ ,

$$d_{s1} = \sqrt{H^2 + 0.15^2 + (H \cdot \cot \beta)^2}. \quad (19)$$

To make the GS signal not be affected by the ANS arc, we deduced that the position of the ANS must meet the following conditions:

$$\begin{cases} (x - 19H)^2 + y^2 \geq -0.4208H^2 + 0.15^2 \\ |y| > \sqrt{-0.4208H^2 + 0.15^2} \end{cases}. \quad (20)$$

The MB launches a vertical cone-shaped composite field into the air, with a signal coverage range of 60-80 m high and a lateral width of 200-400 m. The MB only provides position information to the pilot. Take the MB near the entrance of the runway as an example to analyze the influence of the ANS arc on the MB signal. As shown in Figure 6, the distance between the aircraft and MB is  $d_{s2}$ ,

$$d_{s2} = \sqrt{H^2 + (H \cdot \cot \beta - 1.5)^2}. \quad (21)$$

To make the MB signal not be affected by the ANS arc, we deduced that the position of the ANS must satisfy

$$\begin{cases} (x - 19H)^2 + y^2 \geq 6.602H^2 - 1.197H + 0.04725 \\ |y| > \sqrt{6.602H^2 - 1.197H + 0.04725} \end{cases}. \quad (22)$$

In fact, the altitude of the aircraft when receiving the MB signal is 60-80 m. Therefore, the ANS

Table 3: Experimental results

Experiments	1	2	3	4	5	6	7	8
Position of the N9310 ( $x, y$ )/m	(10, 205)	(20, 210)	(30,-215)	(37, 0)	(140, 100)	(240,-50)	(250,150)	(250,205)
Test values for DDM of LOC	0.091	0.093	0.093	0.088	0.087	0.089	0.092	0.093
Test values for DDM of GS	0.092	0.093	0.093	0.087	0.086	0.087	0.093	0.093

arc has little effect on the MB and will not cause EMI to the MB signal. To prevent the communication between the aircraft and ILS from being affected during the landing, the position of the ANS must satisfy both (18) and (20).

### C. Verification experiment

We set up an experiment to verify the above conclusion. The layout of the verification experiment is shown in Figure 8. The Avionics tester (IFR4000) transmits DDM adjustable LOC or GS signals, and the signal generator (N9310A) as an interference signal source transmits interference signal through the logarithmic antenna. The airborne ILS receiver receives the ILS signal and displays the received DDM.

At the beginning of the experiment, both IFR4000 and N9310A were about 10 m away from the airborne ILS receiver. The  $H$  is set to 0.002 km and the transmit power of the IFR4000 is  $-10$  dbm. According to the above conclusion (18) and (20), when  $H$  is 0.002 km, the ANS position must satisfy

$$\begin{cases} (x-0.038)^2 + y^2 > 0.04085 \\ |y| > 0.2021 \end{cases} \quad (23)$$

First, IFR4000 is connected to the logarithmic antenna, sets the frequency to 108.1MHz, and transmits the LOC signal (or GS signal) with a 0.093 DDM. Adjust the position of the antenna so that the DDM of the received signal is also 0.093 DDM, as shown in Figure 8.

Second, turn on the N9310A. The power is set to  $91 \text{ dB}\mu\text{V/m}$ , and the frequency is 108.1 MHz. So, the frequency of the interference signal is the same as the working frequency of the ILS, and its amplitude is the maximum  $E$ -field strength of the ANS arc radiated.

Third, several experiments were performed by moving the position of the N9310 so that it was at different distances from the ILS receiver. During the experiment, record the DDM value displayed by the ILS receiver. The test results when the N9310 is in some positions are shown in Table 3.

The ILS communication will not be interfered with only when the DDM error between the LOC transmitted signal and the received signal is less than 0.004, and the DDM error between the GS transmitted signal and the received signal is less than 0.006. Otherwise, the com-

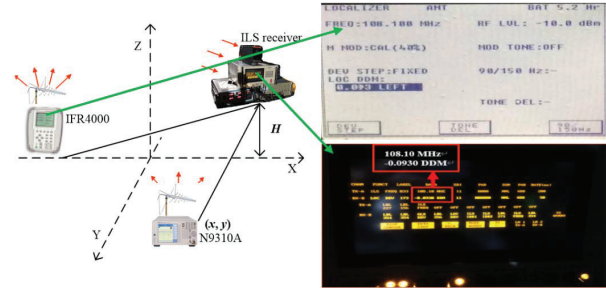


Fig. 8. The verification experiment. (a) The layout of the verification experiment. (b) Parameters of the transmitted ILS signal. (c) Parameters of the received ILS signal.

munication of the airport ILS will be affected.

From Table 3, in the fourth, fifth, and sixth experiments, the coordinates of N9310 did not meet the safe distance indicated by (23). The DDM emitted by the IFR4000 is 0.093; so the DDM error of LOC is greater than 0.004 and the DDM error of GS is greater than 0.006. In other experiments, the position coordinates of N9310 satisfy the relationship of (23) and the DDM error does not exceed the limit. Multiple experiments were performed with the same results.

It can be concluded that when the ANS coordinates satisfy conditions (18) and (20), no matter whether the LOC signal or the GS signal is transmitted, the deviation error of the DDM will not be out of its range. When the ANS coordinate does not meet (18) and (20), the deviation error of DDM will exceed its range. That is, the ILS signal received by the ILS receiver will be interfered. The experiment verified our theoretical results.

## VII. CONCLUSION

We proposed a radiation model of the pantograph arc and an improved LS method to analyze the emission characteristics of the pantograph arc. It concluded that when the train passes through the ANS, it will generate broadband arc emission. The average EME of the ANS arc is 31 dB higher than that of the OP arc. The higher the speed of the train is, the greater the EME of the ANS arc. The average EME of the ANS generated by a 350 km/h train is about 3.5 dB higher than that of a 250 km/h train and about 9dB higher than that of a 120

km/h train. We deduced the position limit of the electrified railway ANS relative to the airport runway, and verified it through experiments. When the aircraft is about to land at a height of 1.5 km, the vertical distance between the ANS and the runway must be greater than 990 m, and the horizontal distance from the runway entrance must be greater than 29.49 km. The MB signal will not be interfered with by the ANS arc. When the ANS position satisfies (16) and (18), the LOC and GS signals will not be interfered with by the ANS arc.

## REFERENCES

- [1] Y. Tang, F. Zhu, H. Lu, and X. Li, "Analysis and suppression of EMI for traction control unit speed sensors of CRH380BL electric multiple unit," *Applied Computational Electromagnetics Society (ACES) Journal*, vol. 33, no. 5, pp. 553-560, Jul. 2018.
- [2] Y. Tang, F. Zhu, and Y. Chen, "Analysis of EMI from Pantograph-catenary arc on speed sensor based on the High-speed train model," *Applied Computational Electromagnetics Society (ACES) Journal*, vol. 36, no. 2, pp. 205-212, Feb. 2021.
- [3] S. Midya, D. Bormann, T. Schütte, and R. Thottappillil, "DC component from Pantograph arcing in AC Traction system—Influencing parameters, impact, and mitigation techniques," *IEEE Transactions on Electromagnetic Compatibility*, vol. 53, no. 1, pp. 18-27, Feb. 2011.
- [4] A. Verdicchio, P. Ladoux, H. Caron, and C. Courtois, "New Medium-voltage DC railway electrification system," *IEEE Transactions on Transportation Electrification*, vol. 4, no. 2, pp. 591-604, Jun. 2018.
- [5] O. Mayr, "Contribution to the theory of static and dynamic arcs," *Arch. Elektrotechnik*, vol. 37, no. 1, pp. 589-608, 1943.
- [6] U. Habedank, "On the mathematical-description of arc behavior in the vicinity of current zero," *etzArchiv*, vol. 10, no. 11, pp. 339-343, Nov. 1988.
- [7] M. T. Cassie and D. B. Fang, "An improved arc model before current zero based on the combined Mayr and Cassie arc models," *IEEE Transactions on Power Delivery*, vol. 20, no. 1, pp. 138-142, Jan. 2005.
- [8] Y. Wang, Z. Liu, X. Mu, K. Huang, H. Wang, and S. Gao, "An extended Habedank's equation-based EMTP model of Pantograph arcing considering Pantograph-catenary interactions and train speeds," *IEEE Transactions on Power Delivery*, vol. 31, no. 3, pp. 1186-1194, Jun. 2016.
- [9] Z. Liu, H. Zhou, K. Huang, Y. Song, Z. Zheng, and Y. Cheng, "Extended Black-box model of Pantograph-catenary detachment arc considering Pantograph-catenary dynamics in electrified railway," *IEEE Transactions on Industry Applications*, vol. 55, no. 1, pp. 776-785, Jan.-Feb. 2019.
- [10] G. Gao, J. Hao, W. Wei, H. Hu, G. Zhu, and G. Wu, "Dynamics of Pantograph-catenary arc during the Pantograph lowering process," *IEEE Transactions on Plasma Science*, vol. 44, no. 11, pp. 2715-2723, Nov. 2016.
- [11] F. Guo, X. Feng, Z. Wang, J. You, X. Wang, D. Liu, and Z. Chen, "Research on time domain characteristics and mathematical model of electromagnetic radiation noise produced by single arc," *IEEE Transactions on Components, Packaging and Manufacturing Technology*, vol. 7, no. 12, pp. 2008-2017, Dec. 2017.
- [12] W. Wei, J. Wu, G. Gao, Z. Gu, X. Liu, G. Zhu, and G. Wu, "Study on Pantograph arcing in a laboratory simulation system by high-speed photography," *IEEE Transactions on Plasma Science*, vol. 44, no. 10, pp. 2438-2445, Oct. 2016.
- [13] D. Bellan, G. Spadacini, E. Fedeli, and S. A. Pignari, "Space-frequency analysis and experimental measurement of magnetic field emissions radiated by high-speed railway systems," *IEEE Transactions on Electromagnetic Compatibility*, vol. 55, no. 6, pp. 1031-1042, Dec. 2013.
- [14] R. Geise, O. Kerfin, B. Neubauer, G. Zimmer, and A. Enders, "EMC analysis including receiver characteristics - pantograph arcing and the instrument landing system," *2015 IEEE International Symposium on Electromagnetic Compatibility (EMC)*, Dresden, pp. 1213-1217, 2015.
- [15] Z. Y. Ming and W. Z. An, "Analysis of airport electromagnetic environment effects from synthesized passenger transportation," *Environ. Technol.*, vol. 2014, no. S1, pp. 181-186, 2014.
- [16] Y. Tang, F. Zhu, and Y. Chen, "Research on the influence of train speed change on the EMI of Pantograph-catenary arc to main navigation stations," *Applied Computational Electromagnetics Society (ACES) Journal*, vol. 36, no. 4, pp. 450-457, Apr. 2021.
- [17] Y. Tang, F. Zhu, and Y. Chen, "For more reliable aviation navigation: Improving the existing assessment of airport electromagnetic environment," *IEEE Instrumentation & Measurement Magazine*, vol. 24, no. 4, pp. 104-112, Jun. 2021.
- [18] X. Li, F. Zhu, H. Lu, R. Qiu, and Y. Tang, "Longitudinal propagation characteristic of Pantograph arcing electromagnetic emission with high-speed train passing the articulated neutral section," *IEEE Transactions on Electromagnetic Compatibility*, vol. 61, no. 2, pp. 319-326, Apr. 2019.

- [19] S. Chatterjee and A. S. Hadi, *Regression Analysis by Example*, 5th ed., New York: Wiley, 2013.
- [20] M. G. Alijani and M. H. Neshati, "A new closed-form expression for dispersion characteristics of fundamental mode of SIW by least squares method," *Applied Computational Electromagnetics Society (ACES) Journal*, vol. 30, no. 8, pp. 930-933, Aug. 2021.
- [21] N. Lu, F. Zhu, and T. Zhou, "Test and analysis of electromagnetic emission characteristics of electrified railway to airport GP," *2019 International Applied Computational Electromagnetics Society Symposium - China (ACES)*, Nanjing, China, pp. 1-2, 2019.
- [22] Railway Applications – Electromagnetic Compatibility - Part 2. Emission of the Whole Railway System to the Outside World, IEC Standard 62236–2, 2018.



**Yingchun Xiao** was born in Gansu Province, China, in 1990. She received the B.S. degree in electronic information science and technology from the Lanzhou University of Technology, Lanzhou, China, in 2012, and is currently working toward the Ph.D. degree in

electrical engineering with Southwest Jiaotong University, Chengdu, China. At the same time, she is a Lecturer with Lanzhou City College.

Her research interests include electromagnetic environment test and evaluation, electromagnetic compatibility analysis and design, and identification and location of electromagnetic interference sources.



**Feng Zhu** received the Ph.D. degree in railway traction electrification and automation from the Southwest Jiaotong University, Sichuan, China, in 1997.

He is currently a Full Professor with the School of Electrical Engineering, Southwest Jiaotong University. His current research interests include locomotive over-voltage and grounding technology, electromagnetic

theory and numerical analysis of electromagnetic field, and electromagnetic compatibility analysis and design.



**Nan Lu** was born in Anhui Province, China, on June 3, 1990. He received the master's degree in electrical engineering from the Anhui University of Science & Technology, Anhui, China, in 2016, and is currently working toward the Ph.D. degree in electrical engineering with Southwest Jiaotong University, Chengdu, China.

His research interests include electromagnetic compatibility, electromagnetic environment test and evaluation, and transmission-line analysis.



**Zixuan Wang** was born in Shanxi Province, China, in 1998. He received the B.S. degree in electrical engineering and automation from Southwest Jiaotong University, Chengdu, China, in 2020.

He is currently working as a Research Assistant with the EMC Laboratory of Southwest Jiaotong University. His research interests include electromagnetic compatibility analysis and electromagnetic signal processing.



**Shengxian Zhuang** is currently working with the School of Electrical Engineering at Southwest Jiaotong University as a professor. He got his M.S and Ph.D degrees, respectively, at Southwest Jiaotong University and the University of Electronic Science and Technology of China in 1991 and 1999. From 1999 to 2003, he did postdoctoral research at Zhejiang University and Linköping University of Sweden. He was a visiting professor at Paderborn University in Germany in 2005 and at the University of Leeds, UK in 2017.

His research interests include power conversion for sustainable energy, motor control and drive systems, power electronics and systems integration, modeling, diagnosis, and suppression of electromagnetic interference of power electronic converters.

# Rule for Mode Coupling Efficiency in Optical Waveguide Crossing

Billel Bentouhami<sup>1,2</sup> and Zaia D. Kaddour<sup>2</sup>

<sup>1</sup>Université Mohamed El Bachir El Ibrahimi de Bordj Bou Arreridj, Faculté des Sciences et de la Technologie, El-Anasser 34030, Algeria  
billelbentouhami@gmail.com

<sup>2</sup>Université des Sciences et de la Technologie Houari Boumediène, Faculté de Physique, Laboratoire d'Electronique Quantique, BP 32 EL Alia 16111, Bab Ezzouar, Algiers, 16311, Algeria  
kaddourz@yahoo.com

**Abstract** – Crossing an optical waveguide requires a beam coupling from free space to waveguide at the entrance plane and another beam coupling from waveguide to free space at the exit plane of the waveguide. The aim of this paper is to provide a simple rule expressing the relationship between the involved numbers of free and guided modes that efficiently rebuild the field at each end of the waveguide. Using a numerical program built on Maple software, the rule was determined to be effective independently of the ratio between the beam spot size and the waveguide radius.

**Index Terms** – Electromagnetic field, mode coupling, optical waveguide.

## I. INTRODUCTION

Hollow dielectric optical waveguides are widely used in optical systems such as resonators [1, 2], optical transmission and communication systems [3], circular waveguide filters [4], and, nowadays, in integrated optics [5].

Many authors have described light propagation in cylindrical optical waveguides [6–9]. Transverse modes inside a waveguide can be divided into three families: transverse electric (TE), transverse magnetic (TM), and hybrid (EH) modes. Each family constitutes a complete and orthogonal set for expressing the radially symmetric electromagnetic field in the waveguide.

Apart from the propagation inside the waveguide, two check points need to be considered when crossing a waveguide which are its entrance and exit ports. At the entrance port, mode coupling occurs from free space to confined one and vice versa at the exit port. For both ends of the waveguide, mode coupling has been studied by considering the ratio between the beam spot size  $w$  and the radius of the waveguide  $a$  [10–13].

At the waveguide entrance plane, Smith [10] described earliest experiments performed by matching

the fundamental mode from a conventional He–Ne laser into a hollow dielectric waveguide. The incident beam was focused in such a way that the beam waist  $w_0$  occurred at the entrance plane of the dielectric waveguide. It is worth noting that Smith performed transmission measurement by matching the fundamental free mode into the fundamental guided mode. For a good matching, he experimentally found a ratio  $w_0/a = 0.49$  which was however considerably different from the theoretical ratio  $w_0/a = 0.728$  he considered.

Always for the entrance plane and as a function of  $w/a$ , Roullard and Bas [11] gave the fraction of the coupled energy from the free fundamental Gaussian mode  $TEM_{00}$  into the two first waveguide modes. They mentioned that an efficient coupling happens at  $w/a = 0.502$ . This value is different from the value  $w/a = 0.6435$  that maximizes coupling with only the first-order waveguide mode as given by Abrams and Chester [12] and Tack [13].

At the waveguide exit plane, the useful approach to release mode coupling is founded on the use of a small number of free space modes but with a choice of a specific ratio  $w/a$ . Indeed, as mentioned by Guerlach [14], to minimize the truncation error in expanding the field emerging from the waveguide, a small value of the ratio is favored. But a small  $w$  results in a large divergence of the beam field and consequently a large truncation error. Avoiding this constraint of the  $w/a$  ratio choice requires a considerable number of modes with numerical problem consequences.

To conclude, either at the entrance or at the exit plane of the waveguide, mode coupling using a reduced number of modes is conditioned by the choice of the appropriate ratio  $w/a$ . Working with an arbitrary ratio, requires a large number of modes that unfortunately leads to numerical problems. Therefore, the question that we ask here is about the optimum number of modes that we should consider for realizing an efficient mode

coupling regardless of a specific ratio  $w/a$ . To reach this goal, a simple rule is then given in this paper.

## II. THEORY AND NUMERICAL RESULTS

Let us consider a hollow dielectric waveguide with a circular cross section of radius  $a$ , a length  $L$ , and a complex refractive index  $v$ . Assume that an incident beam is coming in from the left side as shown in Figure 1.

Crossing an optical waveguide is carried out in three successive steps which are: mode coupling at the entrance plane, propagating the derived guided electromagnetic field along the length  $L$  inside the waveguide, and finally performing mode coupling again at the exit plane to go back to free space. Figure 2 shows the sequence of operations undertaken in the waveguide crossing. This process requires normalized functions for free space and waveguide modes to be given.

In free space for the case of cylindrical symmetry, the normalized Laguerre Gauss functions are given by [15]

$$\begin{aligned} \text{TEM}_{pl} &= \left( \frac{2}{w\sqrt{1+\delta_{0l}} \sqrt{\frac{m!}{\pi(l+m)!}}} \right) \left( \frac{r}{w\sqrt{2}} \right)^l L_m^l \left( 2\frac{r^2}{w^2} \right) \\ &\times \exp \left\{ -\frac{r^2}{w^2} - j\frac{kr^2}{2R} \right\} \begin{cases} \cos(l\varphi) \\ \sin(l\varphi) \end{cases}, \end{aligned} \quad (1)$$

where  $r$ ,  $\varphi$  are the cylindrical coordinates,  $L_m^l$  is the generalized Laguerre polynomials,  $\delta$  is the Kronecker symbol,  $j$  is the complex number such as  $j^2 = -1$ , and  $k$  is the wave number;  $R$  and  $w$  are the phase front radius and the spot size, respectively.

For the waveguide, the normalized hybrid functions with circular symmetry field are [14, 16]

$$\text{EH}_{1n}(r) = \begin{cases} \frac{1}{\sqrt{\pi|J_1(u_{1n})|a}} J_0\left(\frac{u_{1n}r}{a}\right) & r \leq a \\ 0 & r > a \end{cases}, \quad (2)$$

where  $J_0$  and  $J_1$  are the Bessel functions and  $u_{1n}$  is the  $n$ th root of the former one.

Mode coupling at each end of the waveguide is expressed using coupling coefficients  $C_{mn}$ . These coefficients are reached by equalizing the electromagnetic fields at both sides of the considered waveguide port and

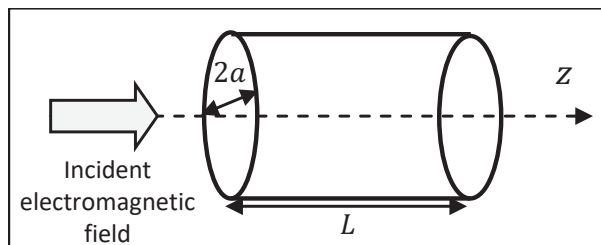


Fig. 1. Incident beam to a cylindrical optical waveguide.

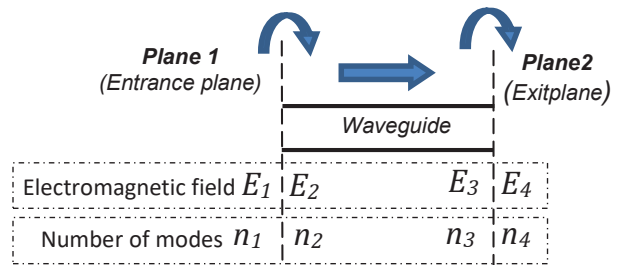


Fig. 2. Sequence of operations undertaken in waveguide crossing.

they are given by [14]

$$C_{mn} = 2\pi \int_0^a r \text{TEM}_m(r) \text{EH}_n(r) dr. \quad (3)$$

As shown in Figure 2, mode coupling occurs at plane 1 using a number of excited guided modes  $n_2$  and at plane 2 using a number of excited free space modes  $n_4$ . Simple rules giving the optimum  $n_2$  and  $n_4$  numbers for an efficient mode coupling are then the subject of Sections II-A and II-C.

### A. Rule for mode coupling at the waveguide entrance plane

The field equality  $E_1 = E_2$  inside the waveguide opening, at the entrance plane, is required for an efficient mode coupling. At both sides of this plane, the electromagnetic field is

$$E_1(r) = \sum_{m=1}^{n_1} a_m \text{TEM}_m(r), \quad (4)$$

for the free space and

$$E_2(r) = \sum_{n=1}^{n_2} C_n \text{EH}_n(r), \quad (5)$$

for the waveguide.

The integers  $n_1$  and  $n_2$  are the number of free space and waveguide modes, respectively;  $a_m$  represents the expansion coefficients of the incoming free field, whereas  $C_n$  are the derived expansion coefficients of the calculated guided field using eqn (3):

$$C_n = 2\pi \sum_{m=1}^{n_1} a_m C_{mn}. \quad (6)$$

Table 1 gives, for each given number  $n_1$  of the used free space modes, the optimum number  $n_2$  of waveguide modes which allows an efficient mode coupling at the waveguide entrance plane. This result is achieved for different  $w/a$  ratios.

The plot  $n_2$  versus  $n_1$  is illustrated by the point curve in Figure 3.

Applying the mathematical fit instructions of Maple software using the data from Table 1, the appropriate function  $n_2 = f(n_1)$ , shown in solid line in Figure 3, is deduced and the following rule for mode coupling at the

Table 1: Optimized number  $n_2$  of waveguide modes as a function of the number  $n_1$  of the used free space modes

$n_1$	$n_2$
3	7
8	8
11	9
15	9
19	10
25	12
38	13
45	15
60	17
80	19
100	21

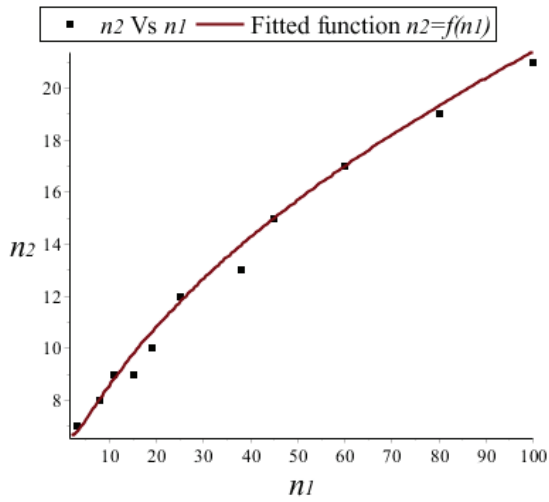


Fig. 3. Optimized number  $n_2$  of waveguide modes as a function of the number  $n_1$  of the used free space modes.

waveguide entrance plane is obtained:

$$n_2 = \left\lfloor 2 \left( \sqrt{n_1} + \frac{2}{\sqrt{n_1}} \right) + 1 \right\rfloor, \quad (7)$$

where the notation  $\lfloor \square \rfloor$  is the floor function.

For different  $n_1$  and according to this rule, Figure 4 shows a very good agreement in field superposition for mode coupling at the entrance plane of the waveguide.

The results shown in Figure 4 (a)–(c) have been computed with  $w/a = 0.91$ ,  $w/a = 0.8$ , and  $w/a = 0.66$ , respectively. But we emphasize that for each case, and thanks to the rule, an efficient mode coupling has been confirmed for other arbitrary ratios  $w/a$ .

### B. Propagation inside the waveguide

Attenuation and relative phase shift of the propagating field, over a distance  $l$  through the waveguide, are calculated by multiplying each guided mode by

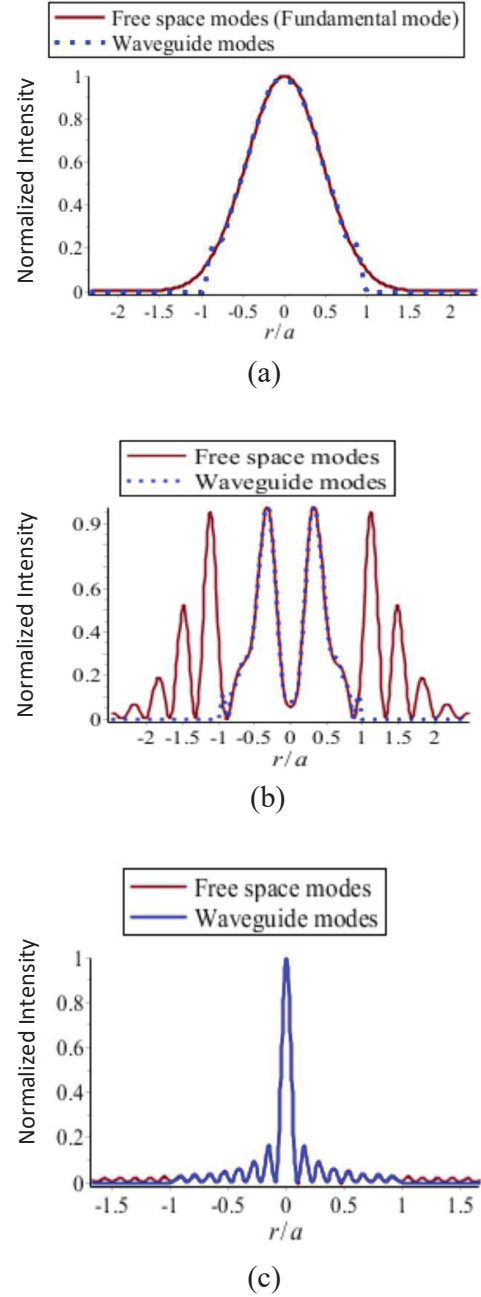


Fig. 4. Superposition of transverse intensity patterns at the waveguide entrance plane with  $a = 0.6$  mm for (a)  $n_1 = 1$ , (b)  $n_1 = 13$ , and (c)  $n_1 = 35$ .

the corresponding element of the following diagonal matrix [14]:

$$CG_{mn} = \delta_{mn} \exp \left[ u_{1m}^2 \left( \frac{l}{ka^2} \right) \operatorname{Re} \left( \frac{v_n}{ka} \right) \right] \times \exp \left[ -\frac{i}{2} (u_{1m}^2 - u_{11}^2) \left( \frac{l}{ka^2} \right) \left( 1 + 2 \operatorname{Im} \left( \frac{v_n}{ka} \right) \right) \right], \quad (8)$$

where  $\delta_{mn}$  is the Kronecker symbol,  $k = 2\pi/\lambda$ ,  $u_{1m}$  is the  $m$ th zero of  $J_0$  and  $v_n = [v^2+1]/2[v^2-1]^{\frac{1}{2}}$  where  $v$  is the complex refractive index of the waveguide material.

Figure 5 shows the electrical field intensity in different positions inside a cylindrical optical waveguide.

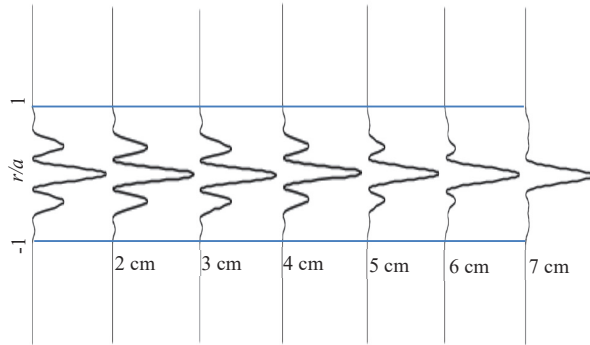


Fig. 5. Transverse intensity patterns at different positions inside an optical waveguide of length  $L = 7$  cm and  $a = 0.6$  mm.

### C. Rule for mode coupling at the waveguide exit plane

Here, the set of waveguide modes must be coupled to a set of free space modes. The field at the left side of the waveguide exit plane is

$$E_3(r) = \sum_{n=1}^{n_3} CG_n EH_n(r), \quad (9)$$

where the integer  $n_3$  is the number of the waveguide modes, which is equal to  $n_2$  obtained from eqn (7), and the  $CG_n$  coefficients are calculated using eqn (8).

The field at the right side of the waveguide exit plane is

$$E_4(r) = \sum_{m=1}^{n_4} C_m TEM_m(r), \quad (10)$$

where  $C_m$  are defined in eqn (6) and the integer  $n_4$  is the considered number of the TEM modes.

Table 2 shows, for each given number  $n_3$  of the used waveguide modes, the optimum number  $n_4$  of free space modes which allows an efficient mode coupling at the waveguide exit plane. This result is achieved for different  $w/a$  ratios.

The plot  $n_4$  versus  $n_3$  is illustrated by the point curve in Figure 6.

Applying the mathematical fit instructions of Maple software, using the data from Table 2, the appropriate function  $n_4=f(n_3)$  is deduced and the following rule for mode coupling at the waveguide exit plane is obtained:

$$n_4 = \lfloor 0.35 n_3^2 + 1 \rfloor. \quad (11)$$

Table 2: Optimized number  $n_4$  of free space modes as a function of the number  $n_3$  of the used waveguide modes

$n_3$	$n_4$
7	16
8	21
9	29
10	36
11	40
12	55
14	70
17	100
19	130
22	175
25	219
30	316

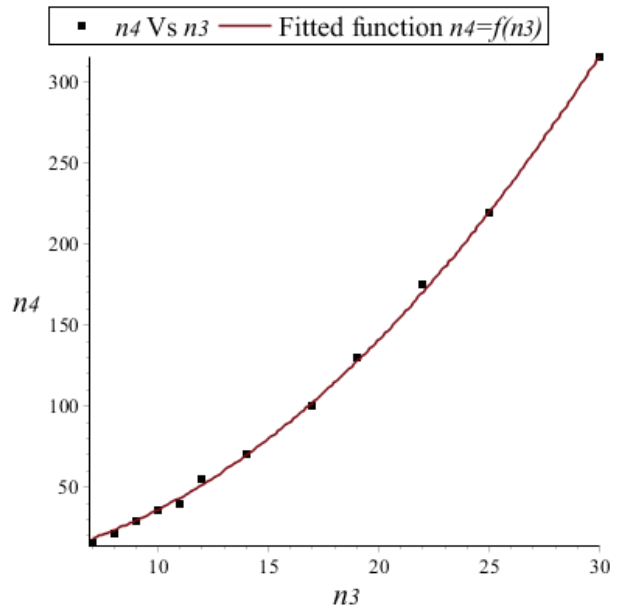


Fig. 6. Optimized number  $n_4$  of free space modes as a function of the number  $n_3$  of the used waveguide modes.

Figure 7 shows mode coupling according to this rule for different values of  $n_3$ .

The results shown in Figure 7 (a)–(c) have been computed with  $w/a = 0.58$ ,  $w/a = 0.5$ , and  $w/a = 0.8$ , respectively. As mentioned in Section II-A, we confirm that for each case, and thanks to the rule, an efficient mode coupling has been verified for other arbitrary ratios  $w/a$ .

It should be noted that at both ports of the waveguide and according to the rule, mode coupling goes successfully independent of the ratio  $w/a$  for values outside the range  $0.45 < w/a < 0.73$  applied by different authors [10–14]. Indeed, the rule works very well

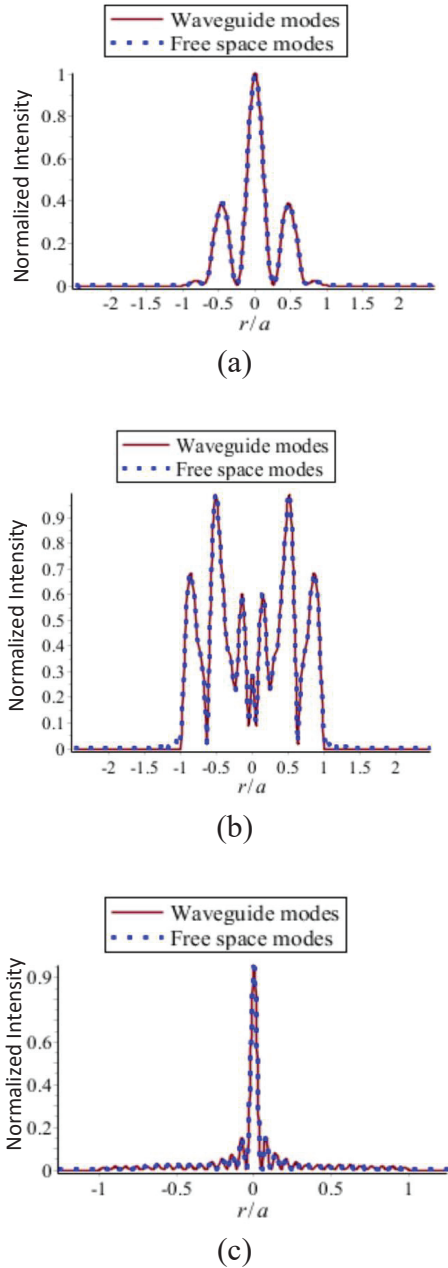


Fig. 7. Superposition of transverse field distribution at the waveguide exit plane with  $a = 0.6$  mm for (a)  $n_3 = 7$ , (b)  $n_3 = 10$ , and (c)  $n_3 = 25$ .

at least in the range  $0.3 < w/a < 0.9$  which is more useful.

#### D. Field beyond the optical waveguide

Propagation through free space beyond the waveguide of the emerged field considered in Figure 7 is shown in Figure 8.

We underline that beyond the waveguide, propagation through any optical path, composed by an apertured

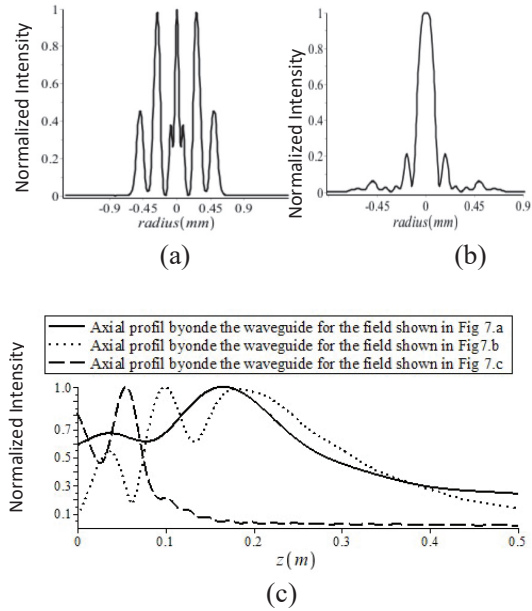


Fig. 8. Transverse distribution of the field shown in Figure 7 (b) at (a)  $z = 15$  mm and (b)  $z = 95$  mm beyond the optical waveguide, respectively, and (c) axial field distribution for the fields shown in Figure 7.

first-order optical system, can be achieved using the ABCD law and the generalized Gouy phase (GGP) shift [16–19].

### III. CONCLUSION

In this paper, waveguide crossing has been solved by giving a simple rule for an efficient mode coupling at both ends of a cylindrical optical waveguide. Using the optimum number of modes given by the rule, crossing of the optical waveguide is achieved successfully regardless of the constraint of the ratio between the beam spot size and the waveguide radius.

### REFERENCES

- [1] Q. Wu, J. Zhang, Y. Yang, and X. Shi, “The temperature compensation for TE011 mode resonator with bimetal material,” *Applied Computational Electromagnetic Society (ACES) Journal*, vol. 34, no. 7, pp. 1070-1075, Jul. 2019.
- [2] M. Stefszky, R. Ricken, C. Eigner, V. Quiring, H. Herrmann, and C. Silberhorn, “Waveguide cavity resonator as a source of optical squeezing” *Phys. Rev Applied*, vol. 7, pp. 044026, 2017.
- [3] S. Pachnicke, *Fiber-Optic Transmission Networks: Efficient Design and Dynamic Operation*, Springer-Verlag Berlin Heidelberg, 2012.
- [4] Á. A. San-Blas and J. M. Roca, “Highly efficient technique for the full-wave analysis of circular waveguide filters including off-centered irises,”

- Applied Computational Electromagnetic Society (ACES) Journal*, vol. 30, no. 11, pp. 1230-1240, Nov. 2015.
- [5] R. G. Hunsperger, *Integrated Optics Theory and Technology*. Sixth Edition, Springer-Verlag New York, 2009.
- [6] E. A. J. Marcatili and R. A. Schmeltzer, "Hollow metallic and dielectric waveguides for long distance optical transmission and lasers," *Bell Syst. Tech. J.*, vol. 43, pp. 1783-1809, 1964.
- [7] J. J. Degnan, "The waveguide laser, A review," *Appl. Phys.*, vol. 11, pp. 1-33, 1976.
- [8] R. L. Abrams, "Coupling losses in hollow waveguide laser resonators," *IEEE J. Quantum Electron.*, vol. QE-8, pp. 838-843, Nov. 1972.
- [9] Y. Wong and N. H. Hiraguri, "Attenuation in lossy circular waveguides," *Applied Computational Electromagnetic Society (ACES) Journal*, vol. 34, no. 1, pp. 43-48, Jan. 2019.
- [10] P. W. Smith, "A waveguide gas laser," *Appl. Phys. Lett.*, vol. 19, pp. 132-134, 1971.
- [11] F. P. Roullard III and M. Bass, "Transverse mode control in high gain, millimeter bore, waveguide lasers," *IEEE J. Quantum Electron.*, vol. QE-13, pp. 813-819, Oct. 1977.
- [12] R. L. Abrams and A. N. Chester, "Resonator theory for hollow waveguide lasers," *Appl. Opt.*, vol. 13, pp. 2117-2125, 1974.
- [13] M. TACK, "The influence of losses of hollow dielectric waveguides on the mode shape," *Journal of Quantum Electronics*, vol. QE-18, pp. 2022-2026, 1982.
- [14] R. Gerlach, D. Wei, and N. Amer, "Coupling efficiency of waveguide laser resonators formed by flat mirrors: Analysis and experiment," *IEEE Journal of Quantum Electronics*, vol. Qe-20, no. 8, pp. 948-963, 1984.
- [15] H. Kogelnik, "Coupling and conversion coefficients for optical mode," in *Proc. Symp. Quasi-Optics*, J. Fox, Ed, Brooklyn, NY: Polytechnic Press, pp. 333-347, 1964.
- [16] H. Kogelnik and T. Li, "Laser beams and resonators," *Proc. IEEE*, vol. 5, no. 4, pp. 1312-1329, 1966.
- [17] A. E. Siegman, *Lasers*, University Science Books Mill Valley, California (1986).
- [18] Z. Derrar Kaddour, A. Taleb, K. Ait-Ameur, and G. Martel, "Revisiting gouy phase," *Optics Communications*, vol. 280, pp. 256-263, 2007.
- [19] Z. Derrar Kaddour, A. Taleb, K. Ait Ameur, G. Martel, and E. Cagniot, "Alternative model for computing intensity patterns through apertured ABCD systems," *Optics Communications*, vol. 281, pp. 1384-1395, 2008.



**Billel Bentouhami** received the engineering degree in physics from the University of Ferhat Abbes, Sétif, Algeria, in 2009 and the Magister degree in quantum electronics from the University of Sciences and Technology Houari Boumediène (USTHB), Algeria, in 2012. He is currently working toward the Ph.D. degree with the University of Sciences and Technology Houari Boumediène.

He is a member of the Quantum Electronics Laboratory LEQ of USTHB and is presently an Assistant Professor of Physics with the University of Bordj Bou Arreridj, Algeria. His research interests include optical waveguides, diffraction, electromagnetic field propagation and quantum electronics.



**Zaia Derrar Kaddour** received the Ph.D. degree in physics from the University of Sciences and Technology Houari Boumediène, Algeria, in 2007.

She is a member of Quantum Electronics Laboratory LEQ and an OSA member. She is currently a Professor of Physics with the University of Sciences and Technology Houari Boumediène, Algeria. Her current research interests include optical resonators, electromagnetic field propagation, and optics.

